DATA ANALYSIS AND DATA ASSIMILATION OF ARCTIC OCEAN OBSERVATIONS

By

Jacob Nathaniel Stroh

A Dissertation Submitted in Partial Fulfillment of the Requirements
for the Degree of

Doctor of Philosophy
in
Numerical Ice/Ocean Modeling and Data Assimilation:
Interdisciplinary Program

University of Alaska Fairbanks
May 2019

APPROVED: Gleb Panteleev, Committee Chair
Nicole Mölders, Committee Co-Chair
Thomas Weingartner, Committee Member
John Rhodes, Committee Member
Javier Fochesatto, Chair
Deparment of Atmospheric Science
Leah Berman, Interim Dean
College of Natural Science and Mathematics
Michael Castellini, *Dean of the Graduate School*

In fond memory of Irene J. Zalegowski (n´ee Przecha),
whose love and home still pervade my heart and dreams.

Abstract

Arctic-region observations are sparse and represent only a small portion of the physical state of nature. It is therefore essential to maximize the information content of observations and observation-conditioned analyses whenever possible, including the quantification of their accuracy. The four largely disparate works presented here emphasize observation analysis and assimilation in the context of the Arctic Ocean (AO). These studies focus on the relationship between observational data/products, numerical models based on physical processes, and the use of such data to constrain and inform those products/models to different ends.

The first part comprises Chapters 1 and 2 which revolve around oceanographic observations collected during the International Polar Year (IPY) program of 2007–2009. Chapter 1 validates pan-Arctic satellite-based sea surface temperature and salinity products against these data to establish important estimates of product reliability in terms of bias and bias-adjusted standard errors. It establishes practical regional reliability for these products which are often used in modeling and climatological applications, and provides some guidance for improving them. Chapter 2 constructs a gridded full-depth snapshot of the AO during the IPY to visually outline recent, previously-documented AO watermass distribution changes by comparing it to a historical climatology of the latter 20th century derived from private Russian data. It provides an expository review of literature documenting major AO climate changes and augments them with additional changes in freshwater distribution and sea surface height in the Chukchi and Bering Seas.

The last two chapters present work focused on the application of data assimilation (DA) methodologies, and constitute the second part of this thesis focused on the synthesis of numerical modeling and observational data. Chapter 3 presents a novel approach to sea ice model trajectory optimization whereby spatially-variable sea ice rheology parameter distributions provide the additional model flexibility needed to assimilate observable components of the sea ice state. The study employs a toy 1D model to demonstrate the practical benefits of the approach and serves as a proof-of-concept to justify the considerable effort needed to extend the approach to 2D. Chapter 4 combines an ice-free model of the Chukchi Sea with a modified ensemble filter to develop a DA system which would be suitable for operational forecasting and monitoring the region in support of oil spill mitigation. The method improves the assimilation of non-Gaussian asynchronous surface current observations beyond the traditional approach.

Table of Contents

List of Figures

List of Tables

Glossary

Term	Definition
ACC	Alaska Coastal current
ADCP	Acoustic Doppler Current Profiler
AW	Atlantic Water
CTD	Conductivity-Temperature-Depth
DAS	Data assimilation system
FWC	Fresh-water content
HFR	High-frequency radar
GDOP	Geometric Dilution of Precision
IPY	International Polar Year
ITP	Ice-tethered Profiler
MIZ	Marginal Ice Zone
OSSE	Observation System Simulation Experiment
PIZ	Pack Ice Zone
PSU	Practial salinity units
PW	Pacific Water
RMSD	Root-mean-squared difference
SST	Sea-surface temperature
SIC	Sea ice concentration
SIT	Sea ice thickness
SIV	Sea ice velocity
SSH	Sea-surface height
SST/S	Sea-surface temperature and salinity
T/S	Temperature and salinity
T_{max}	Maximum temperature
τ_a	Ice-atmosphere wind stress

Acknowledgements

It is impossible for the author to fully express his gratitude for the support (in terms of encouragement and paychecks through advancement to candidacy) and guidance offered by advisor Gleb Panteleev over the years[1]. Dmitry Nicolsky, however, is unequivocally credited for inciting mentorship under Gleb. The author also thanks his patient committee for their commitment to seeing the completion of this degree, however uncertain[2] it looked along the way. Specifically, Nicole Mölders served as academic advisor since September 2018 and is responsible the author's return to the College of Natural Science and Mathematics; she is fiercely thanked for much-needed end-of-game whip-cracking and willingness to take the mantle of committee chair. Tom Weingartner served as the original academic advisor when the College of Fisheries and Ocean Science hosted this degree; he is solely responsible for the author's introduction to *practical* oceanography in Fall 2009 by casually permitting an unenrolled non-student to regularly attend lecture during a particularly ugly period of the author's personal life. John Rhodes served as an integral member not only of this committee, but of the author's previous committee for a degree in the Mathematics department; his careful dissection of early data assimilation notes led to a diagnosis of some significant mis-understandings by the author. Peter Webley acted as an external examiner during advancement and confirmation stages of this degree; his request that the author better communicate the context of this work in relation to the broader scientific community is strongly appreciated.

Additionally, co-authors of accepted works and other collaborators are heartily thanked for their contributions. In particular, Max Yaremchuk, Sergei Kirillov, and Oceana Francis contributed considerably to several of these publications and fleshed out the author's education (and publication presence) with other projects on which he is a co-author. The presented works required extensive access to and administrative support of computational resources; they could not have been completed without the aid of Jim Long and Matt Barkdull.

---

[1] This includes their first encounter in 2004. The author and then-officemate Elçin Jafarov sought I. Polyakov (whom the latter knew socially) for help in understanding geostrophic adjustment for assignments in course taught by Bill Hibler. They instead found Gleb lurking around the International Arctic Research Center, and he willingly spent two hours of his time teaching two first-year in-over-their-heads young mathematicians some basics of geophysical fluids.

[2] Many personal and professional problems beset the author during this program. An inexhaustive list of significant issues is: death of most of the author's immediate family (∼4/5000 of his hometown); restructuring, remodelling, and redirection of the research institution where the author was mentored; a 3-year gap in full-time support immediately following his advancement to candidacy; departure of the author's research advisor from the University of Alaska Fairbanks; the retirement of the author's academic advisor; and the change of college and degree program during the author's final year of study. The author also acknowledges that his role in and reaction to these issues sometimes exacerbated them.

Vladmir Alexeev[3] and Igor Polyakov[4] enabled (in different capacities) the author's participation in time at sea in the high Arctic and an immersive education in climatology. During this opportunity, Andrew Slater mentioned attempting to apply filtering methods to non-stationary observation histories; he is sadly missed as a professional contact, fellow generalist-in-arms, and friend. Uma Bhatt, Mark Johnson, and Javier Fochesatto were crucial sources of non-committee advice and administrative support for changing the host department of this degree in fall 2018. Finally, an interdisciplinary program experience which undergoes multiple leaves-of-absence, changes of advisorship, a change in host colleges and programs, and re-approval of former professors who left the university requires bureaucratic hoop-jumping beyond the comprehension of mortals; nevertheless, paperwork throughout was completed in a timely and efficient manner thanks to the efforts of Christina Sutton, Megan Blanchard, Barbara Day, and Mandi Goddard.

Terminal support which permitted completion this degree is thanks to a one-semester Thesis/Dissertation Completion Fellowship awarded by the University of Alaska Fairbanks Graduate School. The author lastly acknowledges and is thankful for the pervasive culture of interest in Earth throughout the University of Alaska Fairbanks, and for the small-town-esque social complex of people[5] who compose the university.

---

[3] During application to this degree program, V.A. acted as an "interim research advisor" for the purposes of completing paperwork by deadlines.

[4] I.P. provided an excellent one-on-one course on ocean-atmosphere interaction during this degree program. The author is unfortunate to have been unable to continue working with him. Outside influences such as funding issues restricted the author from having time to dedicate to ongoing work together. The author's lack of candidness about it with I.P., rather than the situation in-and-of itself, is the largest regret of this journey.

[5] The author means this broadly and inclusively of e.g. custodians, shuttle drivers, ice scrapers, gardeners, dining and concessionary workers, postal employees, maintenance and facilities workers, &*c.* whose contributions, the author opines, are often overlooked and under-appreciated by the white-collar body of the university.

General Introduction

The importance of numerical modeling in all disciplines of modern geophysics cannot be understated, despite the presence of vast observational data. The now-classical adage that "all models are wrong but some are useful" [*Box*, 1979] reflects an acknowledgement that models are limited in their ability to capture essential observable details. The counterpoint statement that "all observations are wrong" is less commonly accepted despite knowledge that instrument precision and accuracy are also limited; although they are often treated as unconditional references, observations necessarily include estimated errors in spatiotemporal representation as well. The implicit assumption of observations as absolute is seen most clearly in use of the word "errors" when measuring differences between observations and model-equivalent quantities where "difference" would be more appropriate. The synthesis of numerical models and observational data should assume neither is perfect by accounting for their errors. The frameworks of data assimilation (DA) and analysis explored here rely on uncertainties in both models and observations.

This work follows the format of a paper thesis, rather than a manuscript. It includes no primer or introduction to the basic mathematical formulation of the problem at the heart of DA. Readers unfamiliar with the fundamentals of DA are thus referred to *Thacker* [1987]; *Bouttier and Courtier* [2002]; *Kalnay* [2003] for the necessary background.

The first chapter, published as *Stroh et al.* [2015] [1], focuses on the assessment of ocean surface-variable data products in the Arctic region. The commonly-used analyses which provide daily sea-surface temperature (SST) rely primarily on remotely-sensed satellite-derived observations. DA-modeling systems using underlying circulation models rather than pure data-analysis to produce ocean surface quantities also estimate essential climate variable sea-surface salinity (SSS); they also rely heavily on satellite observation as other regional observations are sparse and infrequent. Previous works assessing the quality of Arctic satellite-informed ocean products are primarily validation studies performed with limited observational data. Instead, this paper provides statistical analysis of differences between product and observed quantities by comparing them with year-round pan-Arctic *in situ* data. The observational data included the contents of an online[2] IPY 2007-2008 oceanographic measurement database developed by the author with additional data from other sources covering years 2010–2012. The results benchmark product

---

[1] The work is solely that of the first author with some advice and guidance from the second. The third author was co-principle investigator of the project supporting the work and was thus partially responsible for funding. Subsequent authors contributed either data for post-IPY analysis and/or publication fees.

[2] The public database was offline for most of 2018. It is currently back online as of 2019-03-08, but the author no longer maintains it and does not know whether the host machine will remain supported for long.

reliability in region, and quantify bias and uncertainty of analysis quantities. Use of ice-tethered profiler data to represent foundational SST and SSS in the central Arctic is novel; it provides an estimate of surface data in regions unobservable by satellite due to sea-ice obstruction or orbit limitations. Finally, it provides a statistical estimate of SST-adjustment on the basis of observable sea-ice concentration to improve analysis accuracy.

The second chapter is a published book chapter [*Stroh et al.*, 2018][3] which gives a synopsis of changes in the Arctic Ocean evident at the time of the pan-Arctic IPY 2007–2008 survey. The work is centered around a full-depth snapshot of the Arctic Ocean during 2007–2009 calculated by statistical variational interpolation of the IPY database contents. The numerical code used to refine the pointwise observations into a complete, gridded analysis was developed by GeoHydrodynamic and Environmental Research (GHER); it is the only computational component of this thesis using external algorithms. This processing routine was likewise applied to a private Russian archive of historical measurements by co-authors with access to them. Calculated watermass distributions from the IPY 2007–2008 snapshot reveal developed changes in watermass, heat, and freshwater distributions when compared with the corresponding 1950–1996 climatology. The IPY database contents are further used for variational DA of mid-level currents and sea-surface height (SSH). Data-conditioned modeling suggest the source of some changes in the Pacific domain, including Greenland-region freshwater accumulation in the Beaufort Gyre and influence of SSH depression on inflow through Bering Strait. Though less technical than other works included in this corpus, the breadth of literature cited during the chapter preparation provided a robust survey of Arctic Ocean climate-related research over the past 15 years.

Chapter three is a recently accepted study [*Stroh et al.*, 2019][4] done in collaboration with the research team that currently employs author's research advisor. The paper argues for the use of spatially-variable ice strength parameters in sea ice model rheology, where they are typically

---

[3] The first author prepared and organized the observational data into an online database mentioned previously, and developed the manuscript. In organizing a framework for the project, the author independently learned and implemented the variational interpolation program used to produce the final gridded results. However, the paper is largely based on the final results of the second author who had previously implemented that same routine and had access to the Russian data archive. The third, fourth, and fifth co-authors contributed sections on data assimilation, and the final two authors are responsible for unknown work with the Russian archive.

[4] This work is the result of a close collaboration among the authors. The 1-D model was originally coded by the Naval Research Laboratories (NRL) collaborators, and each co-author played a role in developing, testing, and refining the tangent linear and adjoint models needed to construct the assimilation system. The first author primarily debugged the forward and adjoint models for consistency, and performed extensive initial testing configurations of the DAS using different numerical optimization approaches with an emphasis on ensuring robust convergence. More significant issues regarding adjoint stability were addressed by the NRL crew who developed the adjoint code with respect to rheological parameters. The third author contributed much needed computing resource access to the first author and help in designing appropriate observational system simulation experiments.

assumed to be invariant homogeneous. Experiments apply 2D variational DA to optimize initial data and spatially variable parameter distributions in a 1D viscoplastic sea ice model by ingesting representatives of common sea ice observations (thickness, concentration, and velocity) with realistic errors in data and forcing. Results demonstrate improvement and controllability of the simple model in cases with full ice cover (via rheological parameters) and partial ice cover (via wind stress). In full-ice regimes, simulations using optimized varying compressive ice strength parameters had error statistics that were more normal with lower bias, permitted more clear instances of ice ridging in ice-convergent areas, and generated more ice than those using constant parameters. The same algorithm applied to regimes with significant open water showed assimilation of sea ice velocity data to optimize local wind stress led to improved results, and suggests that remotely-sensed sea ice observations might be used to improve atmospheric boundary data. Extension to more practical 2D ice models is an ongoing work, but requires extensive numerical development to ensure stability of the elastoviscoplastic adjoint model.

The fourth chapter[5] presents the implementation of an ensemble-based DA system (DAS), constructed to assimilate velocity profile and surface current observations in the greater Chukchi Sea area. The DAS applies a modified version the Maximum Likelihood Ensemble Filter (MLEF) to the Regional Ocean Modeling System (ROMS) for the purpose of assimilating moored velocity meter and high-frequency-radar surface current observations during the ice-free summer season. Specifically, the implemented method reflects an ensemble-transform approach to solve the 4D variational cost function using a forward-only sequential optimization process. Linear combinations of ensemble perturbations condition the analysis on timeseries of observations rather than instantaneous representatives. The analysis identifies the mode of the posterior probability distribution in contrast to Kalman-type filters which identify the mean; these statistical estimates differ due to the non-Gaussian nature of the surface current measurements and, by extension, of the model-minus-observation residuals. Two DAS configurations which rely on observed ensemble histories throughout the forecast step are benchmarked and compared with data both assimilated and external. A noteworthy difference in filter response between the HFR observation representations is related to the imparted surface forcing and to the strength of observed nearshore cross-isobath surface currents which the model does not resolve well. Results strongly intimate the advantages of an asynchronous variational DAS for operational environmental disaster miti-

---

[5] This is work solely by the author with some necessary guidance from the author's advisor. The advisor nevertheless acknowledges his committee, each of whom in some way contributed significantly to this work in terms of guidance, resources, and education.

gation over the shelf. The background ROMS model is (unintentionally) ill-configured and gives overall unrealistic results as discussed in the chapter. While the DA is found to greatly improve the forecast model in the region populated by observations, a reconfiguration of the underlying model is necessary for DAS results to be useful as a practical representation of the Chukchi Sea. The current state of this ongoing work is presented here in manuscript form.

Bibliography

Bouttier, F., and P. Courtier (2002), Data assimilation concepts and methods march 1999, *Meteorological training course lecture series. ECMWF*, p. 59.

Box, G. E. (1979), Robustness in the strategy of scientific model building, in *Robustness in Statistics*, pp. 201–236, Elsevier.

Kalnay, E. (2003), *Atmospheric Modeling, Data Assimilation and Predictability*, Cambridge University Press.

Stroh, J.N., G. Panteleev, S. Kirillov, M. Makhotin, and N. Shakhova (2015), Sea-surface temperature and salinity product comparison against external in situ data in the Arctic Ocean, *Journal of Geophysical Research: Oceans*, *120*(11), 7223–7236. DOI: *10.1002/2015JC011005*

Stroh, J.N., S. Kirillov, G. Panteleev, O. Francis, M. Yaremchuk, E. Bloshkina, and N. Lebedev (2018), Changes in Arctic Ocean climate evinced through analysis of IPY 2007–2008 oceanographic observations, in M. Kanao (Ed.), *Arctic Studies-A Proxy for Climate Change*, IntechOpen. DOI: *10.5772/intechopen.80926*

Stroh, J.N., G. Panteleev, M. Yaremchuk, O. Francis, and R. Allard (2019) , Toward optimization of rheology in sea ice models through data assimilation, *Journal of Atmospheric and Oceanic Technology*. (accepted)

Thacker, W. (1987), Three lectures on fitting numerical models to observations. external rep, *Tech. report*, GKSS 87/E/65. GKSS Forschungszentrum Geesthacht, Geesthacht, Federal.

Chapter 1: Sea-surface Temperature and Salinity Product Comparison against External in situ Data in the Arctic Ocean[1]

Abstract

Sea-surface temperature and salinity (SST/S) in the Arctic Ocean (AO) are largely governed by sea-ice and continental runoff rather than evaporation and precipitation as in lower latitude oceans, and global satellite analyses and models which incorporate remotely-observed SST/S may be inaccurate in the AO due to lack of direct measurements for calibrating satellite data. For this reason, we are motivated to validate several satellite sea-surface temperature (SST) data products and SST/S models by comparing gridded data in the AO with oceanographic records from 2006–2013. Statistical analysis of product-minus-observation differences reveals that the satellite SST products considered have a temperature bias magnitude of less than 0.5°C compared to ship-based CTD measurements, and most of these biases are negative in sign. SST/S models also show an overall negative temperature bias, but no common sign or magnitude of salinity bias against CTD data. Ice Tethered Profiler (ITP) near-surface data spans the seasons of several years, and these measurements reflect a sea-ice dominated region where the ocean surface cannot be remotely observed. Against this data, many of the considered models and products show large errors with detectable seasonal differences in SST bias. Possible sources of these errors are discussed, and two adjustments of product SST on the basis of sea-ice concentration are suggested for reducing bias to within less than 0.01°C of ITP near-surface temperatures.

1.1 Introduction

Sea-surface temperature and salinity (SST and SSS, respectively, or SST/S collectively) are designated by the World Meteorological Organization as "essential climate variables" [*GCOS*, 2011]. At the interface of the ocean and atmosphere, they play a role in coupling highly dynamical components of the global climate system and are diagnostic of the present ocean state. Tropical and mid-latitude SST/S are driven largely by precipitation and evaporation, poleward heat transfer via ocean currents, and large basin-scale processes. In contrast, the SST/S of Arctic Ocean (AO) are strongly influenced by sea-ice and related melt waters, brine rejection, continental runoff onto broad continental shelves, and the upward flux of heat from the deeper warm ocean.

The AO is also marked by a cold, fresh surface layer in contrast to the monotonic decrease of

---

[1] Stroh, JN, G. Panteleev, S. Kirillov, M. Makhotin, and N. Shakhova, (2015), Sea-surface temperature and salinity product comparison against external in situ data in the Arctic Ocean. *Journal of Geophysical Research: Oceans*, 120(11), 7223–7236, DOI: *10.1002/2015JC011005*.

temperature with depth common to most world oceans [*Comiso*, 2010]. Surface salinity therefore plays a significant role in the dynamics of the near-surface waters; density of cold water is more sensitive to salinity than temperature. While the AO is small compared to other oceans, a comprehensive understanding of its dynamics is inhibited by the cost and difficulty of directly measuring this extreme environment. At present, observations are dominated by remotely-sensed surface data [cf. *Emery et al.*, 2001; *Kawai and Wada*, 2007; *Donlon et al.*, 2012]. Satellite-derived observations provide much greater spatial coverage than sparse in situ methods, albeit at lower resolution.

The spectral data which compose satellite SST/S observations are restricted to the very uppermost ocean layers. Infra-red (IR) sensors measure "skin" SST at micrometer depths where thermal transfer cools the interface. Below the skin layer lies a meters-thick region where temperatures may exhibit fluctuations due to daily insolation and atmospheric wind. Microwave (MW) sensors which penetrate to millimeter depths are able to measure SST/S at the top of this sub-surface layer where direct solar influences are most pronounced. The base temperature of this layer, independent of diurnal variability, defines foundational SST and is sought as the best near-surface representative of temperature.

The spatial resolution of IR sensors is on the order of 1 km, while that of MW sensors is an order of magnitude larger. Satellite data products may incorporate observations from several sensors with different resolutions and penetration depths to produce accurate representations of SST. Remotely-sensed emissions spectra must therefore be adjusted to foundational SST/S by accounting for cool-skin effects, diurnal insolation, wind, precipitation, and sensor inaccuracies [*Fairall et al.*, 1996]. Such techniques for empirical calibration of satellite measurements are not discussed here but may be found in *Robinson* [2004] and product documentations. Limited in situ data available for tuning and calibrating these algorithms may lead to SST/S inaccuracy in the AO where the mechanisms influencing the vertical temperature structure differ from those in data-abundant regions.

Validation and inter-comparison studies of gridded global satellite SST analyses use in situ data such as Argo drifters [*Martin et al.*, 2012] and other inventories of global in situ measurements [*Dash et al.*, 2012] with sparse AO coverage. *Chen et al.* [2002], *Corlett et al.* [2006], and *Høyer et al.* [2012] use in situ buoy data for AO satellite SST calibration and validation, with the latter studies augmenting their comparison sets with ship and radiometer records, respectively. Recent modeling studies works by *Gammelsrød et al.* [2009] and *Nguyen et al.* [2009, 2011] include in situ T/S for comparison of hydrographic transport and verification of calibrated model parameters, respectively. *Sakov et al.* [2012] compare model T/S to in situ profiles to validate a data-assimilated Arctic model and assess its sensitivity to sub-ice ITP data.

Concern for the uncertainties in transforming satellite-data into foundational SST/S estimates motivates this study which validates selected global satellite SST products and SST/S models in the Arctic region. The relationship of gridded data dependent on satellite temperature measurements to external in situ SST/S measurements is explored statistically in this paper. The investigation relies heavily on the contents of an online-accessible International Polar Year 2007–2008 (IPY) measurement database (http://oregon.iarc.uaf.edu/dbaccess.html[2]) containing more than 12 thousand ship-cast CTD profiles in the Arctic region spanning 2006–2011. Section two summarizes the satellite analyses, model outputs, and in situ data used in this comparison. Section three describes the comparison methodology, section four discusses results of the product-to-data correspondences, and the final section summarizes results. Use of SST, SSS, and SST/S throughout the text refers to foundational values unless otherwise noted.

1.2 Data

Two types of gridded SST/S are discussed here: SST analysis and SST/S model products. The former consist of SST maps and other fields synthesized from algorithmic processing of satellite data and typically in situ data when available. The latter products are generated by programs driven by primitive-equation models which use observational data for parameter calibration or state adjustment (i.e. data assimilation). The terms "analyses" and "models" hereafter succinctly refer to satellite-derived datasets and data-conditioned model output, respectively, and "product" is used to describe data from either source. Several criteria aided in the selection of the product datasets. The data needed to be freely available online, include gridded daily coverage of the Arctic regions between 65°N and 82°N for the majority of years 2006–2009 or 2010–2013.

1.2.1 Analysis Products

Briefly discussed in this section are the included satellite-derived SST products which meet the above-listed requirements. Satellite SSS analyses for the AO meeting the desired criteria were not available at the time of this study.

Three included satellite products target at-depth SST: the NOAA 1/4° Optimal Interpolation SST version 2 (OISSTv2) [*Reynolds et al.*, 2007] available for 1981–present at http://www.ncdc.noaa.gov/

---

[2] See footnotes in the General Introduction for details regarding this database.

oisst, the NCEP Marine Modeling and Analysis Branch 1/12° high-resolution Real-Time Global SST (RTG_HR) [*Thiébaux et al.*, 2003; *Gemmill et al.*, 2007] available for 2006–present at ftp://polar.ncep.noaa.gov/pub/history/sst/ophi/, and the Naval Oceanographic Office 1/10° SST analysis (K10_SST) available for 2008–present at http://podaac.jpl.nasa.gov/dataset/NAVO-L4HR1m-GLOB-K10_SST. Included products which target foundational SST are: the UK Met Office 1/20° Operational SST and Sea Ice Analysis (OSTIA) [*Stark et al.*, 2007; *Donlon et al.*, 2012] available for April 2006–present at http://www.myocean.eu, the NASA Jet Propulsion Laboratory 1/100° Multi-scale Ultra-high Resolution SST (MURSST) [*Chin et al.*, 2013] available for 2002–present at http://podaac.jpl.nasa.gov/Multi-scale_Ultra-high_Resolution_MUR-SST, the Australian Bureau of Meteorology 1/4° Global Australian Multi-Sensor SST Analysis (GAMSSA) [*Zhong and Beggs*, 2008] available for late 2008–present at ftp://podaac-ftp.jpl.nasa.gov/allData/ghrsst/data/L4/GLOB/ABOM/GAMSSA_28km, and the Remote Sensing Systems 1/4° MW-IR SST version 4 (RSS_SST) available for 2002–present at http://www.remss.com/measurements/sea-surface-temperature/.

All analyses are based on MW and IR satellite data except for RTG_HR, which incorporates no MW data, and OISSTv2, which incorporated MW only until October 2011. Algorithms used by the analyses to combine satellite observations and other data into complete gridded fields generally are based either on optimal interpolation or related variational methods. In addition to satellite data, analyses often use in situ data from ships and buoys in their optimization; however, K10_SST and RSS_SST analyses do not use in situ data, and MURSST uses this data for quality control rather than in its variational optimization.

1.2.2 Model Products

The first SST/S model output to be compared comes from the NASA JPL Estimating the Circulation and Climate of the Ocean, Phase II project. The MITgcm-based model generates full-depth global ocean output together with an interactive sea-ice component at 1/4° grid spacing, then assimilates satellite and in situ observations via kernel and adjoint methods [*Menemenlis et al.*, 2005]. The dataset used in this work is the geographically-interpolated NASA/JPL Cube92 model output available at ftp://ecco2.jpl.nasa.gov/data1/cube/cube92. The two-dimensional daily averaged SST and SSS fields from 2006–2012 of that dataset are herein referred to as ECCO2 data, and represent quantities averaged over the top 10 m.

The second model output is produced as part of the US Global Ocean Data Assimilation Experiment. This production system data-optimizes the model state calculated by the Hybrid

Coordinate Ocean Model (HYCOM) using the Navy Coupled Ocean Data Assimilation [*Cummings*, 2005]. This 3-dimensional variational system assimilates satellite and in situ observations including altimeter data, SST, and sea-ice. This study specifically uses the 0 m vertical level of the 3-dimensional temperature and salinity (T/S) from HYCOM + NCODA Global analysis GLBa0.08 experiments 90.6–90.1 (https://hycom.org/dataserver/glb-analysis). These fields correspond to SST and SSS from late 2008–present and are referred to herein as HYCOM data for brevity.

1.2.3 In situ Observations

The direct observational data used for validation include: a rich collection of hydrographical measurements from the 2007–2008 IPY collaboration which extends from 2006 through 2012; hydrographical profiles from Woods Hole Oceanographic Institute (WHOI) cruises to the Beaufort Sea during 2006–2013 and from international cruises to the Eurasian Arctic shelf during 2011–2013; and WHOI ice-tethered profilers (ITPs) adrift starting in 2006 [*Krishfield et al.*, 2008; *Toole et al.*, 2011]. This data is organized into three groups: sets of hydrographical profiles collected during 2006–2009 and 2010–2013, and one set of near-surface measurements from ITP during 2006–2013. The first groups consist of ship-based rosette CTD profiles collected either in the years around the recent IPY or in the years after 2009, supplemented by a small number of expendable CTD (xCTD) readings. For brevity, these groups are identified as "IPY CTD" and "post-IPY CTD" hereafter. The third group comprises T/S data obtained from shallow microCAT sensors attached to ITPs as well as the upper-most profiler readings, and is referred to as "ITP."

The IPY CTD set includes the 2006–2009 ship-based CTD and xCTD profiles from the IPY database as well as Beaufort Sea and Siberian Shelf rosette CTD and xCTD profiles from cruises conducted during 2006–2009. Ship-based CTD observations from 2010–2013 contained in the IPY database are included in the post-IPY CTD set. Much of the IPY and post-IPY CTD data was obtained in pre-processed form with profiles resolved to less than one meter depth using undocumented methods. Therefore, any data between 0 m and 3 m is ignored as its origins are often uncertain. The ITP dataset was obtained online in the form of roughly 30 thousand time-averaged profiles from the WHOI website (http://www.whoi.edu/website/itp), and this data was filtered to retain only data above 10 m depth.

All in situ measurements used contain T/S data; records lacking either were omitted. Profiles with values identically zero or unrealistic temperatures beyond the range −2.2–30°C or salinities beyond 0–40 PSU in the top 10 m are omitted. The inherent instrument errors associated with these datasets are small. CTD sensors typically have accuracies on order 10^{-3} °C (10^{-2} °C for xCTD) for temperature and order 10^{-3} PSU (10^{-2} PSU for xCTD) for salinity [*Sy and Wright*, 2000], with similar initial accuracies established for microCAT sensors. The IPY CTD, post-IPY CTD, and ITP datasets consist of roughly 9800, 1230, and 14,000 near-surface profile representatives, respectively, at locations illustrated in Figure 1.1. Use of "CTD" hereafter refers exclusively to the ship CTD and xCTD records collected in the IPY CTD and post-IPY CTD observation groups unless specified otherwise.

1.3 Methodology

Calculation of foundational SST/S obtained from CTD and ITP profiles requires careful consideration. This study uses the measurement average over the range of 3–7 m to represent foundational SST/S for each profile similar to *Lee et al.* [2010]. Exclusion of the upper 3 m is intended to avoid the most extreme variations in the diurnal temperature cycle and to avoid measurements of questionable origin. For non-ITP records where surface salinity remains above 20 PSU, mean density and temperature profiles show little vertical change over the range 3–7 m (Figure 1.2). Use of the 3–7 m range for averaging is motivated by this observation and analytically justified by way of a constrained variance minimization algorithm as follows. Use R and T to denote the mean density and temperature profiles, respectively, shown in Figure 1.2 between depths 1 m and 10 m, and use $\overline{R}(a,b)$ and $\overline{T}(a,b)$ to denote the averages of those profiles over depths a–b m. Ranges which minimize the total variance in R and T may be sought by finding $\operatorname{argmin}\left[\left(R-\overline{R}(a,b)\right)^2+\left(T-\overline{T}(a,b)\right)^2\right]$ constrained by values such that $a < 2$ m and $a < b < 10$ m. Among the several near-integer solutions with roughly-equal minimum variances in R and T, the range 3–7 m is the optimal solution with the largest difference between endpoints. However, the mean salinity profile has the lowest variance over the range of 1–5 meters as calculated by a similar process. ITP microCATs record T/S data with a minimum depth typically between 5 m and 6 m, and ITP SST/S representatives are thus calculated as an average of 1–3 values measured by profiler data binned at 7 m and shallower microCAT data.

Gridded SST/S product data was linearly interpolated in space and time to produce representative SST/S values collocated with each observation. Validation of data products requires comparison against independent data not used in their generation. The assembled IPY database contents were held privately for data contributors and only recently made publicly available, and roughly one-half of the post-IPY CTD data was obtained from closed sources. Most of the data therefore could not have been used for that purpose as it was not available for real-time production. A small portion of older data included in this study may have been used for quality control purposes by eg. GHRSST in producing low-level background fields on which several analyses are based.

The statistical correspondence between measurements and products quantifies how well the product represents the observed ocean. In situ observations are known with accuracy and certainty, so the quality of a product or model can be roughly ascertained from the fit to the observations. Correlation, product-minus-observation residual bias, and centered root mean squared difference (RMSD) between products and observations data are able to assess how well a product tracks the background state and captures the temporal and spatial variability of the ocean. Anomaly correlation (and associated potential skill) between products and observations is not used; the necessary selection of background climatologies for this metric is likely to favor certain products over others.

1.4 Results

Direct comparison of representative observational data with gridded products permits estimation of product reliability with an operating assumption that 3–7 m averaging of in situ observations targets the same SST/S intended by the gridded data. Figures 1.3 and 1.4 illustrate the quality of fit between the included SST analyses and SST/S models, respectively, and in situ observations. The spatial distributions of these product-minus-observation residuals are charted geographically in Figures 1.5 and 1.6, with residual statistics appearing in Tables 1.1 and 1.2. Negative values in this table may be interpreted as products being cold relative to observations and the true ocean state. Figure 1.7 shows comparison of products to CTD and ITP data groups in the from of Taylor diagrams [*Taylor*, 2000], which resolve second-order statistics and should be considered in conjunction with the biases presented in Tables 1.1 and 1.2. Use of Taylor diagrams is intended to provide a convenient visual comparison and rough ordering of products in relation to how well they match the variability of observations.

1.4.1 Comparison against ship-based CTD datasets

Satellite analysis sea-surface temperatures compare favorably with CTD measurements, and tend to have small negative SST biases. K10_SST and RSS_SST analyses have the smallest biases and RMSDs relative to the IPY dataset. During the post-IPY period, the smallest magnitude biases of

−0.02 °C are found for RSS_SST and MURSST products with the SST of the latter showing slightly more precision. For IPY and post-IPY datasets respectively, GAMSSA SST has the largest overall biases of −0.27 °C and −0.93 °C. The GAMSSA SST cold bias in the AO, previously identified in *Dash et al.* [2012], is exaggerated against post-IPY CTD due to poor representation of SST along the coastal Chukchi and Laptev Seas during the warm and low-ice year 2012. All other included satellite-derived SST analyses have biases and errors against CTD measurements comparable to those found against different in situ measurements in previous studies (eg. [*Donlon et al.*, 2012; *Dash et al.*, 2012; *Høyer et al.*, 2012; *Martin et al.*, 2012]).

Most gridded analyses correlate strongly with CTD observations as visible in the right two-thirds of Table 1.1 and left columns of Figure 1.3. With correlations (as squared Pearson coefficients) universally above 80%, SST analyses track the variability of the IPY CTD set well. Post-IPY CTD correlations are lower in general, with the GAMSSA product showing a low correlation of 59% due to large errors during 2012. OSTIA and MURSST products continue matching 83% and 87%, respectively, of the total CTD variance.

The satellite analyses are similar compared to all CTD measurements, but Taylor diagram in the left plot of Figure 1.7 reveals a rough ranking of all products considered on the basis of second-order statistics. The analyses demonstrate remarkable fit to the variability of CTD SST, with standard errors (as measured by RMSD) within 6% of the true CTD SST standard deviation. The OISSTv2 analysis, despite having the lowest magnitude bias of −0.02 °C, has a larger RMSD and consequently lower overall correlation than other analyses. MURSST analysis appears to be the strongest overall analysis that gives full Arctic coverage without masking sea-ice although OSTIA SST has a higher correlation and lower RMSD in total.

Models show larger biases and error than analyses products, but appear to have statistics comparable with those of the satellite analyses. HYCOM SST has a +0.03 °C bias against post-IPY CTD-derived SST compared to the −0.97 °C bias of ECCO2 SST, and the corresponding RMSD for HYCOM, 1.03 °C, is less than half that of ECCO2 as in Table 1.1. Figure 1.7 shows that HYCOM SST has a higher correlation, lower RMSD, and closer fit to the observed SST variability amplitude than ECCO2 for non-ITP data. In these metrics, the HYCOM+NCODA SST fits CTD SST than the included ECCO2 model does.

The bottom of Table 1.1 includes model-minus-observation SSS residual statistics in the rows labeled "SSS" below each model name, and Figures 1.4 and 1.6 include visualizations of SSS residuals. The ECCO2 and HYCOM SSSs differ in sign of bias; ECCO2 under-represents post-IPY

CTD-derived SSS by an average of −0.58 PSU compared the +1.27 PSU bias of HYCOM, and the RMSD of ECCO2 is roughly 10% lower than that of HYCOM. The difference in bias between these model-derived data consistently exceeds 1 PSU across all observation groups, but both model SSSs correlate well with the CTD data (Figure 1.4, right) with increasing error in model values as observed salinity decreases.

Regional patterns in residuals

Spatial distributions of product SST errors show similarities; see Figure 1.5. Product SSTs are overall slightly cool toward the north Atlantic Ocean with a tendency be warm relative to near-surface CTD toward the Pacific Ocean. In the central AO, there is less agreement: MURSST and GAMSSA SSTs remain cooler than observations while OISSTv2 and RTG_HR analyses are typically warmer. Products also share similar regions where analysis SSTs differ greatly from CTD SST such as the Kara and Beaufort Seas, and the Fram and Bering Straits. Figure 1.6 shows the geographic distribution of SST/S residuals for the two models. Regions of interest in the ECCO2 model are the Greenland and Barents Seas where SST is overestimated in contrast to all other products considered, and the Pacific sector of the Arctic Ocean where the model notably represents the ocean water as too cold and salty both during and after IPY. For commonly resolved CTD data, ECCO2 and HYCOM products appear very salty in the Beaufort and Chukchi Seas. Figure 1.7 shows that against all CTD data, HYCOM SST has a lower overall RMSD and stronger correlation of 93% than even the satellite analyses, but the model SSS has a larger (and positive) bias and does not track the variability found in CTDs as well as ECCO2 does.

For SST/S models, correlations with in situ data are weaker than for SST analyses, and the accuracy of model SST/S values is not constant throughout the AO. HYCOM SST residuals are more uniform across the AO shelves with no discernible change in bias between the Eurasian and Amerasian shelves; the spatial distribution of residuals resembles those of the satellite analyses. ECCO2 SST shows a bias of $-1.72\,^{\circ}\mathrm{C}$ for all CTD measurements along the the Siberian shelves between E60° and E180° while a $+0.25\,^{\circ}\mathrm{C}$ bias is present for CTD measurements in the Norwegian and Barents Seas region.

SSSs in these regions are more accurate in the ECCO2 model, which also lacks the overly-salty Norwegian coastal waters found in HYCOM. The warm, salty surface errors found in the HYCOM representation of the Kara sea contrasts the cool, fresh bias found in ECCO2 throughout the Siberian Shelf. In the central AO, the HYCOM product is cool and salty relative to IPY CTD data while

ECCO2 is slightly warm and fresh. Similar patterns are found compared to the longer time series of ITP measurements. Both model datasets appear cool and strongly salty in the Beaufort Sea region despite large differences in AO-wide SSS biases. MURSST SST also has biases of +0.35 °C and −0.30 °C for these regions, respectively. Similar but smaller differences between errors in these regions are found in GAMSSA and OISSTv2 products. No other large-area differences in regional biases are detected in residuals relative to CTD data but clusters of large errors in several smaller data-abundant regions such as the Kara Sea and northern Svalbard coast beg further investigation not pursued here. In comparison to SSS observations which both models resolve, HYCOM and ECCO2 represent the Beaufort and Chukchi regions with strong positive salinity biases, but this region is more localized in ECCO2 whereas the overly-saline region extends into Bering Sea and the central AO in HYCOM.

Model SST/S and analysis SST are less accurate in regions of runoff influence, such as in the Kara Sea and near outflows of the Lena and Mackenzie Rivers. In these areas, both models over-estimate salinity and many products under-estimate SST. The regional presence of these biases and increased inaccuracy may be due to the choice of averaging CTD data over 3–7 m; the mean profile over all CTD measurements with salinity less than 20 PSU in 0–3 m depths has a monotonic decrease in temperature between 3 m and 10 m. This suggests that calculated SST cold residuals in freshwater regions may be reduced if deeper CTD measurements were averaged to represent observations.

1.4.2 Comparison against ITP near-surface data

ITPs move with the ice and their records form a time-series, so associated residuals are correlated in time and are substantially less independent than the CTD observations. Further, the errors are distributed non-normally due to the constraint on water temperature minimum. Checking products against ITP data may not be as meaningful as it is for CTD data, but this comparison is diagnostic in its own right. Against ITP data in the 3–7 meter range, the SST analyses display more pronounced differences. The K10_SST and RSS_SST analyses sample only about 1200 and 20, respectively, of the approximately 14,000 ITP profiles due to sea-ice masking in those products, and neither analysis is further included in this discussion of fit to ITP-derived SST.

RTG_HR SST shows a distinctive strong positive bias of 0.45 °C and less than 1% correlation with ITP data, and this bias is evident against CTD datasets as well in Figure 1.5. OISSTv2 SST has the lowest bias for ITP data at −0.05 °C, but, along with OSTIA and RTG_HR, over-represents the inherent variance of ITP SST by more than 2.5 times (Figure 1.7, right). MURSST and GAMSSA statistics are nearly identical with biases near $-0.25\,^{\circ}$C and RMSDs roughly $0.14\,^{\circ}$C.

Among the analyses considered, MURSST and OSTIA SST appear equal in providing both strongest correlation and lowest biases to ITP-derived SST for products which include a separate sea-ice analysis. The salinities representing the ECCO2 model have smaller RMSD and bias than those of HYCOM for all datasets including ITP, although they still under-represent the variability of observations. Both models are competitive with satellite analyses in terms bias and RMSD for ITP data. Compared to the ECCO2 product, HYCOM SST has larger RMSD and a more pronounced over-estimation of ITP temperature variability, although the SSS residual second-order statistics are similar for both models. ECCO2 SST exists in a temperature range much smaller than the data while HYCOM SST is opposite (Figure 1.4, bottom).

1.4.3 Improving fit to ITP near-surface data

Hydrographical data beneath sea-ice for sub-surface layers is scarce and none of it is remotely-sensed. Instead, MW satellite bands are able to resolve approximate sea-ice concentration (SIC), and product SST can be relaxed to a freezing-point or other climatological state as SIC approaches 100%. This parametric approach is used by many of satellite analyses with a target freezing-point near $-1.8\,^{\circ}$C implicitly assuming salinities near 35 PSU [*Rayner et al.*, 2003; *Donlon et al.*, 2012]. Roughly 75% of ITP temperature data in the 3–7 meter range used for comparison is within $0.01\,^{\circ}$C of the freezing-point calculated from the observed salinity.

The difference between ITP temperature and freezing temperature calculated from ITP salinity shows a change during Julian days 130–260, when the mean of this difference increases in order from $1/1000\,^{\circ}$C to $1/10\,^{\circ}$C with a corresponding change in standard deviation from $0.027\,^{\circ}$C in winter to $0.138\,^{\circ}$C in summer[3]. Salinity distribution of ITP measurements is multi-modal and shows both seasonal and inter-annual variability, reflecting the changes in freshwater distribution and rapid freshening. The upper-most decile of near-surface averaged ITP salinities never exceed 30.5 PSU for any season in the years 2008–2012.

Different biases of several products are detected in seasonally-partitioned residual statistics presented in the left and center columns of Table 1.2. No seasonal changes in bias appear to be present in RTG_HR, MURSST, GAMSSA, or ECCO2 SSTs. However, biases with seasonal variation are apparent for OISSTv2, OSTIA, and HYCOM residuals against ITP, and differ from

---

[3] See Figure 2.12 later in this document for an illustration.

the total bias of Table 1.2. These products show warm biases of +0.24 °C, +0.14 °C, and +0.09 °C, respectively, in summer contrasting cold biases of −0.16 °C, −0.24 °C, and −0.12 °C, respectively, in winter. The winter biases against ITP data are roughly in the same range as those against the summer-focused CTD data. This suggests that rather than a cold bias in the winter, products are simply warmly biased in the central AO during the summer, and this bias is undetected by CTD measurements concentrated near and on continental shelves. Large errors for ITP data are localized in the Beaufort Gyre where surface freshwater content depend on a complex interaction of terrestrial hydrological cycles, atmospheric modes, and sea-ice melt [*Timmermans et al.*, 2011; *Morison et al.*, 2012]. Inaccuracies in that region may reflect the rapid salinity divergence from previous climatologies in the Beaufort Gyre and Canada Basin where ITPs provide the most data.

An increased warm bias during summer for certain products may be due to under-relaxation of temperatures toward freezing when the presence of surface melt-ponds causes SIC under-estimation. Cold bias in winter for these products is likely the result of prescribed climatological freezing temperatures: freezing-point prescribed near −1.8 °C is significantly cooler than temperatures observed by ITPs. The under-estimation of sea-ice in summer and over-estimation of background salinity is consistent with the seasonally-partitioned correlation diagrams shown in Figure 1.8. In the top row of this figure, summer-time measurements cluster near −1.6 °C while analysis SSTs are frequently warmer by 1/2 °C. The bottom row illustrates strongly constrained temperatures near −1.8 °C while the observed near-freezing temperatures are warmer by roughly 1/6 °C. Another possible sources of summer warm bias in these products is the under-estimation of wind stress used in transforming the satellite skin temperatures to product SST, but this is not explored here.

Product SST P may be corrected to better fit in situ ITP data by using product-minus-observation residuals ΔP and SIC I. In this discussion, I^* is a critical SIC above which ice influences SST. Linear regression of residuals against SIC greater than I^* parametrizes residuals in terms of SIC: $\Delta P = \alpha \cdot I + \beta$ where α, β are statistically determined coefficients. The corrected product values $P_1^* = P + (\alpha \cdot I + \beta) \cdot \{I^* \leq I \leq 1\}$ target the mean full-ice SST observed by ITP and have an improved mean linear relation to ITP near-surface temperature.

Corrected SST P_1^* have biases smaller than 10^{-2} °C against ITP data, but most ITP data are associated with SIC greater than 95%. As a result, the residuals of P_1^* show little improvement in higher-order statistics and the values of (α, β) fluctuate for random sub-samples of ITP data. However, the full-ice SST corrections $\gamma = \alpha + \beta$ are robust and correspond to freezing temperature corrections. Table 1.3 shows (α, γ)-values for several products using critical SIC of 50%. The corrected freezing temperatures $P + \gamma$ are approximately $-1.62\,^{\circ}\mathrm{C}$ for all products presented.

As a result of inadequate variation of SIC among ITP measurements, the method presented above tends to correct only product bias. The frequency of ITP data with respect to SIC resembles a log-normal distribution, so SST correction can be improved using a normalized logarithm of SIC. Transforming SIC into $\widetilde{I} = \log(2 - I)/\log(2 - I^{*})$ redistributes the dense cluster of ITP data associated with high SIC more appropriately onto the interval $0 \leq \widetilde{I} \leq 1$. This decreases the weight of ITP associated with high SIC and yields a better conditioned least-squares problem for linear regression.

Modified product SST values $P_2^{*} = P + (\delta \cdot \widetilde{I} + \eta) \cdot \{0 \leq \widetilde{I} \leq 1\}$ fit the ITP data in the mean more uniformly over the region $I \geq I^{*}$. Table 1.4 shows coefficients (δ, η) for several products whose modified SST absolute biases are less than $5 \cdot 10^{-3}\,^{\circ}\mathrm{C}$. This method produces values of (δ, η) which are considerably more robust for random sub-samples of ITP data, and may also improve higher-order statistical correspondence between product and ITP values. For example, applying independently the summer and winter corrections reduces the RMSD of OISSTv2 and OSTIA residuals by roughly 16% and 14.5%, respectively, and results in corrected SST P_2^{*} with biases smaller than those of P_1^{*}.

1.5 Summary

We extracted near-surface AO temperature and salinity profiles from ship-based CTD rosette casts, xCTD, and ITP data sources during the years 2006–2013. Each profile containing valid T/S in the range 3–7 meters was reduced to the mean over that range to represent observed foundational SST and SSS. These in situ SST/S observations were compared to corresponding values in OISSTv2, OSTIA, MURSST, RTG_HR, K10_SST, and RSS_SST gridded satellite analyses, as well as particular NASA/JPL ECCO2 Cube92 and HYCOM+NCODA data-assimilated model outputs. Against CTD temperature measurements, the satellite products had similar error statistics; correlation ranged between approximately 80% (OISSTv2) and 90% (OSTIA) with relative errors in variability ranging from −6% (GAMSSA and RTG_HI) to +1% (OISSTv2). All analyses showed overall cold biases against averaged ship-CTD profiles, and bias magnitudes were less than 0.5 °C. The warm post-IPY year 2012 generated large errors for many products; exclusion of 2012 CTD profiles reduces bias magnitude to less than 0.3 °C for all products.

Bias statistics against CTD SST data for models were generally worse than those for conditioned satellite products, but the models estimate SSS as well as other key quantities (eg. heat fluxes) not considered. The reader is reminded that satellite MW salinity measurement is a more recent technological advancement [*Lagerloef and Font*, 2010], and is not listed in either model documentation as a data source. The HYCOM product SST showed smaller bias (−0.04 °C) and higher correlation (93%) with ship-based CTD data than any of the satellite analyses but showed a large salinity bias of +1.23 PSU. ECCO2 product SST/S biases were −0.61 °C and −0.42 PSU, respectively, for all ship-based CTD data. ECCO2 matched the variance of the observations with +9% relative temperature error and −17% salinity error while corresponding values for HYCOM were −1% and −43%, respectively. Both models showed overall negative temperature biases similar to satellite analyses. Larger errors in T/S were detected in regions of direct freshwater and sea-ice influence. Generally, ECCO2 Cube92 appears to have a cold and fresh bias in the AO and adjunct shelves while HYCOM+NCODA output is cold and salty in those regions.

Near-surface ITP data reflect year-round T/S below multi-year sea-ice typically found over deep ocean basins in the Central Arctic. Away from the more often surveyed coastal shelves, products showed much lower correlation with ITP temperature measurements despite having small magnitude biases; the strongest non-seasonal correlation (26%) was found for GAMSSA, a product with negative bias of −0.25 °C. Product RMSDs were correspondingly very small due to the narrow range temperature found in ITP-derived data. Considering ITP data during Julian summer days 130–260 separately from winter days, seasonal changes in temperature bias appear in all products except MURSST and ECCO2, with summer temperature biases higher than those found during winter. In OISSTv2, OSTIA, and HYCOM SSTs, these biases are positive in summer and negative in winter. In summer, this is likely a consequence of SIC under-estimation due to melt ponds.

A likely diagnosis for winter-time cold bias is over-estimation of surface salinities in background climatologies. Many products appear to use freezing-point temperatures lower than observed ITP temperatures; during each year of 2009–2012, less than 10% of ITP near-surface salinities in the Canada Basin and Beaufort Sea are above 30.5 PSU while products target freezing temperatures closer to 34 or 35 PSU.

Linear correction of SST on the basis of SIC and the product-minus-ITP temperature allows for reducing product bias, but has difficulty improving second-order statistics due to the relatively low variability in SIC associated with ITP near-surface samples. A suggested linear correction of product SST against logarithmically-transformed SIC may be used to de-bias products as well as reduce RMSD in this case.

Ship-collected CTD profiles and near-surface ITP data as collected are not intended to represent sea surface quantities. ITPs sample waters below sea-ice where the satellite observations are not present. Satellite-derived products and models which rely heavily on satellite SST present SST/S quantities where there are no remotely-sensed data, necessitating the use of available in situ data for validation and quality diagnosis. Improvements to product quality may be made, not only through direct use of these in situ data sources for analysis and state estimation, but additionally by the incorporation of these data to update background fields and to improve the representativeness of remotely-sensible proxy data such as SIC.

Acknowledgements

This study was funded by NOAA grant NA11OAR4310153 for the project "Arctic Ocean Structure during the Period of the International Polar Year" and by NSF grants 1107925 and 1203740. We further thank the support of the Russia government (p220/mega-grant #2013-220-04-157). Organizations contributing data to the IPY AO database are owed a debt of thanks. Other data made available by and collected from: the Beaufort Gyre Exploration Program based at the Woods Hole Oceanographic Institution (http://www.whoi.edu/beaufortgyre) in collaboration with researchers from Fisheries and Oceans Canada at the Institute of Ocean Sciences; the latter three co-authors; and the Nansen and Amundsen Basins Observational System (NABOS) program.

Bibliography

Brodzik, M. J and K. W. Knowles (2002), EASE-Grid: A versatile set of equal-area projections and grids, *Discrete Global Grids*, *5*, 110-125.

Chen, Y., J. A. Francis, and J. R. Miller (2002), Surface temperature of the Arctic: Comparison of TOVS satellite retrievals with surface observations, *J. Climate*, *15*(24), 3698–3708.

Chin, T. M., J. Vazquez, and E. Armstrong (2013), A multi-scale, high-resolution analysis of global sea surface temperature, *Algorithm Theoretical Basis Document*, *Version 1.3*, 1–13.

Comiso, J. (2010), *Polar oceans from space*, vol. 41, pp. 507, Springer Science & Business Media. New York.

Corlett, G. K., I. J. Barton, C. J. Donlon, M. C. Edwards, S. A. Good, L. A. Horrocks, D. T. Llewellyn-Jones, C. J. Merchant, P. J Minnett, T. J. Nightingale, *et al.* (2006), The accuracy of SST retrievals from AATSR: An initial assessment through geophysical validation against in situ radiometers, buoys and other SST data sets, *Adv. Space Res.*,*37*(4), 764–769.

Cummings, J.A. (2005) Operational multivariate ocean data assimilation, *Quart. J. Roy. Meteorol. Soc., Part C*, *131*(613), 3583–3604.

Dash, P., A. Ignatov, M. Martin, C. Donlon, B. Brasnett, R.W. Reynolds, V. Banzon, H. Beggs, J-F. Cayula, Y. Chao, *et al.* (2012), Group for High Resolution Sea Surface Temperature (GHRSST) analysis fields inter-comparisons. Part 2: Near real time web-based level 4 SST Quality Monitor (L4-SQUAM), *Deep-Sea Res. Part II: Topical Studies in Oceanography*, *77*, 31–43.

Donlon, C. J., M. Martin, J. D. Stark, J. Roberts-Jones, E. Fiedler, and W. Wimmer (2012), The operational sea surface temperature and sea ice analysis (OSTIA) system, *Remote Sens. Environ.*, *116*, 140–158.

Emery, W., S. Castro, G. Wick, P. Schluessel, and C. Donlon (2001), Estimating sea surface temperature from infrared satellite and in situ temperature data, *Bull. Am. Meteorol. Soc.*, *82*, 2773–2785.

Fairall, C. W., E. F. Bradley, D. P. Rogers, J. B. Edson, and G. S. Young (1996), Bulk parameterization of air-sea fluxes for tropical ocean-global atmosphere coupled-ocean atmosphere response experiment, *J. Geophys. Res.:Oceans*, *101*(C2), 3747–3764.

Gammelsrød, T., Ø. Leikvin, V. Lien, W. P. Budgell, H. Loeng, and W. Maslowski (2009), Mass and heat transports in the {NE} Barents Sea: Observations and models, *J. Mar. Sci.*, *75*(1-2), 56–69.

Gemmill, W., B. Katz, and X. Li (2007), Daily real-time global sea surface temperature-high resolution analysis at NOAA/NCEP,*NCEP Off. Note 260*, 39 pp.

GCOS (2011), Systematic observation requirements for satellite-based products for climate, 2011 update, *WMO GCOS Rep. 154*, 1–127.

Høyer, J. L., I. Karagali, G. Dybkjær, and R. Tonboe (2012), Multi sensor validation and error characteristics of Arctic satellite sea surface temperature observations, *Remote Sens. Environ.*, *121*, 335–346.

Kawai, Y., and A. Wada (2007), Diurnal sea surface temperature variation and its impact on the atmosphere and ocean: A review, *J. Oceanogr.*, *63*(5), 721–744.

Krishfield, R., J. Toole, A. Proshutinsky, and M.-L. Timmermans (2008), Automated ice-tethered profilers for seawater observations under pack ice in all seasons., *J. Atmos. Ocean. Tech.*, *25*(11).

Lagerloef, G., and J. Font (2010), SMOS and Aquarius/SAC-D missions: The era of spaceborne salinity measurements is about to begin, in *Oceanography from Space*, pp. 35–58, Springer.

Lee, M.-A., M.-T. Tzeng, K. Hosoda, F. Sakaida, H. Kawamura, W.-J. Shieh, Y. Yang, and Y. Chan (2010), Validation of JAXA/MODIS sea surface temperature in water around Taiwan using the Terra and Aqua satellites, *Terr. Atmos. Ocean. Sci.*, *21*(4), 727–736.

Martin, M., P. Dash, A. Ignatov, V. Banzon, H. Beggs, B. Brasnett, J.-F. Cayula, *et al.* (2012) Group for High Resolution Sea Surface temperature (GHRSST) analysis fields inter-comparisons. Part 1: A GHRSST multi-product ensemble (GMPE), *Deep-Sea Res. Part II: Topical Studies in Oceanography*, *77*, 21–30.

Menemenlis, D., I. Fukumori and T. Lee (2005), Using Green's functions to calibrate an ocean general circulation model, *Mon. Weather Rev.*, *133*(5), 1244–1240.

Morison, J., R. Kwok, C. Peralta-Ferriz, M. Alkire, I. Rigor, R. Andersen, and M. Steele (2012), Changing arctic ocean freshwater pathways, *Nature*, *481*(7379), 66–70.

Nguyen, A. T, D. Menemenlis, and R. Kwok (2009), Improved modeling of the Arctic halocline with a subgrid-scale brine rejection parameterization, *J. Geophys. Res. Oceans*, *114*(C11).

Nguyen, A. T, D. Menemenlis, and R. Kwok (2011), Arctic ice-ocean simulation with optimized model parameters: Approach and assessment, *J. Geophys. Res. Oceans*, *116*(C4).

Rayner, N. A., D. E. Parker, E. B. Horton, C. K. Folland, L. V. Alexander, D. P. Rowell, E. C. Kent, and A. Kaplan (2003), Global analyses of sea surface temperature, sea ice, and night marine air temperature since the late nineteenth century, *J. Geophys. Res. 108*(D14), 4407, DOI: *10.1029/2002JD002670.*

Reynolds, R. W., T. M. Smith, C. Liu, D. B. Chelton, K. S. Casey, and M. G. Schlax (2007), Daily high-resolution-blended analyses for sea surface temperature, *J. Climate*, *20*, 5473–5496.

Robinson, I. S. (2004), *Measuring the oceans from space: the principles and methods of satellite oceanography*, 1 ed., Springer-Verlag.

Sakov, A., F. Counillon, L. Bertino, K. A. Lisæter, P. R. Oke, and A. Korablev (2012), TOPAZ4: an ocean-sea ice data assimilation system for the North Atlantic and Arctic, *Ocean Science*, *8*(4), 633–656.

Stark, J. D., C. J. Donlon, M. J. Martin, and M. E. McCulloch (2007), Ostia: An operational, high resolution, real time, global sea surface temperature analysis system, in *OCEANS 2007-Europe*, pp. 1–4, IEEE.

Sy, A., and D. Wright (2000), XBT/XCTD standard test procedures for reliability and performance tests of expendable probes at sea, *3rd Session of JCOMM Ship-of-Opportunity Implementation Panel (SOOPIP-III)*.

Taylor, K. E. (2000), *Summarizing multiple aspects of model performance in a single diagram*, Program for Climate Model Diagnosis and Intercomparison, Lawrence Livermore National Laboratory, University of California.

Thiébaux, J., E. Rogers, W. Wang, and B. Katz (2003), A new high-resolution blended real-time global sea surface temperature analysis, *Bull. Amer. Meteorol. Soc.*, *85*(5), 645–656.

Timmermans, M.-L., A. Proshutinsky, R. A. Krishfield, D. K. Perovich, J. A. Richter-Menge, T. P. Stanton, and J. M. Toole (2011), Surface freshening in the Arctic Ocean's Eurasian Basin: An apparent consequence of recent change in the wind-driven circulation, *J. Geophys. Res.:Oceans*, *116*(C8).

Toole, J. M., R. A. Krishfield, M.-L. Timmermans, and A. Proshutinsky (2011), The ice-tethered profiler: Argo of the Arctic, *Oceanography*, *24*(3), 126–135.

Zhong, A. and H. Beggs, (2008), Operational implementation of global Australian multi-sensor sea surface temperature analysis, *Analysis and Prediction Operations Bulletin*, (77).

Table 1.1. Product bias, RMSD, and correlation for ship CTD data groups. The top portion of the table shows SST analyses with bias and RMSD units in °C. The bottom portion corresponds to model SST/S with units of °C and PSU, respectively, for bias and RMSD. The rightmost portion of the table gives product-observation correlations as squared Pearson coefficients.

	Bias			RMSD			Correlation		
	IPY	p-IPY	All CTD	IPY	p-IPY	All CTD	IPY	p-IPY	All CTD
OISSTv2	+0.05	-0.38	-0.02	1.78	1.62	1.77	0.80	0.76	0.80
OSTIA	-0.22	-0.54	-0.26	1.16	1.40	1.20	0.91	0.82	0.90
RTG_HR	-0.17	-0.35	-0.20	1.47	1.76	1.51	0.85	0.73	0.84
MURSST	-0.14	-0.02	-0.12	1.45	1.22	1.42	0.86	0.87	0.86
GAMSSA	-0.27	-0.93	-0.46	1.09	2.12	1.49	0.92	0.59	0.84
K10_SST	-0.08	-0.13	-0.10	0.86	1.54	1.18	0.93	0.76	0.87
RSS_SST	-0.07	-0.02	-0.05	0.97	1.41	1.18	0.90	0.70	0.86
ECCO2	-0.56	-0.97	-0.61	2.09	2.16	2.10	0.77	0.61	0.76
↪SSS	-0.73	-0.58	-0.71	2.12	2.51	2.17	0.73	0.69	0.74
HYCOM	-0.07	+0.03	-0.03	1.02	1.03	1.03	0.93	0.90	0.93
↪SSS	+0.64	+1.27	0.87	1.67	2.79	2.17	0.79	0.72	0.79

Table 1.2. Product bias, RMSD, and correlation for shallow ITP data. Summer, winter, and total values are given on the left, center, and right thirds of the table, respectively. Bias and RMSD of product-minus-observation residuals, and correlation presented as squared Pearson coefficient, are given in the respective left, center, and right columns of each third. Top rows correspond to SST analyses, and the bottom to SST/S models. K10_SST and RSS_SST are under-sampled and not included. Summer is taken as Julian days 130–260 when ITP SST/S depart from freezing, and winter as the remainder of the year.

	Summer			Winter			Annual		
	Bias	RMSD	ρ^2	Bias	RMSD	ρ^2	Bias	RMSD	ρ^2
OISSTv2	+0.24	0.51	0.42	-0.16	0.23	0.01	-0.06	0.38	0.19
OSTIA	+0.14	0.49	0.35	-0.24	0.14	0.02	-0.14	0.32	0.23
RTG_HR	+0.48	0.43	0.04	+0.45	0.38	0.00	+0.46	0.39	0.01
MURSST	-0.24	0.23	0.30	-0.24	0.11	0.10	-0.24	0.15	0.23
GAMSSA	-0.29	0.22	0.30	-0.25	0.10	0.18	-0.25	0.13	0.26
ECCO2	-0.02	0.22	0.23	-0.04	0.12	0.01	-0.04	0.16	0.10
$\hookrightarrow$SSS	-0.60	2.60	0.04	+0.55	2.00	0.04	+0.25	2.23	0.03
HYCOM	+0.09	0.76	0.31	-0.12	0.26	0.01	-0.08	0.41	0.19
$\hookrightarrow$SSS	+1.95	1.35	0.20	+2.71	1.55	0.06	+2.57	1.54	0.07

Table 1.3. Seasonal least-squares parameters for minimizing residuals regressed over high SIC. Least-squares slope (α) and temperature correction at 100% SIC (γ) for linear correction to various products for SIC above 50%. Original product values, P, better reflect ITP observations by computing $P_1^* = P + \gamma + \alpha \cdot (I - 1)$ for $I > I^* = 0.5$.

	Summer		Winter		Annual	
	α [°C]	γ [°C]	α [°C/%]	γ [°C]	α [°C/%]	γ [°C]
OISSTv2	1.61	−0.15	0.71	0.20	1.11	0.11
OSTIA	0.29	−0.12	0.16	0.24	0.29	0.15
MURSST	0.11	0.24	0.15	0.25	0.14	0.24
ECCO2	0.12	0.03	0.16	0.05	0.15	0.04
HYCOM	−1.26	0.12	0.26	0.10	0.26	0.10

Table 1.4. Seasonal least-squares parameters for residuals regressed over logarithmically-transformed SIC. Least-squares slope (δ) and intercept (η) for residuals regressed over SIC transformed by $\widetilde{I} = \log(2-I)/\log(3/2)$ corresponding to a critical SIC value of 50%. Original product values, P, better reflect ITP observations by computing $P_2^* = P + (\delta \cdot \widetilde{I} + \eta)$ for $I > I^* = 0.5$.

	Summer		Winter		Annual	
	δ [°C]	η [°C]	δ [°C]	η [°C]	δ [°C]	η [°C]
OISSTv2	-0.76	-0.14	-0.34	+0.20	-0.52	+0.12
OSTIA	-0.13	-0.12	-0.08	+0.24	-0.14	+0.15
MURSST	-0.05	+0.24	-0.07	+0.25	-0.07	+0.25
ECCO2	-0.06	+0.03	-0.08	+0.05	-0.07	+0.05
HYCOM	+0.54	+0.12	-0.13	+0.10	-0.13	+0.11

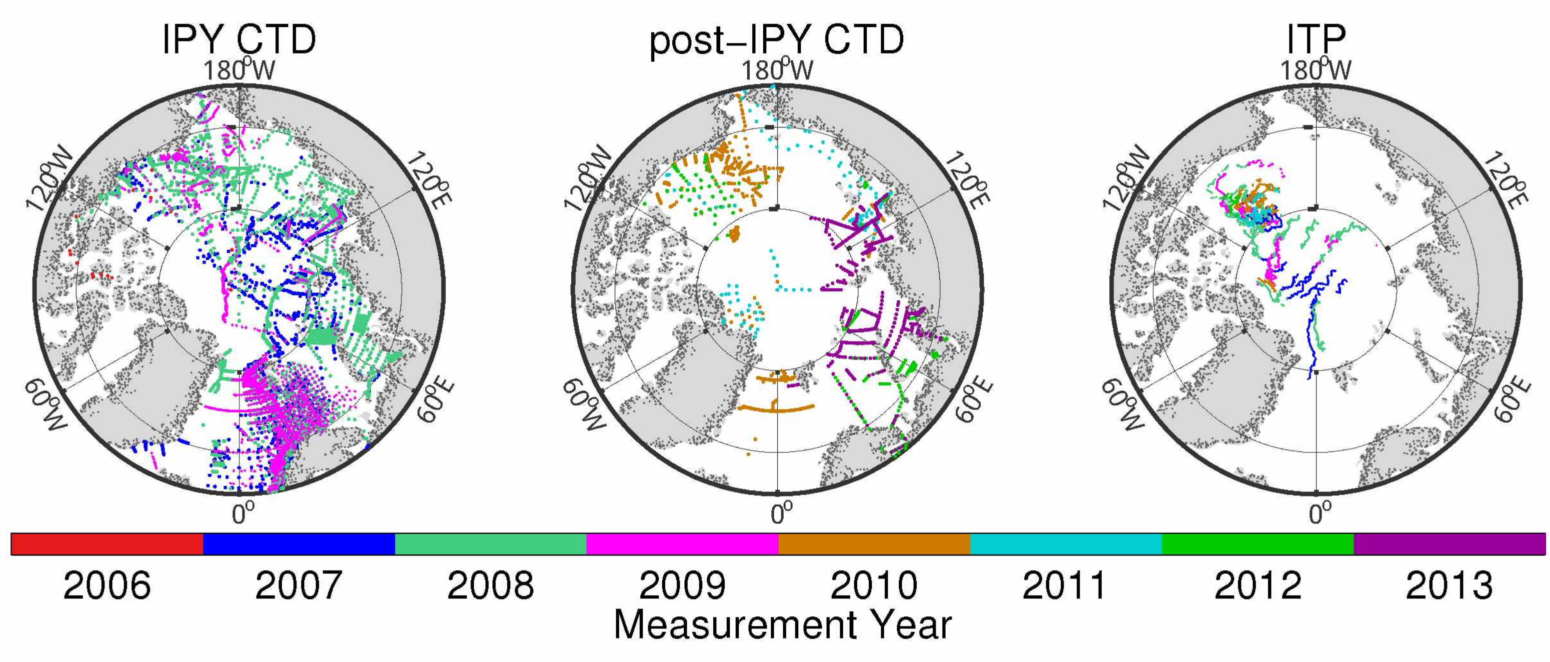

Figure 1.1. Locations of in situ data poleward of 65° N. Observational data referred to, from left to right, as "IPY CTD", "post-IPY CTD", and "ITP", respectively. Colors correspond to measurement year. Plotted points indicate measurements between 3 and 7 meters depth.

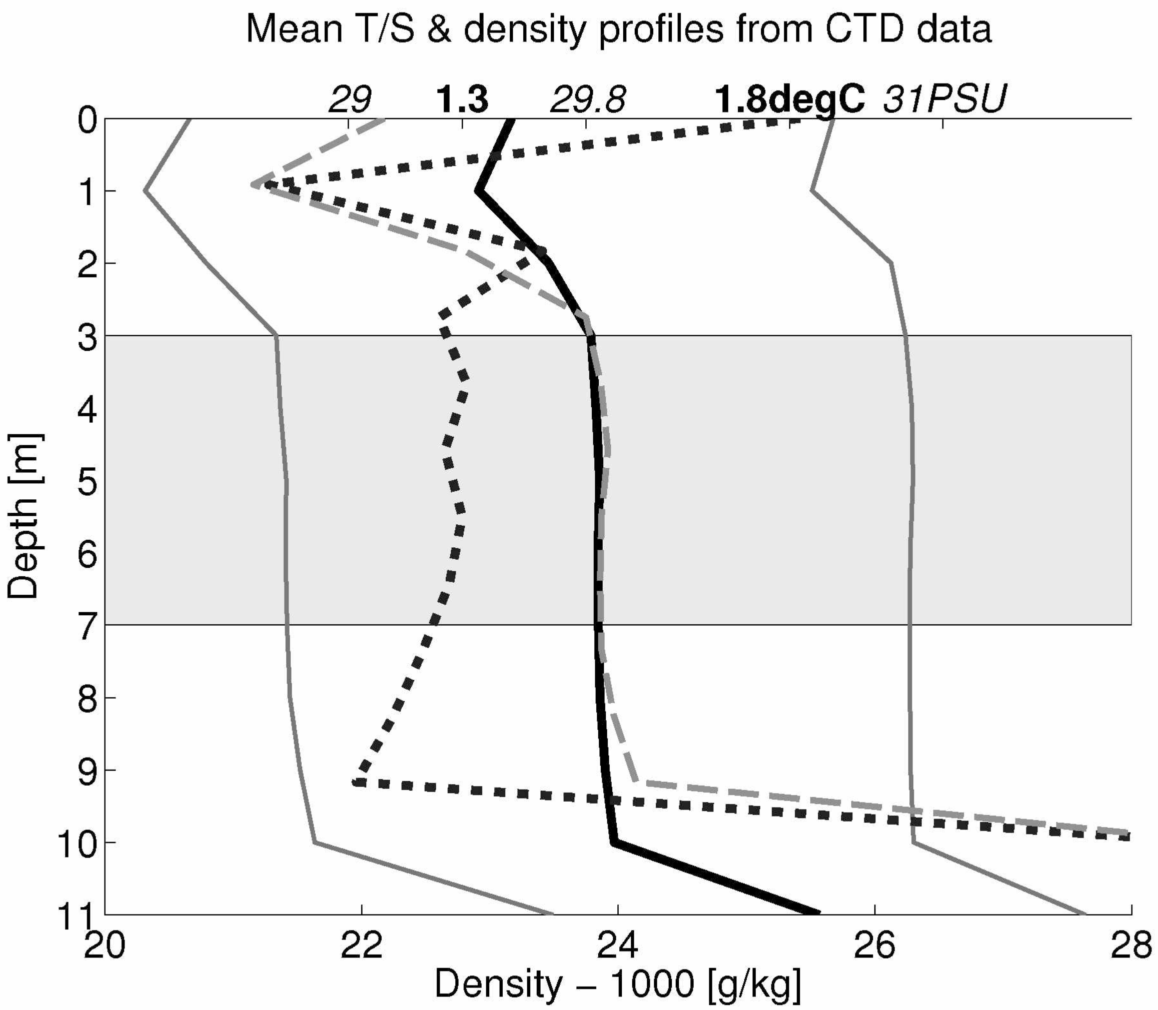

Figure 1.2. Mean T/S and density profiles for all ship CTD data north of 65° N excluding profiles with salinity less than 20 PSU in the uppermost 10 m. The mean density profile is shown in heavy black as the difference from 1000 g kg^{-1}, and thin grey lines at a distance of one standard deviation illustrate density variability. Mean T/S profiles are shown in dotted and broken lines, respectively, with scales given on the top axis in bold and italics, respectively. The shaded rectangle indicates the 3–7 m region where T/S and density are nearly constant, indicating a region representative of sea-surface foundational values.

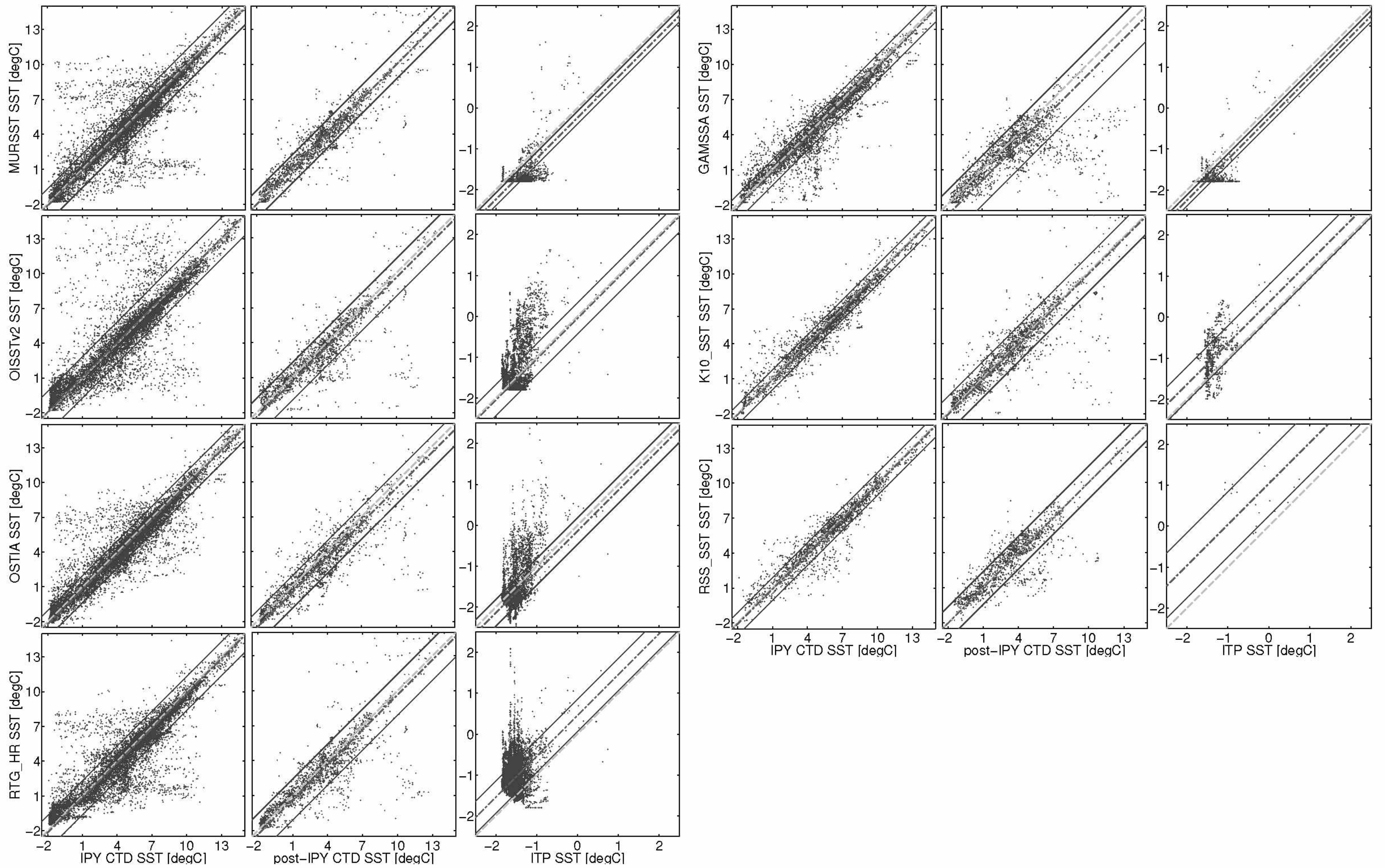

Figure 1.3. Correlation of SST analyses with respect to (left columns) IPY CTD, (center columns) post-IPY CTD, and (right columns) ITP observations. The descending orders of products are: MURSST, GAMSSA, OISSTv2, K10_SST on the left side; and OSTIA, RSS_SST, and RTG_HR on the right. In each plot, the thick light-grey dashed line indicates perfect matching; the thin dark-grey line shows this ideal relation offset by product bias; and the thin solid lines bound the bias-offset fit at a distance of the product-minus-observation RMSD.

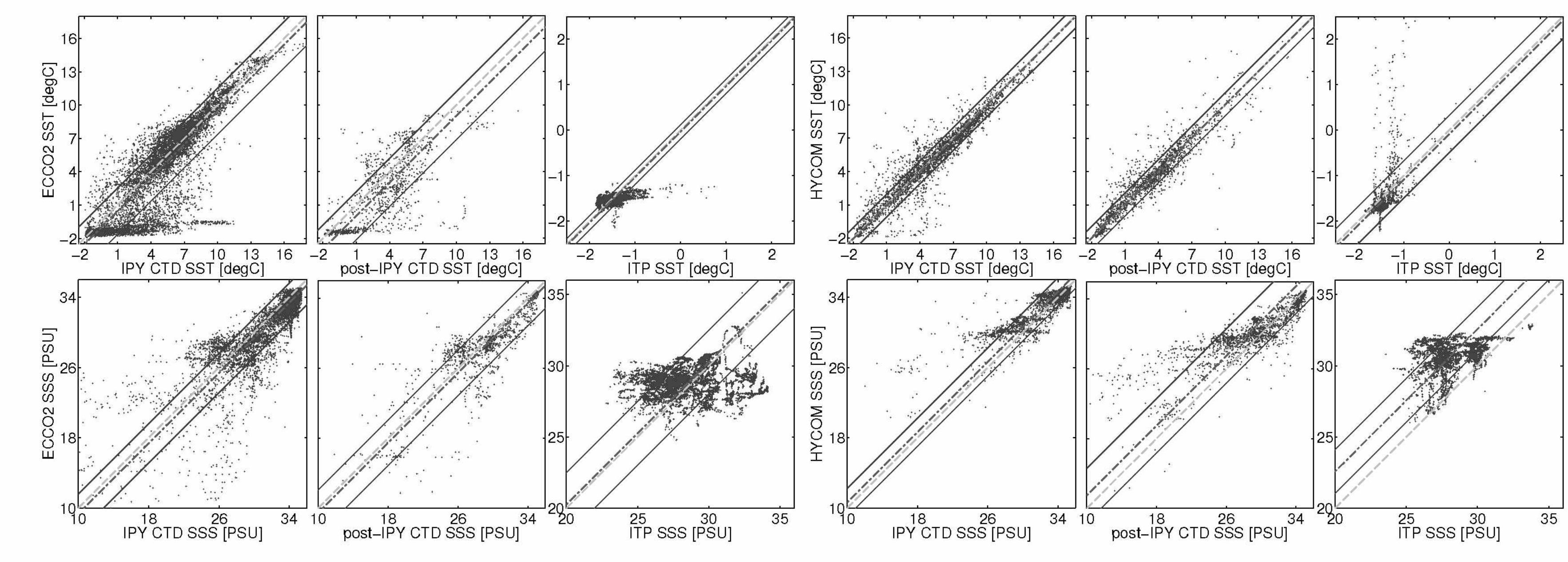

Figure 1.4. Correlation of SST/S model analyses with respect to (left columns) IPY CTD, (center columns) post-IPY CTD, and (right columns) ITP observations. ECCO2 is shown in the left portion and HYCOM in the right. SST comparison illustrated on the top row and SSS on the bottom. The plotted lines are equivalent to those of Figure 1.3.

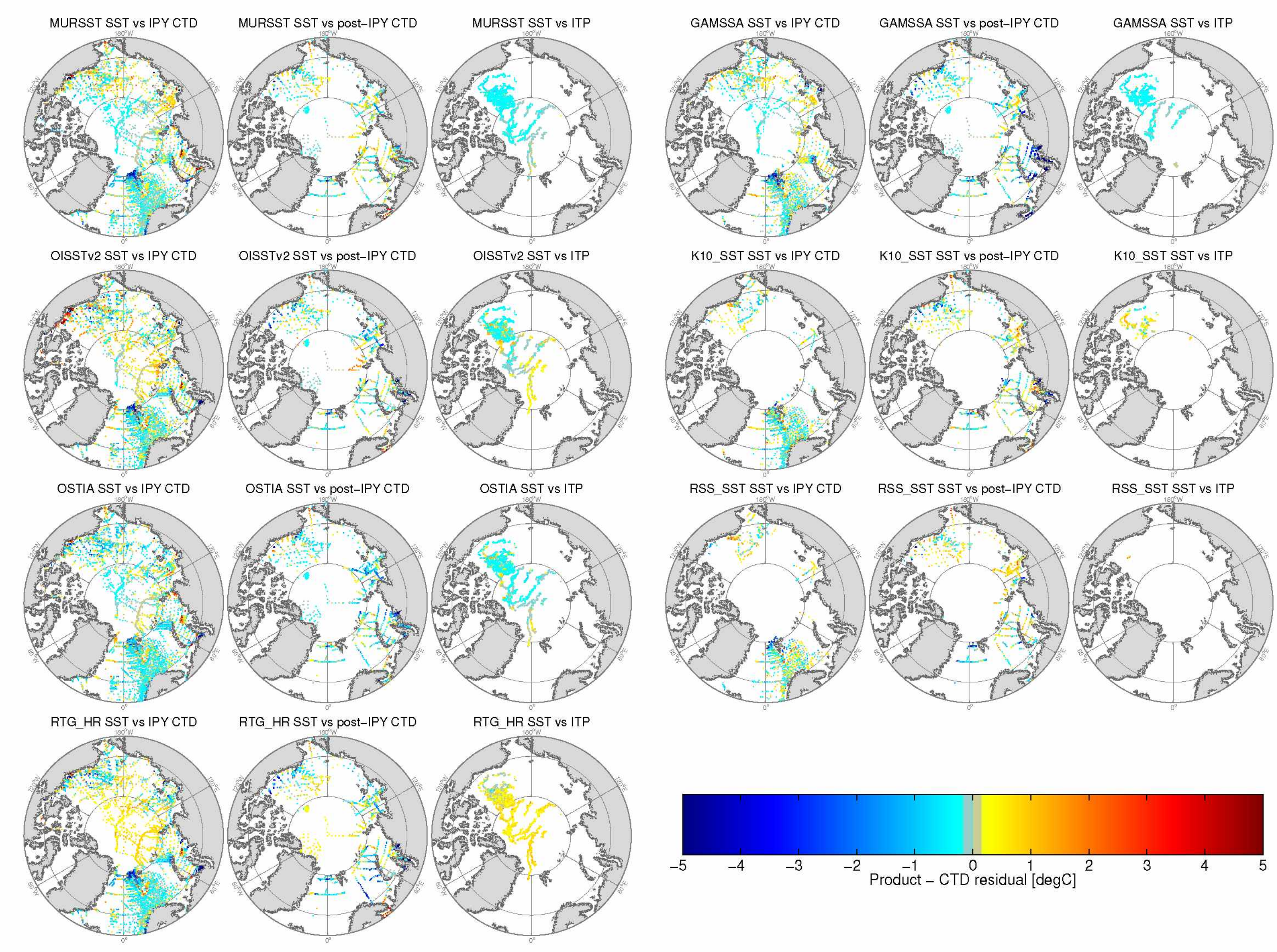

Figure 1.5. Analysis-minus-observations SST residuals. Plot layout is the same as in Figure 1.3. Plotted points represent residuals which are bin-averaged on the AVHRR northern hemisphere 25 km equal-area EASE grid [*Brodzik and Knowles*, 2002] to improve visibility and do not coincide with locations in Figure 1.1. Residual values are indicated by color. Greyish colors indicate residuals smaller than ±0.15 °C.

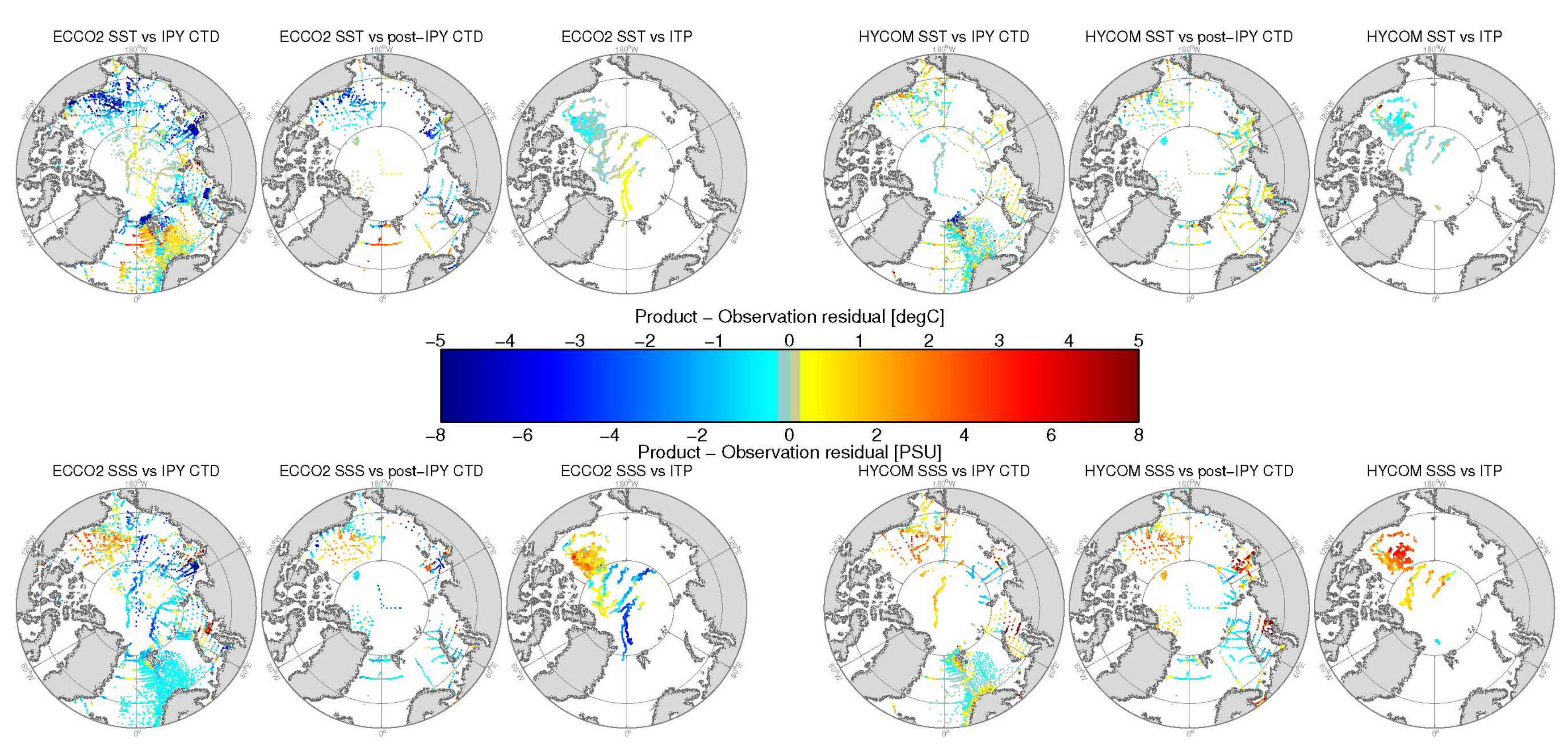

Figure 1.6. Model-minus-observation SST/S residuals. Plot layout is the same as in Figure 1.4, and points are plotted in the same manner as those in Figure 1.5. Greyish colors indicate residuals smaller than ±0.15 °C for SST and ±0.16 PSU for SSS.

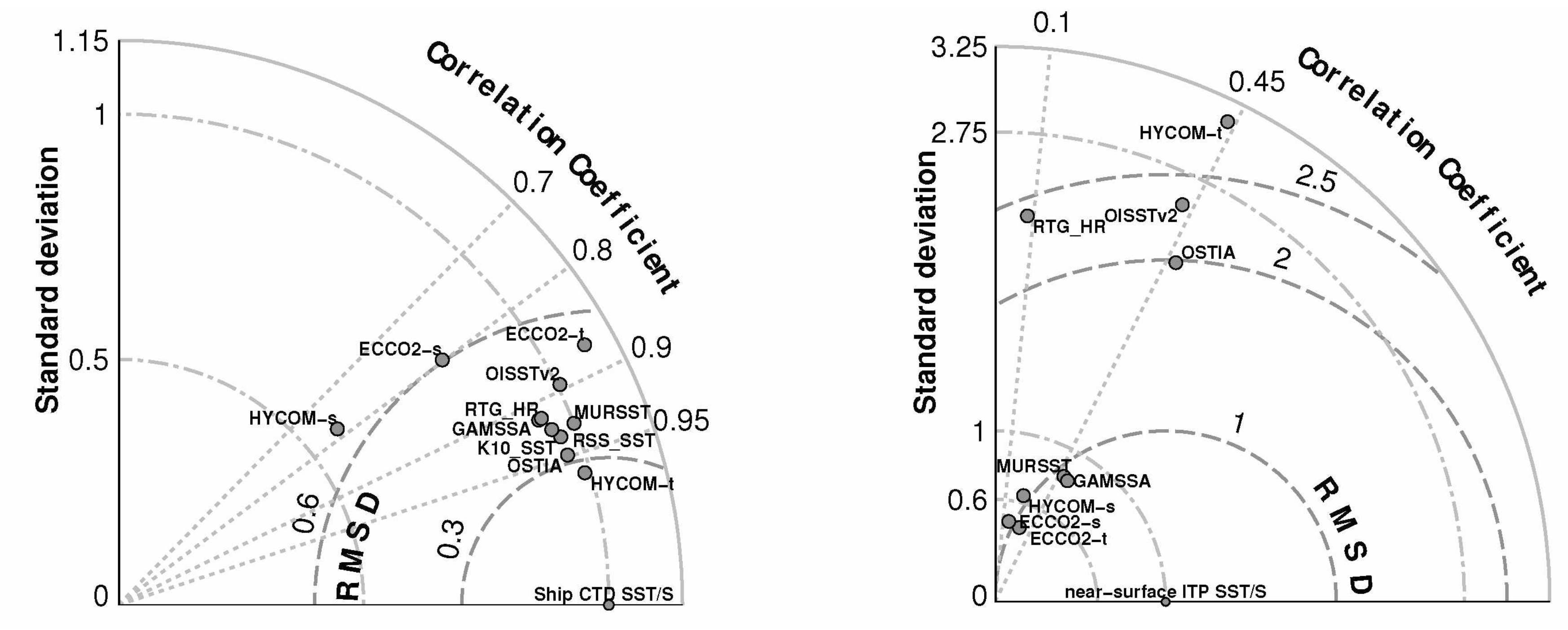

Figure 1.7. Comparison of non-dimensional second-order statistics via Taylor diagram against all ship CTD observations (left) and near-surface ITP observations (right). The relation shown here is independent of bias (first-order difference) and one must consider these in conjunction with Table 1.1.

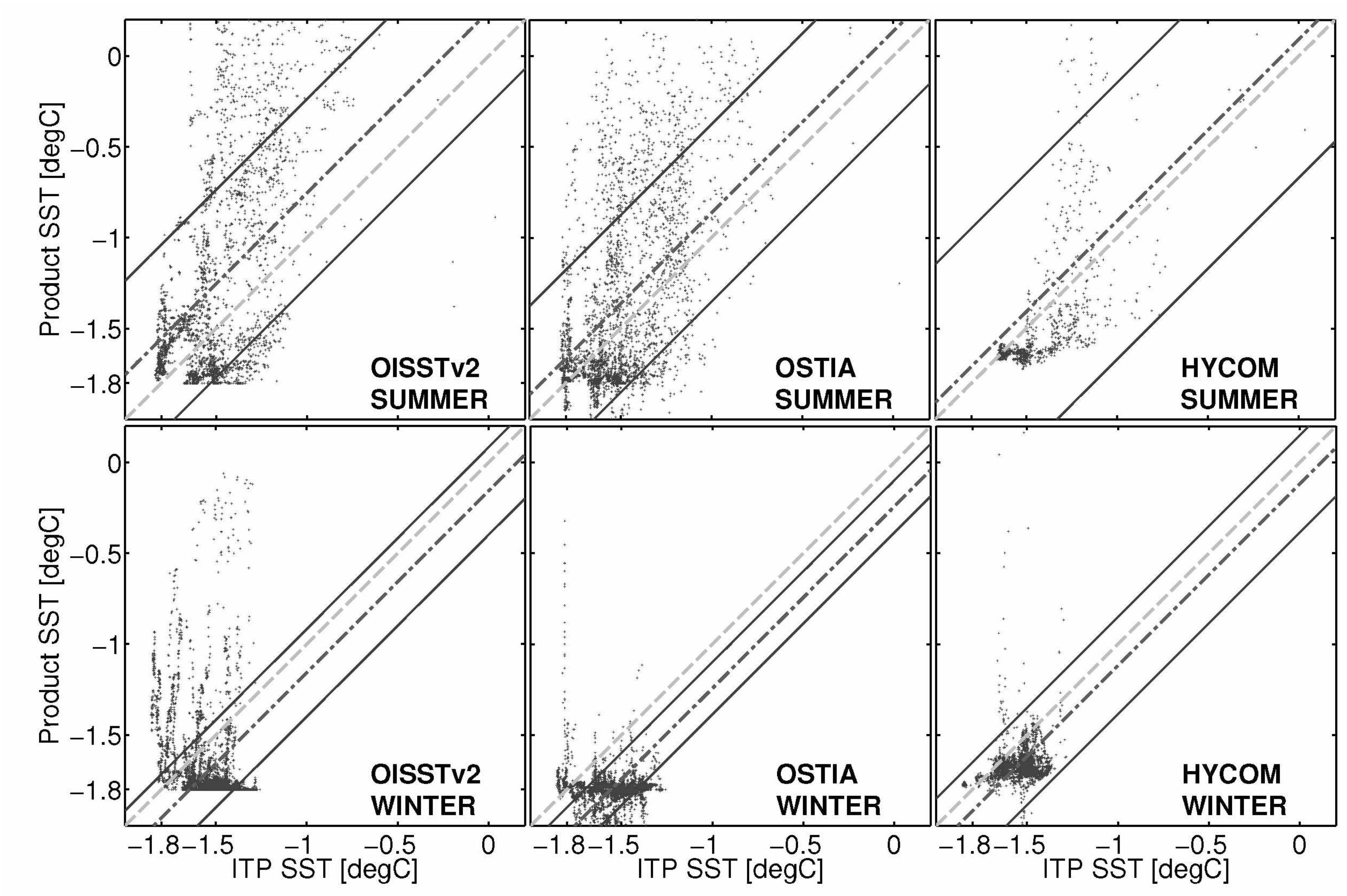

Figure 1.8. Seasonal comparison of select products to ITP measurements. The OISSTv2 (left), OSTIA (center), and HYCOM (right) products are biased positively in summer (top) and negatively in winter (bottom). Summer-time residual distribution shows a less constrained temperature range compared to observed values. Winter residuals show strongly constrained product SST targeting −1.8 °C while actual measurements are centered near −1.6 °C.

Chapter 2: Changes in Arctic Ocean Climate Evinced through Analysis of IPY2007–2008 Oceanographic Observations[1]

Abstract

Full-depth hydrographical surveys conducted in 2007–2009 during the International Polar Year (IPY) collaboration provide an accurate snapshot of the Arctic Ocean (AO) hydrography at a time when the Arctic Ocean Oscillation (AOO) index was highest in recent record. We construct pan-Arctic temperature and salinity (T/S) reference states from these data using variational optimal interpolation, and discuss some key differences between the 2007–2009 state and a similarly constructed climatology from historical 1950–1996 Russian archives. These data provide a recent, known reference state for both qualitative and quantitative future AO climate change studies. Furthermore, we present an analysis sea-surface height (SSH) and upper-layer circulation constructed from the IPY data via 4Dvar data assimilation, and use them to examine circulation and freshwater sources changes visible during IPY.

2.1 Introduction

During the International Polar Year (IPY) 2007–2008, the international scientific community completed an intensive physical survey of the Arctic Ocean (AO). Many countries and institutions contributed to this effort, which generated a significant number of *in situ* hydrographical observations including: stationary full-depth profiles of temperature/salinity (T/S) from conductivity-temperature-depth instruments (CTD) and partial-depth profiles of the upper $\sim$ 700m along Lagrangian tracks followed by Ice-Tethered Profiles (ITP) affixed to sea-ice; measurements of T/S along the tracks followed by sub-marine gliders near coastal areas; and a small number profiles from less accurate expendable CTD and expendable bathythermograph (XBT) instruments.

Arctic T/S distribution is governed largely by water inflow and outflow through the major gateways, the properties of those waters, and regional circulation. AO sources include: the warm saline waters advected with the Norwegian current from North Atlantic [*Rudels et al.*, 1994]; the fresh (relative to mean AO salinity) Pacific waters (PW) entering through Bering Strait [*Zhang and Zhang*, 2001]; and the summertime fresh and warm river discharge the Siberian and North American rivers [*Shiklomanov et al.*, 2000; *Serreze et al.*, 2006]. AO export occurs primarily through Fram Strait by way of the Transpolar and East Greenland Currents, and also through less-studied

---

[1] Stroh, JN, S. Kirillov, G. Panteleev, O. Francis, M. Yaremchuk, E. Bloshkina, and N. Lebedev, (2018), Changes in Arctic Ocean climate evinced through analysis of IPY 2007–2008 oceanographic observations, in M. Kanao (Ed.), *Arctic Studies-A Proxy for Climate Change*, IntechOpen Publishing. DOI: *10.5772/intechopen.80926.*

Canadian Archipelago transport [*Curry et al.*, 2011]. Within the AO, shelf-basin exchanges are typically restricted to bathymetric features, such as Herald and Barrow Canyons in the Chukchi Sea [*Weingartner et al.*, 1998], and St. Anna Trough north of Severnaya Zemlya in the Kara Sea [*Dmitrenko et al.*, 2015]. Regional circulation is governed by topographically-steered boundary currents along shelfbreaks and other topographic features, restricted by density fronts between watermasses of disparate origin, and subject to external forcing including surface heating (cooling) in summer (winter) with significant effects from sea-ice melt/freeze and large-scale atmospheric pressure systems [*Rudels et al.*, 1994, 1999; *Proshutinsky and Johnson*, 1997; *Woodgate*, 2013].

The IPY effort occurred at a significant time, co-incidental with the largest recent positive Arctic Ocean Oscillation (AOO) index, a measure derived from the sea-surface height gradient over the central AO which indicates strength of large-scale anti-cyclonic flow [*Dukhovskoy et al.*, 2006]. Prior to IPY, the AOO index had been in an overall positive regime for nearly two decades while historical records suggest a sub-decadal frequency [*Proshutinsky and Johnson*, 1997, updated at www.whoi.edu/page/preview.do?pid=66578]. Other modes of regional oscillation occur with timescales of 60–80years [*Polyakov and Johnson*, 2000]. At the same time, summer 2007 winds associated with the Beaufort High remained predominantly anti-cyclonic a feature common to the Arctic winter but unusual for summer [*Wang et al.*, 2009], so Beaufort Gyre (BG) sea-level response to atmospheric forcing strengthened the AOO. Additionally, 2007 was a monumental year for river discharge; Eurasian river discharge surpassed the 2002 record by nearly 10% [*Shiklomanov and Lammers*, 2009]. The effects of these drivers, whether purely anomalous or the result of long-term variability, relate to pronounced recent changes in the Arctic marine climate system and were witnessed by the IPY survey efforts. Over a decade has passed since many of the observed strong and rapid warming trends were confirmed as both present and underway. Older climatologies may be inadequate for the study of more recent changes as they may depend on much pre-1996 data when: the positive AOO regime was not a such a strong and permanent feature of the region; thicker and more extensive sea-ice regulated mechanical and thermodynamical fluxes with the atmosphere; continental riverine discharge was less; and the Lomonosov Ridge roughly defined a partition of the Arctic between Atlantic and Pacific upper-ocean layers. The thermal state of the AO over the past decade is above the long-term average, and this warming greatly affects both hydrographic and ice-related processes observed in the high latitudes; changes occurring under these new conditions are of particular interest [*Polyakov et al.*, 2005; *Falck et al.*, 2005; *Alkire et al.*, 2007; *Carmack et al.*, 2008; *Wang et al.*, 2009; *McPhee et al.*, 2009; *Polyakov et al.*, 2011; *Curry et al.*, 2011;

Morison et al., 2012; *Woodgate et al.*, 2012; *Zhong and Zhao*, 2014].

Unlike other oceans, vertical stratification of AO watermasses is governed more by salinity than temperature, and density gradients readily allow for decomposition of profiles into differentiated, typically non-interactive layers. Away from regions of significant freshwater influence, the vertical distribution of watermasses throughout the AO generally comprises a well-mixed surface layer occupying the upper 50–100m, underlain by a layer of intermediate water of Pacific origin (absent in the eastern, Atlantic domain of the Arctic), followed by a layer of warmer more saline water of Atlantic origins, and an Arctic deep water bottom layer. Importantly, the halocline of Pacific-originated waters overlies the warmer Atlantic water deeper in the ocean in the Pacific Sector [*Steele and Boyd*, 1998], buffering sea-ice from the warmer Atlantic waters below. The presence, thickness, and specific properties of each layer vary laterally throughout the Arctic [*Woodgate*, 2013; *Emery*, 2001], and one may distinguish between layers of waters of Pacific and Atlantic origin on the depth of local haloclines and isotherms characteristic within each column.

The remote nature of the AO, together with practical difficulties in observation and navigation due to sea-ice and sparse infrastructure, makes *in situ* sampling of the AO expensive and occasional. Satellite monitoring of the ocean surface is possible but inhibited by ice-cover and clouds. Unfortunately, the accuracy of the satellite surface-observations and their processed (*i.e.* L2–L4) products are often far from optimal: they may contain large errors due to poor calibration, mask large portions of the AO for sea-ice, and thus lack of coverage over the central AO, and may contain anachronistic assumptions in their post-processing algorithms [*Stroh et al.*, 2015]. Modelling efforts and other interdisciplinary studies in need of static background ocean data may need to rely on gridded products that are biased toward older AO regimes or large amounts of surface observations from satellite. Further, climatological studies using older reference states for trend analysis may suffer from amplified trend errors. For example, the Arctic portion of the most recently available Polar Science Center Hydrographic Climatology (PHC 3.0, *Steele et al.* [updated from 2001]) is based on historic observations through 1993 [*Timokhov and Tanis*, 1997].

The concerns listed above motivate this work, which presents a 2007–2009 AO stationary analysis state inferred from algorithmic data-conditioning of pan-Arctic hydrographical surveys and other at-depth observations to provide a snapshot of the non-coastal ocean state with an emphasis on the intermediate layers. The result is a dataset of gridded T/S available in NetCDF at http://bit.ly/2M6qsJ9, from which this chapter discusses mapped watermasses and their differences relative to those mapped from a 1950–1994 climatology. We also use 4Dvar data assimilation to establish an analysis of major circulation changes during IPY relative to the climatological mean and discuss the evident anomalies of July-December 2008 [*Francis et al.*, 2017]. The remainder of this chapter is organized as follows: Section 2 discusses the *in situ* data and the production algorithm for the gridded fields; Section 3 presents an atlas of watermass properties for the IPY and their differences from historical data fields; Section 4 discusses changes in the AO watermass distribution and thermal state evident from use of IPY data and derived climatology; Section 5 presents analysis of circulation anomalies during the IPY; and Section 6 concludes the chapter.

2.2 Observational Data and Gridding

As part of an IPY-initiative, approximately 13,000 CTD/xCTD/XBT profiles along with ITP data were curated into a central database of AO T/S observations from contributors in Japan, Norway, Russia, Canada, USA, Germany, Poland, Sweden, and China. *Stroh et al.* [2015, Figure 1][2] shows the location of profiles over the AO, of which only the IPY CTD and ITP data during 2007–2008 are used here. CTD observations during the sea-ice minimum months of August–October account for approximately 40% of all ship-borne profiles while wintertime November–March account for approximately 30%. ITP apparatuses provide a more temporally uniform stream of profile data for the upper-most ~700m throughout the year; ITP data were collected and made available by the Ice-Tethered Profiler Program [*Krishfield et al.*, 2008; *Toole et al.*, 2011] based at the Woods Hole Oceanographic Institution (http://www.whoi.edu/itp).

The Data-Interpolating Variational Analysis tool [DIVA, *Troupin et al.*, 2012] is a robust finite-element based optimization tool for gridding large 2D, 3D, and 4D datasets and includes error estimates of the analysis. This freely-available program, developed by the GeoHydrodynamics and Environmental Research (GHER, http://modb.oce.ulg.ac.be/), was applied to the observational data described above to construct static full-depth fields on an equal-area polar-centered grid with 50km resolution. Interpolation to 51 vertical levels occurs level-wise within DIVA, to which an internally-applied stability algorithm ensures analyses remain hydrodynamically stable with respect to density throughout the gridding. Bathymetric masking was inferred from the International Bathymetric Chart of the Arctic Ocean [IBCAO v3.0, *Jakobsson et al.*, 2012], and regions with depth less than 200m are masked. The correlation length-scales for observations correspond to 3 grid-cells with a signal-to-noise ratio of 10%. The same procedure applied to historical observations collected during 1950–1994 (privately archived at the Arctic and Antarctic Research Institute of

---

[2] Also, Figure 1.1 earlier in this document.

Russia) generates mean climate dataset for that period used to contrast the gridded IPY data.

2.3 Watermass Distribution Maps

From the gridded T/S analyses for the 1950-1994 and IPY periods, watermass properties reveal qualitative differences between them. Use of density-related properties to distinguish watermasses is less certain than chemical analysis [*Ekwurzel et al.*, 2001; *Alkire et al.*, 2007]. Scarcity of widespread chemical tracer surveys precludes such an approach here, and analysis based on the more common T/S data is adopted. This work chooses to map Atlantic Water (AW) and Summer Pacific Water (SPW) for both their simplicity of definition and importance in the freshwater (FW) and thermal budget of the AO. Characteristics used to identify AW and SPW are adapted from *Emery* [2001] and *Steele et al.* [2004]; *Shimada et al.* [2005], respectively, as described below.

The AW distinguishes an intermediate layer of warm water of Atlantic origin that has entered the Arctic Basin through deep coastal channels and bathymetric steering. Over-basin AW typically has S$\geq$ 34.8 PSU, with T$\geq$ 0°C despite heat loss along the Eurasian shelf. SPW denotes relatively fresh waters with S in the range 31–33 PSU and T$\geq$ -1.4°C entering the AO through the Bering Strait which have cooled after residence on the shallow Chukchi Shelf and include substantial meteoric FW [*Steele et al.*, 2004; *Carmack et al.*, 2008]. These low density waters form a sub-surface layer in the western Arctic typically at depths between 50m and 100m, and often include a local temperature maximum [*Shimada et al.*, 2001; *Bourgain and Gascard*, 2012].

In Figures 2.1–2.11, left-side plots show the identified field for the IPY dataset while the right-side plot shows the corresponding anomaly field relative to the AARI 1950–1994 archive. We refer to each such pair singularly as a figure, and distinguish between the field and its anomaly in context. Figure 2.1 maps the 34.8 PSU isohaline depth. Figure 2.2 shows the integrated FW content (FWC), in meters of freshwater, with respect to 34.8 PSU.

Figures 2.3–2.7 plot the AW core depth, core temperature, heat content, lower boundary depth, and upper boundary depth, respectively. AW here is defined as waters composing a continuous vertical region of positive temperature bounded by 0°C isotherms, which define herein the lower and upper AW boundary depths. The AW core depth and temperature are adopted to be the depth and value of the temperature maximum within the AW layer. Total heat content is calculated as the vertical integral of specific heat with respect to -1.8°C between AW boundaries. Insufficient deep data in near the Canadian Archipelago precludes a resolution of the AW lower boundary and, consequently of the heat content in that area.

Figures 2.8–2.11 show calculated fields for summer Pacific Water, which exists only on the Pacific side of the Arctic. SPW is defined by a local temperature maximum occurring below the surface mixed layer within the salinity range 30.5–33.0 PSU [35]. Upper and lower SPW boundary depths are determined by $T \geq -1.4°C$ and salinity restriction to that range. Figure 2.8 maps the depth of the maximum temperature found in SPW and Figure 2.9 identifies these maxima. Figures 2.10 and 2.11 show the lower and upper boundary depths of SPW, respectively.

2.4 Changes Inferred from T/S Observations

In general, the vertical and spatial patterns of hydrographic parameters in the AO and adjacent North Atlantic had undergone considerable changes by IPY although the large-scale distributions of the watermasses align with the historic climatology. Readers unfamiliar with AO geography and its bathymetric features are encouraged to follow this discussion with an atlas, e.g. https://geology.com/articles/arctic-ocean-features/.

2.4.1 Atlantic Waters

Elevated pan-Arctic heat content due to the extraordinary heat transported to the AO from the North Atlantic is a significant change evident during the IPY period. Advection of relatively warmer AW resulted in anomalous hydrographic state formation over entire deep Arctic Basin [*Polyakov et al.*, 2011; *Bourgain and Gascard*, 2012]. The temperatures within the core of AW were observed 0.3–1.0°C higher comparing to climatic values; mean changes are ~0.65°C over the Eurasian basin and ~ 0.25°C over Canada and Makarov Basins.

Of further note is the warm tongue of AW that appears to be topographically steered by the Lomonosov Ridge; Figure 2.4 shows a clear 0.5°C core temperature anomalous increase extending from the Laptev Sea toward the Greenland Shelf. This feature resides at a depth of about 275m, ~75m surface-ward of the historic AW core depth per Figure 2.3. Over the Makarov Basin, AW expanded ~50m deep into the column [*McLaughlin et al.*, 2009], while the AW core depth has moved 100–150m surfaceward with an associated 0.5–1.0 GJ/m^2 increase in associated heat content. Similar changes including the AW moving surfaceward and retaining more heat at-depth are present throughout most of the AO indicating stronger potential influence on ice-related processes [*Polyakov et al.*, 2010].

By 2007, the intermediate AW layer had deepened and thickened in the Pacific Sector [*Zhong and Zhao*, 2014], but the changes are heterogeneous over the central and Eurasian basins. In particular, the net AW layer thickness appears to have thinned over the Amundsen Basin which is likely a mass balance response to the thickened layer observed on the Pacific side of Lomonosov Ridge. Within the western side of Fram Strait, the AW layer thickened by roughly 70m, moving 20m closer to the surface without change in the core depth.

2.4.2 Pacific Waters

Figure 2.2 shows another of the most drastic changes in the Arctic – the change in freshwater distribution. As a proxy for the AW-PW upper-ocean front in the central Arctic, the strong FW anomaly gradient illustrates the change from the Lomonosov Ridge to the Alpha-Mendeleev Ridge (AMR) system [*Morison et al.*, 2006; *Alkire et al.*, 2007, and references therein]. Further, the boundary marking the extent of present SPW in Figures 2.9–2.11 tracks very directly the local bathymetric minimum of the AMR. Estimates shortly after IPY show that FWC in the Eurasian domain decreased by nearly one-quarter while the American domain increased by the same percentage [*McPhee et al.*, 2009; *Rabe et al.*, 2011]. The influx of PW through Bering Strait was near a record high in 2007, importing anomalously large FW volume and thermal input [*Woodgate et al.*, 2012].

Loss of FWC near the pole and in the western sector likely result from cyclonic AO moving the more AW toward the eastern Amerasian Basin. Simultaneously, the wind-forced anti-cyclonic BG stored fresher SPW in the Pacific sector, accumulating an average of 4m FWC on the Pacific side of the front. Much of this FW had been in place prior to 2007; the IPY FWC in the Beaufort Sea is nearly identical to that found for 2006 [*Carmack et al.*, 2008]. *Carmack et al.* [2008] also find that sea-ice freeze/melt accounts for a net-loss of FWC in the Beaufort Region, with riverine water and PW contributing roughly half of the regional FW. *Ge et al.* [2013] find that the mean annual Yukon River outflow, which is identifed as the most significant meteoric source included in SPW, increased 8% between 1977 and 2006.

An increasing trend in Eurasian catchment outflow also is evident [*Shiklomanov and Lammers*, 2009] and related to changes in permafrost [*Zhang et al.*, 2005] and temporal changes in continental hydrological cycles [*Shiklomanov et al.*, 2007]. Increased Siberian runoff suggests the apparent decreases in FW volumes adjacent to the Laptev and East Siberian Seas arise from changes in seasonal ice and the regional dominance of AW, but these source changes alone do not explain FW accumulation observed in the Beaufort Sea during IPY and beyond [*Proshutinsky et al.*, 2009]. Data-conditioned modeling of the 2008 circulation [*Francis et al.*, 2017] suggests that this accumulation may be supported by transport from the Lincoln Sea [*De Steur et al.*, 2013] and/or regions north of Greenland.

Changes in the organization of water masses have also affected the outflow of AO through Fram Strait, located between Greenland and Svalbard. The Transpolar Drift mode arising from the cyclonic AOO regime impedes PW from reaching the continental shelf north of Greenland. Consequently, PW may only exit the AO via the Canadian Archipelago [*Falck et al.*, 2005] which has been shown to be a significant but variable route for AO export [*Curry et al.*, 2011, 2014; *Beszczynska-Möller et al.*, 2011].

2.4.3 Directly Observed from ITP data

The gridded IPY data do not resolve a surface layer. Sea-surface temperature and salinity (SST and SSS, respectively) are temporally variable as they depend on the strongly seasonal Arctic diurnal effects. Additionally, SST/S in the AO depend seasonally on sea-ice related processes such melt-water strata, brine rejection, rapid winter-time heat loss through sea-ice leads, polynyi, and etc. Models and SST satellite data products often assume a surface freezing temperature (FT) of −1.8°C, implicitly conditioned on a background salinity of ~32.86 PSU. At that T/S state, FT sensitivity is ~ 0.1°C per −0.01 PSU so that inaccuracies in background salinity amplify errors in associated freezing temperature.

Figure 2.12 illustrates the inaccuracies of these assumptions by examining the relationship between near-surface temperatures observed by 2006–2009 ITP and FT calculated from the associated salinity. Observations are primarily over the Pacific sector and central Arctic. The thick diagonal line shows exact correspondence between observed T and FT. In the left plot, colors indicate binned values of T+1.8°C for winter ITP in the left plot, with dashed lines demarcating percentiles as labeled. The right plot is similar with binned values of T-minus-FT for summer ITP. In winter months of November–April, all observations correspond to freezing-point, but only about 25% of measurements have $T \leq -1.64°C$, the freezing temperature associated with ~30 PSU. In summer months of May–October, temperatures clearly depart from freezing but only ~25% of measurements differ from freezing by more that 0.05°C. In both summer and winter, the vertical structure of the plots demonstrates inaccuracy of the −1.8°C at ~32.86 PSU assumption; surface waters in the western Arctic have salinities in the range 30–32 PSU.

2.5 Changes in Circulation

Freshwater changes throughout the Arctic relate to changes in geostrophic current distributions. Over basins, the strengthened FW gradient between the Pacific and Atlantic sectors led to a very significant sea-surface height (SSH) changes, which in turn gives rise to changes in geostrophic currents [*McPhee et al.*, 2009]. The strengthening of geostrophic currents in the Pacific Sector is suspect among the factors for the reduction of multi-year ice over the Canadian Basin [*McPhee*, 2013]. Other factors include deepening AW over the Canada Basin since 2004, enhancing the strength of the BG and its accumulation of freshwater [*Zhong and Zhao*, 2014]. A recent study demonstrates that atmospheric modulation of geostrophic boundary currents and SSH quantifiably relate to the Northern Hemisphere annular mode strength [*Armitage et al.*, 2018]. To analyze the quantitative difference in the mean circulation during the IPY period with respect to the climatological circulation, the IPY dataset was conditioned using the 4-Dimensional Variational (4Dvar) Data Assimilation (DA) approach [*Panteleev et al.*, 2011; *Luchin and Panteleev*, 2014] in two ways.

2.5.1 Quasi-stationary Circulation Analysis

To find a quasi-stationary solution, the process uses 4Dvar optimization of an ocean model forced by the corresponding heat, salt and momentum fluxes inferred from NCEP/NCAR reanalysis and regional Pan-Arctic Ice-Ocean Modeling and Assimilation System (PIOMAS). In the non-stationary reconstructions, all available T/S data were averaged for model grid bins and these mean representative observations were assimilated through the conventional 4Dvar DA approach using a semi-implicit ocean model (SIOM) with resolution of 65km; a framework of the algorithm is described in *Panteleev et al.* [2011, 2010].

The resulting quasi-stationary SSH maps and near-surface currents are shown in Figure 2.13. A comparison indicates the essential re-organization of the circulation in the AO evident during IPY. The most-notable feature is the strong intensification and shift of the BG towards the Alaska. IPY SSH patterns are characterized by a pronounced BG dome which attains a central height greater than 50 cm, while the typical climatological SSH is only about 40 cm. This difference results from intensified westward flow along the Alaskan and Chukchi Sea continental slope. There is also a clear re-centering of the BG resulting from the shift the Trasnspolar Drift axis toward the Canada Basin; this agrees well with recent analysis of the freshwater content and circulations conducted by *Timmermans et al.* [2011].

2.5.2 Short-term Dynamical Circulation Reconstruction

Application of the more advanced 4Dvar reconstruction of non-stationary circulation for July-December 2008 indicates stronger circulation than those directly detected from the *in situ* IPY dataset. The SIOM-4Dvar reconstructed bi-monthly evolution of SSH and circulation at 250m depth during July–December 2008 is shown in Figure 2.14. The SSH patterns are characterized by a pronounced BG dome which gets slightly stronger in November–December (Figure 2.14, right) attaining a 40 cm central elevation. Compared to the relatively smooth and symmetric SSH derived through optimal interpolation of observations [e.g. *McPhee et al.*, 2009], the DA-reconstructed SSH reveals finer features consistent with the observations. During September–October, the SSH pattern is characterized by a secondary SSH maximum at 74°N 140°W, which tends to erode by the end of the year but still persists as a tongue spreading towards Alaska along 140°W. This feature is seen in the AVISO anomalies averaged over the second half of 2008 [*Francis et al.*, 2017].

Another prominent feature is a zonally spreading trough in the region between 72–80°N from Severnaya Zemlya to the Bering Strait. The emergence of this depression could be one of the causes of intensification of the Bering Strait transport due to the increase of the large-scale sea level difference between the Chukchi and Bering Seas. This is supported by the analysis of *Woodgate et al.* [2012, & Figure 1h therein] which estimated the force balance controlling the flow through the Bering Strait and found a significant increase of the pressure head in 2007–2011 with respect to the 1997–2006 period when the Bering Strait transport was smaller. Behavior of the SSH lowering is shown in the bi-monthly SSH fields averaged over the area north of the Bering Strait (upper panels in Figure 2.14), the heights of which are estimated to be -11 cm, -10 cm, and -6 cm respectively. This is consistent with the seasonal decline of the Bering Strait inflow from 1.1 Sv in July–August to 0.5 Sv in November-December 2008 [*Woodgate et al.*, 2012].

The effect of the above mentioned SSH decrease on the transport pattern in the region of the AW inflow is of particular interest. During July-August 2008, the negative SSH anomaly is closely attached to the coastline, creating a positive cross-shelf SSH gradient and a westward geostrophic transport of -2.9 Sv along the shelf break (lower left panels in Figure 2.14). The effect becomes less visible by the end of the year as the negative SSH anomaly detaches from the continental slope; the total transport relaxes to eastward values of 0.8 Sv and 1.0 Sv, respectively, for the September-October and November-December periods. This identified flow reversal agrees well with moored velocity observations from the Nansen-Amundsen Basin Observation Program

(NABOS, http://nabos.iarc.uaf.edu/data), which are indicated by red arrows in Figure 2.14 but were not used to obtain the optimized solution. The DA results immediately provide us with quantitative FWC estimates and permit identification of the regional FW. In particular, the total FWC within the volume bounded within [70.25,80]°N × [140,170]°W above 400m depth was found to be about 20,700 km^3, which is slightly less (~5%) than that found in literature [*Proshutinsky et al.*, 2009, updated at http://www.whoi.edu/website/beaufortgyre/home]. A possible source of this difference is a smaller area of the integration for the 4DVar solution and the off-shore displacement of the BG observed in 2008.

To assess the FW origin accumulated FWC in the BG, FW transports across the eastern, southern, and western boundaries were estimated 0.08 Sv, −0.005 Sv, and −0.075 Sv, respectively (positive oriented gyreward); the boundaries are shown in the top right panel of Figure 2.14, where the eastern boundary follows the figure boundary and the southern one intersects the Alaska coast. Calculated transports suggest that observed changes in the BG FWC were generally caused by the FW transport changes confined to the latitude band of 72–77°N at the eastern boundary of the model domain.

2.6 Summary

This work introduces an IPY snapshot ocean climatology, and discusses freshwater and thermal changes in two principle watermasses to establish, in perspective, sub-surface changes over the central AO as well as consequences of surface freshening. It focuses only on the ocean and readily neglected: continental shelves where important watermass-forming processes occur [*Semiletov et al.*, 2005] but enhanced mixing impedes analysis based on T/S; any resolvable changes in Arctic Bottom Water; and a direct discussion of sea-ice which requires an extensive discussion of the atmosphere and its variability [*Maslanik et al.*, 2007] which are beyond the scope of this presentation.

Changes in the AO are not monotonic as they result from cyclic and quasi-cyclic changes in various superimposed feedback-entangled geophysical components in addition to trends in their background values. Changes may arrive in short bursts or "pulses", and may undergo periods of relaxation towards long-term means. The intensive pan-Arctic IPY survey provides evidence of an AO undergoing significant changes and departure from the longer-term mean of the late 20th century – responding to variations in source content (from the Atlantic, Pacific, and continental waters) and the resulting changes: in freshwater and heat distribution; atmospheric forcing and induced SSH gradients and their associated geostrophic responses; and relative volume and means of exit of various watermasses present in the AO. During IPY, many of these components appeared to be establishing new records. In the decade following, 2011–2012 set records for associated components such as River outflow, Bering Strait inflow, sea-ice minimum, arctic cyclone strength – some of which may have been surpassed by those of 2016–2017. From this perspective, conditions of the AO during IPY 2007–2008 show the region in transition toward a "new normal", and a gridded IPY dataset provides a useful reference state for establishing how far that transition has progressed.

A model-DA system was also applied, and may quantify the observed difference in the T/S distribution brought on climatological and seasonal temporal scales. The reconstructed mean 2007–2009 AO circulation clearly identified global shifts in the BG and axis of the Transpolar drift. Both results are consistent with other qualitative analyses. Analysis of the reconstructed non-stationary circulation for July–December 2008 allowed quantification of several anomalous circulation features including:

a) A reversal of the total transport in the AW inflow region of −2.9 Sv in July-August which later relaxed to an eastward transport of 0.8–1.0 Sv. This reversal of along-slope current is confirmed by independent observations from NABOS moorings.

b) Formation of a prominent SSH trough extending from the eastern Laptev Sea to the Bering Strait. A similar and even stronger structure occurs in the PIOMAS solution and is indirectly evidenced by two NABOS moorings located on the continental slope of the Laptev Sea.

c) The above mentioned SSH depression near the Chukchi Sea tends to increase the large-scale sea level difference between the Bering Sea and the AO. This contributes to the 25% increase in the Bering Strait transport at that time, and agrees with the regional force balance suggesting an increased role of the pressure head between the Bering Sea and AO during 2007–2011 [*Woodgate et al.*, 2012].

d) A significant total FWC of ~20,700 km^3 in the BG during 2008. The FW accumulation agrees with estimates from *in situ* hydrographic observations [*Proshutinsky et al.*, 2009]. Analysis of the FW transports across model boundaries around the BG indicates that FW accumulation in 2008 was mainly caused by the anomalous inflow through the eastern section. The DA model estimate of ~0.8 Sv qualitatively agrees with other works [e.g., *Lique et al.*, 2011; *Proshutinsky et al.*, 2015] that suggest FW sources may include areas near Greenland.

Acknowledgements

J.N. Stroh thanks the University of Nevada Reno DeLaMare Library for document preparation resources. G. Panteleev and M. Yaremchuk were supported by the Office of Naval Research (ONR) project "Arctic data assimilation", Program Element 0602435N. O. Francis was supported by the Coastal Hydraulics Engineering Resilience (CHER) Lab, Department of Civil and Environmental Engineering, and Sea Grant College Program at the University of Hawaii at Manoa. M. Yaremchuk was also supported by the ONR Program Element 0603207N under work on the Navy Earth System Prediction Capability.

Bibliography

Alkire, M. B., K. K. Falkner, I. Rigor, M. Steele, and J. Morison (2007), The return of Pacific waters to the upper layers of the central Arctic Ocean, *Deep Sea Research Part I: Oceanographic Research Papers*, *54*(9), 1509–1529.

Armitage, T. W., S. Bacon, and R. Kwok (2018), Arctic sea level and surface circulation response to the Arctic oscillation, *Geophysical Research Letters*, *45*(13), 6576–6584.

Beszczynska-Möller, A., R. A. Woodgate, C. Lee, H. Melling, and M. Karcher (2011), A synthesis of exchanges through the main oceanic gateways to the Arctic Ocean, *Oceanography*, *24*(3), 82–99.

Bourgain, P., and J. C. Gascard (2012), The Atlantic and summer Pacific waters variability in the Arctic Ocean from 1997 to 2008, *Geophysical Research Letters*, *39*(5).

Carmack, E., F. McLaughlin, M. Yamamoto-Kawai, M. Itoh, K. Shimada, R. Krishfield, and A. Proshutinsky (2008), Freshwater storage in the northern ocean and the special role of the Beaufort Gyre, in *Arctic–subArctic ocean fluxes*, pp. 145–169, Springer.

Curry, B., C. Lee, and B. Petrie (2011), Volume, freshwater, and heat fluxes through Davis Strait, 2004–05, *Journal of Physical Oceanography*, *41*(3), 429–436.

Curry, B., C. Lee, B. Petrie, R. Moritz, and R. Kwok (2014), Multiyear volume, liquid freshwater, and sea ice transports through Davis Strait, 2004–10, *Journal of Physical Oceanography*, *44*(4), 1244–1266.

De Steur, L., M. Steele, E. Hansen, J. Morison, I. Polyakov, S. Olsen, H. Melling, F. McLaughlin, R. Kwok, W. Smethie, *et al.* (2013), Hydrographic changes in the Lincoln Sea in the Arctic Ocean with focus on an upper ocean freshwater anomaly between 2007 and 2010, *Journal of Geophysical Research: Oceans*, *118*(9), 4699–4715.

Dmitrenko, I. A., B. Rudels, S. A. Kirillov, Y. O. Aksenov, V. S. Lien, V. V. Ivanov, U. Schauer, I. V. Polyakov, A. Coward, and D. G. Barber (2015), Atlantic water flow into the Arctic Ocean through the St. Anna Trough in the northern Kara Sea, *Journal of Geophysical Research: Oceans*, *120*(7), 5158–5178.

Dukhovskoy, D., M. Johnson, and A. Proshutinsky (2006), Arctic decadal variability from an idealized atmosphere-ice-ocean model: 2. Simulation of decadal oscillations, *Journal of Geophysical Research: Oceans*, *111*(C6).

Ekwurzel, B., P. Schlosser, R. A. Mortlock, R. G. Fairbanks, and J. H. Swift (2001), River runoff, sea ice meltwater, and Pacific water distribution and mean residence times in the Arctic Ocean, *Journal of Geophysical Research: Oceans*, *106*(C5), 9075–9092.

Emery, W. (2001), Water types and water masses, *Encyclopedia of ocean sciences*, *6*, 3179–3187.

Falck, E., G. Kattner, and G. Budéus (2005), Disappearance of Pacific Water in the northwestern Fram Strait, *Geophysical Research Letters*, *32*(14).

Francis, O. P., M. Yaremchuk, G. G. Panteleev, J. Zhang, and M. Kulakov (2017), Anomalous circulation in the Pacific sector of the Arctic Ocean in July–December 2008, *Ocean Modelling*, *117*, 12–27.

Ge, S., D. Yang, and D. L. Kane (2013), Yukon River basin long-term (1977–2006) hydrologic and climatic analysis, *Hydrological Processes*, *27*(17), 2475–2484.

Jakobsson, M., L. Mayer, B. Coakley, J. A. Dowdeswell, S. Forbes, B. Fridman, H. Hodnesdal, R. Noormets, R. Pedersen, M. Rebesco, *et al.* (2012), The International Bathymetric Chart of the Arctic Ocean (IBCAO) version 3.0, *Geophysical Research Letters*, *39*(12).

Krishfield, R., J. Toole, A. Proshutinsky, and M.-L. Timmermans (2008), Automated ice-tethered profilers for seawater observations under pack ice in all seasons, *Journal of Atmospheric and Oceanic Technology*, *25*(11), 2091–2105.

Lique, C., G. Garric, A.-M. Treguier, B. Barnier, N. Ferry, C.-E. Testut, and F. Girard-Ardhuin (2011), Evolution of the Arctic Ocean salinity, 2007–08: contrast between the Canadian and the Eurasian basins, *Journal of Climate*, *24*(6), 1705–1717.

Luchin, V., and G. Panteleev (2014), Thermal regimes in the Chukchi Sea from 1941 to 2008, *Deep Sea Research Part II: Topical Studies in Oceanography*, *109*, 14–26.

Maslanik, J., S. Drobot, C. Fowler, W. Emery, and R. Barry (2007), On the Arctic climate paradox and the continuing role of atmospheric circulation in affecting sea ice conditions, *Geophysical Research Letters*, *34*(3).

McLaughlin, F. A., E. C. Carmack, W. J. Williams, S. Zimmermann, K. Shimada, and M. Itoh (2009), Joint effects of boundary currents and thermohaline intrusions on the warming of Atlantic water in the Canada Basin, 1993–2007, *Journal of Geophysical Research: Oceans*, *114*(C1).

McPhee, M., A. Proshutinsky, J. H. Morison, M. Steele, and M. Alkire (2009), Rapid change in freshwater content of the Arctic Ocean, *Geophysical Research Letters*, *36*(10).

McPhee, M. G. (2013), Intensification of geostrophic currents in the Canada Basin, Arctic Ocean, *Journal of Climate*, *26*(10), 3130–3138.

Morison, J., M. Steele, T. Kikuchi, K. Falkner, and W. Smethie (2006), Relaxation of central Arctic Ocean hydrography to pre-1990s climatology, *Geophysical Research Letters*, *33*(17).

Morison, J., R. Kwok, C. Peralta-Ferriz, M. Alkire, I. Rigor, R. Andersen, and M. Steele (2012), Changing Arctic Ocean freshwater pathways, *Nature*, *481*(7379).

Panteleev, G., D. A. Nechaev, A. Proshutinsky, R. Woodgate, and J. Zhang (2010), Reconstruction and analysis of the Chukchi Sea circulation in 1990–1991, *Journal of Geophysical Research: Oceans*, *115*(C8).

Panteleev, G., M. Yaremchuk, P. J. Stabeno, V. Luchin, D. A. Nechaev, and T. Kikuchi (2011), Dynamic topography of the Bering Sea, *Journal of Geophysical Research: Oceans*, *116*(C5).

Polyakov, I. V., and M. A. Johnson (2000), Arctic decadal and interdecadal variability, *Geophysical Research Letters*, *27*(24), 4097–4100.

Polyakov, I. V., A. Beszczynska, E. C. Carmack, I. A. Dmitrenko, E. Fahrbach, I. E. Frolov, R. Gerdes, E. Hansen, J. Holfort, V. V. Ivanov, *et al.* (2005), One more step toward a warmer Arctic, *Geophysical Research Letters*, *32*(17).

Polyakov, I. V., L. A. Timokhov, V. A. Alexeev, S. Bacon, I. A. Dmitrenko, L. Fortier, I. E. Frolov, J.-C. Gascard, E. Hansen, V. V. Ivanov, *et al.* (2010), Arctic Ocean warming contributes to reduced polar ice cap, *Journal of Physical Oceanography*, *40*(12), 2743–2756.

Polyakov, I. V., V. A. Alexeev, I. M. Ashik, S. Bacon, A. Beszczynska-Möller, E. C. Carmack, I. A. Dmitrenko, L. Fortier, J.-C. Gascard, E. Hansen, *et al.* (2011), Fate of early 2000s Arctic warm water pulse, *Bulletin of the American Meteorological Society*, *92*(5), 561–566.

Proshutinsky, A., R. Krishfield, M.-L. Timmermans, J. Toole, E. Carmack, F. McLaughlin, W. J. Williams, S. Zimmermann, M. Itoh, and K. Shimada (2009), Beaufort Gyre freshwater reservoir: State and variability from observations, *Journal of Geophysical Research: Oceans*, *114*(C1).

Proshutinsky, A., D. Dukhovskoy, M.-L. Timmermans, R. Krishfield, and J. L. Bamber (2015), Arctic circulation regimes, *Phil. Trans. R. Soc. A*, *373*(2052), 20140,160.

Proshutinsky, A. Y., and M. A. Johnson (1997), Two circulation regimes of the wind-driven Arctic Ocean, *Journal of Geophysical Research: Oceans*, *102*(C6), 12,493–12,514.

Rabe, B., M. Karcher, U. Schauer, J. M. Toole, R. A. Krishfield, S. Pisarev, F. Kauker, R. Gerdes, and T. Kikuchi (2011), An assessment of Arctic Ocean freshwater content changes from the 1990s to the 2006–2008 period, *Deep Sea Research Part I: Oceanographic Research Papers*, *58*(2), 173–185.

Rudels, B., E. Jones, L. Anderson, and G. Kattner (1994), On the intermediate depth waters of the Arctic Ocean, *The polar oceans and their role in shaping the global environment*, pp. 33–46.

Rudels, B., H. J. Friedrich, and D. Quadfasel (1999), The Arctic circumpolar boundary current, *Deep Sea Research Part II: Topical Studies in Oceanography*, *46*(6-7), 1023–1062.

Semiletov, I., O. Dudarev, V. Luchin, A. Charkin, K.-H. Shin, and N. Tanaka (2005), The East Siberian Sea as a transition zone between Pacific-derived waters and Arctic shelf waters, *Geophysical Research Letters*, *32*(10).

Serreze, M. C., A. P. Barrett, A. G. Slater, R. A. Woodgate, K. Aagaard, R. B. Lammers, M. Steele, R. Moritz, M. Meredith, and C. M. Lee (2006), The large-scale freshwater cycle of the Arctic, *Journal of Geophysical Research: Oceans*, *111*(C11).

Shiklomanov, A., and R. Lammers (2009), Record Russian river discharge in 2007 and the limits of analysis, *Environmental Research Letters*, *4*(4), 045,015.

Shiklomanov, A., R. Lammers, M. Rawlins, L. Smith, and T. Pavelsky (2007), Temporal and spatial variations in maximum river discharge from a new Russian data set, *Journal of Geophysical Research: Biogeosciences*, *112*(G4).

Shiklomanov, I., A. Shiklomanov, R. Lammers, B. Peterson, and C. Vorosmarty (2000), The dynamics of river water inflow to the Arctic Ocean, in *The freshwater budget of the Arctic Ocean*, pp. 281–296, Springer.

Shimada, K., E. C. Carmack, K. Hatakeyama, and T. Takizawa (2001), Varieties of shallow temperature maximum waters in the western Canadian Basin of the Arctic Ocean, *Geophysical Research Letters*, *28*(18), 3441–3444.

Shimada, K., M. Itoh, S. Nishino, F. McLaughlin, E. Carmack, and A. Proshutinsky (2005), Halocline structure in the Canada Basin of the Arctic Ocean, *Geophysical Research Letters*, *32*(3).

Steele, M., and T. Boyd (1998), Retreat of the cold halocline layer in the Arctic Ocean, *Journal of Geophysical Research: Oceans*, *103*(C5), 10,419–10,435.

Steele, M., R. Morley, and W. Ermold (2001), PHC: A global ocean hydrography with a high-quality Arctic Ocean, *Journal of Climate*, *14*(9), 2079–2087.

Steele, M., J. Morison, W. Ermold, I. Rigor, M. Ortmeyer, and K. Shimada (2004), Circulation of summer Pacific halocline water in the Arctic Ocean, *Journal of Geophysical Research: Oceans*, *109*(C2).

Stroh, J., G. Panteleev, S. Kirillov, M. Makhotin, and N. Shakhova (2015), Sea-surface temperature and salinity product comparison against external in situ data in the Arctic Ocean, *Journal of Geophysical Research: Oceans*, *120*(11), 7223–7236.

Timmermans, M.-L., A. Proshutinsky, R. A. Krishfield, D. K. Perovich, J. A. Richter-Menge, T. P. Stanton, and J. M. Toole (2011), Surface freshening in the Arctic Ocean's Eurasian Basin: An apparent consequence of recent change in the wind-driven circulation, *Journal of Geophysical Research: Oceans*, *116*(C8).

Timokhov, L., and F. Tanis (1997), Environmental working group joint US-Russian atlas of the Arctic Ocean, *National Snow and Ice Data Center, Boulder, CO USA*, DOI: *10.7265/N5H12ZX4*.

Toole, J. M., R. A. Krishfield, M.-L. Timmermans, and A. Proshutinsky (2011), The ice-tethered profiler: Argo of the Arctic, *Oceanography*, *24*(3), 126–135.

Troupin, C., A. Barth, D. Sirjacobs, M. Ouberdous, J.-M. Brankart, P. Brasseur, M. Rixen, A. Alvera-Azcárate, M. Belounis, A. Capet, *et al.* (2012), Generation of analysis and consistent error fields using the Data Interpolating Variational Analysis (DIVA), *Ocean Modelling*, *52*, 90–101.

Wang, J., J. Zhang, E. Watanabe, M. Ikeda, K. Mizobata, J. E. Walsh, X. Bai, and B. Wu (2009), Is the dipole anomaly a major driver to record lows in Arctic summer sea ice extent?, *Geophysical Research Letters*, *36*(5).

Weingartner, T. J., D. J. Cavalieri, K. Aagaard, and Y. Sasaki (1998), Circulation, dense water formation, and outflow on the northeast Chukchi shelf, *Journal of Geophysical Research: Oceans*, *103*(C4), 7647–7661.

Woodgate, R. (2013), Arctic Ocean circulation: Going around at the top of the world, *Nature Education Knowledge*, *4*(8), 8.

Woodgate, R. A., T. J. Weingartner, and R. Lindsay (2012), Observed increases in Bering Strait oceanic fluxes from the Pacific to the Arctic from 2001 to 2011 and their impacts on the Arctic Ocean water column, *Geophysical Research Letters*, *39*(24).

Zhang, T., O. W. Frauenfeld, M. C. Serreze, A. Etringer, C. Oelke, J. McCreight, R. G. Barry, D. Gilichinsky, D. Yang, H. Ye, *et al.* (2005), Spatial and temporal variability in active layer thickness over the Russian Arctic drainage basin, *Journal of Geophysical Research: Atmospheres*, *110*(D16).

Zhang, X., and J. Zhang (2001), Heat and freshwater budgets and pathways in the Arctic mediterranean in a coupled ocean/sea-ice model, *Journal of Oceanography*, *57*(2), 207–234.

Zhong, W., and J. Zhao (2014), Deepening of the Atlantic Water core in the Canada Basin in 2003–11, *Journal of Physical Oceanography*, *44*(9), 2353–2369.

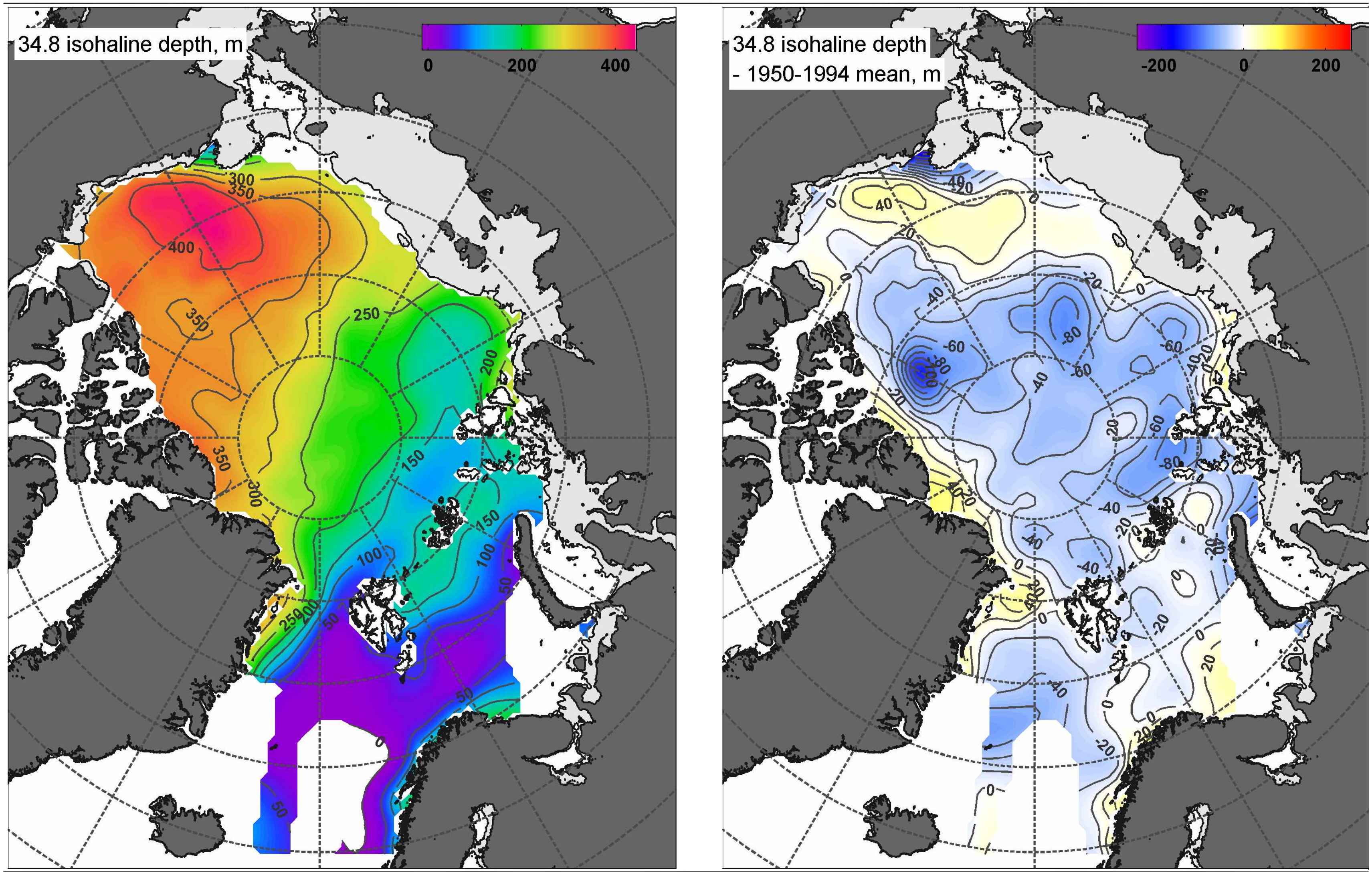

Figure 2.1. 34.8 PSU Isohaline depth - IPY *(left)* and anomaly *(right)*. Values are given in meters.

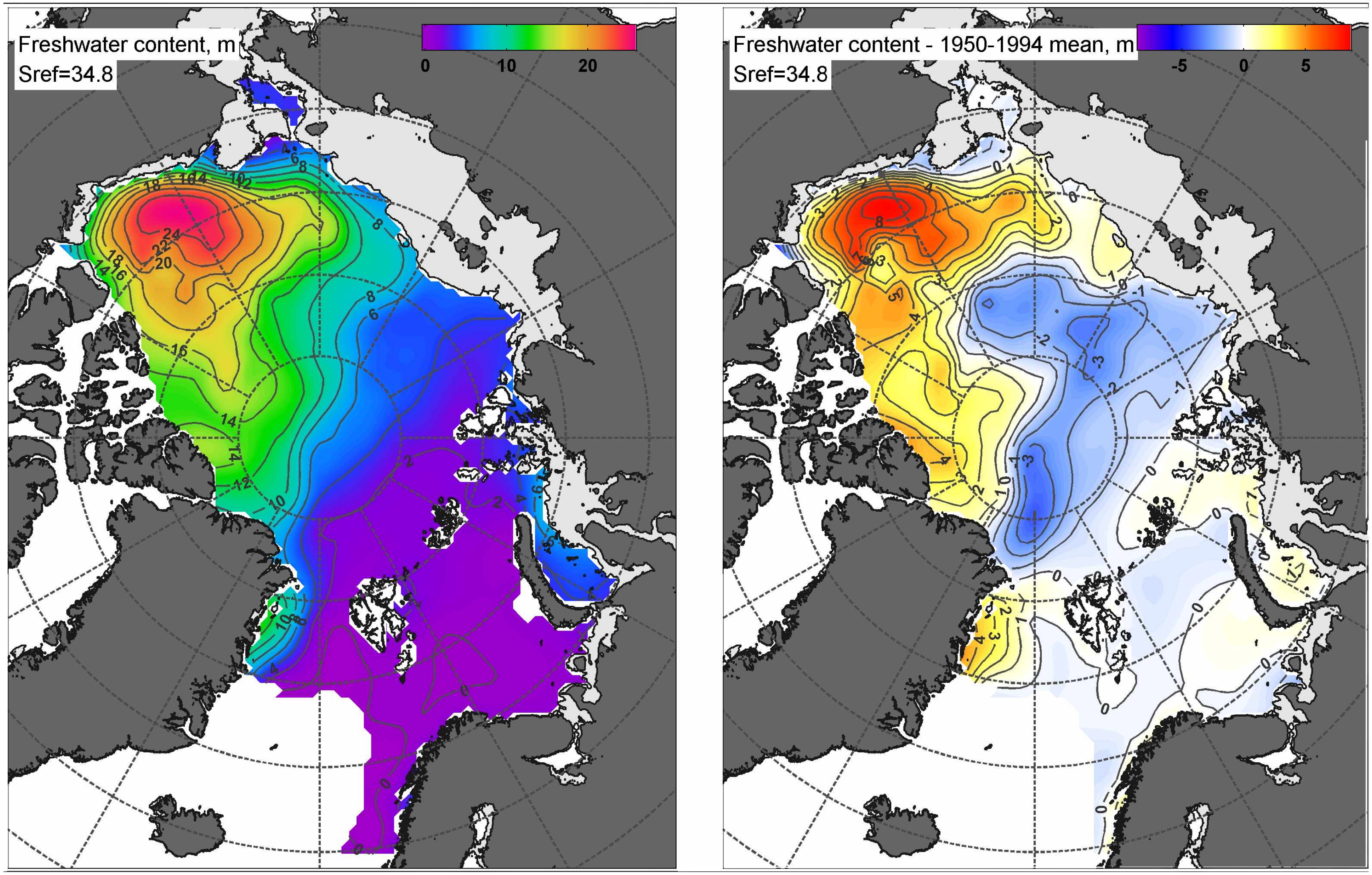

Figure 2.2. FWC relative to 34.8 PSU Isohaline - IPY *(left)* and anomaly *(right)*. Values are given in meters.

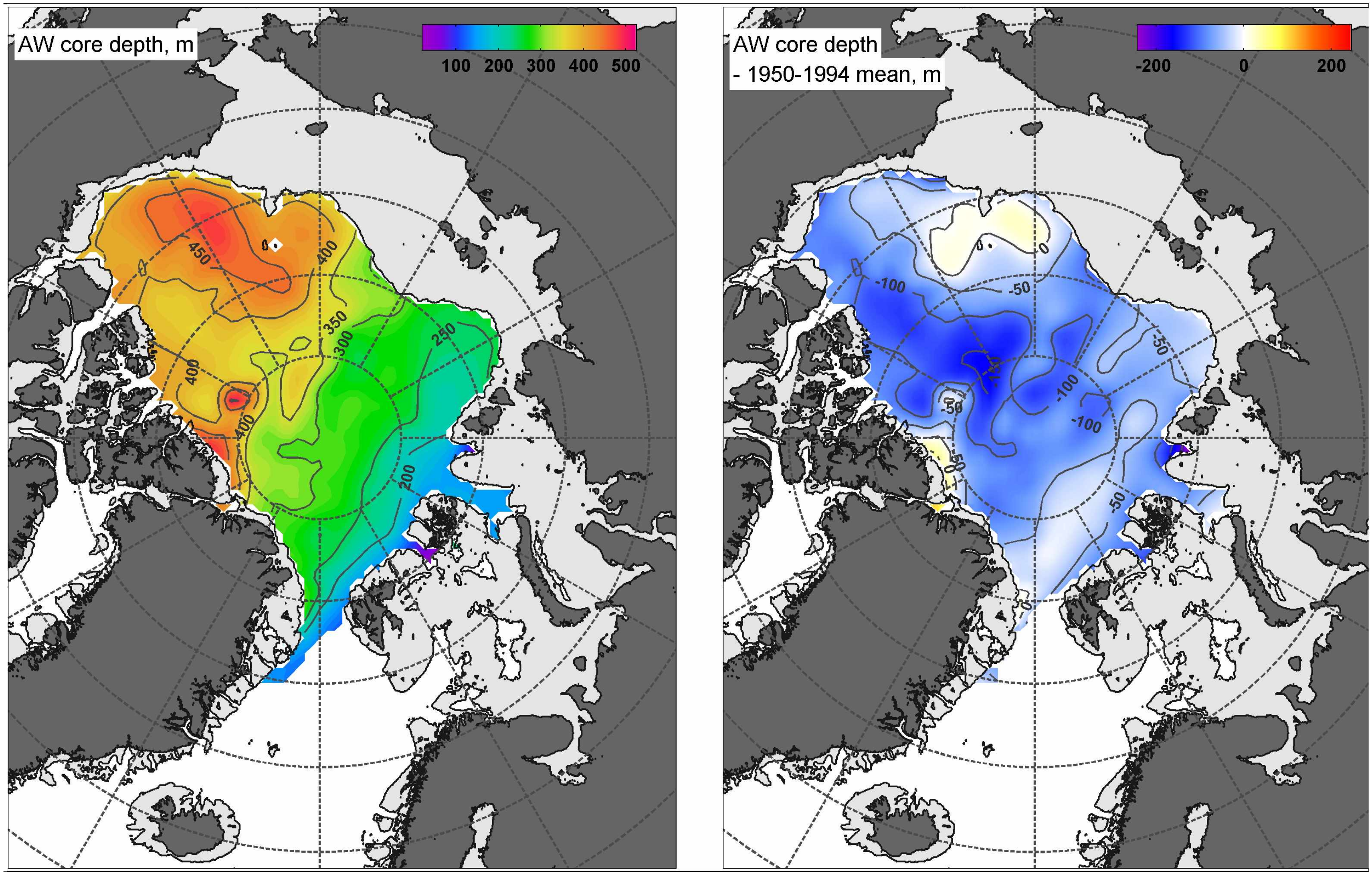

Figure 2.3. AW core depth - IPY *(left)* and anomaly *(right)*. Values are given in meters.

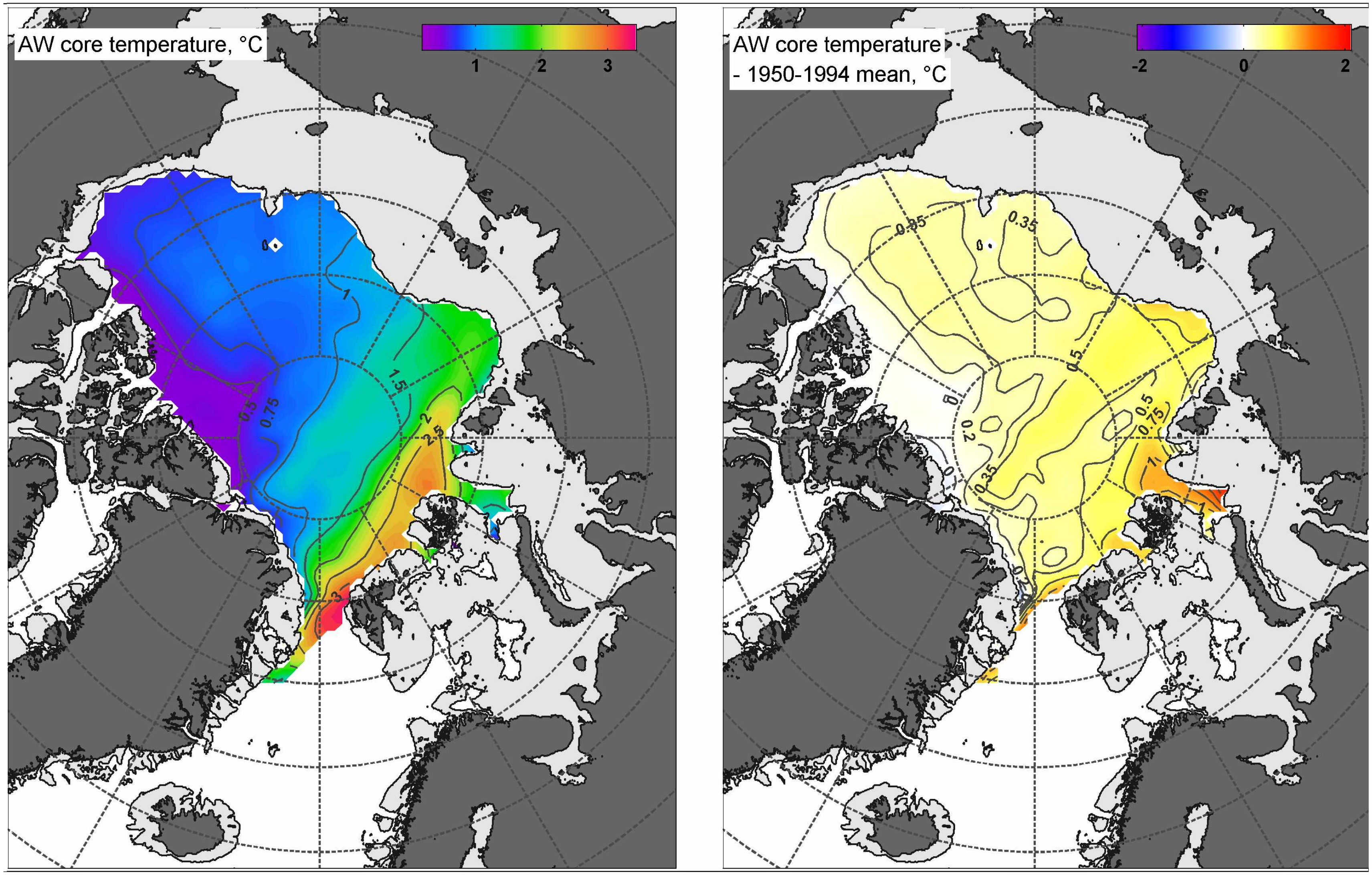

Figure 2.4. AW core temperature - IPY *(left)* and anomaly *(right)*. Values are given in ° C.

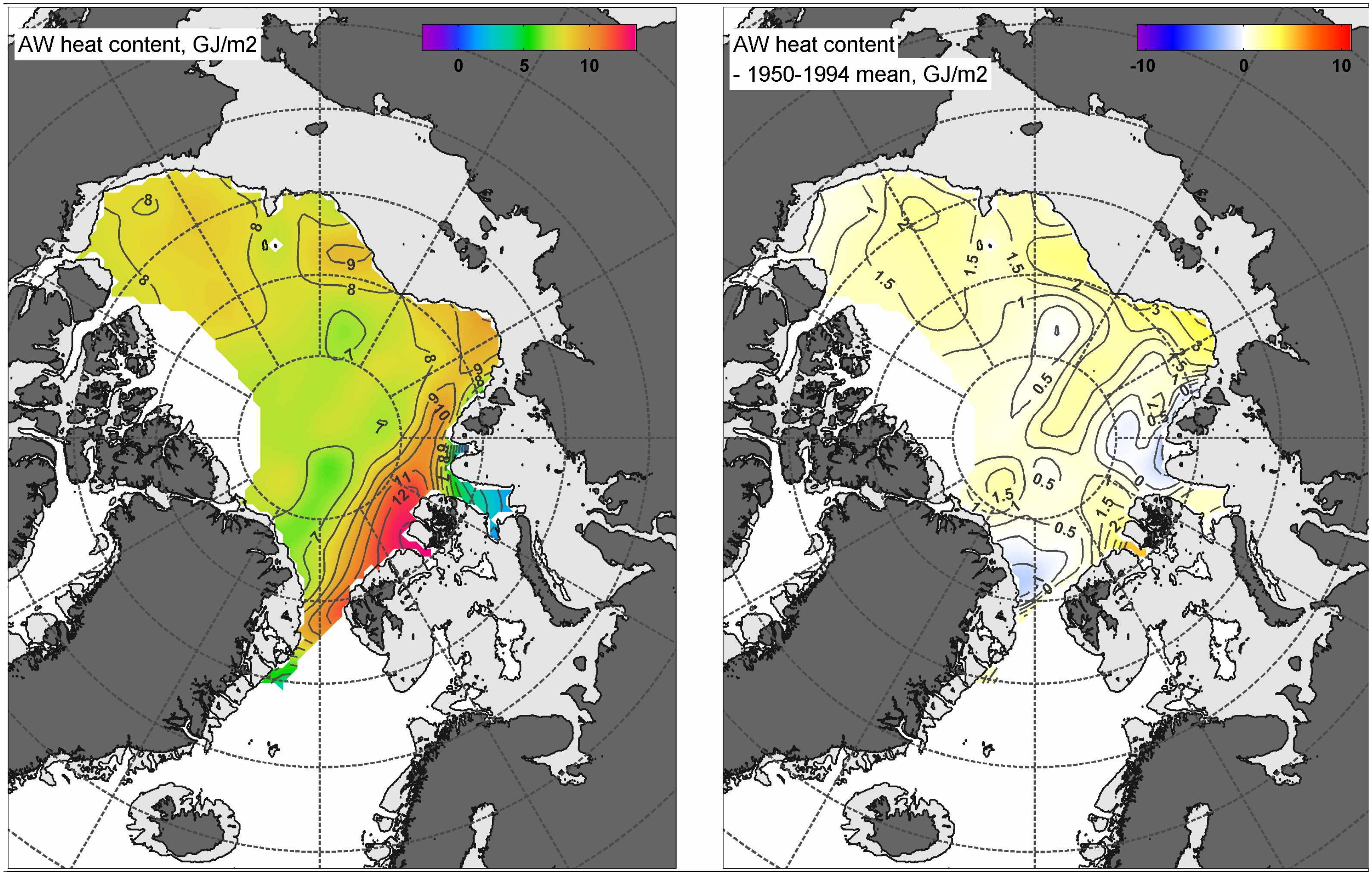

Figure 2.5. AW Heat Content - IPY *(left)* and anomaly *(right)*. Values are given in GJ/m^2 (or 10^9 J/m^2).

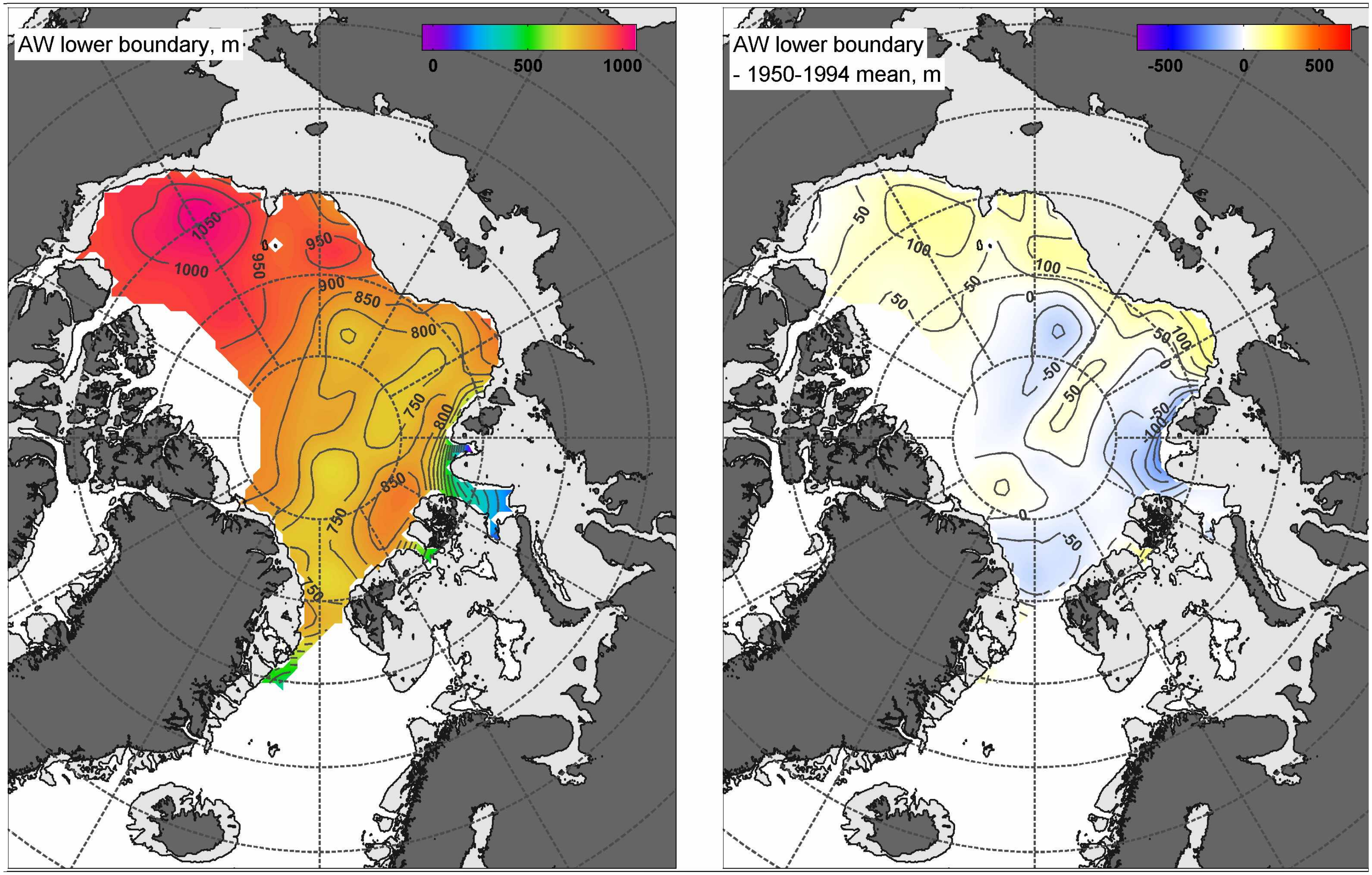

Figure 2.6. AW Lower Boundary - IPY *(left)* and anomaly *(right)*. Values are given in meters.

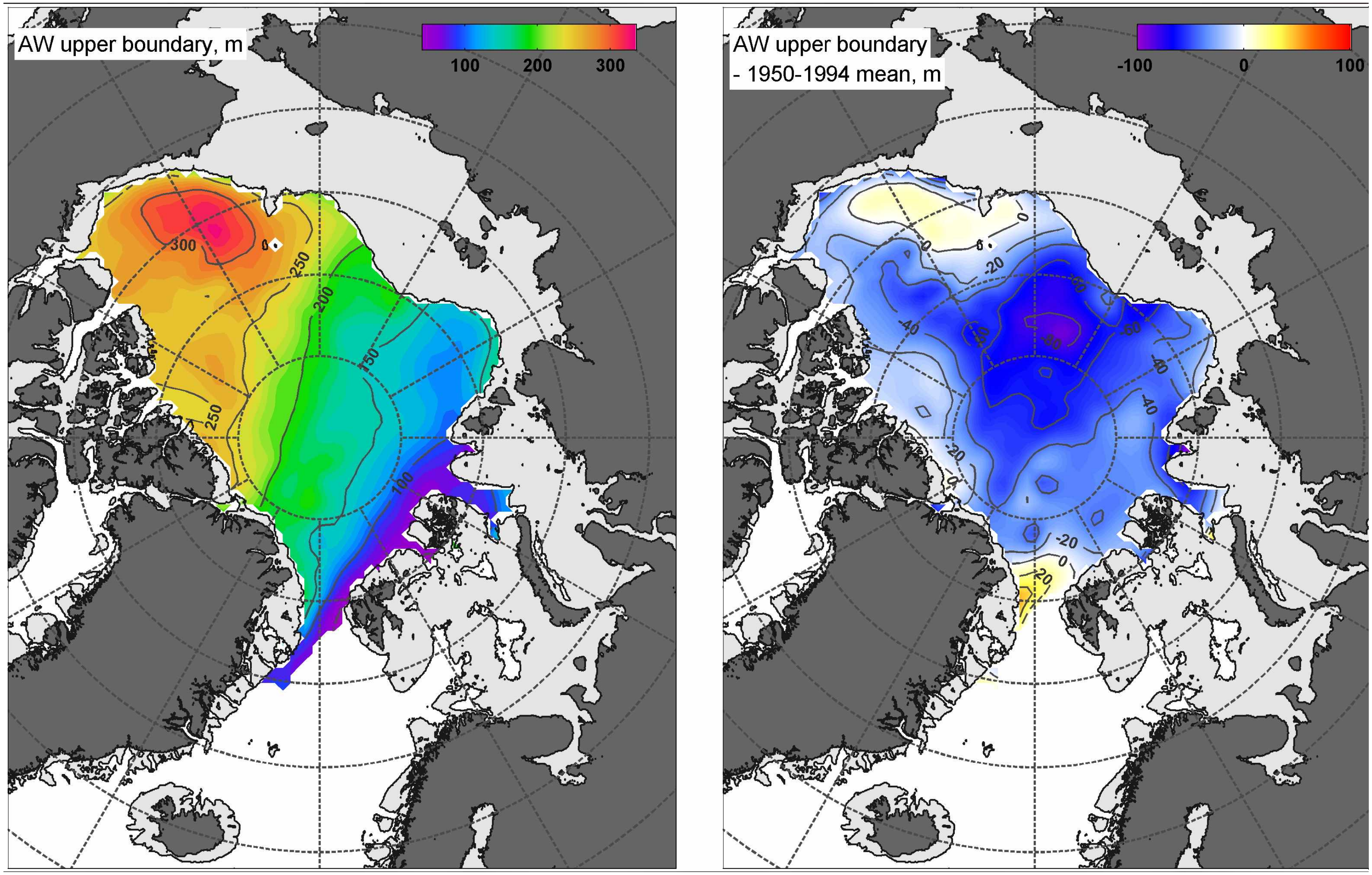

Figure 2.7. AW Upper Boundary - IPY *(left)* and anomaly *(right)*. Values are given in meters.

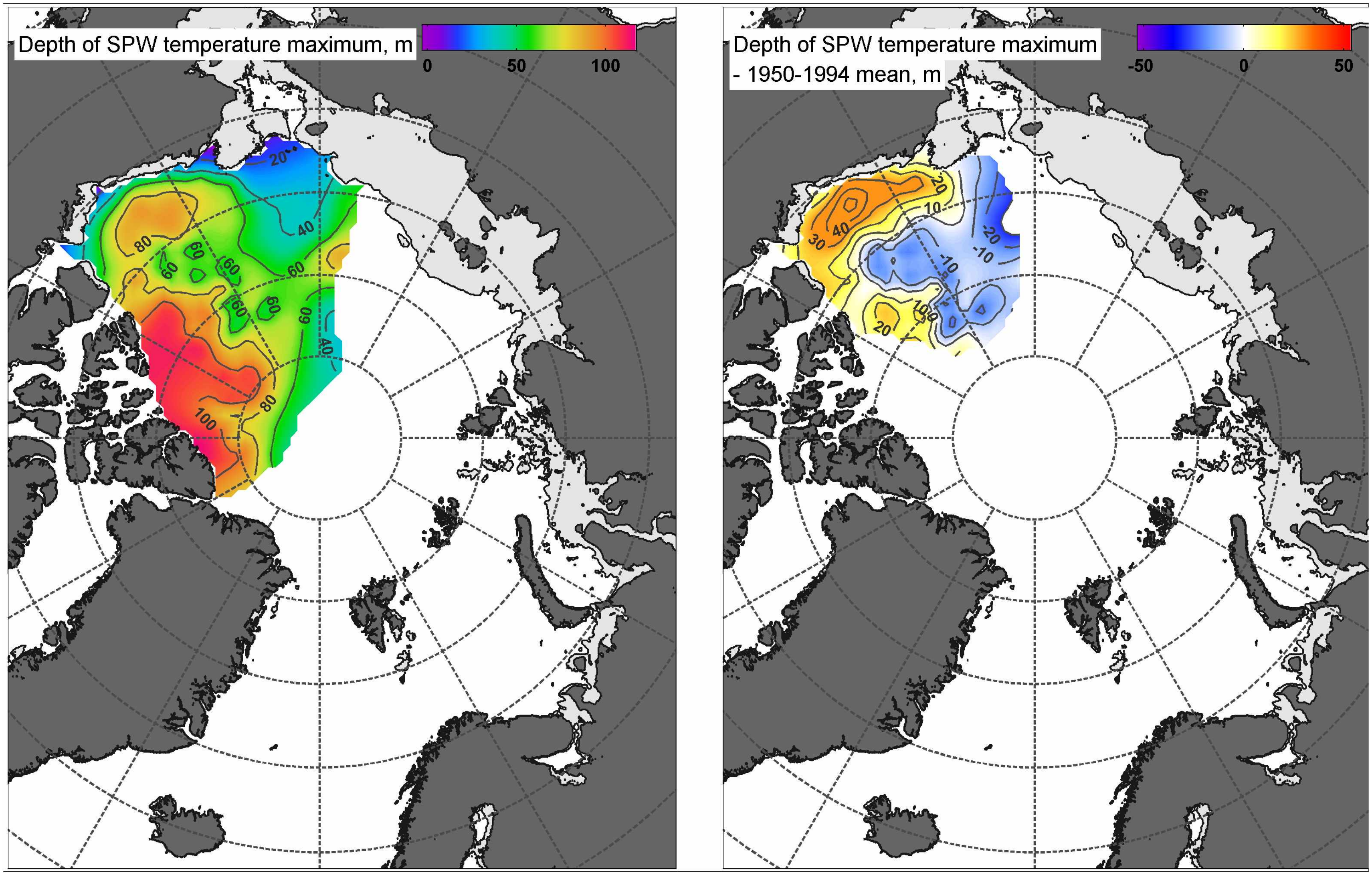

Figure 2.8. Summer PW depth of T_{max} - IPY *(left)* and anomaly *(right)*. Values are given in meters.

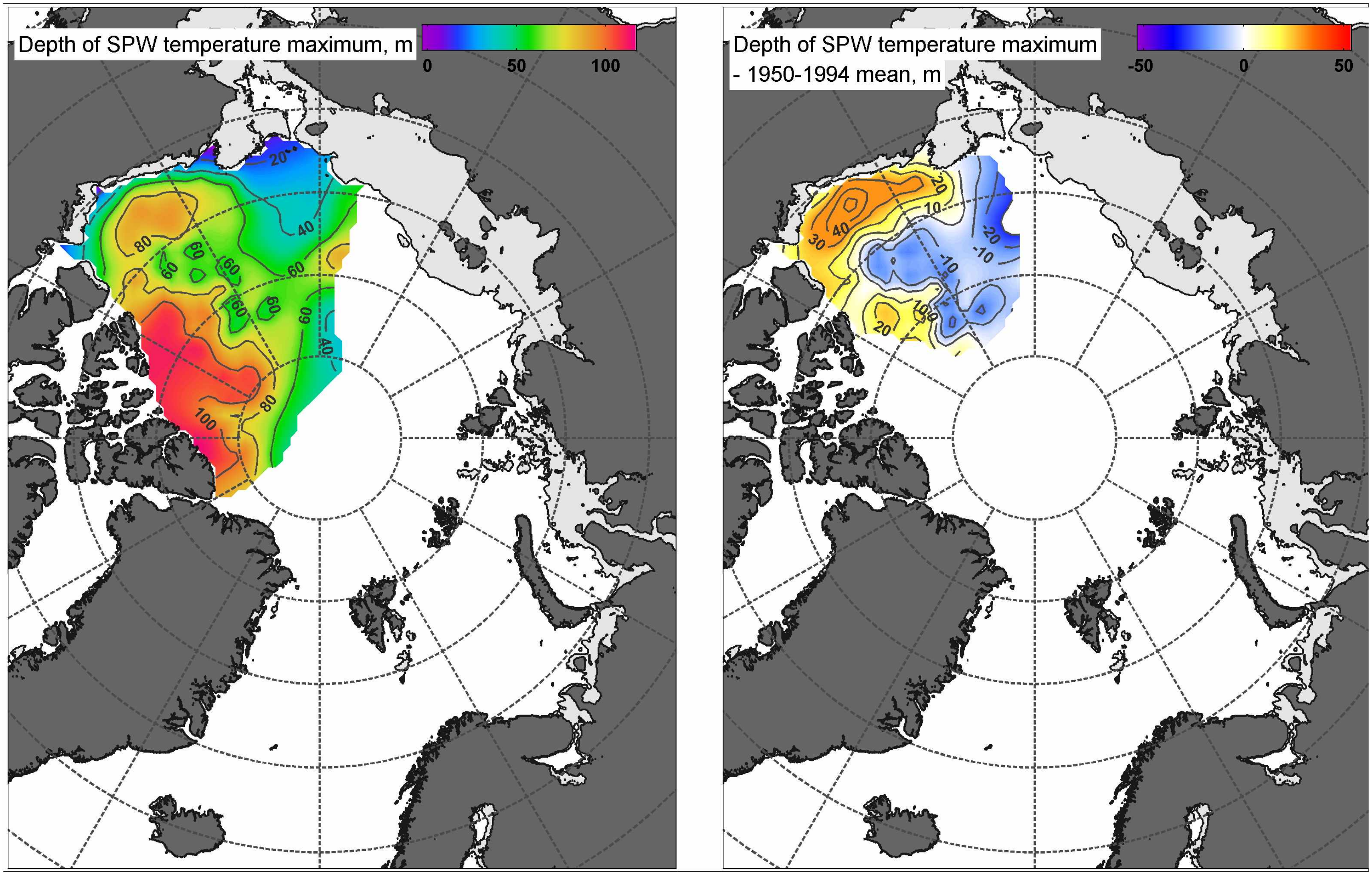

Figure 2.9. Summer PW T_{max} - IPY *(left)* and anomaly *(right)*. Values are given in °C.

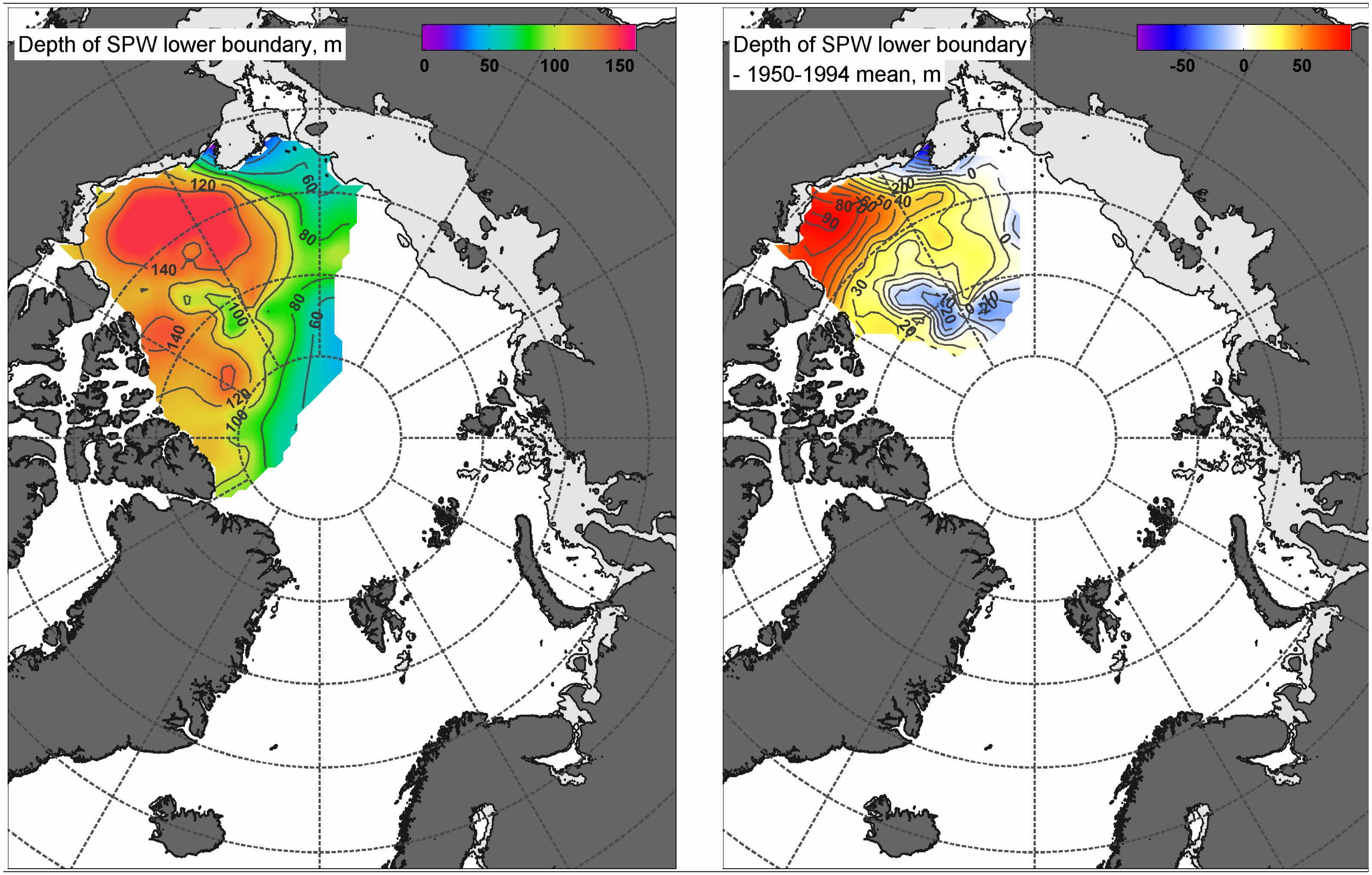

Figure 2.10. Summer PW Lower Boundary Depth - IPY *(left)* and anomaly *(right)*. Values are given in meters.

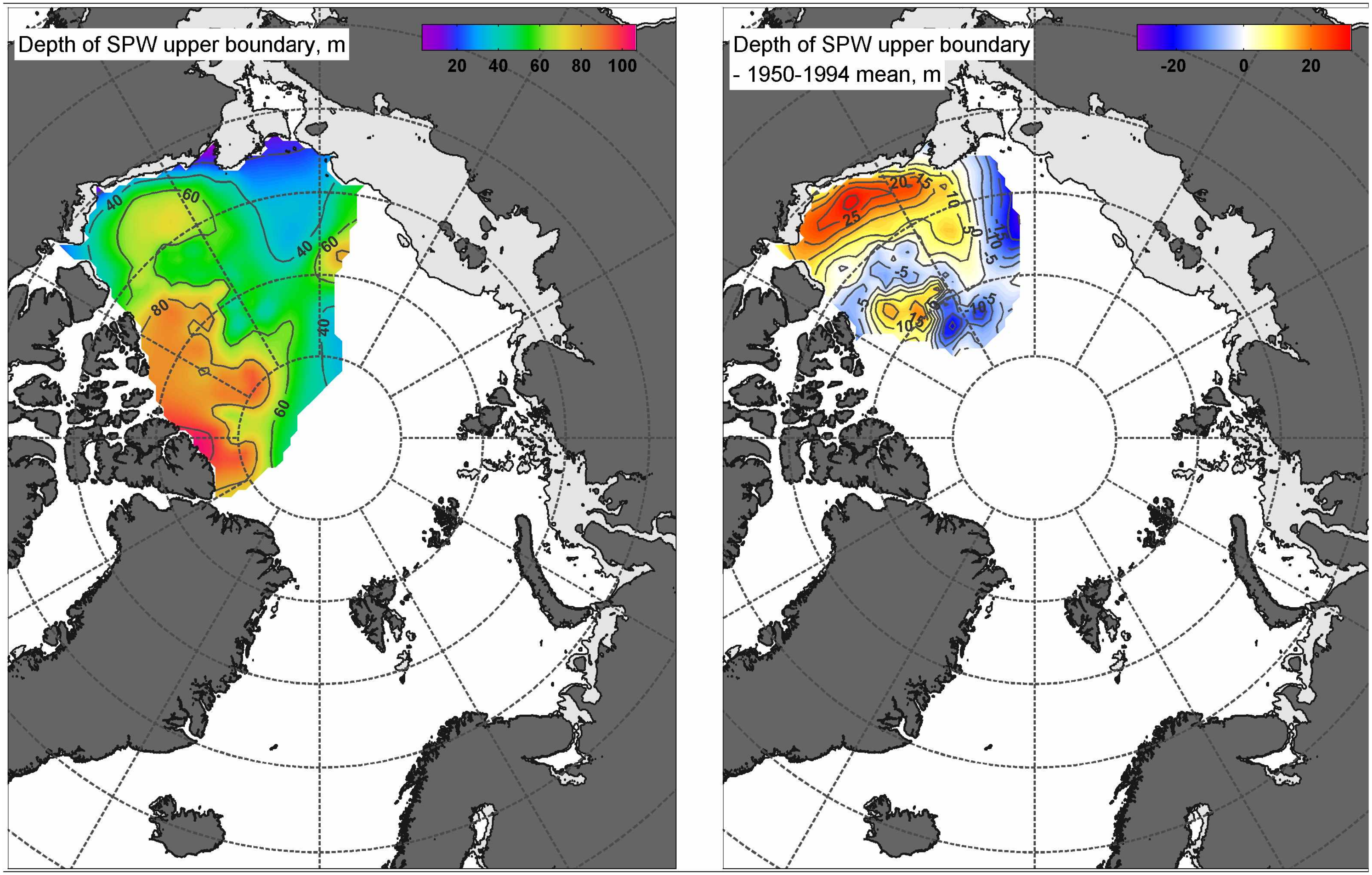

Figure 2.11. Summer PW Upper Boundary Depth - IPY *(left)* and anomaly *(right)*. Values are given in meters.

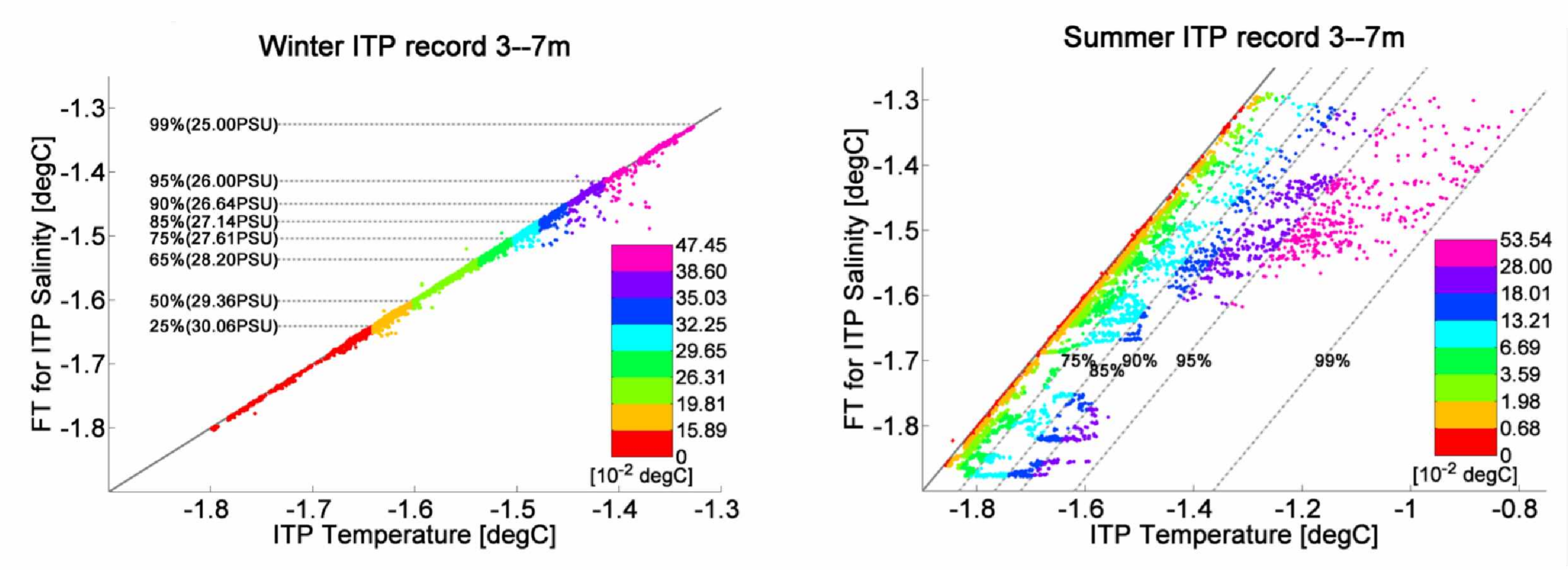

Figure 2.12. Shallow ITP observed temperatures and associated freezing temperature from ITP salinities - winter *(left)* and summer *(right)*. All axes are given in °C. In the left plot, bins are horizontal because distance from the horizontal line FT=−1.8 is calculated. In the right plot, bins are parallel with the thick diagonal reference line T=TF since pointwise departures of T from TF are considered.

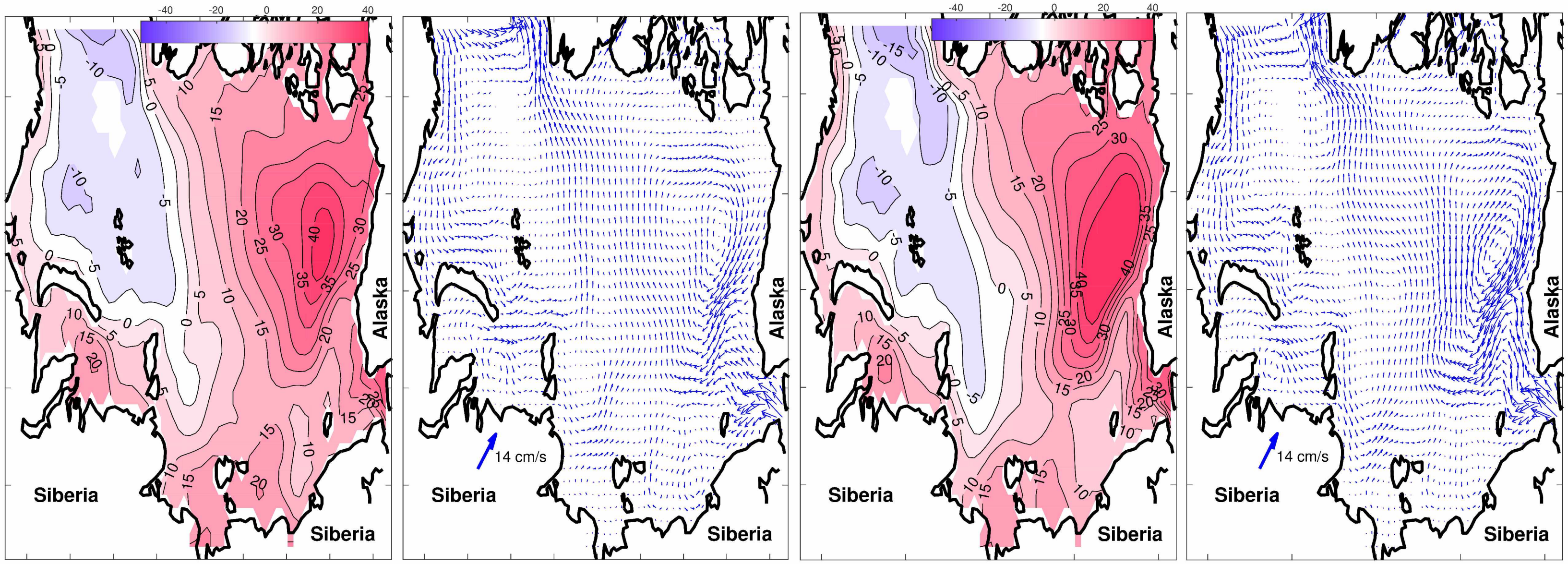

Figure 2.13. Quasi-stationary model reconstruction of SSH and near-surface currents from historical 1900–2006 data *(left plots)* and the IPY data *(right plots)*. SSH contours are given in cm while velocities are scaled with respect to the 14 cm/s arrow indicated over western Siberia.

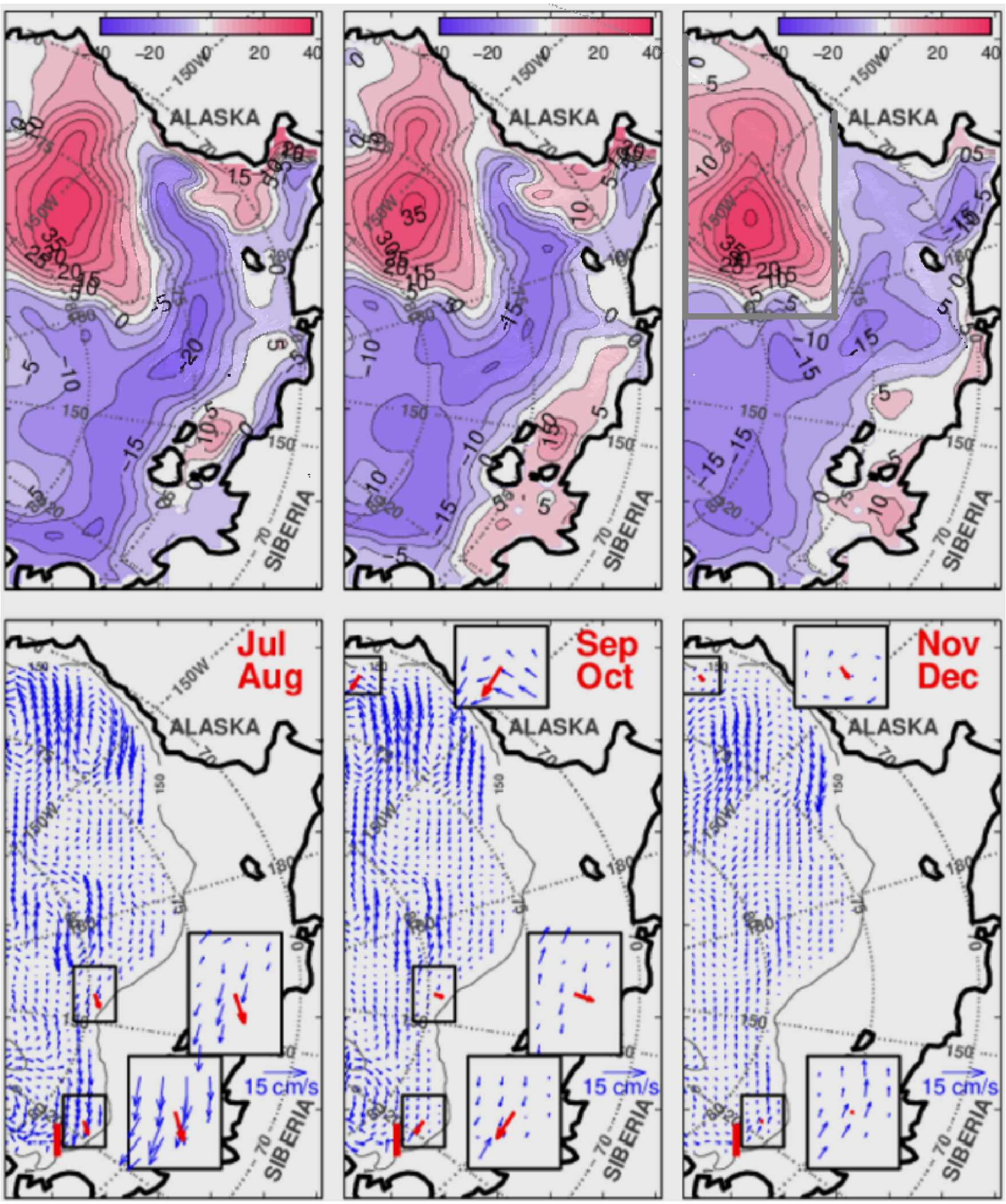

Figure 2.14. Bi-monthly averaged fields for SSH (*upper panels*, in cm) and 250m currents (*lower panels*, with respect to the shown 15 cm/s reference arrow scale). NABOS mooring-observed velocities are shown as red arrows in insets. The boundary used for calculating the total FW flux around BG is indicated by the thick grey line around the upper right panel; the grey line adjacent to the figure panel frame is the "eastern" boundary around BG through which FW transport is positive (gyreward).

Chapter 3: Toward Optimization of Rheology in Sea Ice Models through Data Assimilation[1] [2]

Abstract

Sea ice models which allow for deformation are primarily based on rheological formulations originally developed by *Hibler* [1979]. In both the original visco-plastic (VP) and elastic-VP schemes, the internal sea-ice pressure term is modeled as a function of variable sea ice thickness and concentration with empirical parameters for ice-strength and atmospheric wind stress prescribed as constants throughout the domain. This work considers a spatially-variable extension of those parameters in the one-dimensional VP sea ice formulation of *König Beatty and Holland* [2010]. In areas where ice cover is complete, experiments which assimilate synthetic ice-state observations using variable rheological parameters show larger improvements than equivalent experiments using homogeneous parameters. For partially ice-covered regions where internal ice stresses are negligible, experiments assimilating synthetic sea ice velocity observations demonstrate reasonable reconstruction of spatially variable wind stresses. These results suggest practical benefits attainable by using sea ice velocity, thickness, and concentration to optimize spatially-varying rheological parameters and to improve sea ice state reconstruction and forecast.

3.1 Introduction

Sea ice models are an important component of any ice-ocean Data Assimilation (DA) system in the Arctic Ocean (AO). Currently, there are several DA systems which are widely applied to reconstruct ice conditions in the Arctic in reanalysis or quasi-operational mode. For example, there are systems based on the MITgcm [*Menemenlis et al.*, 2008; *Heimbach*, 2008; *Forget et al.*, 2015; *Fenty et al.*, 2017], ROMS [*Budgell*, 2005], HYCOM [*Lisæter et al.*, 2007; *Sakov et al.*, 2012]), PIOMAS [*Zhang and Rothrock*, 2003; *Lindsay and Zhang*, 2006], and NEMO [*Vancoppenolle et al.*, 2009; *Massonnet et al.*, 2015]. Several new methods of sea ice modeling have been proposed during the last decade including Lagrangian models [*Rampal et al.*, 2015; *Bouillon and Rampal*, 2015a] and finite element models [*Danilov et al.*, 2015]. In spite of these new technologies, practically all sea ice DA systems implement sea ice models based on the visco-plastic (VP) rheology proposed by *Hibler* [1979] and/or the elasto-VP

---

[1] Stroh, JN, G. Panteleev, O. Francis, M. Yaremchuk, and R. Allard, (2019), Toward Optimization of Rheology in Sea Ice Models through Data Assimilation, *Journal of Atmospheric and Oceanic Technology, accepted.*

[2] Reviewers have provided important feedback and concerns that could not be fully addressed before submission deadlines of this document to the University of Alaska Fairbanks Graduate School; footnotes throughout the chapter comment on these issues. However, the footnotes are not an adequate guide to a major revision. The author openly acknowledges his *extreme* self-disquiet at formally committing this administratively-reviewed chapter with known errors and oversights that have elsewhere been corrected already; an interested reader is well-encouraged to email the author personally or otherwise seek an updated version of this work.

(EVP) modification [*Hunke and Dukowicz*, 1997]. The essential advantage of these models is the efficient and relatively simple approximation of sea ice dynamics in terms of the VP/EVP rheology which is based on a rigorous theoretical framework developed in the past century [*Timoshenko and Goodier*, 1951; *Goodier and Hodge*, 1958] with an adjunct practical stability analysis theory for sea ice applications [*Gray and Killworth*, 1995; *Schulkes*, 1996; *Dukowicz*, 1997; *Pritchard*, 2005].

According to *Hibler* [1979], the sea ice model rheology is defined by three parameters (e, P^*, c^*) describing respectively the yield ellipse eccentricity, the dimensional maximum ice strength per unit-thickness, and non-dimensional scaling of ice strength with its compactness. Ice strength within a grid cell is a mean value, although the intracell strength distribution is unknown. The idea of approximation to sea ice dynamics through the VP rheology is that spatiotemporal variations in plastic deformation rates are statistically representable by a viscosity term [*Hibler*, 1977]. Therefore, practical VP viscosity reflects a subgrid parametrization of variable local strength properties without fully resolving the underlying floe distribution. However, one notes that this interpretation implicitly assumes a uniform distribution of cracks and other ice weaknesses throughout the grid cell.

Over the last decades, estimates of sea ice rheological parameters (RPs) have been made from the satellite and in situ ice observations. These estimates, however, range within significant limits [*Harder and Fischer*, 1999]. For example, *Tremblay and Hakakian* [2006] bounded P^* between 35 and 45 kN/m^2 while earlier historical literature suggests a range of 15 kN/m^2 to 27.5 kN/m^2 may be more appropriate [*Weeks and Assur*, 1967; *Timco and Weeks*, 2010][3]. These works' authors emphasize the significant variability of their P^* estimates, which may be attributed to spatial and temporal variation of Arctic sea ice and better represented using a non-elliptic form of the yield curve [e.g. *Tremblay and Hakakian*, 2006].

For modeling landfast ice, an additional parameter k_T has been introduced to model tensile strength [*König Beatty and Holland*, 2010] which is omitted in the traditional [i.e. *Hibler*, 1979] elliptical yield curve formulation. Numerical experiments with a coarse resolution pan-Arctic CICE-NEMO model find that $k_T = 0.2$ provides the best agreement with landfast strength measurements in the Kara Sea region, with ellipse ratio $1.2 \leq e \leq 1.4$ providing the best fit to the sea ice observations [*Lemieux et al.*, 2016]. *Lemieux et al.* [2016] emphasizes the significant impact

---

[3] A reviewer correctly identified that the manuscript mis-cited *Kreyscher et al.* [1997], *Hibler III and Walsh* [1982], and *van Scheltinga et al.* [2010] for estmates of P^*. An unpublished 2010 work by van Scheltinga *et al.* (http://www.met.reading.ac.uk/~xv901096/research/Terwisscha-2010.pdf) gives seasonal pan-Arctic distributions of P^* bounded between 10 and 40 kN/m^2 based on assimilative modelling. Improved citation of studies providing rheological parameter estimates is forthcoming in the revision.

the ellipse parameter value has on simulation results, which intimates variability of e, noting that "tensile strength should depend on other factors such as sea ice salinity, the ice temperature, the history of deformation of sea ice, etc".

Recently, the impact of spatial non-uniformity of the ice strength parameter P^* was analyzed by *Juricke et al.* [2013]. AO sea ice models in that study generated greater ice volume and lower ice cover area when P^* was stochastically perturbed, and the authors found that such effects could not be reproduced from global modifications of P^*.

Thus, analysis of sea ice observations and numerical modeling results suggest that an optimized spatially-varying set of RPs (i.e. $e(x,y)$, $P^*(x,y)$, $c^*(x,y)$, $k_T(x,y)$) may significantly improve the results of numerically modeled sea ice. Obviously, it is tempting to methodically resolve RP dependence on observable sea ice properties and analytically derive optimal estimates from them. However, a poor theoretical understanding of ice floe interactions subject to various external and internal forces precludes this approach. One also anticipates temporal variability of RPs, as the ice state variables which influence their values vary seasonally as well as spatially.

An alternative method is to empirically optimize sea ice RPs through the assimilation of available sea ice observations into a sea ice model using the Variational (Var) data assimilation technique [*Le Dimet and Talagrand*, 1986]. This approach looks feasible given the tremendous increase of the satellite sea ice observations during the last decades suitable for model constraint. When ice cover is not full, the permitted advection exponentially reduces the importance of internal stresses so the benefit of variable internal RPs may be relatively unimportant for sea ice model dynamics in this case. In such regions, however, model dynamics may benefit from local optimization of wind-imparted surface stresses [*Miller et al.*, 2006], and a common assimilation approach can be generally applied to find optimal RP and/or wind stress, depending on the region. Temporally fixed RPs are sought here for the purposes of improving short-term reconstruction and forecast of the ice state.

Currently available are relatively accurate observations of sea ice concentration (SIC) and sea ice velocity (SIV) from optical or SAR images [*Komarov and Barber*, 2014; *Bouillon and Rampal*, 2015b]. There are several satellite projects that may potentially provide daily SIV and sea ice thickness (SIT) in the near future (e.g. NASA ICEsat-2 and CSA RADARSAT Constellation Mission) given the right data processing. A properly-developed variational algorithm can assimilate these sea ice observations to optimize spatially variable sea ice RP in the Arctic region, with temporal variability resolved by sequential assimilation. Nevertheless, open questions remain regarding the tangent linearity and controllability of VP/EVP ice models through sea ice RPs.

This study adopts the simplified one-dimensional sea ice model of *König Beatty and Holland* [2010] and explores some of these questions using a corresponding variational DA system (VarDAS). The work posits that addressing these issues is important before including spatial variability into modern sea ice models (e.g. CICE) and developing the associated tangent linear and adjoint models. The developed VarDAS may be formally applied to estimate sea ice rheology in narrow straits or small-scale regions where sea ice is essentially one-dimensional such as in ice ridging areas. The approach uses Observation System Simulation Experiments (OSSEs) to evaluate the optimizability of the two major sea ice RPs (e and P^*), wind stress, and initial ice state distributions on the basis of simulated incoming satellite observations. The paper is organized as follows: Section 2 describes the implemented ice model and applied DA algorithm; Section 3 describes the underlying OSSE hypotheses and experiment design; Section 4 discusses results of the OSSEs; and Section 5 summarizes the work and comments on future research.

3.2 Optimization Method

This section provides details of the implemented sea ice forward-time model and its associated linearizations, outlines the variational data assimilation system (DAS) applied to optimize model parameters, and describes the synthetic observations used to do so.

3.2.1 Forward, Tangent Linear, and Adjoint models[4]

This work considers the thermostatic sea ice model [*Hibler*, 1979] with tensile strength [*König Beatty and Holland*, 2010] and localized variability in ice-strength parameters. The standard one-dimensional sea ice constituent equations with fixed boundaries on a domain of length L=1800 km are given by:

$$m\frac{\partial u}{\partial t} = \frac{\partial \sigma}{\partial x} + \tau_a - \tau_o, \qquad u(x,0) = u_0(x) \tag{3.1}$$

$$\frac{\partial h}{\partial t} = \frac{\partial (uh)}{\partial x}, \qquad h(x,0) = h_0(x) \tag{3.2}$$

$$\frac{\partial a}{\partial t} = \frac{\partial (ah)}{\partial x}, \qquad a(x,0) = a_0(x) \tag{3.3}$$

---

[4] This section contains numerous inaccuracies, including major errors in the presented equations. There are also several undiscussed assumptions. An interested reviewer is cautioned to these problems.

with a stress tensor defined by[5]:

$$\sigma = \frac{e(x)^2 + 1}{e(x)^2} \frac{P - T}{2} \left(\frac{1}{\Delta} \frac{\partial u}{\partial x} - 1 \right) \tag{3.4}$$

$$P = P^*(x) \cdot h \cdot \exp[-c^*(x)(1 - a)] \tag{3.5}$$

$$T = k_T(x) \cdot P \tag{3.6}$$

$$\Delta = \max \left\{ \Delta_{min}, \left| \frac{\partial u}{\partial x} \right| \sqrt{\frac{e(x)^2 + 1}{e(x)^2}} \right\} \tag{3.7}$$

where $e(x)$, $k_T(x)$, $P^*(x)$, and $c^*(x)$ are spatially (piece-wise) varied functions of ellipse ratio, tensile strength factor, and empirical ice-strength parameters respectively; the symbol Δ_{min} defines the creep limit; $u(x,t), h(x,t)$, and $a(x,t)$ identify SIV, SIT, and SIC, respectively; and τ_a and τ_o denote respective atmospheric and oceanic stresses. Initial ice conditions implicitly determine the fixed boundary values, with ice velocities maintained at zero at each boundary. Note that this model omits dynamical effects due to sea surface tilt and Coriolis effects.

Discretization of equations (3.1)–(3.7) over a B-grid at time k yields a tridiagonal matrix equation

$$\mathbf{A}_k \left(\mathbf{u}^k, \mathbf{h}^k, \mathbf{a}^k \right) \mathbf{u}^{k+1} = \mathbf{b}^k \tag{3.8}$$

[*König Beatty and Holland*, 2010], defining an implicit map from current state variables and parameters $\mathbf{b}^k$ to forecast velocities $\mathbf{u}$. The map $\mathbf{A}_k$ is clearly non-linear as it depends on the current SIV, SIT, and SIC distributions $\mathbf{u}^k$, $\mathbf{h}^k$, and $\mathbf{a}^k$, respectively. Equivalently-discretized continuity equations (3.2)–(3.3) provide updates of concentration and thickness once velocities are known, and may be used to augment Equation (3.8) for an implicit complete state update.

The implemented numerical sea ice model used a 1800 km domain discretized with 10 km resolution, and was integrated for a period of 5.5 days with a 4-day data assimilation window. For simplicity, ice-ocean interaction is neglected ($\tau_o = 0$) and fixed boundary conditions are imposed on velocity, concentration, and thickness. Formally, these Dirichlet boundary conditions together with neglected ice-ocean drag may result in model instabilities during long model integration or in the presence of very strong winds, but no instabilities were observed during experiments discussed herein due to relatively short integration periods. Atmospheric wind and initial sea ice

---

[5] A reviewer has correctly noted that the form of Equation (3.4) pre-assumes that $T = 0$, so that $T = -T$. Further, the form of the equation is incorrectly simplified. The equation without this assumption is Equation 25 of *König Beatty and Holland* [2010]. Also, there is a concern that use of a scalar stress omits cross terms in $\nabla \cdot \sigma$, making this formulation inaccurate for a 1.5-D problem or using certain kinds of boundary conditions.

conditions were specified analytically by combinations of trigonometric functions, while RPs were specified by piece-wise linear functions. Numerical model parameters are largely adopted from *König Beatty and Holland* [2010] and assembled in Table 3.1.

Exact tangent linear and adjoint models associated with Equation (3.8) were developed analytically with respect to a control vector **c** comprising initial state distributions ($u_0(x)$, $a_0(x)$, $h_0(x)$), wind stress τ_a, and RP vectors $P^*(x)$, $e(x)$, $c^*(x)$, and $k_T(x)$. Note that the 1-d rheology parametrization non-uniquely represent compressive ice strength P and net pressure factor $P - T$ in terms of (P^*, c^*) and (P, k_T), respectively. Omission of $c^*(x)$ and $k_T(x)$ from **c** results in equivalent control with reduced control vector dimension, although the models retain these variables for possible future development in 2D where this is not true. Spatial variability of RP is therefore only allowed for $P^*(x)$ and $e(x)$, with invariant values set for c^* and k_T as in Table 3.1. Artificially enforced inequality constraints $22000 \leq P^*(x) \leq 37000$ and $1.5 \leq e(x) \leq 2.5$ intend to restrict the feasible controls to those giving realistic solutions. These ranges suffice for experimental purposes, and should be widened appropriately for practical application.

Numerical solutions to Equation (3.8) and its associated linearization/adjoint are accomplished using GMRES routines [*Saad and Schultz*, 1986, https://www-users.cs.umn.edu/~saad/software/]. These solutions are used to determine an optimal control vector on the basis of observations using the VarDAS described below. Functional minimization within the algorithm uses the N1QN3 routine of *Gilbert and Lemarechal* [1993], which implements a quasi-Newton method [*Wright and Nocedal*, 1999]. Preliminary numerical experiments determined that sequential minimization over different control components yielded better results; simultaneous optimization of SIV, SIT, and SIC initial conditions occurs first, followed by optimization of the remaining components $P^*(x)$, $e(x)$, and τ_a together.

3.2.2 Variational Assimilation Method

The update of an ice-model state implied by Equation (3.8) together with discretized continuity equations define a numerical forward-time state map. By iterating this function, model states depend only on the initial data and static model parameters which compose the control vector: $\mathbf{x} = \mathfrak{M}(\mathbf{c})$ where $\mathbf{x}$ denotes the trajectory of model ice variables $u(x,t)$, $h(x,t)$, and $a(x,t)$; $\mathfrak{M}$ is the iterated forward-time map; and $\mathbf{c}$ is a control vector comprised of complete initial state conditions along with other model parameters. The associated tangent linear model $\delta\mathbf{x} = \mathbf{M}\delta\mathbf{c}$ identifies variations of the model state $\delta\mathbf{x}$ with respect to control vector variations $\delta\mathbf{c}$; the adjoint model,

$\delta\mathbf{c} = \mathbf{M}^T\delta\mathbf{x}$ where $(\cdot)^T$ is the matrix transpose, identifies the control variations associated with a change in state. The optimal control vector is sought to ensure that observations of model states $\{h(\mathbf{x})\}$ lie close to known observations $\{\mathbf{y}\}$ by minimizing the standard quadratic variational cost function $J(\mathbf{c})$ [*Le Dimet and Talagrand*, 1986] in two dimensions. This unknown minimum is distinguished by the vanishing gradient of J at $\mathbf{c}_{opt}$, and may be identified from an initial $\mathbf{c}_0$ by solving:

$$\mathbf{0} = \mathbf{B}^{-1}\mathbf{M}\delta\mathbf{c} + \sum_{k=0}^{N}\mathbf{M}_k^T\mathbf{H}_k^T\mathbf{R}^{-1}\left(\mathbf{H}_k\mathbf{M}_k\delta\mathbf{c} - \mathbf{d}^k\right) \tag{3.9}$$

where $\mathbf{B}$ and $\mathbf{R}$ are the background model and observation error covariance matrices, respectively; $0 \leq k \leq N$ are model time indices of the assimilation window; $\mathbf{H}_k$ denotes the linearization of the observation operator h at time k; and $\mathbf{d}^k = \mathbf{y}^k - h\left(\mathfrak{M}(\mathbf{c}_0)_k\right)$ is the first guess difference from observation at time k. The symbol $\mathbf{M}_k$ denotes application of the tangent linear model from the initial time to time k, and $\mathbf{M}_k^T$ identifies the adjoint model at time k. Error covariances in this study are diagonal with entries defined by component-wise estimates of appropriate variances. The optimal control $\mathbf{c}_{opt} = \mathbf{c}_0 + \delta\mathbf{c}_{opt}$ contains optimal initial state conditions and sets of RPs reported in the following sections; the trajectory of ice-model states $\mathfrak{M}(\mathbf{c}_{opt})$ is reported hereafter as the optimal model solution. Components of the control may be readily omitted from optimization in experiments by preventing their update to formally retain their presence in $\mathbf{c}$.

3.2.3 Observations

For experimental purposes, observational data of the sea ice state are required for assimilation. This work aims to represent synthetic equivalents of the following high-resolution satellite observations, which are currently available or developing.

The first data are accurate SIC observations, of which there are currently multiple gridded products based on various remote sensing instruments with different spatial resolutions. Example datasets include the Passive Microwave Sea Ice Concentration with 25 km resolution [*Peng et al.*, 2013, https://nsidc.org/data/g02202], MASAM2 with 4 km resolution (https://nsidc.org/data/g10005), and the Advanced Microwave Scanning Radiometer 2 (AMSR2) with 10 km resolution (https://gportal.jaxa.jp/). After additional pre-processing, these observations are routinely used in DASs [e.g. GOFS 3.1 DA system, *Cummings and Smedstad*, 2013] with a nominal spatial resolution of 5 km and regionally low SIC representation errors [~5%, *Yaremchuk et al.*, 2019].

The second set are SIT observations which contain moderate errors[6] Currently, the primary source of such data is CryoSat-2, with gridded 2-day averaged observations from the Center for Polar Observations and Modeling (http://www.cpom.ucl.ac.uk/csopr/seaice.html). *Laxon et al.* [2013] conducted a detailed survey of this processed product and found 0.62 m mean difference between CryoSat-2 and in situ SIT observations; the estimation errors are largely due to uncertainties in converting remotely-observed freeboard height to equivalent SIT. In the future, novel observational platforms will likely provide better spatial coverage (i.e., over the entire Arctic) and higher accuracy. For experiment purposes, this work posits future inaccuracy by imposing SIT observation errors of 0.35 m in the mean.

Accurate observations of the sea ice velocities compose the third group. An example product is the daily 25 km SIV analysis of various satellite sources (https://nsidc.org/data/nsidc-0116), although its production ended in 2015. However, similar velocity maps with higher spatial resolution can be derived by sequential comparison of SAR images with accuracy of 0.05 m/s [*Komarov and Barber*, 2014] which suggest the possibility of ongoing and future SIV observations.

A fourth set of data is needed to optimize atmospheric forcing and comes in the form of wind stress information. Atmospheric wind stress is usually estimated using the 10m wind speed from atmospheric reanalysis or weather forecast systems, rather than observations. The inaccuracy of such data in the central Arctic region likely results from limited in situ observations for calibration rather than inaccuracies in the atmospheric boundary layer parametrization in the existing models. Evaluation of product accuracy by *Jakobson et al.* [2012] suggests that standard wind speed errors are typically 1.5 m/s in the central AO; the corresponding wind stress uncertainty calculated at full ice cover using parameters in Table 3.1 is about 0.04 N/m^2 and scales linearly with open water fraction. However, this estimate fails to account for uncertainties in the static ice-air friction coefficient or errors in SIC estimates. Further, the 1D wind stress discussed here lacks a vorticity component that must be accounted for in realistic 2D applications. For these reasons, the observation errors for data associated with 1D wind stress are assumed to be much larger with a standard error of 0.125 N/m^2.

This work assumes that spatial resolution of synthetic observation representatives is the same as the model resolution, and also that observations are available at each model time step. Practical applications justify spatio-temporal interpolation of existing sea ice datasets because they are

---

[6] A reviewer correctly noted that no reference was provided for SIT and SIV observations. See the published revision for citations.

already gridded, daily analyses of asynchronous satellite swaths. Here, assumptions are motivated by simplicity and the desire to avoid specifying additional smoothing terms needed to regularize the ill-posed optimization problem [i.e. *Neumaier*, 1998, and references therein].

3.3 Observation System Simulation Experiments

Sea ice model presented in Equations (3.1)–(3.7) suggests two major dynamical regimes depending on ice coverage. This grouping motivates the organization of experiments as their dynamics are distinct.

The first regime occurs where sea ice covers the entire ocean surface and is identified as the pack ice zone (PIZ) and characterized by $a(x) \approx 1$. Within this case, internal stress σ plays a significant role in the sea ice dynamics and SIC continuity (Equation (3.3)) may be readily ignored by assuming $a(x) = 1$. Formally, this assumption of constant, full ice cover is equivalent to immediate sea ice formation in regions where SIC slightly decreases due to ice divergence. Equation (3.4) naturally suggests that, in this case, spatial variability of RPs should significantly affect the presence of the convergence (causing ridging).

The second regime occurs where sea ice is present but only partially covers the ocean surface; it is identified as the marginal ice zone (MIZ) and characterized by concentrations $0.2 \leq a(x) \leq 0.8$ in this work. Numerically, this case differs numerically from that of the PIZ because Equation (3.3) is required in the solution to Equation (3.8). In the MIZ, the impact of the internal stress σ is low as ice movement is not fully constrained. Dynamics of the presented sea ice model in this regime are controlled by atmospheric/oceanic forcing, with Coriolis effects in the 2D case.

Wind stress is naturally the most important component of the external forcing in this ice model, and accuracy of the wind forcing is important to secure quality reconstruction and forecast of the sea ice state. It is thus reasonable to conduct OSSEs for cases which involve both realistic[7] and idealized, error-free atmospheric forcing. It is also important to evaluate separately the impact of the optimization with respect to the various control components: the initial ice state ($u_0(x)$, $a_0(x)$, $h_0(x)$), the wind stress τ_a, and the RP distributions ($P^*(x)$, $e(x)$).

To assess the quality of reconstructed sea ice states using various controls and data sources, OSSEs are conducted in which poorly-initialized model results are compared with identically-

---

[7] A reviewer correctly noted that no mention was made of the unrealistic timescale of the wind forcing in the OSSEs. The wind stress is constant over a 5.5 day period in the presented experiments. The VarDAS was successful in reconstructing the ice-state under more realistic (noisy, non-stationary, and slowly varying) wind fields in the MIZ, but such experiments were conducted early in this research and were not targeted at wind stress reconstruction. Work in this direction is ongoing.

initialized DAS solutions. The conventional OSSE methodology [*Houtekamer and Mitchell*, 1998] is briefly described here.

First "true" solutions are generated with a given atmospheric forcing, initial/boundary conditions, and rheological parameters. Initial SIT and SIC condition are specified as the sum of several smooth cosine and sine functions. Initial SIV condition are specified by ice model integration for 10 time steps (100 minutes). Then synthetic observational data are generated by contaminating these true, known solutions with spatially-correlated noise whose scale and form depends on the type of observation the data is intended to represent; the noise amplitudes are chosen to reflect realistic mean error magnitudes for each data type discussed in the previous section. The model is then reinitialized with poorly-informed first guess (FG in figures) initial data, wind stress, and RP which compose the initial control $\mathbf{c}_0$. The variational assimilation scheme presented previously is applied to determine the optimal control by assimilating observations at each timestep. The optimal model state trajectory and parameters (OPT in figures) result from initialization at day 0.0[8].

In discussing experimental results, it is often necessary to distinguish between the initial condition and the trajectory (or solution) resulting from it. For example, a first guess control $\mathbf{c}_0$ includes initial state data for SIV, SIT, and SIC at $t = 0$ as well as parameter distributions for RP and τ_a; application of the forward model results in the first guess solution $\mathbf{x}_0 = \mathfrak{M}(\mathbf{c}_0)$. The true and optimal solutions are defined analogously by the initial conditions and parameters comprising their associated control vectors. Figure 3.1 attempts to meaningfully communicate this distinction to the reader.

The estimates of the model skill are calculated separately for the assimilation period, spanning the first 4 days of integration (ie. $0 \leq t < 4$), and forecast period for the 1.5 days following (ie. $4 \leq t \leq 5.5$). Skill of the DAS reconstruction/forecast is quantified by the root-mean-squared errors (RMSE) of optimal quantities ($u(x,t)$, $a(x,t)$, $h(x,t)$, τ_a) with respect to their true counterparts. The RMSEs reported for OSSEs corresponds only to ice variable values of the innermost 1660 km of the domain; the boundary regions are discarded in skill calculation to omit boundary errors likely caused by dynamical imbalance between forcing and boundary conditions. Wind stress errors are reported for the entire length of the domain. Conducted OSSEs are detailed concisely in Table 3.2.

---

[8] That is to say, when $t = 0.0$ days. By "at" in relation to times, the author throughout this document means "at the start of" or "when time is instantaneously equal to" in the way one uses "at 5 o'clock". One reviewer felt this was ambiguous as it could be interpreted as "during" because days are not typically referred to in this way. It does feel very unnatural to say "at Tuesday" as days colloquially denote time intervals rather than instants.

3.4 Results and Discussion[9]

3.4.1 Pack Ice Zone

Figure 3.2a shows the true solution associated with PIZ experiments (OSSE-3,-3w, and -3n). The true parameters are piecewise linear distributions for $P^*(x)$ and $e(x)$ in the form of triangular waves with a period of 300 km, and a smooth quasi-sinusoidal distribution for wind stress with typical amplitude about 0.25 N/m^2. Evolution of the ice thickness, shown in the fifth row of Figure 3.2a, indicates that this configuration results in ice convergence with a discontinuity in the SIT distribution (row four) between 1200 km and 1300 km. This discontinuity is clearly seen in the SIV and SIT distributions at day 4 of the model integration, shown by solid black lines in Figure 3.3a,b.Throughout the text below, we identify this feature of the true solution as "ridging" behavior. It is also necessary to note that prescribed SIV and SIT boundary conditions are unbalanced with the wind forcing; the non-zero wind forcing near the boundaries results in unrealistic sharp decreases of SIT near those boundaries. Ideally, the ice thickness and concentration should decrease in these areas due to off-shore ice transport under the influence of accelerating offshore winds. However, the SIC distribution is spatially invariant with $a(x) = 1$ throughout each PIZ experiment.

True wind stress forcing, SIV, and SIT are modified by adding spatially correlated smooth functions with amplitudes corresponding to the errors discussed above above; the noise-contaminated values are used as simulated observational data. Mean RMSE between data and true solution for these fields were 0.13 N/m^2, 0.03 m/s, and 0.21 m, respectively, with associated maximum differences of 0.3 N/m^2, 0.10 m/s and 0.6 m. Figure 3.3 illustrates the typical differences between true solution and synthetic observations for these fields.

To initialize the DAS, the true initial conditions for SIV, SIT, and SIC are contaminated in a similar way as the data-supplying model, but with a larger spatial decorrelation scale and different noise. The larger spatial scales provide a smoother initial state whose trajectory evolves away from the true solution; smaller spatial decorrelation scales produced dynamical state differences which dissipated rather than evolve. These initial conditions, conventional RPs $P^*(x) = 27500$ N/m^2 and $e(x) = 2$, and exact wind stress characterize OSSE-3.

The errors of the OSSE-3 first guess with respect to true fields are shown in Figure 3.2b. The small (~0.03 m/s) mean RMSE for first guess SIV is due to the exact wind stress forcing provided

---

[9] This section includes analysis based on some incorrectly identified RMSEs for the observations and forecast/hindcast solutions. One notes that in several of the figures, the forecasts are more accurate than the hindcasts. This clearly does not make sense, and a reader is further cautioned against viewing this section when updated versions of this chapter exist.

in the experiment. The corresponding RMSE for SIT is more significant, equaling 0.19 m and 0.23 m for hindcast and forecast periods respectively. Maximum differences in first guess SIT occur in the domain between 900 km and 1200 km and reach ~0.8 m in height, which is approximately 25–30% of the local true SIT (Figure 3.2a).

Figure 3.4a underscores the significant qualitative difference between true and first guess solutions. In particular, the first guess thickness (identified by the dashed green line, bottom) is rather smooth in the central part of the model domain (900–1300 km) and does not reflect the ridging discontinuities clearly seen in the true SIT identified by the solid black line. There also exist problems near the boundaries; these are due to non-zero wind and fixed boundary conditions which are not in dynamical balance.

The optimized $P^*(x)$ and $e(x)$ distributions and difference between optimized and true solutions are shown in Figure 3.2c. Assimilation of SIV and SIT observations results in a spatial distribution of $P^*(x)$ more representative of the true solution, although this improvement is not uniform. The optimized distribution for $e(x)$ is generally inaccurate, which suggests that the elliptical yield curve eccentricity is of modest importance in the optimization. It is worthwhile to note that the optimized solution yields better recovery of the $P^*(x)$ distribution with large reconstruction errors for $e(x)$ in the center of the domain, while the opposite appears to be true in the boundary regions. In spite of this, RPs and SIV/SIT initial condition optimization reduces the difference between optimized and true SIT.

The average effect of the SIT optimization is more profound for the forecast period where mean RMSE is 0.13 m (42% improvement over the first guess) and smaller for the hindcast period where mean RMSE is 0.16 m (15% improvement over the first guess). Yet these average errors do not provide a complete picture; Figure 3.4a clearly demonstrates that the difference between first guess and true SIT can be as large as ~1m near 1200 km and even larger near the boundaries, while optimized SIT is very close to the true SIT across the most of the modeled region after the first day.

Errors in the optimal hindcast SIT are mostly due to the underestimation of SIT in the center of the domain around 900km for the first day of simulation; the optimized SIV and SIT outperform first guess solution (e.g. Figure 3.4a) in the rest of the domain, boundary areas excluded. Additionally, the first guess SIT errors are corrected by as much as 0.9 m over the central domain in the optimum. Also note that the optimal solution contains an SIT discontinuity between 1100 km and 1300 km that is qualitatively the same as that found in the true solution, while the first guess solution with uniform rheological parameters does not.

The top row of Figure 3.5 highlights the effect of RP variation and optimization on the error distributions in SIT and SIV. The first guess solution of OSSE-3, where RP are constant, statistically underestimates SIT by about 0.3m, and the error structure is rather uniformly distributed over the range -0.5–0.0 m. In contrast, the optimized SIT errors show statistically desirable qualities of low bias and approximate normality. Improvements in SIV error distribution are also evident.

Figures 3.6a,b present the result of the more realistic OSSE-3w which uses inaccurate wind stress in its first guess and observation data. The true state, ice-state observations, and first guess for SIV and SIT are the same for this case as in OSSE-3 (Figure 3.2a, Figure 3.3a), although the resulting model trajectories differ as a result of the incorrectly specified wind forcing. The control vector for OSSE-3w includes initial conditions, RPs, and wind stress. In the optimized solution, imperfect wind information results in poor reconstruction of $P^*(x)$ and $e(x)$ in OSSE-3w (Figure 3.6b, top panels), while the reconstructed wind stress is accurate. Despite this poor RP estimation, optimized SIV and SIT solutions (Figure 3.6, bottom) are significantly closer to the true model state than the first guess solution (Figure 3.6a, bottom). The applied DAS reduces SIV errors by 71% (from 0.07 m/s to 0.02 m/s) during reconstruction and by 60% (from 0.07 m/s to 0.02 m/s) during forecast, with averaged error reductions of 59% and 65% obtained for SIT hindcast and forecast, respectively. Similar to the OSSE-3, the major optimization impact is clearly observed in the central part of the modeled region away from 1000–1200 km; here, the absolute differences between true and optimized SIV/SIT are about 0.01 m/s and 0.1 m, respectively. Again, the structure of SIV and SIT error distributions (Figure 3.5, middle) shows approximate debiasing of both fields. However, the posterior errors for SIV retain the bimodal structure of the first guess errors.

The OSSE-3w instantaneous SIV and SIT distributions at the end of the hindcast period (day 4) are shown in Figure 3.4b by the blue line and show significant superiority over the first guess solution (green). Interestingly, the additional optimization of the wind stress provides a smoother SIT solution near the boundary than that of the first guess. In the ridging area (near 1200 km), optimized SIT still demonstrates some level of discontinuity, but the feature is not as pronounced as in the OSSE-3 case with perfect wind. Small scale noise in some optimal solutions is visible, e.g. OSSE-3 optimal SIT around 1100 km in Figure 3.4a. In additional OSSEs not detailed here, additional regularization was given in the form of cost function gradient penalties encouraging SIV and SIT smoothness; results suggest that such regularization is capable of eliminating this small scale noise but inhibits formation of intended discontinuities in ridging regions. This problem may be formally overcome by implementing a more advanced non-uniform smoothing, but such an approach would require additional information to formulate a reasonable regularization constrain [e.g., *Fomel*, 2007].

Figures 3.4c and 3.6c visualize OSSE-3n, which is similar to OSSE-3w but optimizes only initial conditions and wind stress while RP are held uniformly as in the first guess solution. Figure 3.6c shows that partial optimization still yields SIT distribution improvement, with SIT forecast and hindcast improving the first guess by 11.5% and 7%, respectively. However, these improvements are modest compared to reductions of 65% and 58% achieved using full control in OSSE-3w. Figure 3.4c clearly indicates that without variable RP included in the optimized control, there are marked difference from the true SIT in the central domain (900–1300 km) and optimized SIT lacks the discontinuity near 1200 km. The OSSE-3n optimal initial state and wind stress are otherwise similar to those of OSSE-3w, which confirms that variable RP significantly affect the evolution of the sea ice state. This is further supported by examination of the optimized SIT error structure for OSSE-3n (Figure 3.5, bottom left) which shows little change from the corresponding first guess errors and continues to underestimate SIT.

Optimization of the initial conditions in OSSE-3n has a minor impact on the forecast SIV, which remains close to the first guess SIV for the entire forecast period (Figures 3.4c and 3.6c). This similarity likely results from identical rheological parameters and a small difference between first guess wind stress and wind stress observations. The optimization does, however, reduce SIV bias from ~0.04 m/s to ~0.01 m/s (Figure 3.5, bottom right). Thus, the comparison of OSSE-3w and OSSE-3n optima clearly indicates the significant impact $P^*(x)$ and $e(x)$ optimization has on obtaining accurate short range sea ice forecast in the idealized PIZ region.

To more clearly identify the roles of $P^*(x)$ and $e(x)$ separately, two additional OSSEs were performed where the true solutions were obtained using RPs with either P^* or e taken as uniform. Results showed that optimization over each non-uniform RP independently provides approximately the same hindcast/forecast mean errors in SIV and SIT distributions, and were larger than errors in OSSE-3w. However, optimization of $e(x)$ with constant $P^*(x)$ did not provide reconstruction of the SIT discontinuities discussed above. This result suggests that the 1D $e(x)$ does not influence the formation of discontinuities. In all cases, identified ridges are located in true and optimized solutions where $P^*(x)$ attains a local minimum. Therefore, optimization with respect to spatially variable $P^*(x)$ appears to be more important for short range hindcast/forecast than e in the 1D case; this is also suggested by the quality of SIT/SIV reconstruction in OSSE-3 despite inaccurate reconstruction of $e(x)$.

An interesting result of OSSE-3 and OSSE-3w together is that first guess solutions with constant PRs show a clear negative SIT bias with respect to the true SIT solution, while optimization using spatially variable $P^*(x)$ and $e(x)$ significantly reduces this underestimation (cf. Figure 3.5, left panels). This is in strong agreement with aforementioned results of *Juricke et al.* [2013], which found that simulations using varied P^* led to central Arctic SIT could not be reproduced with reduced fixed P^*.

Observed biases in sea ice thickness and volume in some modeling systems [e.g. the Arctic Cap Nowcast/Forecast System, *Posey et al.*, 2015] may be reduced after conditioning SIT initialization on observations [*Allard et al.*, 2018], and the results of OSSEs here suggest that observational-conditioning with variable RPs may provide similar benefits in more realistic applications.

3.4.2 Marginal Ice Zone

As discussed previously, the MIZ regime greatly limits the role rheological stresses play in the sea ice dynamical balance; the VP internal pressure with 80% SIC is less than 2% of its value at 100% SIC with other parameters unchanged. One expects the impact of spatial variability in RP to be negligible as well, so spatially uniform parameters, $P^* = 27000$ N/m^2 and $e = 2$, reflect these assumptions in MIZ OSSEs. To avoid instabilities in model simulation, the amplitude of the supplied wind stress τ_a is reduced to avoid violation of CFL conditions. In a less idealized setting where ice-ocean stress (τ_o) is included in the dynamical forcing, ocean drag would naturally reduce the net imposed stress[10].

The MIZ OSSEs further assume that true SIC is proportional to true SIT for convenience, although this constraint is not imposed on the DAS. The evolution of the true MIZ solution is shown in Figure 3.7a. Ice in the model solution moves toward to the center of the domain similarly to the PIZ case, but lacks the marked discontinuities in ice state variables.

The generation of observations and first guess solution for MIZ OSSEs follows those described previously for OSSE-3w. Figure 3.7b shows the evolution of the first guess solution, and 3.8 provides an example of the day 4 observations which now include SIC data. Note that both first guess wind stress and observations differ significantly from the true wind stress with mean RMSEs of 0.04 N/m^2 and 0.02 N/m^2 respectively and are aligned with 10m wind error estimates calculated

---

[10] A reviewer correctly pointed out that ignoring τ_o could be effectively regarded as taking τ_a to represent the *net* interface stress rather than the wind stress. While this has no effect on the experimental results, there may be implications for the use of SIV to inform boundary-layer winds in atmospheric models and products. Namely, such use require additional estimates of ocean surface currents. This discussion is ongoing among co-authors.

from reanalysis products [*Jakobson et al.*, 2012]. In OSSE-4, the optimization was conducted with respect to initial state conditions (which now includes SIC) and wind stress, and results of the optimization are shown in Figure 3.7c.

Clearly, optimized solution shows considerable improvement in the hindcast (forecast) SIV, SIC, and SIT distributions which improve over the first guess by 66% (60%), 43% (50%), and 36% (23%), respectively. In particular, Figure 3.9a compares true, first guess, and optimized solutions at day 4 and suggests that the most significant improvements occur in optimized SIV which is five times closer to the true solution than the first guess SIV. Interestingly, the optimized τ_a is much closer to the true wind stress with RMSE of ~0.01 N/m^2 despite large errors (~0.04 N/m^2) in the supplied wind stress observations. This is a consequence of assimilating SIV observations, which relate directly to wind velocity; in the absence of the internal rheological stress and ocean drag, sea ice velocities are linearly related to the atmospheric wind stress by Equation (3.1). This suggests prerequisite use of SIV observations for estimation of atmospheric stress in the MIZ. Further, it suggests SIV may be utilized in conjunction with other ice-state estimates as additional atmospheric observations to improve atmospheric reconstruction and forecast.

To better illustrate this possibility, OSSE-4w is conducted identically to OSSE-4 only with more accurate SIV observations; the data are contaminated with noise of 1/3 the amplitude (~0.01 m/s) of those used in OSSE-4 as shown in Figure 3.8 (second plot, blue line). The optimized solution is shown in Figure 3.10 and improves the reconstructed wind stress as well as ice-state distributions beyond the results of OSSE-4. With all else equal, the threefold increase in accuracy of assimilated SIV observations yields a threefold decrease in reconstructed wind stress errors (viz. from ~0.009 N/m^2 in OSSE-4 to ~0.003 N/m^2 in OSSE-4w). It is worth reminding that ocean influence is ignored in this regime, or is at least treated as spatially constant to decrease the net forcing imparted by the wind.

The comparison of OSSE-4 and OSSE-4w suggests that high-accuracy SIV observations may significantly benefit hindcast/forecast quality of the sea ice state and in weather forecast systems as well. Such accurate SIV observations are typically obtained from analysis using the Maximum Cross-Correlation (MCC) method applied to sequential SAR images [*Fily and Rothrock*, 1987; *Komarov and Barber*, 2014]. In this method, the presence of the open-water generally allows for more accurate estimation of the cross correlations between two data images. Based on this, one expects more accurate SIV estimates in the MIZ than in the PIZ where ice concentration is more homogeneous.

3.5 Summary

This study addresses the feasibility of optimizing spatially-varied rheological parameters (RPs) and wind stress (τ_a) by assimilating simulated satellite observation of sea ice velocity, concentration, and thickness (SIV, SIC, and SIT respectively) with realistic errors. To study this problem, developed tangent linear and adjoint models were implemented into a variational data assimilation algorithm for a simple 1D sea ice model which has been previously used to analyze a modified rheology and numerical scheme [*König Beatty and Holland*, 2010; *Auclair et al.*, 2017].

In all observation synthesis simulation experiments (OSSEs) conducted for the pack-ice zone (PIZ, where SIC is maintained at 100%), optimization of variable rheological parameters resulted in improved hindcast/forecast of the sea ice state variables. Of note is that this improvement is achieved even when the RMSE of optimum RPs is larger than those of the first guess when the true solution has spatially variable parameters (as in OSSE-3). The PIZ OSSEs here suggested that optimized variable RPs yielded model evolution with more (thicker) ice and corrected SIT underestimation of the first guess solutions, which was not the case in experiments with non-variable RPs. This results agrees with those of *Juricke et al.* [2013], which found simulation using stochastically perturbed strength parameter cannot be reproduced with a fixed, uniform P^*. OSSE results also show that partial optimization using a subset of rheological terms may significantly improve hindcast/forecast of the sea ice state.

Individual optimization of $P^*(x)$ and $e(x)$ yielded similar improvements in SIV and SIT states in the case of full ice-cover. However, optimization of strength parameter $P^*(x)$ allowed solutions to form discontinuous SIT distributions which can be associated with ice-ridging regions. Results also suggest that accurate reconstructions are achieved when the optimal $e(x)$ is inaccurate, suggesting that its role is of less relative important in the 1D case than wind stress and spatially variable $P^*(x)$. However, sea ice state reconstruction strongly depends also on accuracy of the wind stress forcing and assimilated observations. OSSEs in this study used simulated high-accuracy SIV and SIC observations such as those currently available (0.03 m/s and 3% respective RMSE), along with moderately accurate simulated wind stress and SIT observations (0.125 N/m^2 and 0.2 m respective RMSE). Actual SIT observations are less accurate than assumed in these experiments, although forthcoming observational platforms and methodologies should provide SIT observations with uncertainties less than those currently available and comparable to those simulated.

In the marginal ice zone (MIZ, where ice coverage is between 20 and 80%), the effects of internal sea ice stress are negligible and optimization of the rheological parameters relatively unimportant. Instead, the conducted OSSEs revealed that wind stress, in the absence of ocean forcing, is successfully optimized through the assimilation of SIV observations. This results mostly from the known linear relationship between wind stress and sea ice velocity in the MIZ, and consequently the quality of the wind stress correction is roughly proportional to the accuracy of assimilated SIV observations.

Pack ice is the prevalent regime over most of the central Arctic Ocean throughout the year, so these results clearly indicate *practical* benefits of including spatially varied $P^*(x)$ and $e(x)$ into sea ice models and developing the proper optimization algorithms to handle the more dynamically complex 2D case. Notably, optimizations which included variable RPs resulted in SIT solutions with considerably less bias than first guess solutions using fixed RPs. This may partially explain the source of observed SIT underestimation in some sea ice models employing a set of constant RPs. However, thermodynamic components of modern sea ice models, which are not considered in the presented short-term experiments, need to be considered in assessing impacts and biases in longer simulations.

Development of this algorithm will also allow for estimation of local wind stress in the MIZ, which accounts for significant portion of the Arctic Ocean in the summer months. At present, the simplified model is limited to one dimension, and a proper MIZ implementation must account more complicated physical considerations such as imposed wind stress curl, Coriolis coupling of velocities, effects of ice-ocean drag, geostrophic currents with sea surface tilt, and different ice types. More research and development are needed to extend the idealized experimental results to practical settings.

The sea ice model is non-linear, and the cost function of the DAS has multiple local minima; the calculated optimal solution therefore depends on the first guess solution. However, assimilation of a significant volume of sea ice observations should provide sufficient correction and constraint to the model evolution that the optimization scheme targets an optimum which is "close enough" to the "true" solution after several assimilation cycles. This suggests that future developments toward realistic applications implementing the assimilation methodology described here should focus on hindcast periods with abundant data.

Also, the modern analysis of SAR images and other satellite observations permits accurate identification of different ice types [e.g. multiyear/first year ice, deformed first year ice; *Zakhvatkina et al.*, 2013, 2017] and leads [*Murashkin et al.*, 2018]. New methods of processing satellite data resolve additional sea ice characteristics which affect its material properties, such as ice age [*Korosov et al.*, 2018] which has long been known to affect ice strength [*Weeks and Assur*, 1967; *Timco and Weeks*, 2010]. Such information may be efficiently used to reduce of the dimension of the rheological control vector through regional definitions. For example, one could partition a pan-Arctic model domain into sub-regions based on the maturity and type of sea ice present, and prescribe to each a set of local strength distribution $P^*(x)$. Such an approach, of course, requires experimentation to empirically determine optimal RPs for each ice category. Furthermore, the ongoing work of resolving sea ice properties from remote sensing provides a base of information necessary to establish a proper regularization scheme (e.g. through spatially variable smoothing) for the optimization problem presented here. The need for sophisticated regularization is clear in some pack-ice OSSEs; without it, large errors in observational data may produce artificially noisy ice states, while imposing spatially homogeneous regularization prevents the formation of physically relevant and appropriate discontinuities.

These results are encouraging, but are based on a relatively simple 1D sea ice model employing the VP rheology proposed by *Hibler* [1979]. The most widely used sea ice models are two-dimensional and use an elastic-VP rheology, which is more efficient for parallel implementation on super computers [*Hunke et al.*, 2010; *Bouillon et al.*, 2013]. These models also have a different numerical formulation which may result in more-difficult-to-avoid instabilities in their associated adjoint models. Development of full tangent linear and adjoint for existing community sea ice models (e.g. CICE) is a long term project. In the meantime, continued research and OSSEs with a more realistic 2D sea ice model are the next steps toward achieving locally optimal rheology through data assimilation.

Acknowledgments
J.N. Stroh received no funding or support during this research, and thanks the University of Nevada Reno for liberal access to library resources during document preparation. The NRL authors were supported by the Office of Naval Research program elements 0603207N (Navy Earth System Prediction Capability) and 0602435N (Arctic Data Assimilation). Oceana Francis was supported by the Coastal Hydraulics Engineering Resilience (CHER) Lab, the Civil and Environmental Engineering Department, and the Sea Grant College Program at the University of Hawaii at Manoa.

Bibliography

Allard, R. A., S. L. Farrell, D. A. Hebert, W. F. Johnston, L. Li, N. T. Kurtz, M. W. Phelps, P. G. Posey, R. Tilling, A. Ridout, *et al.* (2018), Utilizing cryosat-2 sea ice thickness to initialize a coupled ice-ocean modeling system, *Advances in Space Research*, *62*(6), 1265–1280.

Auclair, J.-P., J.-F. Lemieux, L. B. Tremblay, and H. Ritchie (2017), Implementation of Newton's method with an analytical Jacobian to solve the 1d sea ice momentum equation, *Journal of Computational Physics*, *340*, 69–84.

Bouillon, S., and P. Rampal (2015a), Presentation of the dynamical core of neXtSIM, a new sea ice model, *Ocean Modelling*, *91*, 23–37.

Bouillon, S., and P. Rampal (2015b), On producing sea ice deformation data sets from SAR-derived sea ice motion, *The Cryosphere*, *9*(2), 663–673.

Bouillon, S., T. Fichefet, V. Legat, and G. Madec (2013), The elastic–viscous–plastic method revisited, *Ocean Modelling*, *71*, 2–12.

Budgell, W. (2005), Numerical simulation of ice-ocean variability in the Barents Sea region, *Ocean Dynamics*, *55*(3-4), 370–387.

Cummings, J. A., and O. M. Smedstad (2013), Variational data assimilation for the global ocean, in *Data Assimilation for Atmospheric, Oceanic and Hydrologic Applications (Vol. II)*, pp. 303–343, Springer.

Danilov, S., Q. Wang, R. Timmermann, N. Iakovlev, D. Sidorenko, M. Kimmritz, T. Jung, and J. Schröter (2015), Finite-element sea ice model (FESIM), version 2, *Geoscientific Model Development*, *8*(6), 1747–1761.

Dukowicz, J. K. (1997), Comments on "stability of the viscous–plastic sea ice rheology", *Journal of Physical Oceanography*, *27*(3), 480–481.

Fenty, I., D. Menemenlis, and H. Zhang (2017), Global coupled sea ice-ocean state estimation, *Climate Dynamics*, *49*(3), 931–956.

Fily, M., and D. Rothrock (1987), Sea ice tracking by nested correlations, *IEEE Transactions on Geoscience and Remote Sensing*, *GE-25*(5), 570–580.

Fomel, S. (2007), Shaping regularization in geophysical-estimation problems, *Geophysics*, *72*(2), R29–R36.

Forget, G., J.-M. Campin, P. Heimbach, C. Hill, R. Ponte, and C. Wunsch (2015), ECCO version 4: An integrated framework for non-linear inverse modeling and global ocean state estimation, *Geoscientific Model Development*, *8*(10), 3071–3104.

Gilbert, J.-C., and C. Lemarechal (1993), The modules m1qn3 and n1qn3, *Program documentation, INRIA*.

Goodier, J. N., and P. G. Hodge (1958), *Elasticity and Plasticity: The Mathematical Theory of Elasticity*, vol. 1, John Wiley & Sons.

Gray, J., and P. D. Killworth (1995), Stability of the viscous-plastic sea ice rheology, *Journal of Physical Oceanography*, *25*(5), 971–978.

Harder, M., and H. Fischer (1999), Sea ice dynamics in the weddell sea simulated with an optimized model, *Journal of Geophysical Research: Oceans*, *104*(C5), 11,151–11,162.

Heimbach, P. (2008), The MITgcm/ECCO adjoint modelling infrastructure, *Clivar Exchanges*, *44*(13), 1.

Hibler, W. (1977), A viscous sea ice law as a stochastic average of plasticity, *Journal of Geophysical Research*, *82*(27), 3932–3938.

Hibler, W. (1979), A dynamic thermodynamic sea ice model, *Journal of Physical Oceanography*, *9*(4), 815–846.

Hibler III, W. D., and J. E. Walsh (1982), On modeling seasonal and interannual fluctuations of arctic sea ice, *Journal of Physical Oceanography*, *12*(12), 1514–1523.

Houtekamer, P. L., and H. L. Mitchell (1998), Data assimilation using an ensemble Kalman filter technique, *Monthly Weather Review*, *126*(3), 796–811.

Hunke, E., and J. Dukowicz (1997), An elastic–viscous–plastic model for sea ice dynamics, *Journal of Physical Oceanography*, *27*(9), 1849–1867.

Hunke, E. C., W. H. Lipscomb, A. K. Turner, N. Jeffery, and S. Elliott (2010), CICE: the Los Alamos Sea Ice Model documentation and software users manual version 4.1 la-cc-06-012, *T-3 Fluid Dynamics Group, Los Alamos National Laboratory*, *675*.

Jakobson, E., T. Vihma, T. Palo, L. Jakobson, H. Keernik, and J. Jaagus (2012), Validation of atmospheric reanalyses over the central Arctic Ocean, *Geophysical Research Letters*, *39*(10).

Juricke, S., P. Lemke, R. Timmermann, and T. Rackow (2013), Effects of stochastic ice strength perturbation on arctic finite element sea ice modeling, *Journal of Climate*, *26*(11), 3785–3802.

Komarov, A. S., and D. G. Barber (2014), Sea ice motion tracking from sequential dual-polarization RADARSAT-2 images, *IEEE Transactions on Geoscience and Remote Sensing*, *52*(1), 121–136.

König Beatty, C., and D. M. Holland (2010), Modeling landfast sea ice by adding tensile strength, *Journal of Physical Oceanography*, *40*(1), 185–198.

Korosov, A. A., P. Rampal, L. T. Pedersen, R. Saldo, Y. Ye, G. Heygster, T. Lavergne, S. Aaboe, and F. Girard-Ardhuin (2018), A new tracking algorithm for sea ice age distribution estimation, *The Cryosphere*, *12*(6), 2073–2085.

Kreyscher, M., M. Harder, and P. Lemke (1997), First results of the sea-ice model intercomparison project (simip), *Annals of Glaciology*, *25*, 8–11.

Laxon, S. W., K. A. Giles, A. L. Ridout, D. J. Wingham, R. Willatt, R. Cullen, R. Kwok, A. Schweiger, J. Zhang, C. Haas, *et al.* (2013), Cryosat-2 estimates of Arctic sea ice thickness and volume, *Geophysical Research Letters*, *40*(4), 732–737.

Le Dimet, F.-X., and O. Talagrand (1986), Variational algorithms for analysis and assimilation of meteorological observations: theoretical aspects, *Tellus A: Dynamic Meteorology and Oceanography*, *38*(2), 97–110.

Lemieux, J.-F., F. Dupont, P. Blain, F. Roy, G. C. Smith, and G. M. Flato (2016), Improving the simulation of landfast ice by combining tensile strength and a parameterization for grounded ridges, *Journal of Geophysical Research: Oceans*, *121*(10), 7354–7368.

Lindsay, R., and J. Zhang (2006), Assimilation of ice concentration in an ice–ocean model, *Journal of Atmospheric and Oceanic Technology*, *23*(5), 742–749.

Lisæter, K., G. Evensen, and S. Laxon (2007), Assimilating synthetic Cryosat sea ice thickness in a coupled ice-ocean model, *Journal of Geophysical Research: Oceans*, *112*(C7).

Massonnet, F., T. Fichefet, and H. Goosse (2015), Prospects for improved seasonal Arctic sea ice predictions from multivariate data assimilation, *Ocean Modelling*, *88*, 16–25.

Menemenlis, D., J.-M. Campin, P. Heimbach, C. Hill, T. Lee, A. Nguyen, M. Schodlok, and H. Zhang (2008), ECCO2: High resolution global ocean and sea ice data synthesis, *Mercator Ocean Quarterly Newsletter*, *31*, 13–21.

Miller, P. A., S. W. Laxon, D. L. Feltham, and D. J. Cresswell (2006), Optimization of a sea ice model using basinwide observations of arctic sea ice thickness, extent, and velocity, *Journal of Climate*, *19*(7), 1089–1108.

Murashkin, D., G. Spreen, M. Huntemann, and W. Dierking (2018), Method for detection of leads from Sentinel-1 SAR images, *Annals of Glaciology*, pp. 1–13.

Neumaier, A. (1998), Solving ill-conditioned and singular linear systems: A tutorial on regularization, *SIAM Review*, *40*(3), 636–666.

Peng, G., W. Meier, D. Scott, and M. Savoie (2013), A long-term and reproducible passive microwave sea ice concentration data record for climate studies and monitoring, *Earth System Science Data*, *5*(2), 311–318.

Posey, P., E. Metzger, A. Wallcraft, D. Hebert, R. Allard, O. Smedstad, M. Phelps, F. Fetterer, J. Stewart, W. Meier, *et al.* (2015), Assimilating high horizontal resolution sea ice concentration data into the us navy's ice forecast systems: Arctic Cap Nowcast/Forecast System (ACNFS) and the Global Ocean Forecast System (GOFS 3.1)., *Cryosphere Discussions*, *9*(2).

Pritchard, R. S. (2005), Stability of sea ice dynamics models: Viscous-plastic rheology, replacement closure, and tensile cutoff, *Journal of Geophysical Research: Oceans*, *110*(C12).

Rampal, P., S. Bouillon, E. Ólason, and M. Morlighem (2015), neXtSIM: a new Lagrangian sea ice model., *Cryosphere Discussions*, *9*(5).

Saad, Y., and M. H. Schultz (1986), GMRES: A generalized minimal residual algorithm for solving nonsymmetric linear systems, *SIAM Journal on Scientific and Statistical Computing*, *7*(3), 856–869.

Sakov, P., F. Counillon, L. Bertino, K. Lisæter, P. Oke, and A. Korablev (2012), TOPAZ4: an ocean-sea ice data assimilation system for the North Atlantic and Arctic, *Ocean Science*, *8*(4), 633.

Schulkes, R. (1996), Asymptotic stability of the viscous–plastic sea ice rheology, *Journal of Physical Oceanography*, *26*(2), 279–283.

Timco, G., and W. Weeks (2010), A review of the engineering properties of sea ice, *Cold Regions Science and Technology*, *60*(2), 107–129.

Timoshenko, S., and J. Goodier (1951), Theory of Elasticity, *New York*, *412*, 108.

Tremblay, L., and M. Hakakian (2006), Estimating the sea ice compressive strength from satellite-derived sea ice drift and NCEP reanalysis data, *Journal of Physical Oceanography*, *36*(11), 2165–2172.

van Scheltinga, A. D. T., P. G. Myers, and J. D. Pietrzak (2010), A finite element sea ice model of the Canadian Arctic Archipelago, *Ocean Dynamics*, *60*(6), 1539–1558.

Vancoppenolle, M., T. Fichefet, H. Goosse, S. Bouillon, G. Madec, and M. A. M. Maqueda (2009), Simulating the mass balance and salinity of Arctic and Antarctic sea ice. 1. Model description and validation, *Ocean Modelling*, *27*(1-2), 33–53.

Weeks, W. F., and A. Assur (1967), The mechanical properties of sea ice, *Tech. rep.*, Cold Regions Research and Engineering Lab Hanover, NH.

Wright, S., and J. Nocedal (1999), Numerical optimization, *Springer Science*, *35*(67-68), 7.

Yaremchuk, M., T. Townsend, G. Panteleev, D. Hebert, and R. Allard (2019), Advancing short-term forecasts of ice conditions in the Beaufort Sea, *Journal of Geophysical Research: Oceans*, *124*.

Zakhvatkina, N., A. Korosov, S. Muckenhuber, S. Sandven, and M. Babiker (2017), Operational algorithm for ice–water classification on dual-polarized RADARSAT-2 images, *The Cryosphere*, *11*(1), 33–46.

Zakhvatkina, N. Y., V. Y. Alexandrov, O. M. Johannessen, S. Sandven, and I. Y. Frolov (2013), Classification of sea ice types in ENVISAT synthetic aperture radar images, *IEEE Transactions on Geoscience and Remote Sensing*, *51*(5), 2587–2600.

Zhang, J., and D. Rothrock (2003), Modeling global sea ice with a thickness and enthalpy distribution model in generalized curvilinear coordinates, *Monthly Weather Review*, *131*(5), 845–861.

Table 3.1. Model and DAS configuration parameters

Name	Symbol	Value(s)
Domain size	L	1800 km
Grid size	dx	10 km
Timestep	dt	600 s
Integration Time	T	5.5 days
Assimilation Window		$0 \leq T \leq 4$ days
Ice-ocean stress	τ_o	0
Creep Limit	Δ_{min}	$0.1\ \mathrm{s}^{-1}$
Background Wind Speed	u_a	$20 \cos\left(\frac{x}{L} - \frac{1}{2}\right)\ \mathrm{m\ s}^{-1}$
Compactness Strength Parameter	c^*	20
Tensile/Compressive Strength ratio	k_T	0
Base Strength Parameter	$P^*(x)$	$[22, 37]\ \mathrm{kN\ m}^{-2}$
Yield curve eccentricity	$e(x)$	$[1.5, 2.5]$
Atmospheric Drag Coefficient	c_a	0.001
Fixed leftt boundary values	$[u(0,t), h(0,t), a(0,t)]$	$[u_0(0), h_0(0), a_0(0)]$
Fixed right boundary values	$[u(L,t), h(L,t), a(L,t)]$	$[u_0(L), h_0(L), a_0(L)]$

Table 3.2. For OSSE-3, -3w, and -3n, the DAS incorporates noisy sea ice velocity and thickness observations while $a(x) = 1$ is fixed in keeping with PIZ assumptions. Ice velocity, thickness, and concentration observations are used in OSSE-4 and -4w with RP held constant. Wind stress observations are assimilated in all cases subject to inexact wind forcing.

OSSE-	Description	Goal	Control ($\mathbf{c}$)
3	PIZ with $a(x) = 1$, spatially varied $(P^*(x), e(x))$, exact wind forcing, and inaccurate first guess parameters/state	Evaluate RP impact under accurate wind forcing.	$[u_0(x),\ h_0(x),\ P^*(x),\ e(x)]$
3w	PIZ with $a(x) = 1$, spatially varied $(P^*(x), e(x))$, inaccurate first guess parameters/state, and reasonable errors in wind and ice-state observations	Evaluate RP impact under reasonable errors in wind forcing and observations.	$[u_0(x),\ h_0(x),\ \tau_a(x),\ P^*(x),\ e(x)]$
3n	PIZ with $a(x) = 1$, spatially varied $(P^*(x), e(x))$, inaccurate first guess state, and reasonable errors in wind and ice-state observations	Evaluate initial-condition impact under reasonable errors in wind forcing and first guess state.	$[u_0(x),\ h_0(x),\ \tau_a(x)]$
4	MIZ with $0.2 < a(x) < 0.8$ and spatially uniform $(P^*(x), e(x))$, inaccurate first guess state, and reasonable errors in wind and ice-state observations with low-accuracy SIV observations	Evaluate initial condition impact under inaccurate wind forcing and low-accuracy ice-velocity data.	$[u_0(x),\ h_0(x),\ a_0(x),\ \tau_a(x)]$
4w	MIZ with $0.2 < a(x) < 0.8$ and spatially uniform $(P^*(x), e(x))$, inaccurate first guess state, and reasonable errors in wind and ice-state observations with high-accuracy SIV observations	Evaluate initial condition impact under inaccurate wind forcing and high-accuracy ice-velocity data.	$[u_0(x),\ h_0(x),\ a_0(x),\ \tau_a(x)]$

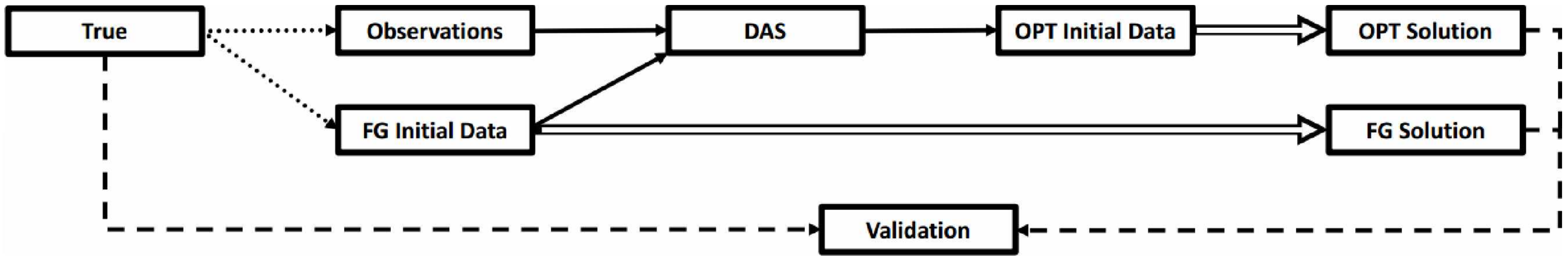

Figure 3.1. Schematic of an OSSE. The general idea of an OSSE is to generate noisy observations from an a priori true solution, do/do not assimilate those data into an inaccurately initialized model, and compare the resulting solutions with the true one. Dotted arrows correspond to noisy processes, and hollow arrows to application of the forward model.

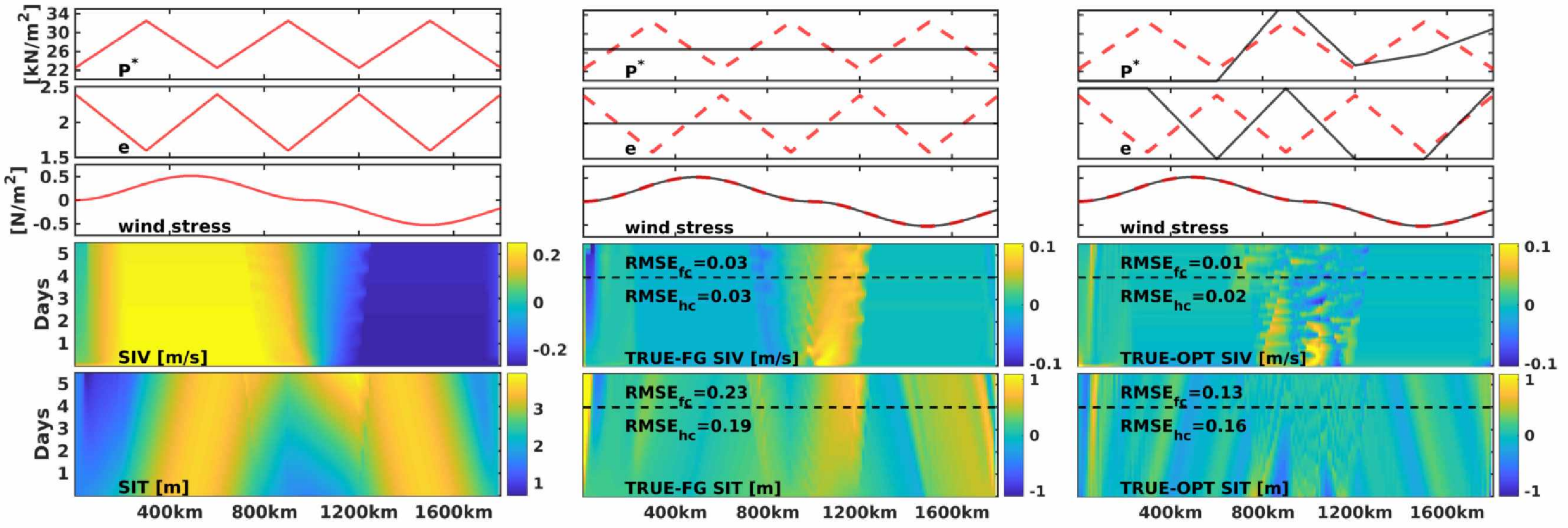

a.) True b.) OSSE-3 FG vs True c.) OSSE-3 OPT vs True

Figure 3.2. PIZ OSSE-3 Results. Panels in column a.) show the true parameter distributions (upper 3 plots) and solution (lower 2 panels) for PIZ experiments (OSSE-3,-3w, and -3n). Subplots from top to the bottom show respectively spatial variability of the $P^*(x)$, $e(x)$, and wind stress (τ_a), and evolution of SIV and SIT. Panels of column b.) show the OSSE-3 first guess parameters and solution in relation to the true solution. The upper three plots of b.) show true and first guess distribution by the dashed red and black lines, respectively. The lower two plots show the true-minus-first guess evolution of SIV and SIT, respectively. The dashed black line identifies the end of the assimilation window, with the RMSE for hindcast (hc) and forecast (fc) periods shown. Panels of column c.) show the OSSE-3 optima the same way as column b.).

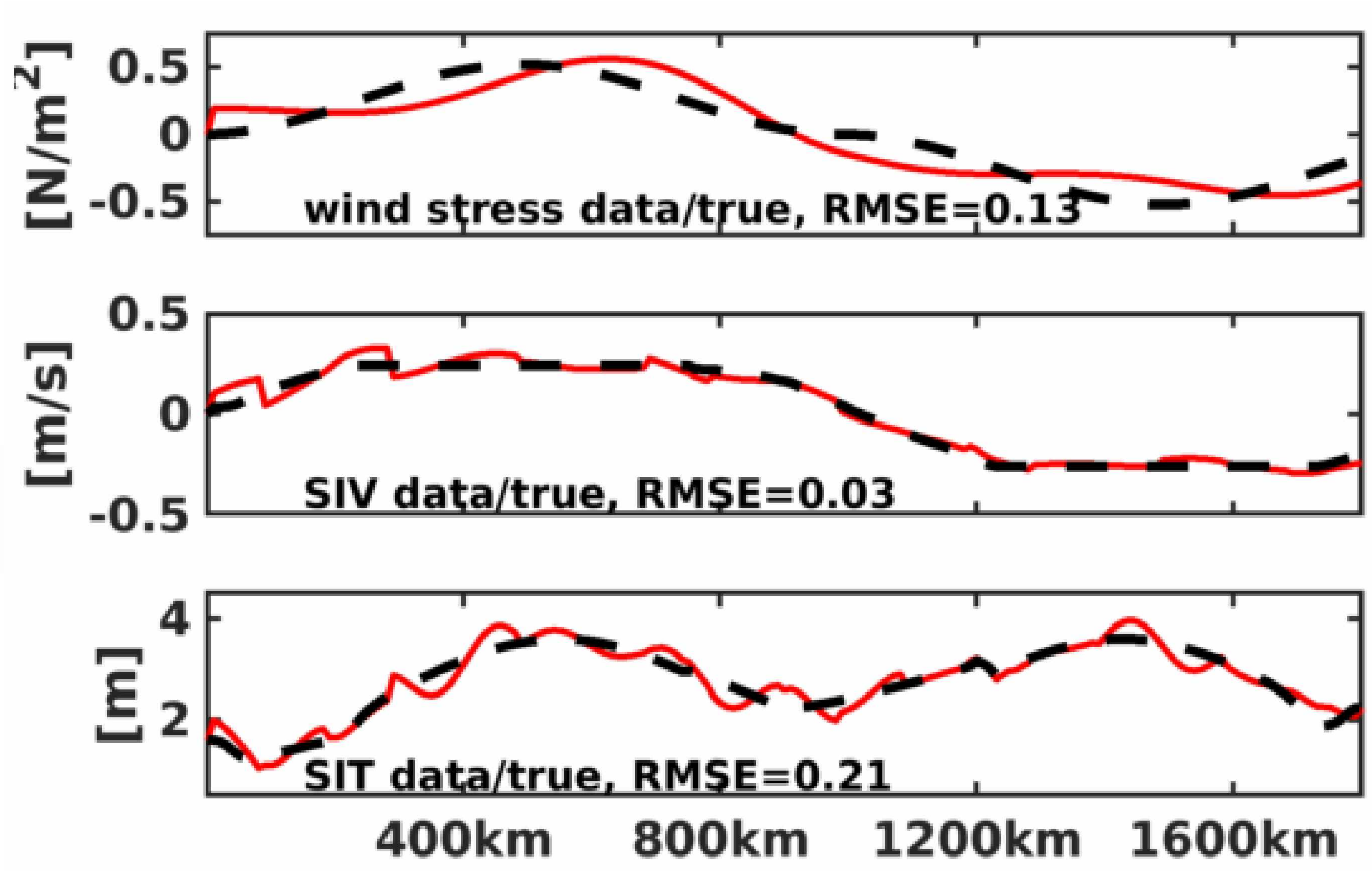

Figure 3.3. PIZ OSSE Example Observations of τ_a, SIV, and SIT. Solid lines in the upper, middle, and lower plots exemplify observations of the wind stress, SIV, and SIT used in PIZ OSSEs at the start of day 4 of the model run. Dashed lines represent the true solutions from which observational data (red) are generated.

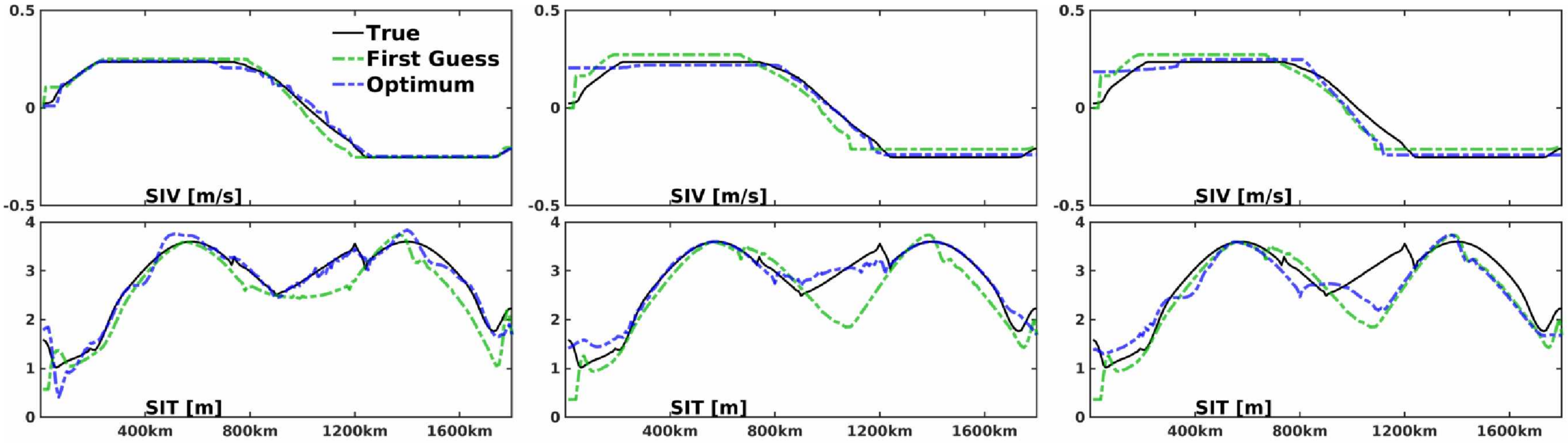

a.) OSSE-3 b.) OSSE-3w c.) OSSE-3n

Figure 3.4. PIZ OSSE Solutions at Day 4. Panels show SIV (top row) and SIT (bottom row) at the start of day 4 for each simulation. Solution distributions are shown for each of OSSE-3, OSSE-3w, and OSSE-3e in the left, center, and right columns, respectively. True, first guess, and optimal distributions are shown in solid black, dashed green, and dashed blue curves, respectively, in each panel. The black curves are identical the black, dashed curves in Figure 3.3.

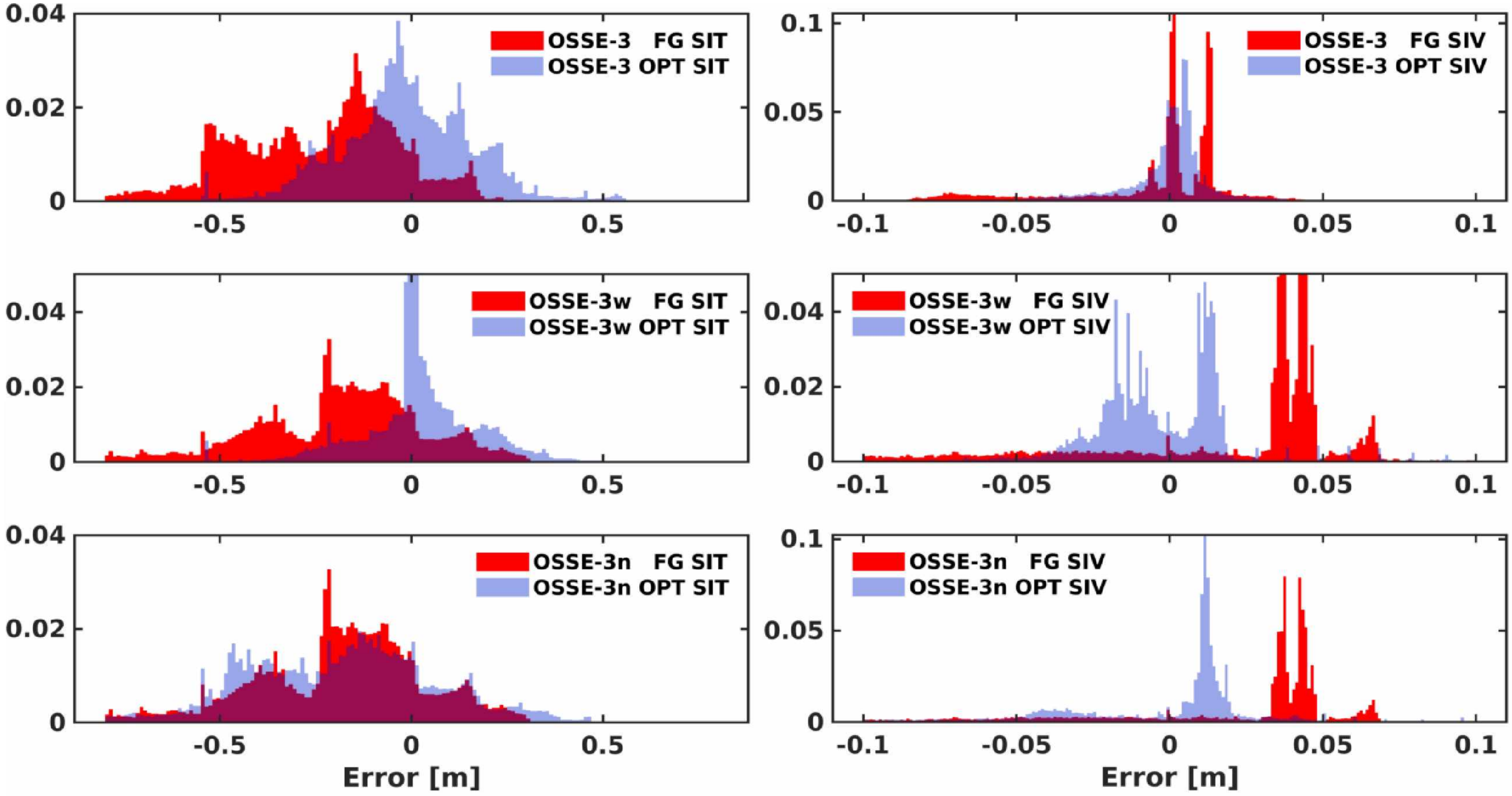

Figure 3.5. PIZ OSSE Error Distributions. Error distributions for OSSE-3, -3w, and -3n are shown in the top, middle, and bottom row of panels, respectively. Plots in the left (right) column correspond to SIT (SIV) errors, calculated as experiment-minus-true, with first guess solution errors presented in red and optimal solution errors in blue.

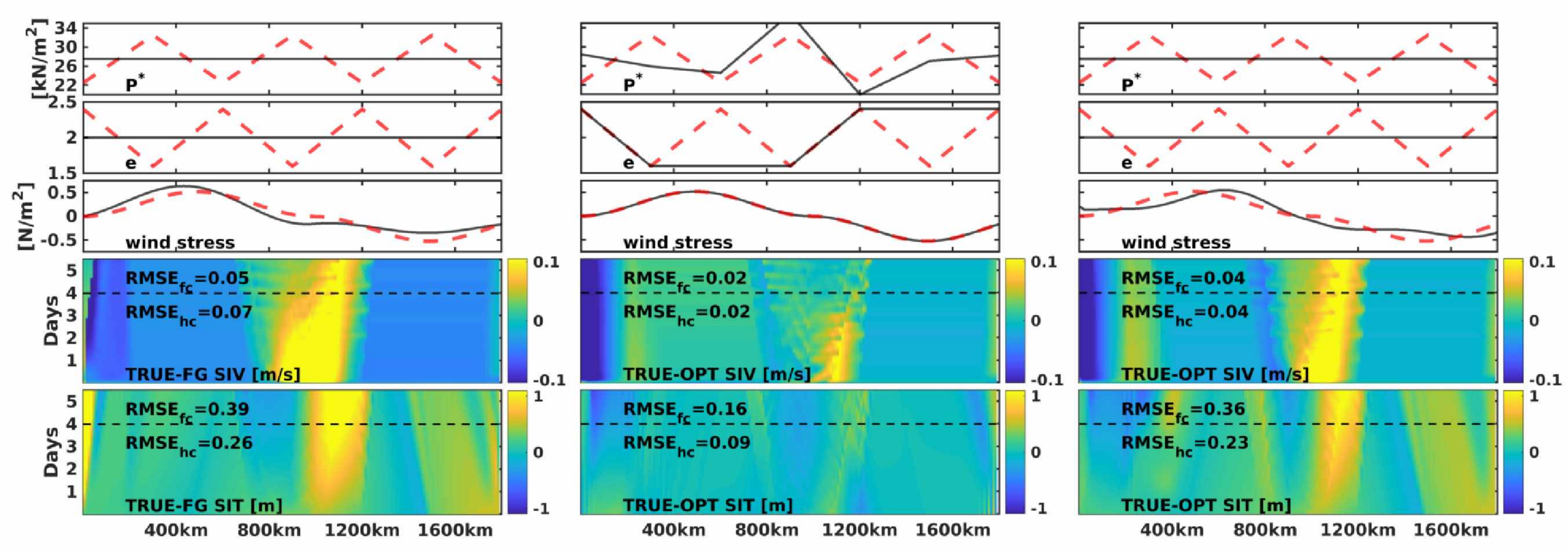

a.) OSSE-3w FG vs True b.) OSSE-3w OPT vs True c.) OSSE-3n OPT vs True

Figure 3.6. OSSE-3w/n First Guess and Optimal Parameters/Solutions. Panels in column a.) show first guess parameter distributions (upper 3 plots) and solution (lower 2 panels) of OSSE-3w, with column b.) showing the relation of the OSSE-3w optimum. The layout mirrors those of Figures 3.2 b. and c., respectively, showing results in relation to the true parameters/solution. Column c.) shows the optimized results of OSSE-3n in relation to the true parameters/solution.

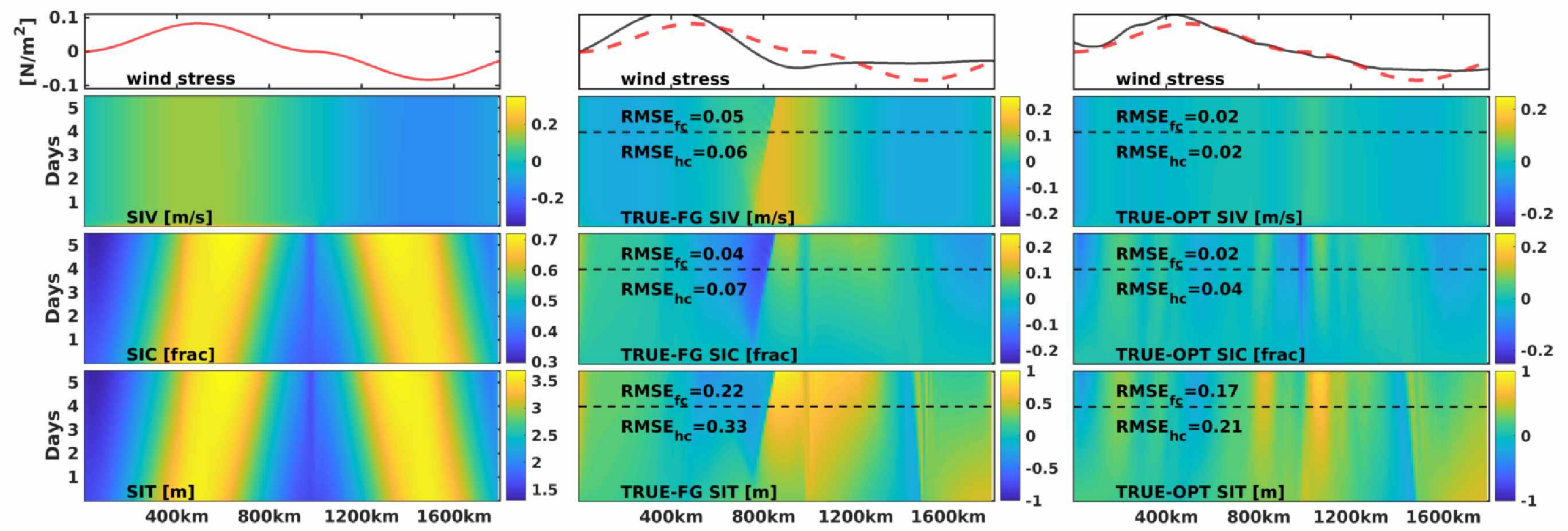

a.) True b.) OSSE-4 FG vs True c.) OSSE-4 OPT vs True

Figure 3.7. MIZ OSSE-4 Results. Panels in column a.) show the true wind stress (top panels) and solution (lower 3 panels) for MIZ experiments (OSSE-4,-4w). Subplots from top to the bottom show respectively spatial variability of the wind stress (τ_a), and evolution of sea ice state. Panels of column b.) show the OSSE-4 first guess parameters and solution in relation to the true solution. The upper plot of b.) shows true and first guess τ_a by the dashed red and black lines, respectively. The lower plots, from top to bottom, show the true-minus-first guess evolution of SIV, SIC, and SIT, respectively. The dashed black line identifies the end of the assimilation window, with the RMSE for hindcast (hc) and forecast (fc) periods shown. Panels of column c.) show the OSSE-4 optima the same way as column b.). Rheological parameters $P^*(x) = 27000$ N/m^2 and $e(x) = 2$ remain fixed throughout and are not shown. Plotted red lines in each of the top three rows illustrate the true parameter distribution.

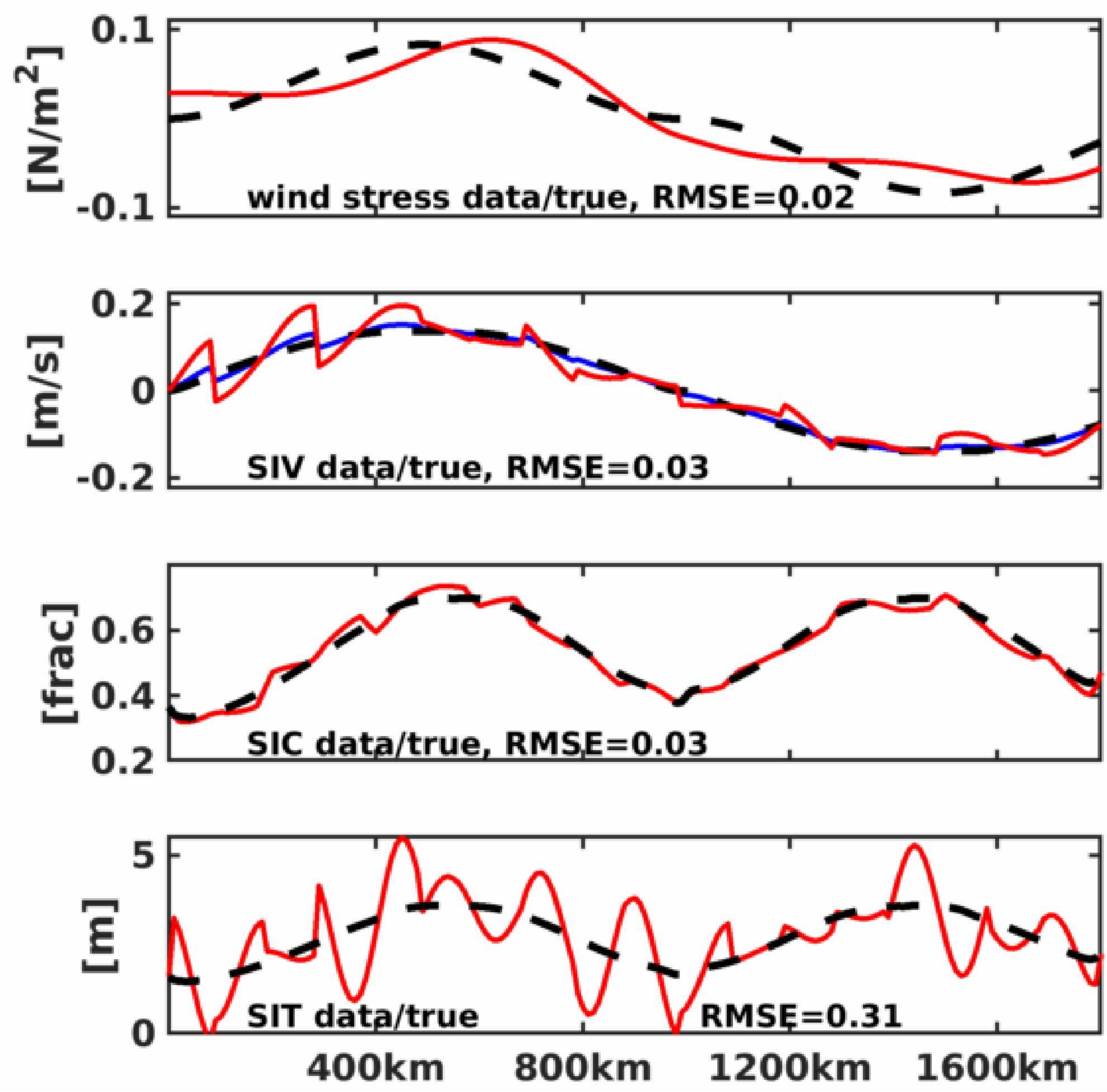

Figure 3.8. MIZ OSSE Example Observations of τ_a and Ice-State at Day 4. Plots show, from top to bottom, the observations of wind stress, SIV, SIC, and SIT, respectively, used as model constraint at the start of day 4. Solid red lines show example observations for OSSE-4, while the dashed black lines track the true solution., for the day 4 of the model run. The RMS errors identify the statistical difference between true state and synthetic data throughout the assimilation window. The blue line of the SIV plot represents the high-accuracy (RMSE of 0.01 m/s) ice velocity observations used in OSSE-4w.

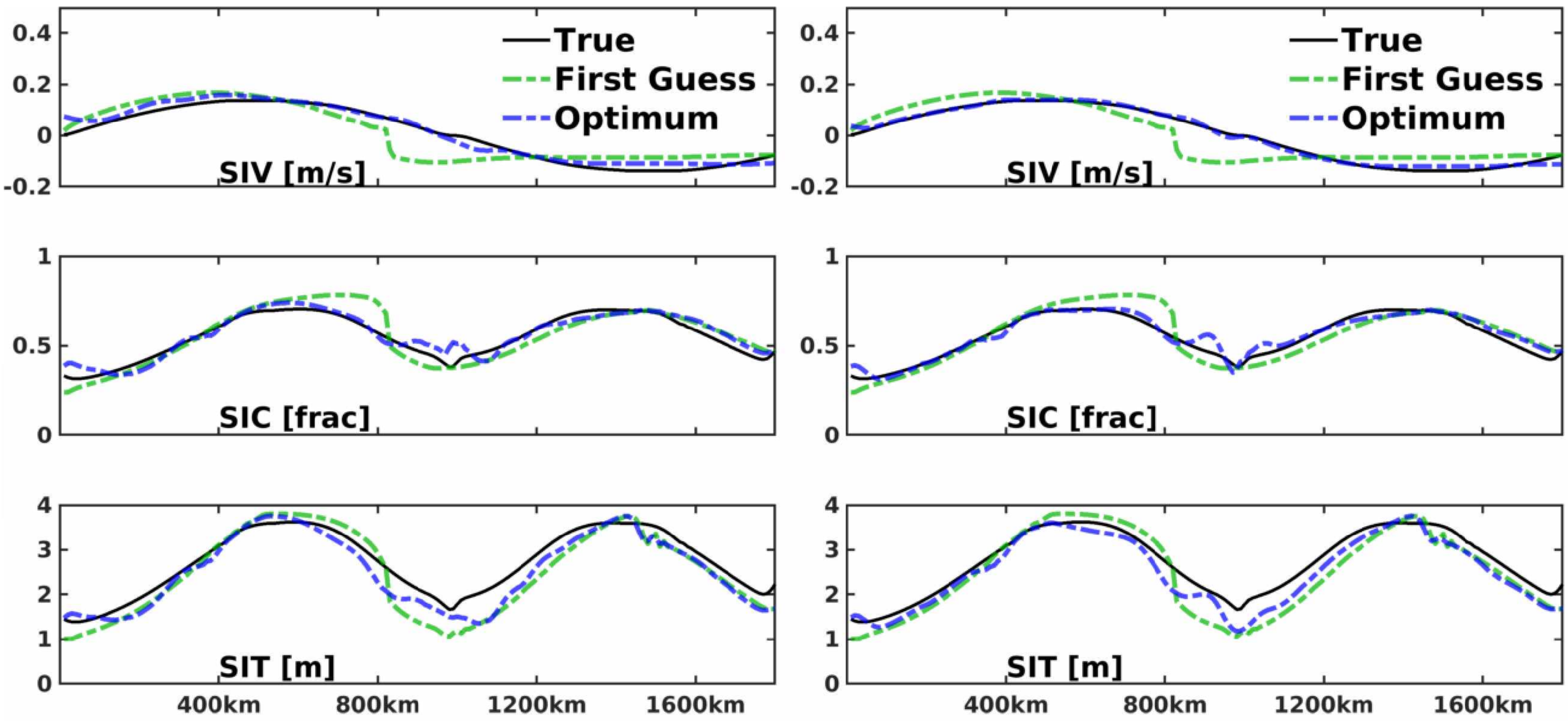

a.) OSSE-4

b.) OSSE-4w

Figure 3.9. MIZ OSSE Solutions at Day 4. OSSE-4 (a) and OSSE-4w (b) model states at the start of day 4 are shown. Top, middle, and bottom rows illustrate SIV, SIC, and SIT distributions, respectively.

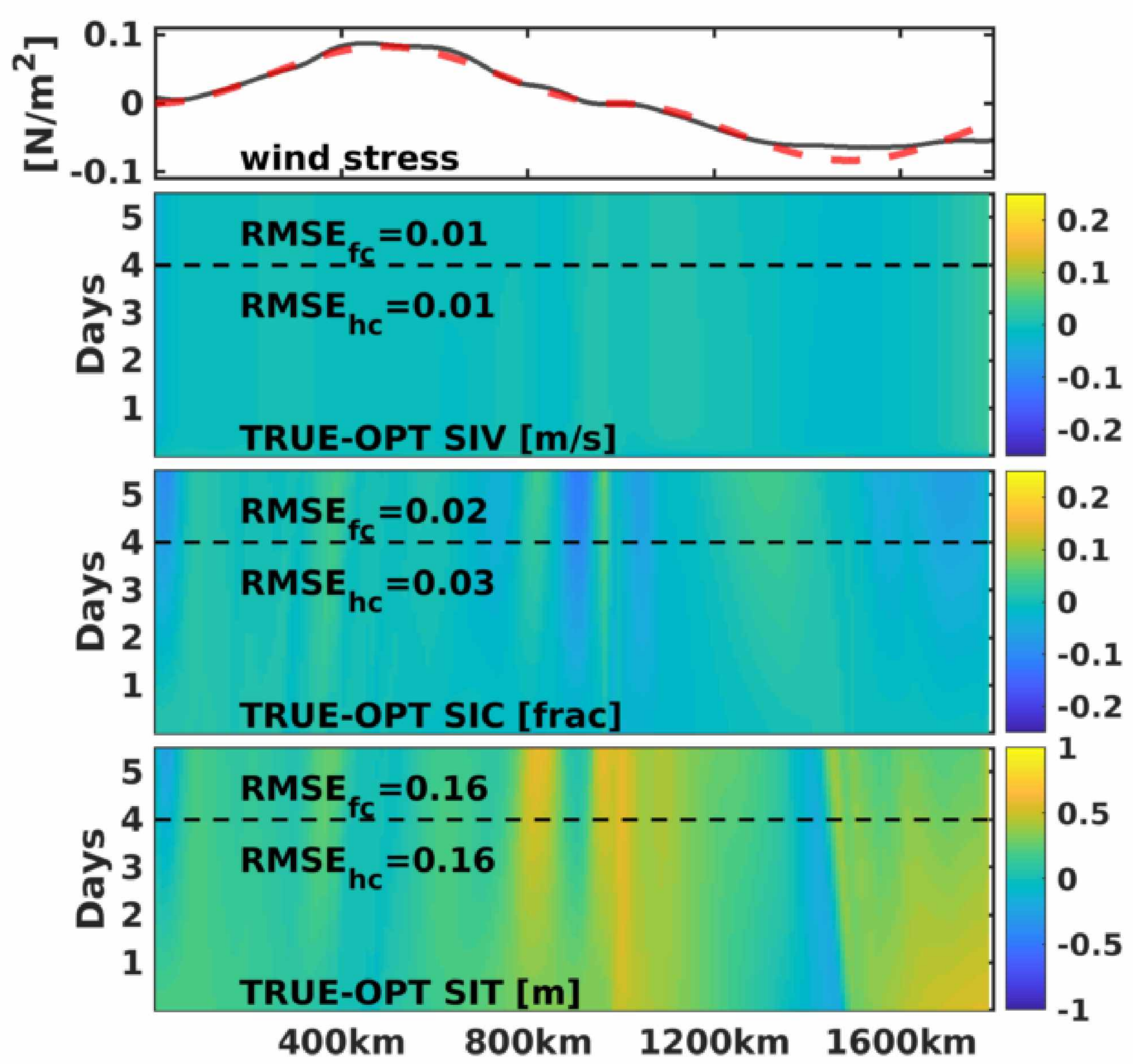

Figure 3.10. Optimal OSSE-4w Solution Errors. The errors for the optimized solution for the OSSE-4w (high accuracy ice velocity observations) are shown as in 3.7c. Subplots from top to the bottom show errors in the optimized wind stress distribution, and evolution of errors in the optimal SIV, SIC, and SIT, respectively. Standard error of optimized solution with respect to the true solution shown in each forecast and hindcast region.

Chapter 4: Ensemble-Transform Filtering of HFR & ADCP Velocities in the Chukchi Sea[1]

Abstract

The Chukchi Sea (CS) is the gateway to the Arctic Ocean (AO) for Pacific waters entering from Bering Strait (BS) and also a potential location for future offshore oil extraction. Since 2010, regional CS data has become more plentiful with acoustic Doppler current profilers (ADCP) moored throughout the northwestern portion of the shelf along with coastal high-frequency radar (HFR) surface current monitoring during the ice-free summer season. This work develops a data assimilation system (DAS) for these observations which applies an asynchronous variational ensemble filter to a Regional Ocean Modeling System (ROMS) CS domain. Two configurations of the DAS applied during August–November 2012 are tested and compared with observations from several sources, including unassimilated external data. The tested DAS configurations performed when assimilating surface as a full timeseries of observations rather than as forecast-interval means. The resulting system could be used for future operational forecast refinement in the region well suited for application to surface monitoring and forecast for regional oil spill mitigation. Failures of background model which limit further analysis are discussed.

4.1 Introduction

The Chukchi Sea (CS) is an essential constituent of the Arctic Ocean (AO) where Pacific waters entering through Bering Strait (BS) conflow with water masses originating from the Atlantic Ocean and the Siberian Shelf, the Canada Basin, and seasonal sea-ice. In addition to its key role in the AO freshwater and heat budgets, the region is also important to resident and migratory wildlife, potentially subject to energy development, and likely to see increased commercial maritime activity in the coming years. At present, the region lacks an operational surface monitoring forecast system suitable to aid in mitigation of oil spills or other advected contaminants. Such considerations motivate attentive monitoring of the region and the development of possible data-informed forecast systems.

The CS is shallow, with depth rarely exceeding 60 m, but lies above a broad continental shelf with area roughly 770^2 km^2 and contributes over half the total coastal water territory of the USA. Regional flow is primarily by the sea-surface geopotential difference between the North Pacific and Arctic Oceans [*Coachman et al.*, 1975; *Woodgate et al.*, 2005] which is strongly regulated by both large-scale atmospheric dynamics [*Danielson et al.*, 2014; *Peralta-Ferriz and Woodgate*, 2017].

---

[1] This work is still in preparation. Anticipated ordered list of authors is: Stroh, J.N., G. Panteleev, and T. Weingartner

Circulation through the CS is governed by topographic depressions which trifurcate the incoming BS northward flow into three channels: a western flow through Herald Canyon [*Pickart et al.*, 2010; *Itoh et al.*, 2012; *Gong and Pickart*, 2015], a flow through the Central Channel [*Weingartner et al.*, 2005], and the Alaska Coastal Current (ACC). A local map of the region and flow may be found in *Weingartner et al.* [2005]. Relative distribution of flow through each branch varies with seasonal changes in wind forcing and strength of baroclinic flow components. Higher frequency flow modulation results from local wind forcing [*Weingartner et al.*, 1998, 2017a], external inflow variation [*Woodgate et al.*, 2005; *Danielson et al.*, 2014], and baroclinic effects from the presence of different watermasses [*Pisareva et al.*, 2015; *Pickart et al.*, 2016].

In the eastern CS, Hanna Shoal together with minor topographic features and the continental shelf break influence the CC to merge with the ACC near the northernmost reach of the Alaska coast. This common flows reaches Barrow Canyon (BC), a nearshore along-coastal depression that serves as the major entrypoint for relatively warm Pacific and post-Eurasian flow Atlantic waters to the Arctic basins. *Itoh et al.* [2013] estimates annual flow through Barrow Canyon as 0.45 Sv near the mouth with much higher rates of transport (~1.0Sv) in summer when winds are coherent with the stronger background pressure gradient than in winter (~0.1 Sv) when southward-blowing winds oppose a weaker pressure gradient. *Okkonen et al.* [2009] found that flow into Barrow Canyon is strongly modulated by wind and buoyancy effects of the source ACC flow. *Williams et al.* [2014] investigate water-mass exchanges over the shelf-breaks along the boundaries of the CS, while more recent work by *Corlett and Pickart* [2017] studies the current structure along the shelfbreak. Many of these studies have been aided by moored acoustic Doppler current profilers (ADCP, or moorings) and coastally-installed high-frequency radar (HFR) to monitor circulation over the region.

The earliest data assimilation (DA) study in the Chukchi region which combined observational data and numerical modeling into a DA system (DAS) reconstructed the ecohydrology of the north Bering and southern Chukchi Seas using the 3-dimensional variational (3DVar) assimilation method [*Brasseur and Haus*, 1991]. More recent regional DAS applications focus on: optimal north Pacific state reconstruction [*Awaji et al.*, 2003], circulation of the Bering Sea and model sensitivity to moorings [*Panteleev et al.*, 2009], Chukchi circulation during data-rich years 1990–1991 [*Panteleev et al.*, 2010], reconstruction of Bering Sea SSH [*Panteleev et al.*, 2011] and circulation [*Panteleev et al.*, 2012], configuration and optimization of HFR sites for Bering Strait monitoring [*Panteleev et al.*, 2013, 2015], and CS thermal state regime reconstruction for 1941–2008 [*Luchin and Panteleev*, 2014].

A more recent work by *Francis et al.* [2017] applies a DAS to examine regional sea-ice loss effects on local circulation. These contemporary studies all implement the 4-dimensional variational (4DVar) data assimilation method [*Le Dimet and Talagrand*, 1986] as oceanographic studies generally prioritize reconstructive smoothing over operational forecast [*Kalnay*, 2003; *Gustafsson*, 2007].

These recent studies, however, have not used new regional HFR data sources in an assimilative study. Ensemble-based DA methods are implemented into operational or real-time monitoring and forecast system more easily than the 4DVar methodology (which requires a separate adjoint model), and provides better scalability with modern parallel computing resources. This work presents a DAS for the Chukchi Sea using the maximum-likelihood ensemble filter [MLEF, *Zupanski*, 2005]) and the Regional Ocean Modeling System [ROMS, *Shchepetkin and McWilliams*, 2005] to assimilate surface velocities measured by HFR and timeseries of moored observations. The remainder of this study is presented as follows. Section 2 describes the monitoring sources and observational data. Section 3 provides brief details of the MLEF algorithm and a practical extension to assimilate timeseries of observations. Section 4 describes the model setup, tests and validates the DAS, and presents results. Section 5 summarizes the work and comments on failures of the background model. Dates herein are written in ordinal date format (YYYY-ddd.dd, per ISO 8601) or are referred to by ordinal day prefixed by 'jd' with the year provided in context.

4.2 Observational data

4.2.1 HFR

HFR antenna installations along the North Slope of Alaska have existed since 2010, with operational systems since 2012 near communities of Point Lay (69.74°N, 199.99°E), Wainwright (70.64°N, 199.97°E), and Utqiagvik/Barrow (71.38°N, 203.52°E). Another antenna at Simpson (71.06°N, 205.27°E) became operational in 2013 to resolve surface currents eastward of Barrow. The monitoring system observes velocities during the summer months to a distance approximately 180 km offshore; Figure 4.1 identifies the antenna locations and observable CS region within the model. The antennae broadcast frequencies of 4.75–4.8 MHz correspond to bulk surface observations over an effective depth of about 2.5 m [*Stewart and Joy*, 1974].

HFR resolution of 2D velocity fields requires simultaneous observation by independent antenna, so associated gridded datasets contain both temporary gaps exist due to signal intermittence and persistent gaps due to radar geometry. Regional measurements further suffer night-time pollution from ionospheric backscattering [*Teague et al.*, 2001] between 0600 and 1200 UTC (roughly

10pm–4am local time), which reduces the number of observations during that interval by about half. One expects that HFR-conditioned states show some evidence of degraded coherence with these observations at daily 12Z analyses. In spite of these uncertainties and limitations, HFR remain among the most cost-effective regional observation systems and it is therefore important to maximize the information collected from them. The HFR data is available from the Coastal Observing Research and Development Center (http://hfrnet.ucsd.edu), and consists of hourly-averaged velocity records together with associated geometric dilution of precision (GDOP) fields estimating spatial accuracy degradation [*Chapman et al.*, 1997].

4.2.2 Moored ADCP

In the northeast CS, the Hanna Shoal and Barrow Canyon region have been the locus of moored ADCP installations supported by BOEM, NOAA, and local industry. Figure 4.1 identifies the locations of moorings during 2012–2014 and Table 4.1 provides further specific details. Acquired mooring data files include 2D timeseries of velocities which are binned at approximately 1 m intervals from 2–3 m below the surface to 8–10 m above the ocean floor. Per source file documentation, hourly profile representatives result from interpolation with 6th order low-pass Butterworth filtering with a 36-hour cutoff threshold.

4.2.3 Drifters and CTD

Dynamical data from 22 drifters released in the central Chukchi region on 2012-225 and 2012-236 serve as external data for comparison to model and DAS counterpart trajectories. Table 4.2 provides a record of drifter metadata for reference. The drifter observations,obtained from http://research.cfos.uaf.edu/chukchi-beaufort/data_archive.php, comprise hourly or half-hourly drifter velocity and position measured by satellite. Deployment time and locations were assumed to be the first time and position of each record. However, the first record in each timeseries includes a velocity, and are therefore suspected not to correspond directly with physical deployment. A set of CTD observations are also used for quality assessment of vertical temperature and salinity (T/S) profiles in the model.

4.3 Assimilation Method

Data assimilation (DA) is a technical framework for combining numerical modeling and observational data, and is an essential component of modern geoscience. In its most direct form, sequential DA methods use empirical data to constrain and adjust primitive equation model evolution [*Kalnay*, 2003; *Jazwinski*, 2007]. The objective of a DAS is to determine a model state most representative of provided data, given the uncertainties in those data. Among the most commonly employed DA algorithms are the ensemble Kalman Filter (EnKF) [*Burgers et al.*, 1998; *Houtekamer and Mitchell*, 1998; *Evensen*, 2003] and variants, whereby a collection of model iterations statistically approximate the classical Kalman Filter (KF) (which is itself a least-squares optimization method [*Sorenson*, 1970]). The general idea of KF-type methods is to use an ensemble of solutions to empirically construct model (and/or observational) covariances, from which an minimum-variance unbiased estimator (MVUE) of the joint model-data probability distribution (PD) may be calculated algebraically. Variational methods, in contrast, seek to iteratively identify the mode of this PD and may be more robustly applied in cases where the relationship between model states and observations is nonlinear or involved PDs are non-Gaussian. The standard DA notation and nomenclature of *Ide et al.* [1997] are assumed here for brevity.

In the maximum-likelihood ensemble filter, correction of the forecast state is defined as a linear combination of N ensemble perturbations about the forecast state [*Zupanski*, 2005] unlike Kalman-type filters where perturbations are centered around the ensemble mean. Specifically, the analysis is given by $x^a = x^f + \mathbf{P}^{1/2}w^*$ where w^* is an optimal weight vector for columns of $\mathbf{P}^{1/2}$, which is a matrix whose columns are scaled ensemble differences from the unperturbed forecast x^f. The scaling, by $\sqrt{N}$, is such that $\mathbf{P}^{1/2}\mathbf{P}^{T/2}$ is an empirical rank-N approximation to the full model error covariance $\mathbf{P}$ with $\cdot^T$ indicating matrix transposition. The analysis x^a is identified by minimizing the common variational cost function

$$J(x) = \frac{1}{2}\left\|\mathbf{P}^{-1/2}\left(x - x^f\right)\right\|^2 + \frac{1}{2}\left\|\mathbf{R}^{-1/2}\left(y^o - \mathcal{H}(x)\right)\right\|^2. \tag{4.1}$$

over the N-dimensional subspace $\{x^f + \mathbf{P}^{1/2}w\}$ parametrized by $w \in \mathbb{R}^N$. Here, $\mathbf{R} = \mathbf{R}^{1/2}\mathbf{R}^{T/2}$ is the observational error covariance matrix. The Hessian matrix of $J(x^a)$ identifies the posterior covariance error matrix [*Thacker*, 1989]. From a Bayes' Rule perspective, this optima is the mode of the posterior PD produced when the forecast model PD is updated on the basis of observations [*Purser*, 1984; *Purser and Parrish*, 2003; *Wikle and Berliner*, 2007] with the analysis state corresponding to the maximum *a posteriori* estimate. The forecast error covariance square-root factor $\mathbf{P}^{1/2}$ is updated to reflect this posterior PD by computing the square-root factor of the Hessian term associated with Equation (4.1) at the analysis [*Zupanski*, 2005]. The columns of this posterior factor define state variations to initiate the next ensemble forecast step via model integration.

The observation operator $\mathcal{H}$ typically defines a mapping between analysis-time model states and observed data. The nature of many EnKF-like DA schemes allow for representing observations at non-analysis times via linear combinations of the observed forecast $\mathcal{H}(x^f)$ and its observed perturbations $\mathcal{H}(x^f + p_i)$ at those times. This correspondence is approximate when $\mathcal{H}$ is nonlinear, and may formally require treatment of temporal covariance among the observations [*Sakov and Bocquet*, 2018]. Filter assimilation of observations at times different than the present analysis-time is referred to as "asynchronous filtering" although it could be referred to as a sequential smoother [*Sakov et al.*, 2010; *Sakov and Bocquet*, 2018]. For simplified notation in diagrams and figures, the so-called innovation vector d quantifies the difference between observation and model counterparts, with $d^{bg} = y^o - \mathcal{H}(x^{bg})$ and $d^f = y^o - \mathcal{H}(x^f)$ used for the background and forecast innovations, respectively.

In the application discussed here, asynchronous observation operators corresponding to HFR and ADCP data are quasi-linear operators which output a 6-hour timeseries of hourly velocities. For a state in the target subspace represented by w, the associated model observation is the forecast timeseries plus the same linear combination of observed ensemble perturbations. A formal linearization gives $\mathcal{H}(x) = \mathcal{H}(x^f) + \mathbf{P}_{\mathcal{H}}^{1/2} w$ where columns of $\mathbf{P}_{\mathcal{H}}^{1/2}$ are the observed (via application of $\mathcal{H}$) ensemble variations with respect to the observed forecast timeseries; these empirical quantities are easily output and stored during the ensemble forecast step (*i.e.* model integration). The approach is an alternative for incorporating all records of data without shortening the forecast-analysis DA cycle to 1-hour intervals.

The base algorithm identifies the mode of the posterior PD, rather than finding the best linear unbiased estimator under the constraint of minimum variance as in algebraic KF-type filters [*Zupanski et al.*, 2008]. This distinction is of primary concern when involved PDs are non-Gaussian [*Pires et al.*, 2010], so that the posterior mode and variance minimizer differ [*Talagrand*, 2003]. The nature of surface currents as measured by HFR [*Ashkenazy and Gildor*, 2011] or other means [*Bracco et al.*, 2003] are known to be non-Gaussian, and by extension the presumed error structures [*Purser and Parrish*, 2003] are as well. This motivates the use of the variational approach rather than algebraic method, as the mode would more robustly represent the general disagreement between the model and observations. Whereas MLEF directly targets a subspace optima of the 3Dvar cost function given in Equation (4.1), its asynchronous extension approximately solves the 4Dvar cost function at the analysis time over the ensemble-spanned subspace. The method circumvents the need for an adjoint model to propagate future-time changes in observed errors to initial-time changes in state. The analysis state and covariance structure among the ensemble perturbations stores information as data is assimilated. In contrast with 4DVar, this ensemble method offers no correction of the entire model trajectory; the analysis step updates only the instantaneous model state rather than its history over the prior forecast interval. It does, however, provide an estimation of analysis uncertainty at no additional cost.

4.4 Results and Discussion

For this study, the ROMS model domain encompasses the region [58.76N,83.34]°N × [168.12, 229.28]°E with grid-scale of approximately 16km at the boundaries tapering to approximately 12km over the central 1/9th of the domain. The domain is artificially large to maintain ongoing ensemble variations, which are suppressed by low-dimensional dynamics of the Bering Strait, and to limit interaction between the open boundaries and the analysis region. Previous experiments with a smaller domain suffered from instabilities due to the formation of a spurious large scale gyres over the deep northeastern that was driven by numerical boundary currents. Extant sea-ice over the shelf is thin and rapidly retreats from the continental shelf during the model period of August–October, and is ignored in the ice-free model configuration implemented here. The area of interest resolved at approximately 12km is outlined by a dark grey box in Figure 4.1; this region is used to localize the model analysis and posterior covariance update. Importantly, the domain intends to be kept reasonably coarse for reduced computational time desirable when employing an ensemble of model instances.

Domain bathymetry is sampled from the Alaska Region Digital Elevation Model v2 [*Danielson et al.*, 2015]. The vertical grid comprises 15 terrain-following vertical levels with prescribed Mellor-Yamada Level 2.5 closure scheme. Initial data fields are generated by linear interpolation of Hybrid-Coordinate Ocean Model (HYCOM) analysis GLBa0.08 variables (accessible via open-DAP at https://tds.hycom.org/thredds/dodsC/glb_analysis) to the model grid. An identical method and source generated open-boundary values for the duration of model integration. Boundary behaviors were set as radiation/nudging, Flather, and explicit Chapman conditions for full-depth variables, barotropic velocities, and free-surface, respectively.

The 6-hourly ERA-interim fields [*ECMWF*, 2012] supply ocean surface forcing during simulation. For each year 2012–2014, background models integration begins at jd180 with fixed boundary values, and forcing undergo a 30-day integration with 90-second timesteps to relax dynamical imbalance. Following this adjustment period, initial HYCOM T/S data was re-prescribed and then integrated from jd180 to jd210 with larger timesteps (2.5 minutes) to achieve a fit between the currents and model parameters without disrupting the T/S distribution during cold-start adjustment.

The DAS described in Section 4.3 was initialized with an ensemble of $N = 30$ model instances perturbed by random velocity and free-surface variations throughout the ocean domain 24-hours before the first analysis time. The analysis steps occur every 6 hours through the summer periods jd214.00–310.00, which approximately frame the availability of HFR measurements. The observation error covariance factor $\mathbf{R}^{1/2}$ is supplied as a diagonal matrix using to estimated standard errors σ_m, σ_h modified as follows. Entries corresponding to moored velocities are set to a constant value σ_m, while those for HFR are a constant σ_h multiplied pointwise by its spatial GDOP factor. Temporally averaged HFR GDOP factors for 2012-215–300 are shown in Figure 4.2 to illustrate the spatial structure of these uncertainties, although the figure suppresses their temporal variability.

In the described experiments, background σ_m and σ_h are set to 0.1 m/s and 0.33 m/s, respectively. With this uncertainty model, zonal HFR observation error components are at maximum approximately 0.16 m/s nearshore increasing linearly to 0.2 m/s at the furthest observable extent, with meridional error components of 0.14 m/s where beams are oriented northward growing to 0.5 m/s where each antenna beam has the largest azimuth. Early experiments found that this GDOP scaling of prescribed HFR uncertainty yielded smoother posterior ensemble perturbations less prone to model blow-ups. For both ADCP and HFR, prescribed error scales are considerably larger than documented instrumental uncertainties as they subsume errors associated with gridding and pre-processing observations, errors in model representation of true states, and model-space errors incurred by applying $\mathcal{H}$.

The model re-initialization after each analysis requires that barotropic velocity estimates be recalculated for each ensemble member, which depends on the free surface in the terrain-following coordinates. Three-dimensional velocity fields as well the free-surface variable compose the state vector x so that it includes all dynamical fields needed for model update.

4.4.1 Filter Configuration

Ensemble Generation and Size To test the effect of ensemble size on analysis quality of assimilated observations, DAS experiments were conducted employing ensembles with 30, 60, and 91 perturbed members, respectively. This test configuration assimilated 6-hour mean HFR data and hourly ADCP timeseries, but did not include the free-surface variable ζ in the model state vector.

A base ensemble of 30 perturbed members was produced by adding random noise to the initial background state at day 210, integrating for varying number of 3-hour increments to define a variation about the background state at jd214. An additional set of 30 members was generated by adding random noise with a 60 km decorrelation length scale at jd210 and propagating to jd214. Initial standard deviations of noise added to the velocity fields in these two cases was 10 cm/s, with the latter smoothed by a 5-gridpoint radius Gaussian filter to the imposed noise. Finally another 31 perturbations were created by adding random noise (mean amplitude 5%) to Fast Fourier-transformed copies of the background state at jd214 to generate 31 additional ensemble elements with smooth spatial variations. Figure 4.3 shows that additional members of the ensemble did not improve the quality of the forecasts in an evident way. One concludes that a 30-member ensemble of forecast variations is sufficient, although some intermittent improvement (<2% mean) for HFR is possible at the cost of doubling or tripling total model integration time.

Approximate Optimization Minimization of the nonlinear cost function J with respect to the control vector $\xi \in \mathbb{R}^N$ is at the heart of the analysis. In relation to the variable w discussed in Section 4.3,

$$\xi = \left[I_N + \mathbf{Z}(x^f)^T\mathbf{Z}(x^f)\right]^{1/2} w \tag{4.2}$$

gives the ensemble-transform coefficient in a Hessian pre-conditioned form ξ. This change-of-variables intends to make the control space isotropic by scaling the ensemble expansion coefficients according to their correlation structure. The analysis optimization step of the ROMS-MLEF DAS implements a secant line search algorithm [*Wright and Nocedal*, 1999] to iteratively update the control variable ξ in sequentially orthogonal subspaces determined by a conjugate gradient (CG) method, closely following *Navon and Legler* [1987] and *Zupanski et al.* [2008]. To check to effectiveness and efficiency of this approach (identified to as "NLCG-ss") compared to an immediately accessible method, an optimal analysis is found by computing $\arg\min |\nabla J|$ over the control space using the internal MATLAB function "fminopt" .

The left plot of Figure 4.4 illustrates the small difference (<3% mean over the 90-day period) in the quality of the analyses produced by the search-based and proprietary optimization methods. However, the right plot of the figure demonstrates that mean computation times differ significantly. The NLCG-ss and "fminopt" methods average 78.4 and 486.4 seconds per analysis, respectively. Assimilation cycles at which the optimization times are similar correspond to instances of few observations. The difference in computation time accumulates to nearly 40 hours over the 90-day period shown, roughly doubling the total time needed to apply the 30-element DAS using 20 CPUs.

4.4.2 Improved Fit to Assimilated Data

Section 4.3 discussed how ensemble-transform filters applied asynchronously may be utilized to assimilate timeseries of observations over analysis windows. The MLEF-ROMS DAS could be configured in several ways depending on whether HFR was represented by hourly timeseries of data (*i.e.* asynchronously) or as 6-hour temporal means ending at the analysis time (*i.e.* synchronously). To compare the effects of the different HFR observation treatments, DAS application using otherwise identical initialization and configurations was performed. Here, Case 1 assimilated HFR as a vectorized 6-hour timeseries while Case 2 assimilated the average record of that timeseries. A model initialized from the same state as the assimilative model run, but which assimilated no data, is used as a background reference to assess the impact of DA. Figures 4.5 and 4.6 schematically show the relation of model observations and measurement data in the asynchronous and synchronous cases, respectively. These schemes differs from the classical filtering method in that model observation timeseries (or its mean) cannot be generally constructed from the analysis-time model state without explicit call to the nonlinear model. Alternately, the mean of the timeseries may also be compared to model observations averaged over the forecast window as in Case 2. In both cases, moored ADCP profiles are always treated asynchronously and assimilated as timeseries, with observation-space possibilities represented by ensemble expansion of the forecast and ensemble histories. Note that throughout this discussion, the identification of Case 2 as "synchronous" is imprecise in that Case 2 observations depend directly albeit implicitly on the full history of HFR data during the forecast period. Nevertheless, this term is used to distinguish it from the explicitly asynchronous approach of Case 1.

Figures 4.7 and 4.8 show the temporally-smoothed evolution of uncertainty-weighted differences between observations and DAS forecast states relative to those of the background model. The figures show results of Case 1 and Case 2, respectively, presented by comparing case-to-background error ratios. Results presented in this form do not depend on the number of observations which differ between cases; otherwise, one naturally expects that errors in Case 2 be less than those of Case 1 due to smaller vector length. This effect was noted in early experiments conducted to assess the impact of including the free surface (ζ) as a state vector component: assimilation of only analysis-time HFR data in runs which included ζ had errors 1–2% larger than those which did not because of the slightly increased weight given to the background cost term. However, inclusion of ζ when moorings were assimilated appeared to reduce the scale of artificial gravity waves generated by analysis changes of the velocity field, yielding smoother forecasts and more stable integration of perturbed models[2]. Alternate methods of suppressing adjustment waves from the analysis [*Barth et al.*, 2007] were attempted without success.

The results shown in these figures are qualitatively comparable; errors in the background model are reduced by 20–35% on average. Both DAS applications successfully constrain and correct model trajectories by comparable amounts when considering all forecast-minus-observations (black lines), although the asynchronous case has a clear advantage most of the time. Specifically, in relation to the background errors, Case 1 errors against HFR (ADCP) decrease by 11% (32%) in the mean while the corresponding error(s) for Case 2 reduce by 5% (20%).

The qualitative similarity is expected, as the two representations of HFR data are related directly. However, the corresponding volume of HFR observations is not identical; pointwise HFR observations in Case 1 are about 5 times more numerous than in Case 2. This results in significantly different filter response: the error reduction in Case 1 is balanced between HFR and ADCP errors, while Case 2 total errors closely track the errors in the more numerous ADCP data. Thus, the asynchronous assimilation of HFR helps to even the relative weight of the two observation types. This effect is most pronounced between jd240 and jd250 when HFR observations are most numerous. During this period, Case 1 errors generally decrease from ~85% to ~60% while Case 2 errors are maintained at ~85% relative to the those of the background model.

Influence of Wind Regimes Of key note is the difference in filter response between cases as it depends on the local wind forcing. The mean relative improvement of ADCP errors is 11% greater than that of Case 2, which is solely due to the method of HFR velocity assimilation. Previous observation-based studies found that sustained winds exceeding 6 m/s blowing southeast (240±20° CCW from east) coincided with measured surface flow reversal [*Weingartner et al.*, 2013; *Potter et al.*, 2014], and agree with previous modeling showing barotropic flow reversal when winds critically exceed ~6.4 m/s [*Winsor and Chapman*, 2004]. In the background model here, trial-and-error

---

[2] In the official ROMS modeling forums, the program's main numerical developer discouraged free-surface data assimilation as it results in a "volumetric buoyancy forcing" which is "non-physical, and you do not expect anything good out of it" [A.Schepetkin, posted to the ROMS forum 2011-12-06 (https://www.myroms.org/forum/viewtopic.php?f=14&t=2475). However, updating ζ on the basis of velocities produced improved dynamical balance of analysis barotropic states, resulting fewer waves and model instabilities at model-reinitialization.

exploration suggested that winds directed toward 225 ± 60° (measured counterclockwise from east) with magnitude exceeding 5 m/s correlate moderately (57%) with differences between the mean surface (2.5–10 m) flow and deeper (10–30 m) mean flows means in shallow regions of the central CS where depth is between 35 and 50 m.

This wider range and lower critical limit are roughly established parameters which have not been optimized, but are qualitatively similar to cited ranges. With a temporal restriction that they persist for more than 30 hours with gaps less than 12 hours ignored, these events are herein referred to as "opposing" winds and are designated by blue wind vectors in Figures 4.7 and 4.8. The associated periods are shown in blue-shaded regions of Figure 4.9 which compares the relative errors of ADCP fit for the two cases. During these periods, Case 1 strongly reduces errors in both HFR and ADCP while Case 2 errors vary with little net reduction. Averaged over such periods, Case 1 relative mean fit to ADCP improves by ~1.8%/cycle more than Case 2. In the asynchronous case, the larger volume of HFR data better encourages the analysis toward the observed sheared flow. Meanwhile, Case 2 experiences a unique occurrence in which errors for HFR in Case 2 are lower than the overall error. This suggests that the large near-surface errors during this time are strongly corrected in Case 2 at the expense of quality of fit to local moorings (*viz.* moorings #23 and #24).

However, strong conclusions regarding isolated periods must be cautioned to flow-dependence; states are effectively conditioned on all previously assimilated data and are identical only before the first HFR is assimilated at jd214.25. Also, some persistent differences between HFR and DAS forecast may be a consequence of the ensemble-transform methodology. This is to say that a common linear combination of ensemble vectors may not be able to simultaneously adjust direction of the surface flow measured by HFR and the at-depth velocity profiles measured by ADCP when vertically sheared flow variation is not present among ensemble perturbations. One alternative explanation is that the opposing wind events lead to more diverse behavior in the ensemble forecasts, which has the effect of increasing the orthogonality among the ensemble variations; this leads to more efficient optimization as resolution of errors in the column span of $\mathbf{P}^{1/2}$ is improved.

Nevertheless, periods do exist in where Case 2 outperforms Case 1. This is clear from the red shaded regions of Figure 4.9, which identifies "supporting" wind events where atmospheric forcing is aligned with the background flow. Such events are characterized here by the following conditions: having eastward wind components exceeding 4 m/s or exceeding 2.5 m/s when winds are directed within ±8° of due east, and a duration than 30 hours with gaps less than 12 hours ignored. Averaged over such periods, Case 2 relative mean fit to ADCP improves by ~0.3%/cycle more than Case 1 although most of this difference is due to faster degradation of Case 1 fit to ADCP. A clear example is the sustained constraint of model behaviour between jd281–289 where wind stress is aligned with the background flow. During this period, Case 2 shows relative errors of around 60% while errors are around 72% in Case 1. Interestingly, the HFR errors directly account for a small fraction (~20%) of this difference; strong reduction of errors in fit to ADCP accounts for most of this improvement. This coincides with an onshore wind event, so a likely explanation is that the Case 2 optimum strongly fits the coastal and at-depth ADCP data while the more strongly-weighted HFR reduces the quality of fit to those ADCP in Case 1. This period also marks the start of a large systematic disturbance of the domain generated by a short-duration of rapid inflow from the western boundary along the East Siberian Shelf (not shown). The strong pulse enters the domain as a wave, and follows the Russian coastline to the Bering Strait where it disrupts and reverses the Bering Strait northward transport. Transient consequences are felt throughout the northeast Chukchi shelf until dynamical balance is returned around jd295. No attempt was made to correct or condition the boundary data which are interpolated directly from the HYCOM source to the ROMS domain.

A noteworthy observation regarding DAS behaviour is that zonal components are corrected by HFR more strongly than meridional ones, particularly in shallow regions. Primary reason for this seems to be that onshore, cross-isobath velocities frequently present in the HFR observations are strongly resisted by potential vorticity balance in the model which tends to direct flow along isobaths in shallow regions. It is further noted that the HFR-imposed constraint in shallow regions is stronger due to the increased number of σ-coordinate levels used to represent modeled observation counterparts.

The difference in case-wise filter performance under the two wind regimes may be explained by examining the spatial distribution of analysis errors relative to HFR during the events. Figure 4.10 (4.10) shows the HFR observations *(left panel)* and analysis errors for Case 1 *(upper right panel)* and Case 2 *(lower right panel)* temporally averaged over all periods of opposing (supporting) wind. During opposing winds, surface currents are generally slow with a maximum onshore HFR component of ~25 cm/s. During this period, Case 1 has a clear advantage across the observed region, particularly along the coast (8–20 cm/s *vs.* 10–25 cm/s) and western lobe (4 cm/s *vs.* 7 cm/s). Significantly, Case 1 errors are comparatively lower over deeper waters above the head Barrow Canyon (15 cm/s vs.21 cm/s) and the southern/eastern side of Hanna Shoal (3 cm/s *vs.* 8 cm/s);

both regions have HFR observations with westward components. This suggests that Case 1, while having simultaneously lower errors against back-flow aligned ADCP measurements, is better at resolving the surface-sheared flow than Case 2.

During supporting wind events, mean HFR observations show larger magnitude observations, and westward velocities are present in the eastern lobe only following the isobaths southward from east of Hanna Shoal toward Barrow Canyon. Analysis-HFR errors under supporting wind events are generally worse throughout the domain except over the shelfbreak (*i.e.* beyond the 70 m isobath) in the northeast extent of the HFR observation. Onshore components of averaged HFR observations near the head of Barrow Canyon are in the range 50–70 cm/s with a maximum of 1.2 m/s. For this region, both cases exhibit errors in the range of 10–25 cm/s. However, Case 2 errors are lower than Case 1 near the the shoals and over the central shelf (5–8 cm/s *vs.* 8–10 cm/s) and throughout the western lobe (6 cm/s *vs.* 7 cm/s). The along-isobath band of increased error following the 40 m isobath is present in both cases, while the HFR observations are approximately orthogonal to isobaths. This strongly supports the notation that the model fails to represent cross-isobath flow as the DAS is consistently unable to resolve these flows.

Without onshore and cross-isobath components resolved among the ensemble variations, the DAS cannot improve fit-to-observations in either case. For the observations near the head of Barrow Canyon, the GDOP of both velocity components is low and the observations are given large weight in producing the analysis. When HFR signals have larger and more regular onshore and cross-isobath velocities that are poorly resolved by the model, Case 1 simply has a larger volume of such data to optimize against. The inability to resolve this data in the ensemble variation leads to a degradation of Case 1 fit to all data; the weight of unresolvable components acts as an additional constraint on the asynchronous cost function and inhibits fit-to-ADCP in this case. In contrast, lower volume of such unfittable data has less net weight in the synchronous cost function, so Case 2 is able the fit to the ADCP instead.

The quality of fit to HFR and ADCP seen in Figures 4.7–4.9 during the 2012 season is overall better for the case of asynchronously assimilated HFR. Evidence is also presented that during supporting wind events, Case 1 suffers a loss of fidelity with observations due to abundant unresolved velocity components. However, the frequency and duration of these events during summers 2012–2017, shown in Figure 4.12, indicates that the asynchronous method would be more advantageous overall. That the 2012 ice-free season has the largest number of identified supporting wind days suggests one should expect a stronger benefit of asynchronous HFR treatment in subsequent years.

4.4.3 Comparison to external drifter data

DAS forecasts in this discussion show improvement in model-observation velocity correspondence. Observational data in the form of Lagrangian drifter position and velocity follow flow patterns and are not easily assimilated using the DAS presented here. Instead, the dynamical data from drifters released in the central Chukchi region on 2012-225.42 and 2012-236.71 serve as external data for validation of forecast velocity. The drifter observational data comprise hourly-averaged velocities and position data. Table 4.2 lists details for each drifter and Figure 4.1 plots relevant portions of drifter trajectories in purple. Model drifters are tracked at an effective 0.0 m depth, while physical drifters in the comparison were deployed with drogues at 1 m depth. This disparity in representative depth is a consequence of an incorrect assumption by the author based on the presence of surface temperature measurements and lack of documentation in the data files. In fact, many of the physical drifters used 10 m drogues; they are omitted from this discussion but remain listed in Table 4.2.

The first record associated with each physical drifter determines the deployment time and location for the corresponding model trajectory. The simulated counterparts of each drifter are calculated from geographical positions output by the model, which are assessed in two ways to determine model fidelity with observations. First, output position data is used to compute a timeseries of hourly mean distances from the observed drifter position. Second, the difference in simulated mean hourly distance is used to calculated average velocity for correlation comparison to velocities identically calculated from drifter GPS data.

Vector correlation, needed for the latter evaluation, typically measures the common variability of a velocity time-series [*Davis*, 1985; *Kim et al.*, 2009]. However, preliminary assessment using direct vector correlation hourly velocities (or 3-hour velocity timeseries) suggested that these comparisons of deviations provided little insight as they do not account for differences in mean flow direction. Instead, a more useful method of scoring first-order model-observation coherence is through a skill that directly compares model-observation differences, rather than a fit of variability. Considered here is a quantity $r(t)$ that measures the relative size and direction of differences at some time t:

$$r(t) = 1 - \frac{\text{mean}\left((\mathbf{w}^o - \mathbf{w}^f)^2\right)}{\text{mean}\left((\mathbf{w}^o)^2\right) + \text{mean}\left((\mathbf{w}^f)^2\right)} \tag{4.3}$$

where $\mathbf{w} = [u_1\ v_1\ u_2\ v_2\ u_3\ v_3]^T$ denotes the 1D-vectorization of a short 3-hour timeseries series of 2D velocities for the forecast and observations. In a more geometric notation, this skill may be written as

$$r(t) = 1 - \frac{\left\|\mathbf{w}^o - \mathbf{w}^f\right\|^2}{\left\|\mathbf{w}^o\right\|^2 + \left\|\mathbf{w}^f\right\|^2} = \frac{2\,(\mathbf{w}^o)^T\,\mathbf{w}^f}{\left\|\mathbf{w}^o\right\|^2 + \left\|\mathbf{w}^f\right\|^2}, \tag{4.4}$$

from which one may see desirable properties such as: $r = \pm 1$ if and only if $\mathbf{w}^o = \pm\mathbf{w}^f$, and $r = 0$ if and only if $\mathbf{w}^o \perp \mathbf{w}^f$ and not both zero. The values of $r(t)$ are calculated at 3-hour intervals using 3-hour timeseries of hourly velocities. The quantities are referred to herein as "correlations" as they have properties similar to those of a correlation coefficient, and correspondingly express fractional values as percentages. Nevertheless, this naming is formally incorrect as $r(t)$ measures coherence among magnitude and direction rather than among second-order moments.

Figures 4.13 and 4.14 show the mean evolution of distance and correlation metrics for drifters deployed on jd225.42 and jd236.71, respectively, of 2012. The former are deployed in the vicinity of Hanna Shoal while the latter are deployed offshore north of the Alaska Coastal Current (*cf.* Figure 4.1). In the region west of Hanna Shoal, simulated drifters in both Case 1 and Case 2 remain closer to the physical data than those of the background model, with Case 1 diverging from the observations at 28% the rate of the background. The improvement in Case 2 is modest compared to Case 1, as it assimilates less voluminous HFR data in the region. Note the periodic oscillations in the graphed distances, which likely result from inertial oscillations in the data. The DAS forecast oscillations are larger than those of the background, especially in Case 1. Small-scale oscillatory behaviour of the DAS forecasts in the region appears to persists until around jd231 when constraint by moorings #25 and #26 begins; conditioning the analysis on these additional data appears to limit the generation of gravity waves and artificial inertial oscillations caused by corrections to surface velocities from assimilated HFR observations. Note that there is a large temporal gap in HFR data during jd220–224.75 (*cf.* Figures 4.7), so both DAS forecasts starting at jd225.25 may still be in the process of adjusting to a relatively large change in model state. With regard to velocity correlation, all simulated solutions rapidly decorrelate in the first 3-hours after deployment reaching to as low as 9% in Case 1. However, the Case 2 and the background reach zero uncorrelated after 11 hours whereas Case 1 maintains positive correlation until around 19 hours. At further times after deployment, correlations in all cases oscillate about zero with amplitudes of about 20%.

Figure 4.14 shows model correspondence with drifters deployed north of the Alaska Coastal Current south of Hanna Shoal. Improvement of DAS solutions over the background model are evident in both plots, with Case 1 again showing advantages over Case 2. Case 1 diverges from the observation 34% more slowly than the background case over the 2-day period following deployment, and 51% more slowly over the first 30 hours. In contrast, the 10% relative divergence rate reduction is a modest 10%. Background, Case 2, and Case 1 solutions remain within 12km (corresponding to the width of one local grid cell) of the observation for approximately 22 hours, 28 hours, and 39 hours, respectively. Distance in Case 1 remains less than half that of the background case for the first 42 hours after deployment. With regard to correlation, the *r*-metric for Case 1 decays linearly from 100% to 50% over the 27 hour period following deployment. In contrast, the background and Case 2 solution drifters show oscillation in their metrics with periods of approximately 5.5 hours; the mean±amplitude for these curves are 41±11% and 54±22% during the first 24 hours. The corresponding lack of oscillation in distances suggests that the background and Case 2 velocities are out of phase with inertial oscillation present in observations while Case 1 velocities are in phase. DAS correlations are stronger here than for the the jd225.41 drifter group, which is owed in part to the regularity of HFR data; the region is closer to the antenna and thus the DASs are better informed by HFR. And while the behavior of the correlation metrics varies between the DAS cases, their strong qualitative similarity is likely due to identically assimilated data from nearby moorings (*cf.* Figure 4.1) combined with a background model that performs moderately well in the region.

The analysis in this section is based on the average of 4–5 drifters deployed *en masse*, and do not reflect tracking of individual drifters. One notes that the physical drifters are tracked in periods when model forcing contains strong and abrupt changes in wind direction, during which the HFR errors in both cases exhibit large intermittent errors (*cf.* wind profiles in Figures 4.7 and 4.8) which may have diminished the tracking performance of surface drifters. Correctly specifying drifter depths should greatly improve the quality of these results, as the comparison here takes place between 1 m observations and 0 m simulations. Such improvement would apply in both background model and DAS cases, with stronger improvements expected in the latter where assimilated HFR more appropriately reflects 1 m velocities (*i.e.* those actually influencing the drifter) than the 0 m surface velocities assumed here. Further, the excluded 10m-drogued observations are likely to have less noise and longer-scale spatiotemporal variability, which suggests they may be better represented by coarse model representatives than drifters nearer the surface. Properly tracking depths of the 1 m and 10 m drifters awaits future DAS runs, as the approximate streamline tracking is not achievable by post-processing.

4.4.4 Comparison to external CTD data

While velocity and circulation and their relation to assimilated data are of specific interest, it is worthwhile to consider the quality of other hydro-dynamical circulation aspects within the model. A collection of ~250 conductivity-temperature-depth (CTD) instrument casts taken during 2012 surveys of the eastern Chukchi Sea provides a dataset of temperature and salinity (T/S) observations for further testing. All considered observational profiles are contained within the 12km-resolution model subdomain; spatiotemporal locations of the data, which were acquired internally from University of Alaska Fairbanks Institute of Marine Science, are hidden for brevity. The T/S observations are interpolated to ROMS σ-coordinates via cubic splines for comparison to background and DAS model representatives. Figure 4.15 exemplifies CTD-observed temperature and its associated cubic interpolant which poorly-resolves its thermocline; similar problems exist in representation of salinity observations. Some inherent errors are thus expected, particularly in the area of the pycnocline.

Figure 4.16 plots the CTD T/S observation representatives and relative differences of the background, Case 1, and Case 2 forecast models. Without respect to geolocation, the chronology of CTD observations shows a general trend toward surface cooling and freshening between jd230 and jd270. Cases 1 and 2 show differences from CTD representatives which look very similar to the background model errors.

Unfortunately, the scale and structure of T/S errors in the background model dominates the errors of Case 1 and Case 2. Within all models, differences from CTD observations increase in time, with profiles progressing toward vertically uniform T/S distributions. Figure 4.17 shows T/S profiles from observations and models 40 days apart to illustrate this problem. Correction of this behavior was attempted by changing vertical mixing/closure options (from the Mellor-Yamada 2.5-layer scheme to K-profile parametrization or generic length-scale mixing) with a variety of different T/S mixing options. However, none of these alternatives gave rise to significantly improved vertical T/S distribution.

A more in-depth diagnosis is warranted; three appropriate places to begin investigation are the external HYCOM used for initial/boundary data, the vertical coordinate distribution selected in the model, and the evolution of vertical structure at the point of Bering Strait inflow. Cursory topical analysis shows that modeled Bering Strait inflow T/S is unstratified, whereas the HYCOM initialization data resolves a surface freshwater layer several meters thick. The loss of a surface freshwater layer in the model may further reflect the omission of significant freshwater sources, such as the Yukon River discharge averaging ~0.1 Sv in modeled months per USGS monthly flow rates at Pilot Station, AK. However, this volume is insufficient to balance the model volume BS flow. The strengthening warm bias of modeled temperature profiles compared to CTD is also noted, but its cause is not speculatively diagnosed here in the absence of further experimentation. Such errors and shortcomings of the background model reflect strong systematic biases [*Dee and Da Silva*, 1998; *Chepurin et al.*, 2005; *Dee*, 2005], and cannot be corrected by traditional assimilation of T/S data which only serve as model constraints. Improvement of the background model to include meteorologic freshwater sources and preserve vertical stratification over the Chukchi Shelf is obviously necessary.

4.4.5 (Failed) Transport Estimates of Summers 2012–2014

Figure 4.18 identifies a set of model transects defined for posterior estimation transport of volume, heat, and freshwater. Each transect is oriented with a northernmost initial point and leftward-normal orientation as the transect is traversed. Each normal direction is thus defined with a positive eastward component. Note that the northern Central Channel (CCn) is oriented with the positive side pointing into the region bounded by transects and the coast.

Across each defined transect, vertically-integrated estimates of volume flux (V'), freshwater volume flux (V'_{FW}), and heat flux (Q') can be calculated from the respective equations:

$$V'(t,l) = \int_{-h}^{0} u_{\perp}\, dz, \tag{4.5}$$

$$V'_{FW}(t,l) = \int_{-h}^{0} \frac{\rho}{\rho_{FW}} \left(1 - \frac{S}{S_{ref}}\right) u_{\perp}\, dz, \qquad \text{and} \tag{4.6}$$

$$Q'(t,l) = \int_{-h}^{0} C_s\, \rho \left[\theta - \theta_{ref}\right] u_{\perp}(x,y,z)\, dz \tag{4.7}$$

where $u_{\perp}$ is the velocity component normal to the transect, ρ_{FW} is the density of fresh-water, C_s is the state-dependent seawater heat capacity, θ is potential temperature, and S_{ref} and θ_{ref} are adopted reference values (*e.g.*, 34.8 PSU and -1.9°C are common). Integrals of the fluxes along the length of transect give the associated total transports V, V_{FW}, and Q.

The gross inaccuracy and unrealistic behaviour of T/S in all models disparages their use in calculating Q' and V'_{FW}. Nevertheless, the assimilative model discussed previously demonstrates sufficient coherence with velocity observations and regional dynamics to estimate mass transport. Mass transports are estimated using 24-hour forecast records of velocity data, computed from mean velocities calculated during the DAS forecast step.

Inflow Sources Long Strait (LS) flow is directly related to HYCOM boundary data from HYCOM, with seasonal transport estimates of 5.7 mSv, 5.5 mSv, and 6.9 mSv for the modeled years excluding the anomalous inflow events centered around 2012-223 and 2012-292 outflow event 2014-297. Net eastward transport of those years roughly agrees with estimates calculated using results of *Francis et al.* [2017].

Regional circulation dependence on Bering Strait (BS) transport is well established [*Danielson et al.*, 2014; *Weingartner et al.*, 2017b]. Recent observational studies of moored ADCP find BS inflow near or above 1.0 Sv in the months of August–October during the modeled years [*Woodgate et al.*, 2015; *Woodgate*, 2018]. However, modeled BS quantities are far lower and typically in the range of 0.45–0.65 Sv. The only months which show near agreement are September and October of 2012, where model (observed) transports are 0.5 Sv (0.43 Sv) and 0.41 Sv (0.49 Sv), respectfully. (The BS flow reversal around 2012-298 caused by the anomalously strong inflow pulse from the ESS is omitted from October 2012 estimation.) Model results from 2013 are dubious, with vertically-averaged model northward flow through BS in 2013 of approximately 0.25 m/s with standard deviations 0.07 m/s. In other years, the rates generally decreases from 0.6 m/s to 0.4 m/s over jd214–300 with deviations about that trend of 0.05 m/s. Current meter estimates from *Woodgate et al.* [2015]; *Woodgate* [2018] show that realistic flow rates should be roughly twice these values, with model 2013 BS transport underestimated by ~75%. These errors, which are determined by the background model and only slightly influenced by the DAS, could not be corrected by adjusting some model parameters throughout the domain. For example, experiments with the background model showed: decreasing the viscosity from 12 m^2/s to 1.2 m^2/s yielded only a 5% increase in BS flow rate. As previously noted, riverine water sources are ignored but are insufficient to account for the BS flow deficit in the model. The poor transport resolution through BS profoundly impacts the modeled transports throughout the domain.

Subregional balance estimates A consistency check of the model transport estimates shows that the primary CS inflow and outflows are in approximate balance. This is justified by comparing the sum of incoming water from the Long Strait and Bering Strait and the outgoing water across the Barrow Canyon. The seasonal mean differences between these quantities for 2012–2014 are -0.036 Sv, -0.012 Sv, and -0.023 Sv, respectively. These estimates omit a low-volume source north of Wrangell Island and outflow along shelfbreak current which bypasses Barrow Canyon. An estimate of the latter during 2009–2011 by *Brugler et al.* [2014] is about 0.02–0.04 Sv, which agrees with the missing component of the budget.

In 2012 and 2014, flow across the southern Central Channel transect is slightly greater than the concurrent Bering Strait transport of ~0.6 Sv. This suggest that the Siberian Shelf flow volume directed though the southern CCs transect slightly exceeds (by ~0.005 Sv) any BS transport flowing northward through Herald Canyon.

The polyline transect composed of the Central Channel (CCn,CCs) transects together with the western transect of the Alaska Coastal Current (ACCw) forms a closed region bounded by the Alaska coast. Forecast transports across the boundaries show an approximate closure, with outflow of through CCs and ACCw accounting for about 97% of the ACCs inflow across all three years. This error results from a combination of excluded shallow coastal flow, numerical errors in collocating C-grid velocities and bathymetry, and failure to account for changes in free surface. Regional transport distribution in 2012 and 2014 is similar, with northward transport across CCn measuring 16.9% and 16.8%, respectively, of the incoming flow measured across CCs. The remaining portions, calculated at 80.5% and 83.1% respectively, exit the region eastward through ACCw, with standard deviations of about 2%. In 2013, model BS throughout the season is approximately 0.24 Sv less than the 2012/2014 mean. Consequently CCs inflow is reduced, and the CCn mean outflow is only 12.5% of the CCs with 82.6% leaving through ACCw. Local wind forcing does not appear to play a significant role in regulating this balance; correlation coefficients calculated for variations in transport against wind components normal to transects with a 0.5day lag are uniformly less than 10%.

DAS transport estimates through BC are expected to be inaccurate due to poorly represented BS flow in the background model. Respective 2012–4 seasonal mean flows in the DAS analysis are 1.2 Sv, 0.31 Sv, and 0.94 Sv. Ignoring 2013, these contrast with the accurate observational estimates in the 0.45 Sv range for the head of BC [*Weingartner et al.*, 2017b] and better align with estimates late-summer flow at the mouth of BC [*Itoh et al.*, 2013]. Up-canyon transport events occurs only in 2013, despite the observational expectation of ~-0.1 Sv in the latter half of each modeled season [*Weingartner et al.*, 2017b]. Two plausible reasons for this inconsistent behavior involve the model and the DAS itself, beyond those induced by BS underestimation. First, the 12 km model resolution may be insufficient to fully resolve the flow dynamics of the ACC; *Okkonen et al.* [2009] found that a 9km resolution of the ACC was insufficient for simulating the BC regional flow. Second, low BS inflow causes an overall reduction velocities in region where the DAS analysis localized. The data-optimized solution attempts to match data that reflects larger observed velocity components, so that latent bias-adjustment (artificially) increases flow in the ACC and consequently through BC. This latter point underscores the need for BS inflow to be accurately supplied or resolved for regional analysis.

4.5 Remarks and Summary

The work focuses on the development of a DAS for assimilating HFR and ADCP data in the Chukchi Sea. The system consists of an ice-free ROMS model enveloped by a modified ensemble filter. The implemented method is based on MLEF, which variationally identifies the optimal analysis as the maximum *a posteriori* estimate, modified to assimilate timeseries or synchronous representatives rather than observations directly derived from the analysis-time model state. The resulting asynchronous variational ensemble filter is a sequential approximation to the 4DVar method for observations such as HFR surface currents which are known to be non-Gaussian and for which algebraic Kalman-type filters may be ill-suited.

The study compares a pair of DAS results which differed only in treatment of HFR data; Case 1 treated HFR observations over the forecast period asynchronously as a vectorized historical timeseries while Case 2 treated them as a synchronous average observation. Both methods rely on the history of observations and ensemble of observed model counterparts, unlike the traditional filter methods which consider only data at the time of analysis. ADCP data were consistently assimilated as timeseries in both cases. The results were then compared to available 2012 data to assess the quality of improvement, and to diagnose failures. The findings support that the analysis resulting from fully-asynchronous filtering surpasses that of the averaged case. Both cases improve upon the forecast quality of the background model and unpresented early cases which assimilated data using the classical (instantaneous) approach, which ignores 5/6 of surface observations when a 6-hour forecast/analysis cycle is used.

Compared to ingested 2012 data, the asynchronous approach to assimilation was shown to have advantages over the averaged approach. In particular, assimilated HFR timeseries yielded a stronger reduction in forecast-minus-observation errors compared to the background model background than averaged HFR. Significantly, asynchronous assimilation of HFR improved the Case 1 analysis fit with ADCP observations by 12% more than Case 2 relative to the background model errors. The direct comparison of ADCP errors (co-relative to associated errors in the common background model) shows that the assimilation of HFR timeseries has the effect of simultaneously improving overall fit to ADCP observations and HFR observations despite the larger relative weight given to HFR observations in Case 2. On this point, it is noted that increasing model spatial resolution is an alternate method of naturally changing the balance between the number of HFR and ADCP observations; the former increases with lateral model resolution whereas the latter does not.

The scale of overall error improvement is difficult to quantify consistently due to temporal irregularity of regional dynamics and volume of available data, and also because of the flow-dependent nature of sequential filtering. However, the magnitude of difference between case-wise DAS improvements is generally greatest during times when local winds oppose the prevailing background flow or contain a strong onshore component (*cf.* jd240–260 and jd280–290 of Figures 4.7 and 4.8). Averaged over these intervals, Case 1 errors for HFR (ADCP) are 14% (16%) lower than those of Case 2.

The quality of fit to observation was shown to vary with wind regime, with Case 1 more advantageous when strong winds induced vertically-sheared flow against the background flow. Strong optimization constraint imposed on the filter by onshore, cross-isobath HFR observations unresolved by the model (and thus the observed ensemble variations) under eastward blowing winds is implicated in the observed degradation of model-observation fidelity for Case 1 during such events. However, the spatiotemporal distribution of winds in recent years suggests that local summertime forcing is predominantly shear-inducing, and suggests that the asynchronous treatment of observations is appropriately suited to the region.

Unassimilated Lagrangian drifter observations provided an external reference for comparing the DAS forecasts. For drifters released offshore, the case with fully asynchronous assimilation diverge from observed data 34% slower than the background model, compared with a more modest ~10% reduction in rate when ingesting averaged HFR. Case 1 drifter position remained within 12km (1 grid-width) of observations for an additional 13 hours with positive velocity correlation for an additional 8 hours, while the corresponding improvements in Case 2 were 1 hour and 0 hours, respectively. Results for drifters released nearer to the coast were similar, with the interesting result that Case 1 velocity correlation tended to decay linearly (at a rate of ~2.1%/hr) for the first day rather than oscillating. This trajectory correspondence between DAS forecast and unassimilated drifter data supports the use of asynchronous filtering for ongoing regional application.

An alternate scheme for applying the presented asynchronous ensemble-transform DA involves optimizing the *initial* model state rather than the forecast state. In this approach, the optimal ensemble-expansion coefficient vector (w^* in Section 4.3) may be used to define an optimized initial condition for each model integration step, with the analysis state defined by the integrated optimum. The resulting trajectory would have improved fit to the data on which it is conditioned. Additionally, the states generated in this way will be fully model-constrained as in the strong 4DVar method. This contrasts the presented method in which linear combinations of constrained states are not guaranteed to satisfy nonlinear primitive equations. The initial state in this case would be conditioned on data at future times, and it would more properly be considered a smoother rather than a filter. The implementation would require only minor modifications of the current DAS, although it would double the total model integration time as each model instance is propagated twice between each analysis cycle. Work in this direction is ongoing.

As metrics for the DAS effectiveness in 2012, the work compared DAS forecast quantities with those of a background model which assimilates no data. The DAS configuration of Case 1 was found to strongly improve the quality of fit to observations, and it was applied to equally configured ROMS models of 2013 and 2014. Poor background model dynamics were evident, especially with respect to T/S distributions and mass/volume transport estimates which clearly do not correspond with observations beyond the analysis subregion. The employed model inaccurately resolves Bering Strait inflow in terms of both volume transport and vertical freshwater distribution. Crucially, the model omits the Yukon River, which is a significant contributor to both. These background model failures must be corrected when considering a region which hosts a confluence of waters climatically important for the Pacific sector of the AO, and preclude the inclusion of sea ice for extending the modelable season.

The systematic problems with the model affect both the background model and model component of the DAS equally. This justifies the approach taken in this work, which compares different DAS outputs in relation to a common background model. A more properly configured model would obviously produce a more accurate background trajectory. It would would also serve as a better basis for assimilation schemes, such as those explored here, which are primarily developed to constrain and refine model states via temporally-independent corrections rather than overcome persistent model bias [*Dee and Da Silva*, 1998; *Dee*, 2005]. However, the variational formulation of MLEF permits inherent correction of the bias component in the span of $\mathbf{P}^{1/2}$, which implies that a bias-aware version of the algorithm must account for this component. Specifically, the bias-adjustment methods of *Dee* [2005] are formulated for KF-type methods which define the forecast as the ensemble mean, and adjust that forecast based on a non-zero of mean of the posterior innovation (*i.e.* mean(d^a)) computed prior to the forecast step. Further experimentation is necessary to implement such a correction in variational form for MLEF, which requires a different relationship between the forecast state and ensemble perturbations. Bias-aware modification to the DA component cannot, however, correct model deficiencies originating outside of the analysis region, such as the poorly modeled BS flow.

Ensemble filtering offers a forward-model only method of assimilation which easily scales as computer resources become available, making them more practical than than strong-constraint variational methods for operational forecasting. As HFR surface observations are known to be non-Gaussian, a mode-tracking objective for optimization should thus be be sought. The variational ensemble filter implemented here satisfies both of these requirements, and is tested in its capacity to resolve surface currents in the Chukchi Sea region by assimilating real data in two ways. The quality of coherence between DAS surface forecast and various forms of velocity data presented indicate the strong candidacy of an asynchronous variational ensemble filter for regional application when timeliness of analysis is crucial, such as the monitoring of surface contamination by shipborne heavy fuel oil or other spills.

Acknowledgements
The author thanks: R. Potter, E. Dobbins, and H. Statscewich of the University of Alaska Institute of Marine Science for their roles in collecting and pre-processing observational data; D. Nechaev of the University of Southern Mississippi Department of Marine Science at NASA Stennis Space Center for partial support in early stages of this work; and K. Ide and B. Hunt at the University of Maryland for their roles in organizing and leading the 2013 *Data Assimilation in Geophysics* instructional workshop.

Table 4.1. Moored ADCP information. The table shows the internal mooring reference number, name in previous studies, geographical location, and deployment/retrieval dates. The names corresponds to Barrow Canyon (BC), Hanna Shoal Northeast/Northwest (HS-NE/NW) in *Weingartner et al.* [2017a], and East and West Barrow Canyon (EBC, WBC). The dates are rounded to the first analysis time with a complete 6-hour record, and date specified as '-' indicates data through 2014-310.

ID	*Name*	*Lat.*(°N)	*Lon.*(°E)	*Start*	*End*
Mooring 13	BC2	70.92	200.06	2012-255.50	-
Mooring 16	CS_1 #01	72.26	201.93	2013-290.50	-
Mooring 17	CS_2 #02	72.30	202.27	2013-287.50	-
Mooring 18	CS_3 #03	72.34	202.55	2013-287.75	-
Mooring 19	CS_4 #04	72.39	202.85	2013-287.75	-
Mooring 20	CS_5 #05	72.43	203.16	2013-287.75	-
Mooring 21	FM_1 #06	72.26	201.96	2013-300.75	-
Mooring 22	HS-NE_40m	72.12	199.50	2012-236.25	-
Mooring 23	HS-NE_50m	72.16	200.88	2012-236.50	-
Mooring 24	HS-NE_60m	72.18	201.45	2012-236.75	-
Mooring 25	HS-NW_40m	72.28	196.47	2012-231.50	-
Mooring 26	HS-NW_50m	72.53	195.90	2012-231.25	-
Mooring 27	HS-NE_40m	72.12	199.51	2013-254.00	-
Mooring 28	HS-NE_50m	72.16	200.88	2013-254.00	-
Mooring 29	HS-NE_60m	72.18	201.45	2013-253.75	-
Mooring 30	HS-NW_40m	72.28	196.47	2013-254.75	-
Mooring 31	HS-NW_50m	72.53	195.90	2013-254.75	-
Mooring 34	EBC	71.38	203.12	2011-233.75	2012-245.50
Mooring 36	WBC	71.57	202.30	2012-286.75	2013-248.75

Table 4.2. Drifter Information. The table shows the internal drifter reference number, name in previous studies, geographical location, and deployment/termination date. Drifter IDs identify the deployment locations for paths shown in in Figure 4.1. The names corresponds to the corresponding public data records, available and visualizable at research.cfos.uaf.edu/chukchi-beaufort/data/drifters/ under heading "BOEM 13-August-2012".

ID	*Name*	*Lat.*(°N)	*Lon.*(°E)	*Start*	*End*
72	UAFSFOS-MS-0001	71.628	195.277	2012-225.42	2012-284.54
73	UAFSFOS-MS-0003	71.570	199.303	2012-236.71	2012-261.08
74	UAFSFOS-MS-0004	71.627	195.290	2012-225.42	2012-296.12
75	UAFSFOS-MS-0005	71.628	195.280	2012-225.42	2012-296.54
76	UAFSFOS-MS-0006	71.628	195.280	2012-225.42	2012-285.67
77	UAFSFOS-MS-0007	71.626	195.290	2012-225.42	2012-285.88
78	UAFSFOS-MS-0008	71.568	199.301	2012-236.71	2012-250.33
79	UAFSFOS-MS-0009	71.628	195.284	2012-225.42	2012-259.83
80	UAFSFOS-MS-0011	71.569	199.302	2012-236.71	2012-290.00
81	UAFSFOS-MS-0012	71.569	199.304	2012-236.71	2012-278.62
82	UAFSFOS-SVP-0001	71.568	199.296	2012-236.71	2012-319.17
83	UAFSFOS-SVP-0002	71.634	195.255	2012-225.42	2012-317.04
84	UAFSFOS-SVP-0003	71.634	195.264	2012-225.42	2012-311.29
85	UAFSFOS-SVP-0004	71.570	199.296	2012-236.71	2013-041.83
86	UAFSFOS-SVP-0005	71.635	195.262	2012-225.42	2013-041.83
87	UAFSFOS-SVP-0006	71.634	195.255	2012-225.42	2013-041.83
88	UAFSFOS-SVP-0007	71.572	199.288	2012-236.71	2013-012.08
89	UAFSFOS-SVP-0008	71.629	195.259	2012-225.42	2012-332.67
90	UAFSFOS-SVP-0009	71.573	199.296	2012-236.71	2012-255.62
91	UAFSFOS-SVP-0010	71.634	195.261	2012-225.42	2012-330.71
92	UAFSFOS-SVP-0011	71.571	199.287	2012-236.71	2013-041.83
93	UAFSFOS-SVP-0012	71.577	199.283	2012-236.71	2013-007.88

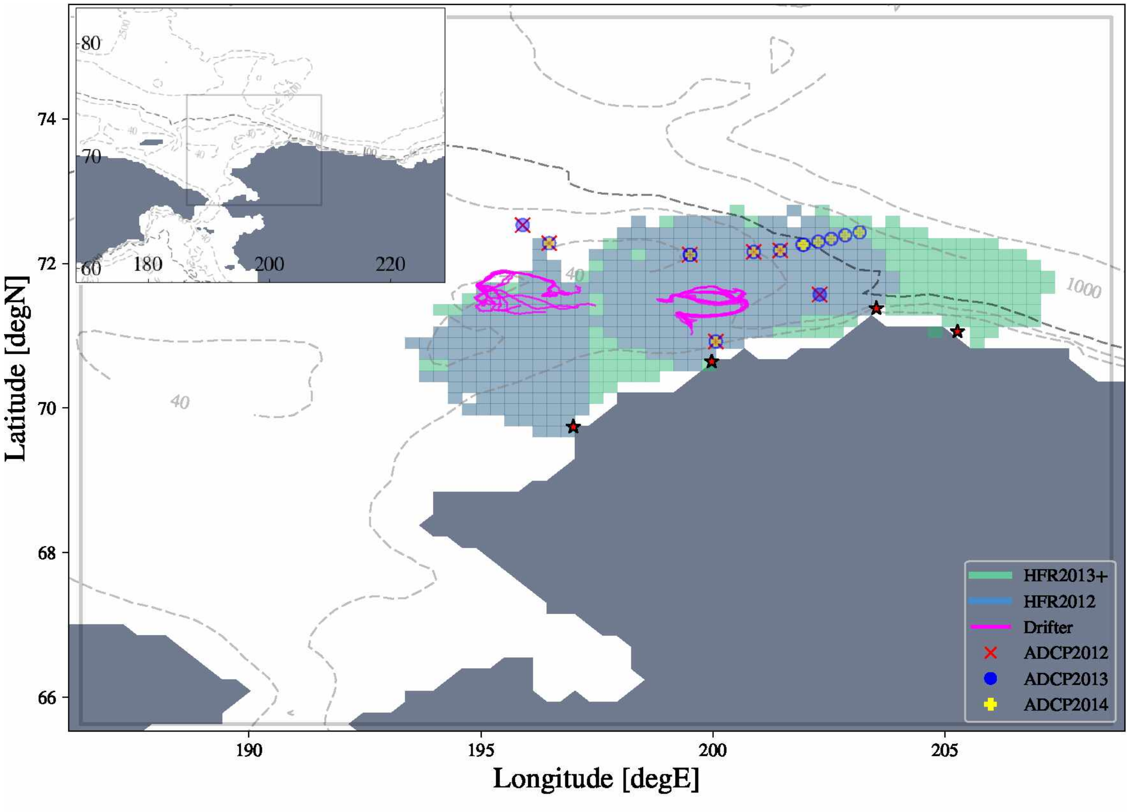

Figure 4.1. Chukchi domain and observations for 2012–2014 shown focused on subregion resolved at approximately 12km bordered in light grey line; the inset image shows the entire domain. Stars identify approximate locations of HFR antennae.

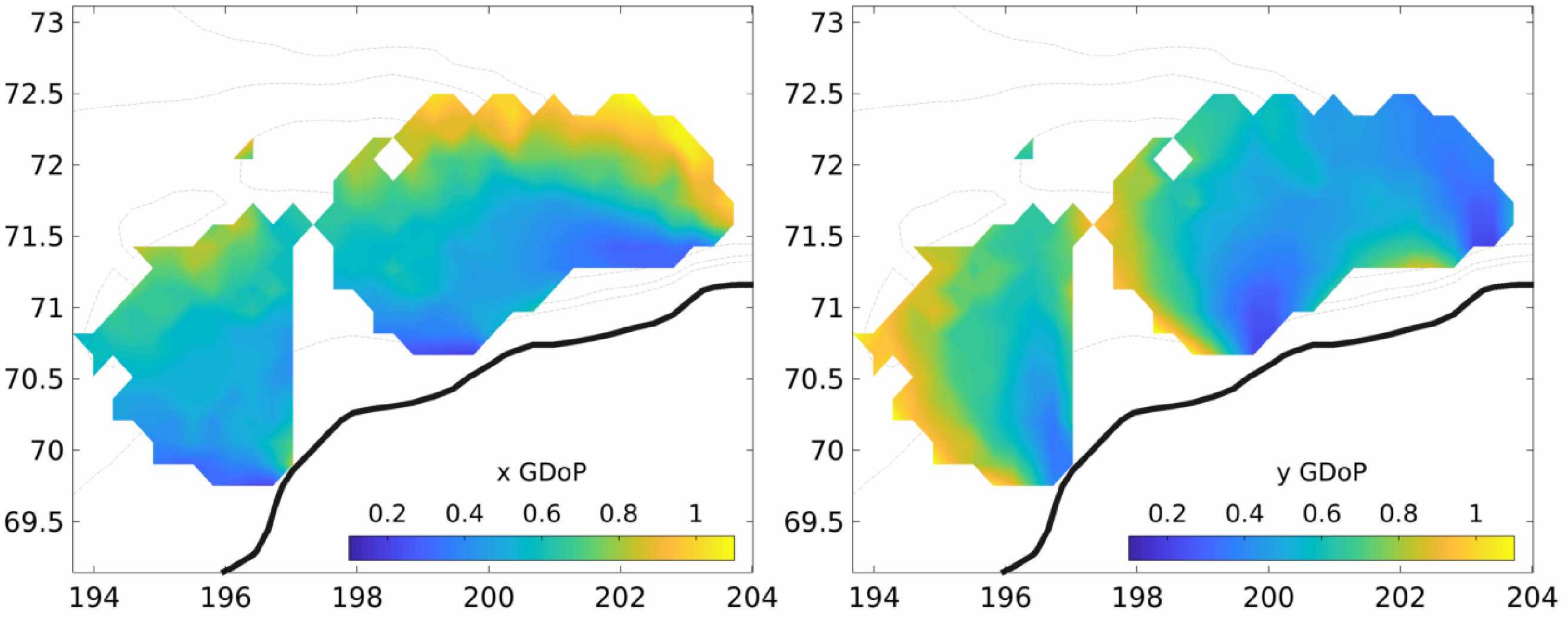

Figure 4.2. Temporally averaged HFR GDOP fields. Temporally averaged HFR GDOP fields are shown to illustrate the scaling applied to σ_h to generate the pointwise values in error covariance matrix factor $\mathbf{R}^{1/2}$.

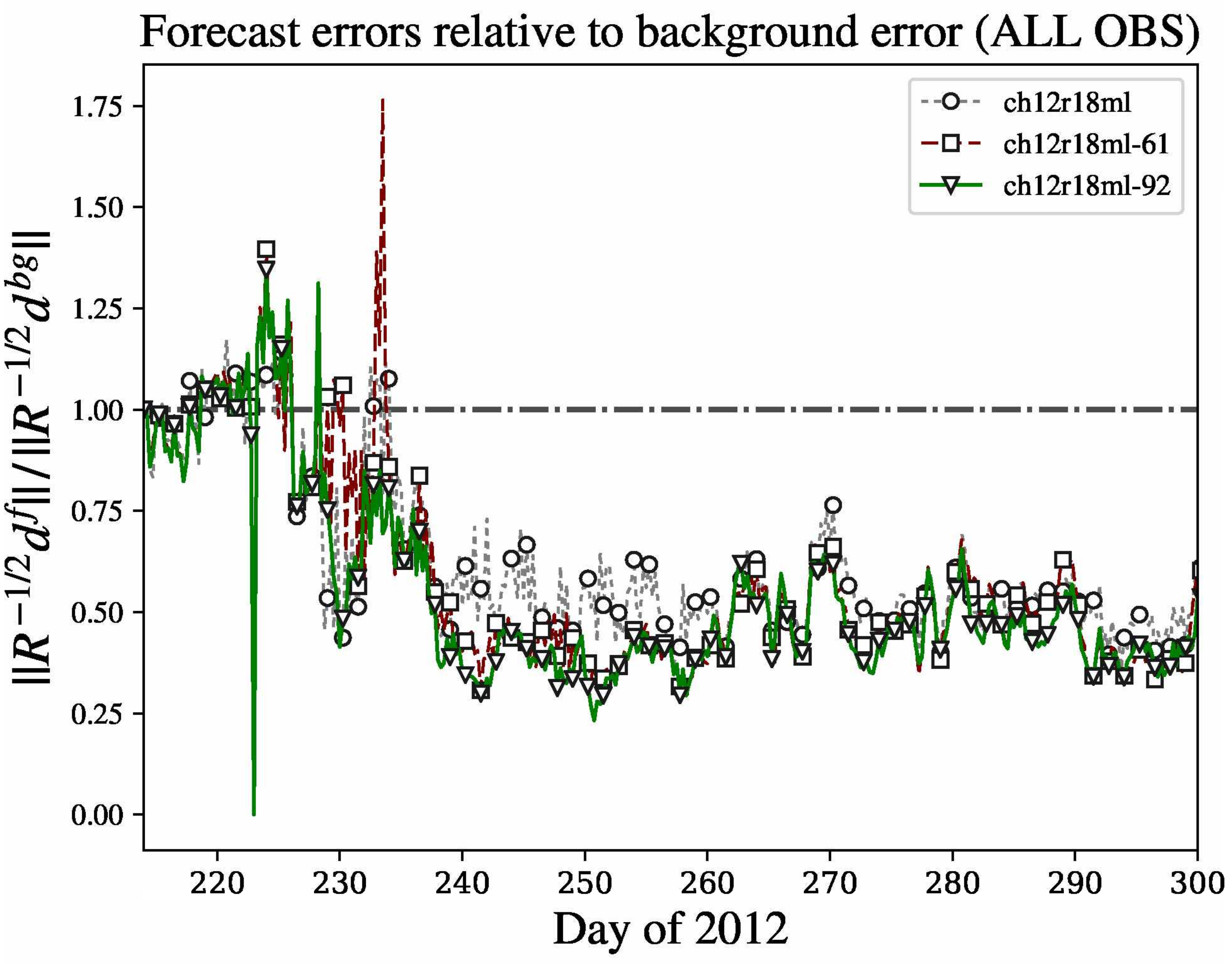

Figure 4.3. Forecast-minus-observation relative differences for different ensemble size. Varying ensemble-size forecast model errors $\left\|\mathbf{R}^{-1/2}d^f\right\|$ relative to the background for all observations. The horizontal grey line indicates the covariance-weighted background innovation norm errors $\left\|\mathbf{R}^{-1/2}d^{bg}\right\|$ used as a reference. The 30, 61, and 92 element filters are indicated by lines with circle, square, and triangle markers, respectively.

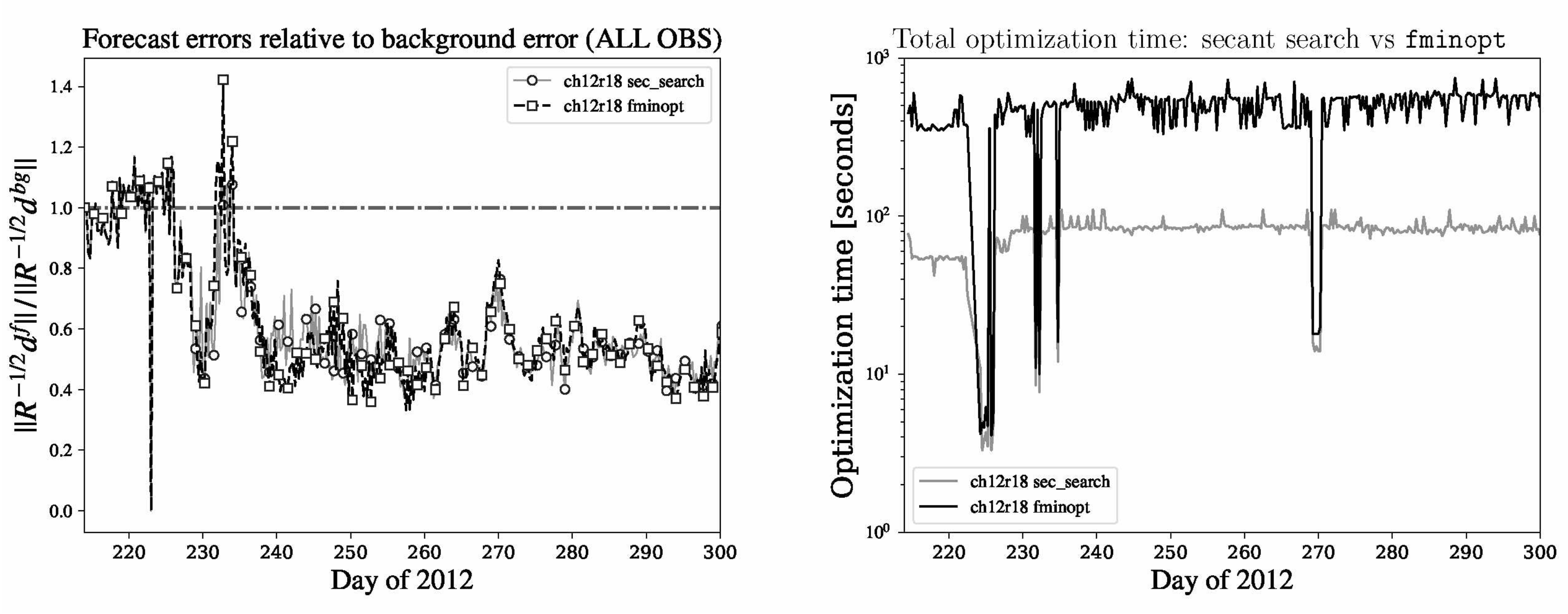

Figure 4.4. Efficiency of optimization schemes. Time series of relative errors (left) and computation time for optimization (right) via secant-search and "fminopt" algorithms. The right plot suggests that the custom optimization code finds the same optima as the proprietary optimization routine, but does so approximately one order of magnitude (~6.5 times) faster.

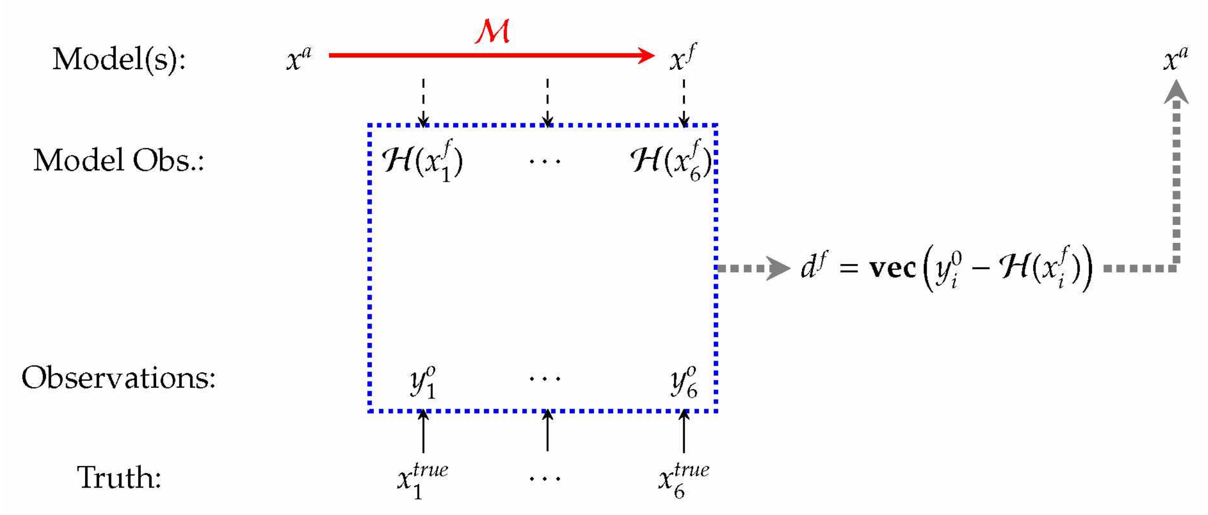

Figure 4.5. “Asynchronous” Assimilation Process. The conceptual relationship between the true ocean, observational data, modeled data, and model states is shown. The red arrow and application of the nonlinear model comprise the forecast stage. The analysis update uses the comparison of observations shown in the blue box. In the asynchronous case, observations at various times during the forecast stage inform the analysis.

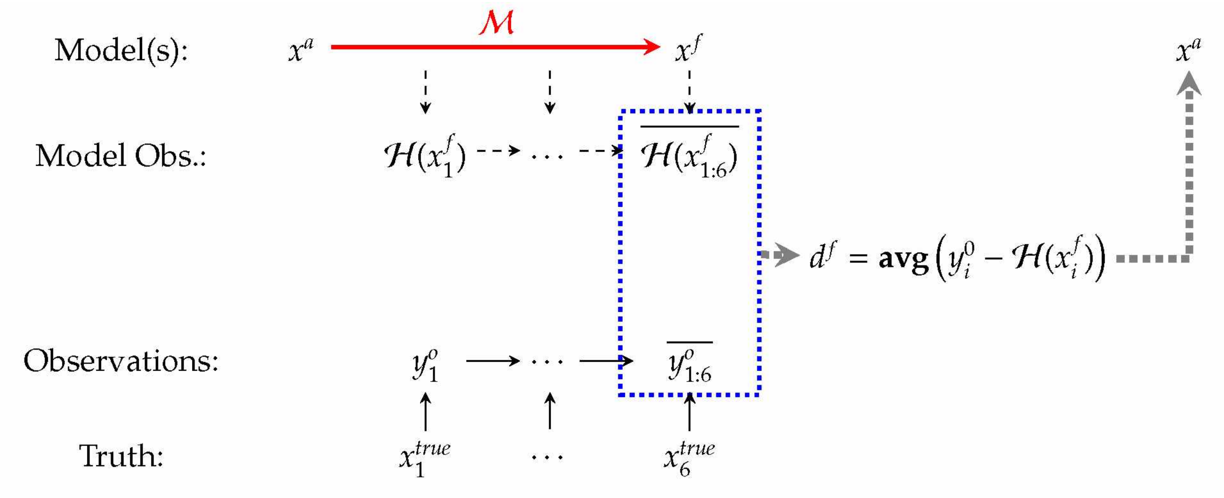

Figure 4.6. "Synchronous" Assimilation Process. The conceptual relationship between the true ocean, observational data, modeled data, and model states is shown for one case of synchronous observations. In this synchronous case method, observations are represented by averaging HFR over the forecast stage.

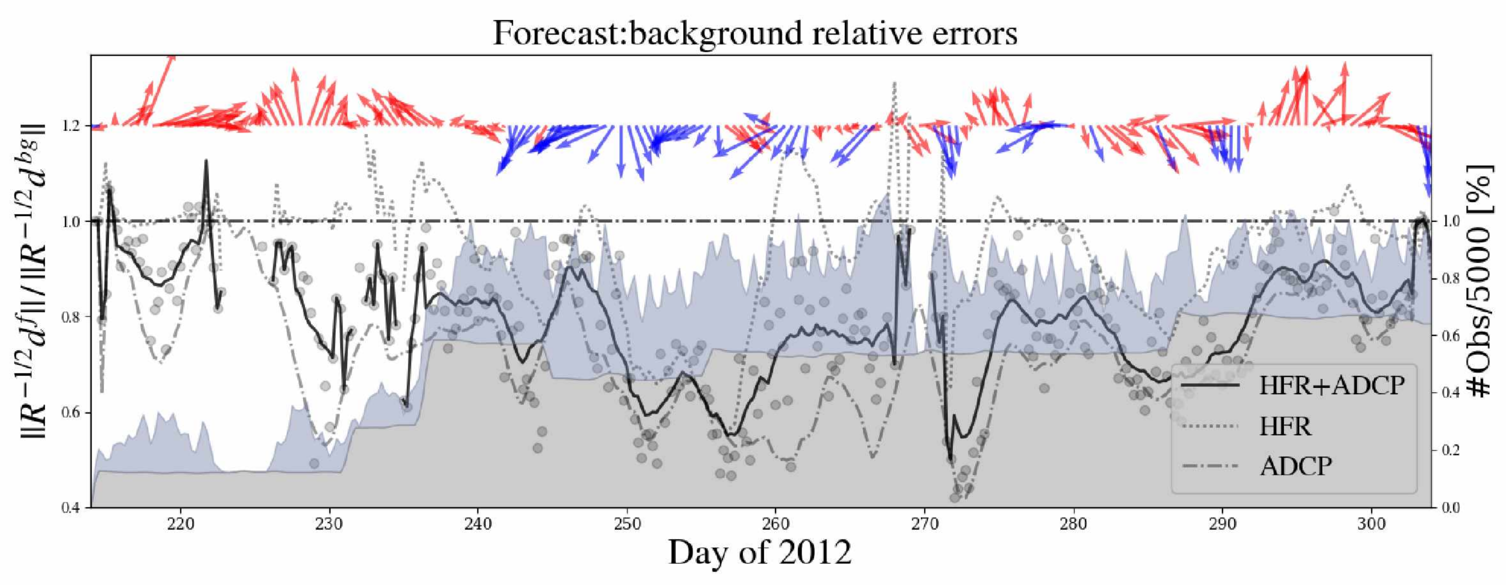

Figure 4.7. Relative Error Reduction for the 2012 Asynchronous Case. Forecast errors during summer months of 2012 are shown for the case of asynchronously assimilated HFR data. Values are smoothed over 48-hour periods and normalized against the corresponding errors in the background model indicated by the unit horizontal line. Solid black, dotted grey, and dashed grey lines correspond to normalized error values of all observations, HFR observations, and ADCP observations respectively. Pointwise values of total error are shown by grey circles. The local wind forcing vectors in the region are shown at the top of the plot, and assimilated HFR (ADCP) data volume data is shown shaded in blue-gray (beige) for reference. Blue wind vectors denote wind with magnitude greater than 5 m/s and blowing toward 225 ± 60° (measured counterclockwise from east).

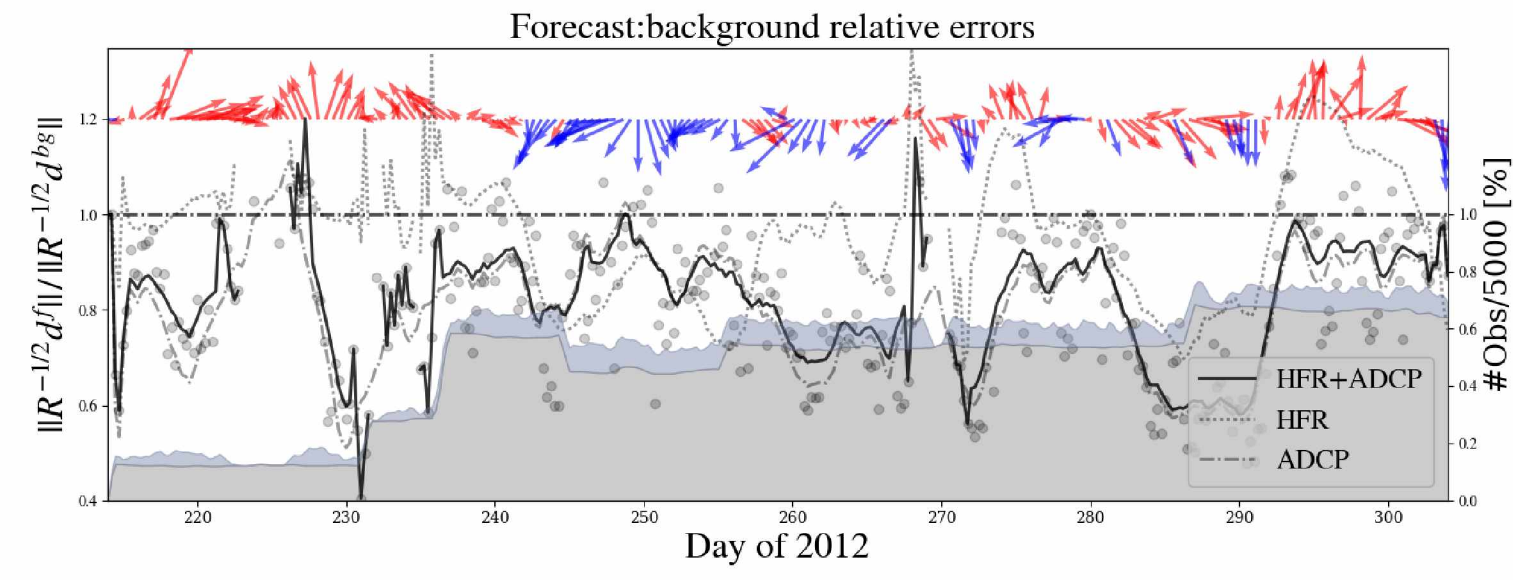

Figure 4.8. Relative Error Reduction for the 2012 Synchronous Case. Forecast errors for the case of averaged HFR assimilation. Figure layout follows that of Figure 4.7 and shows results of Case 2 which assimilates mean HFR data.

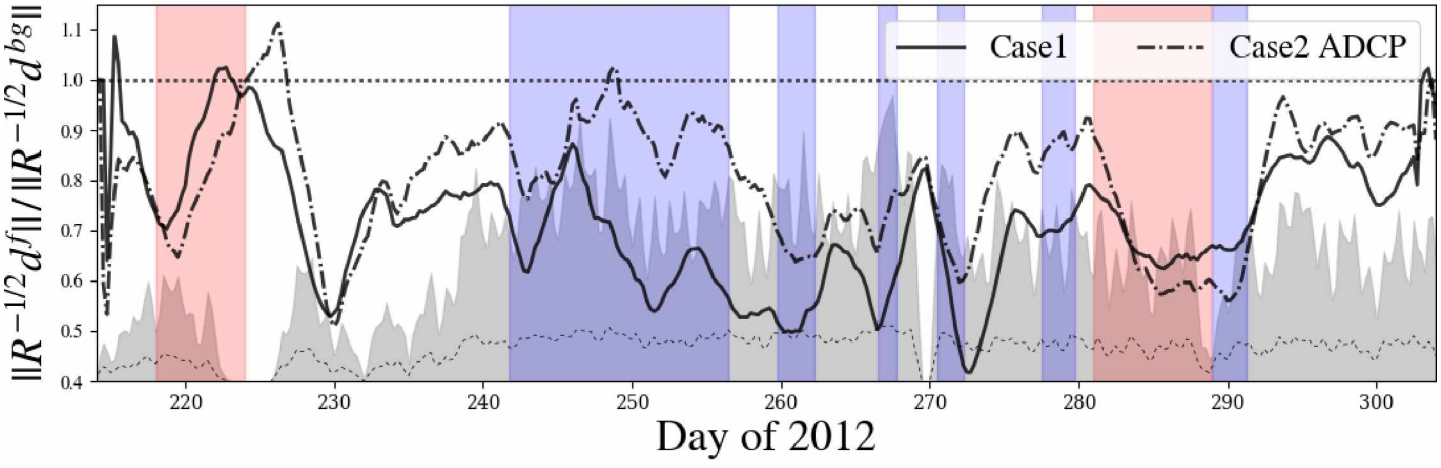

Figure 4.9. ADCP errors with Identified Wind Regime. The figure shows relative ADCP errors with the solid (dot-dash) line showing Case 1 (Case 2). Normalization with with respect to background errors, as in previous plots. Blue and red regions identify times with "opposing" and "supporting" winds, respectively, as described in the text. The volume of HFR observations for Case 1 is shown in the grey background for reference, with the low, dotted line indicating the volume of averaged HFR observations.

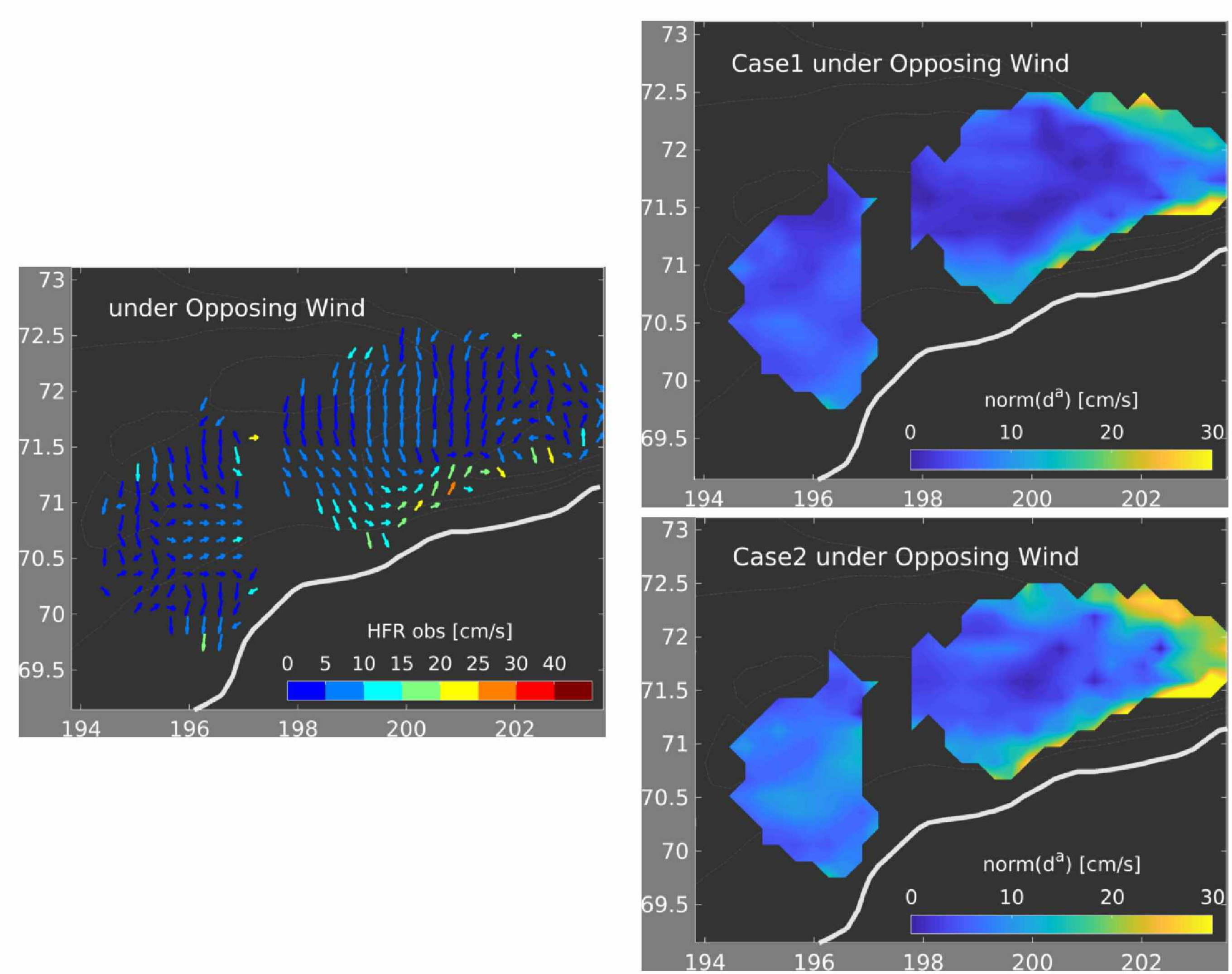

Figure 4.10. Mean HFR Observations and Analysis Errors under Opposing Winds. Arrows indicate the temporally-averaged HFR observations during opposing wind events in the left panel, with colors indicating magnitude. The corresponding averaged errors for Case 1 and Case 2 are shown in the upper right and lower right panels, respectively. The heavy white line identifies the approximate Alaska coast from the model 3 m bathymetry. Dotted contours identify the 50, 50, and 70 m model isobaths.

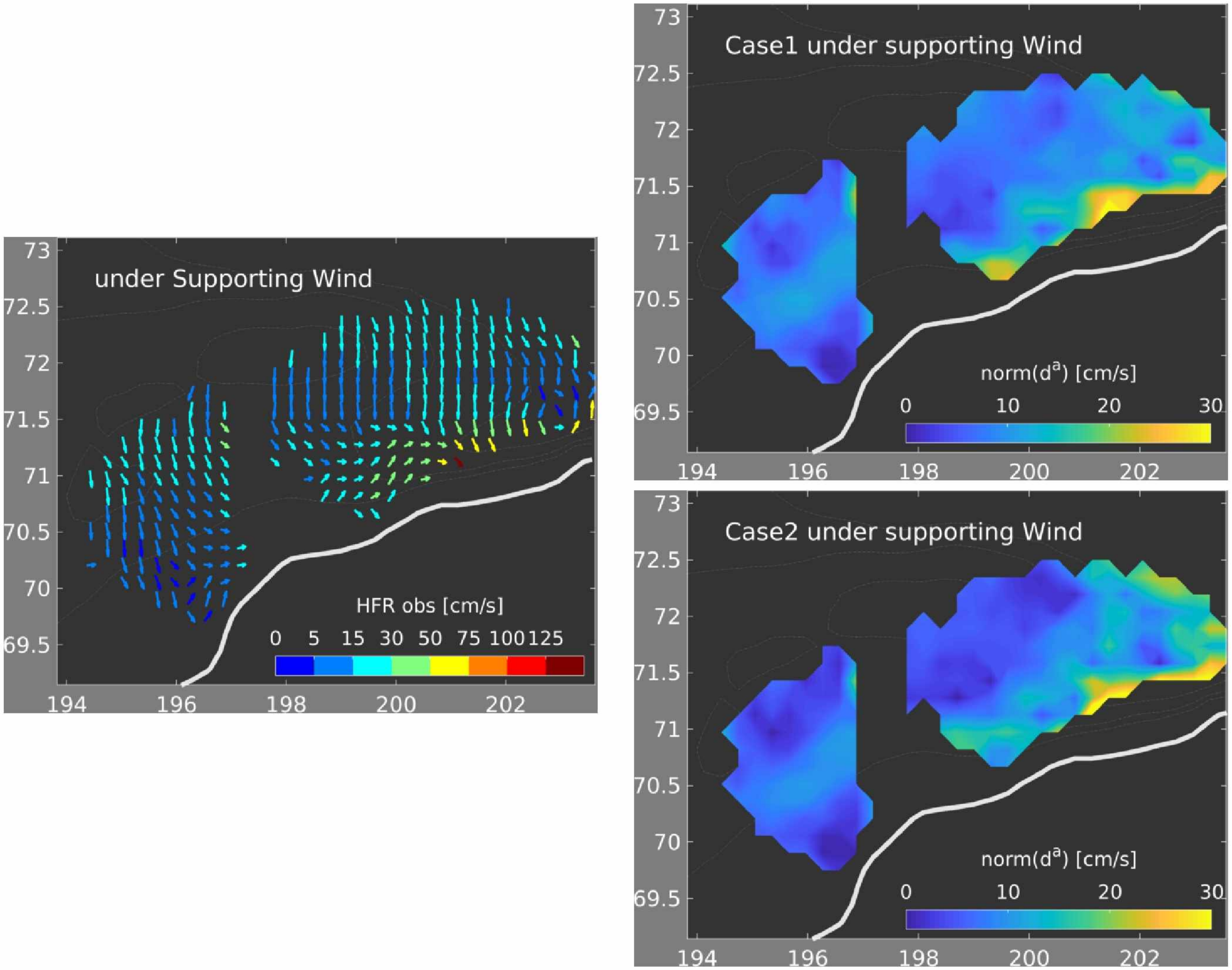

Figure 4.11. Mean HFR Observations and Analysis Errors under Supporting Winds. The plot layout is identical to that of Figure 4.10, only for supporting wind events.

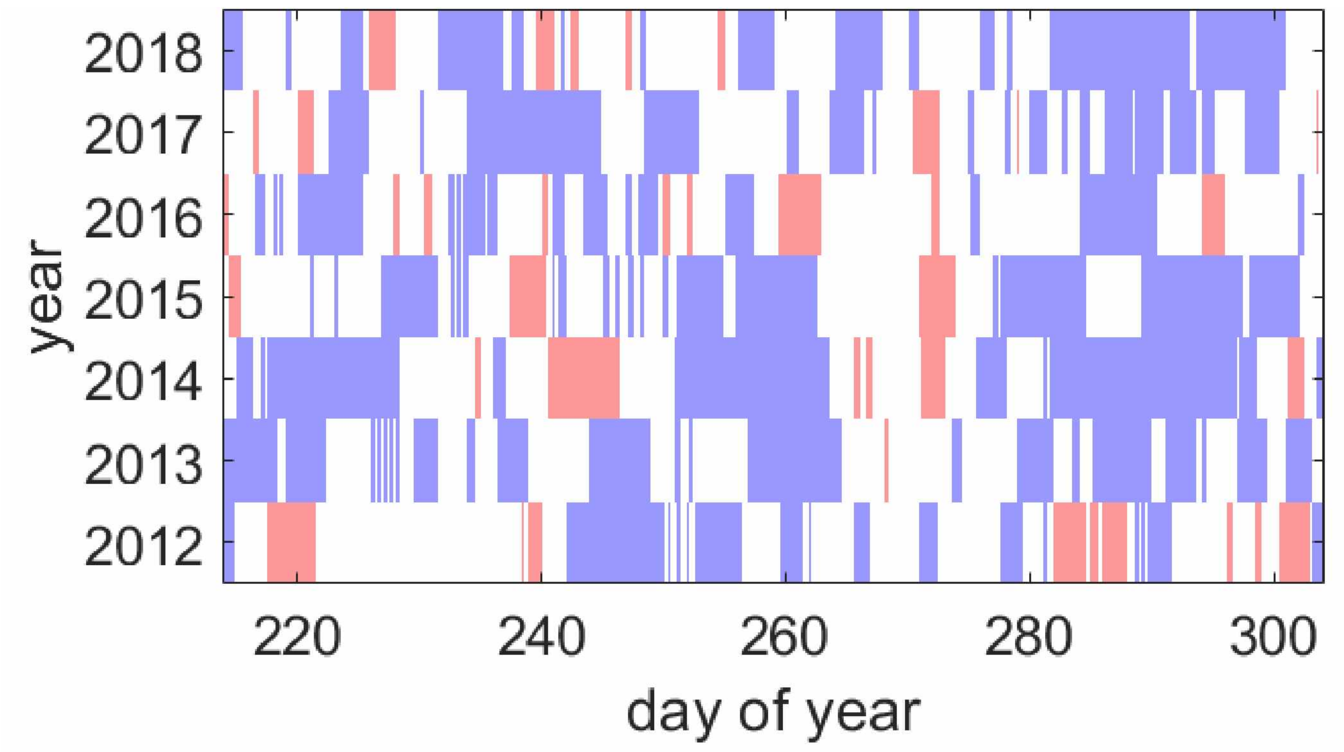

Figure 4.12. Temporal Map of Wind Regimes for 2012–2017 Summers. Shown in red and blue are the opposing and supporting wind events from spatial means of ERA-Interim 6-hourly 10 m wind analysis over the 12km model region. The criterion used to establish the supporting wind events omits the temporal restrictions.

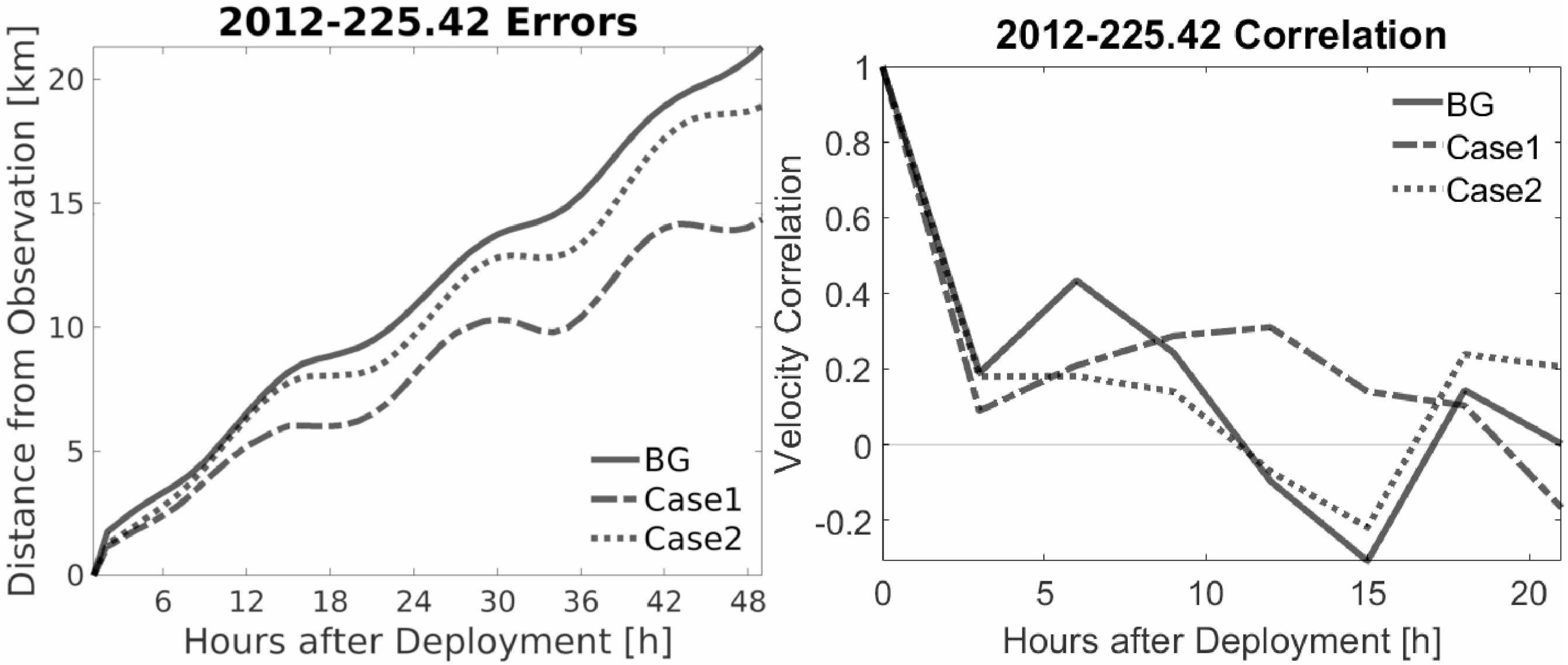

Figure 4.13. Shoal Region Model-Drifter Position and Velocity Correspondence. Correspondence between forecast and drifters deployed on 2012-225.42 is shown here, with calculated distance from observation in the left panel and timeseries of correlation $r(t)$ in the right panel.

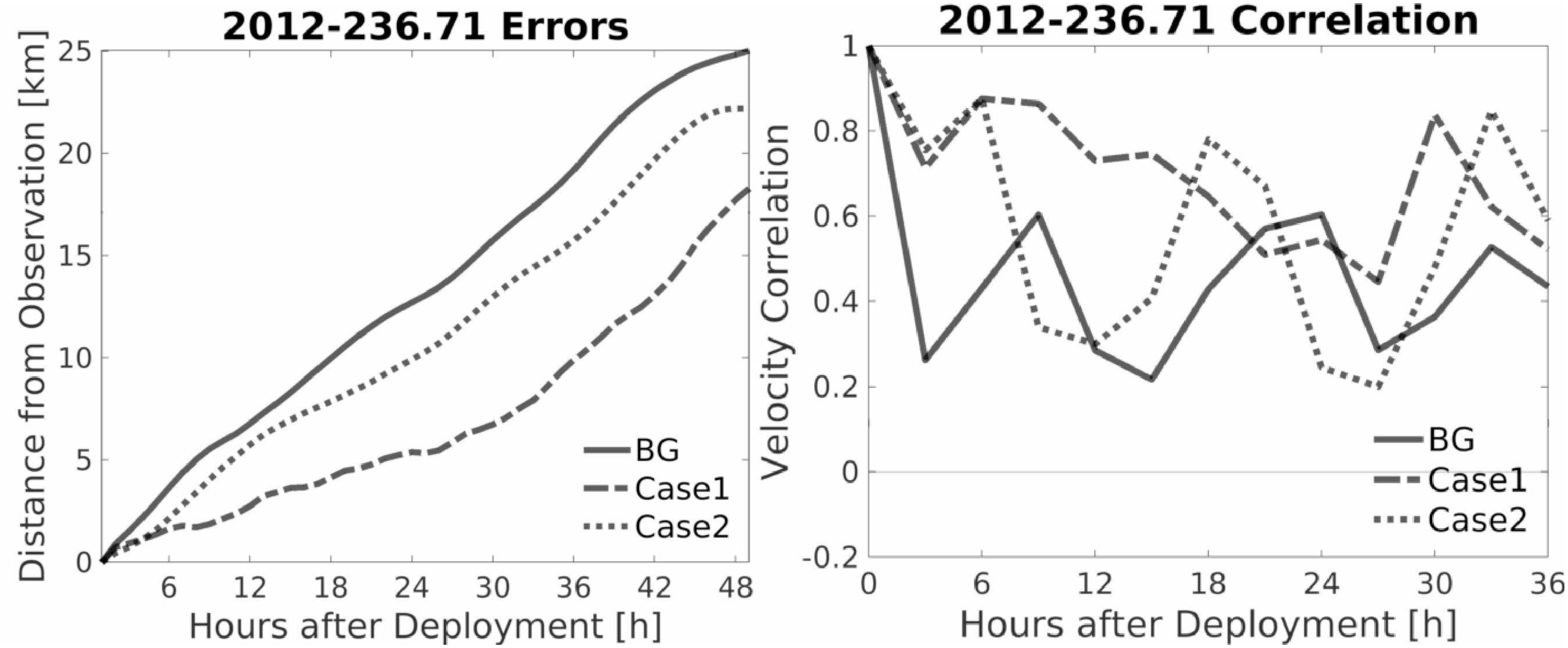

Figure 4.14. ACC Region Model-Drifter Position and Velocity Correspondence. Correspondence between forecast and drifters deployed on 2012-236.71 is shown, with the panels presented as in Figure 4.14.

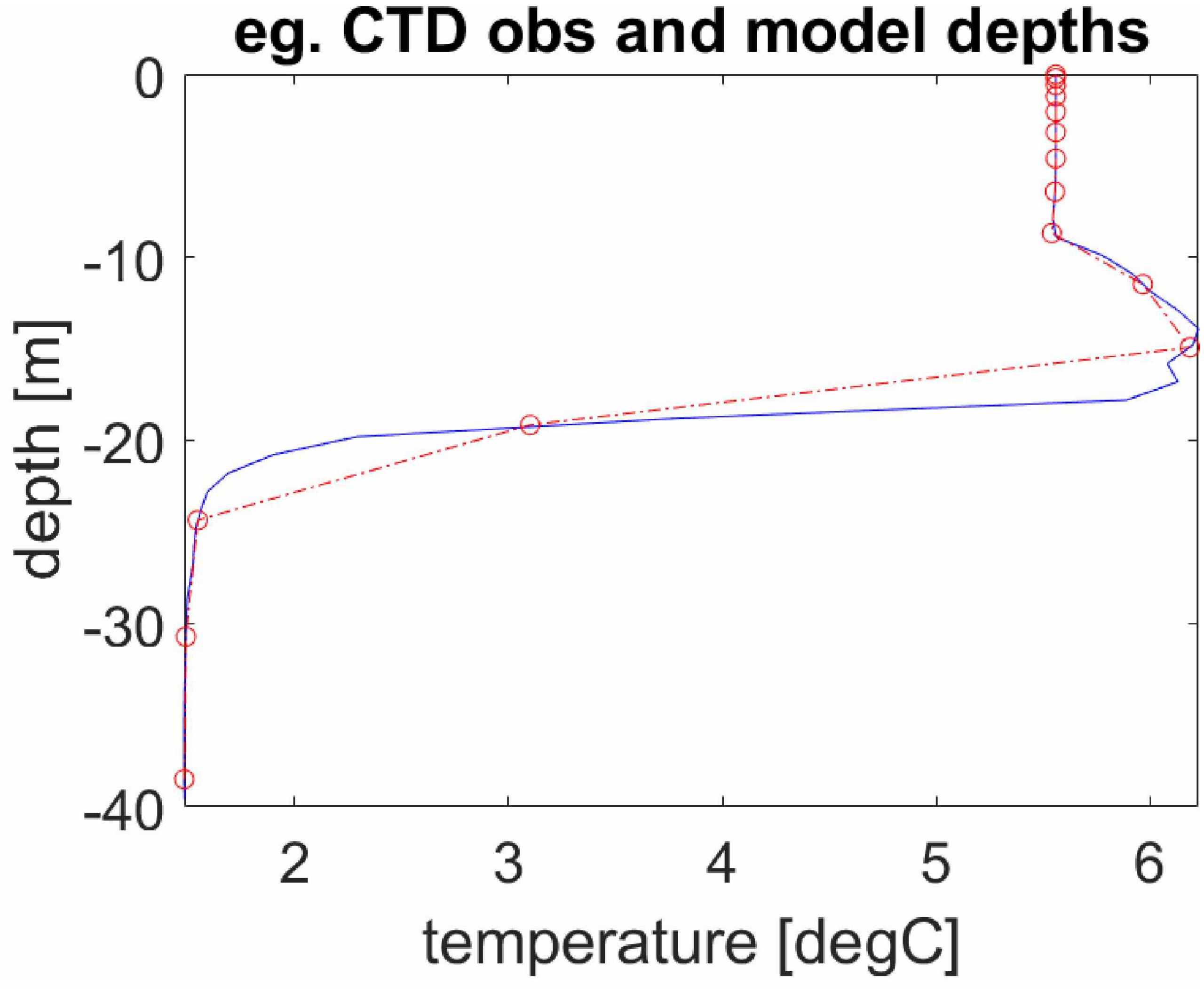

Figure 4.15. Example CTD observation and model representative. The blue curve shows temperature plotted against depth as represented in observational data. The projection onto modeled vertical coordinates using cubic spline interpolation is shown by the dashed red curve, with circles indicating values at ROMS vertical coordinate depths.

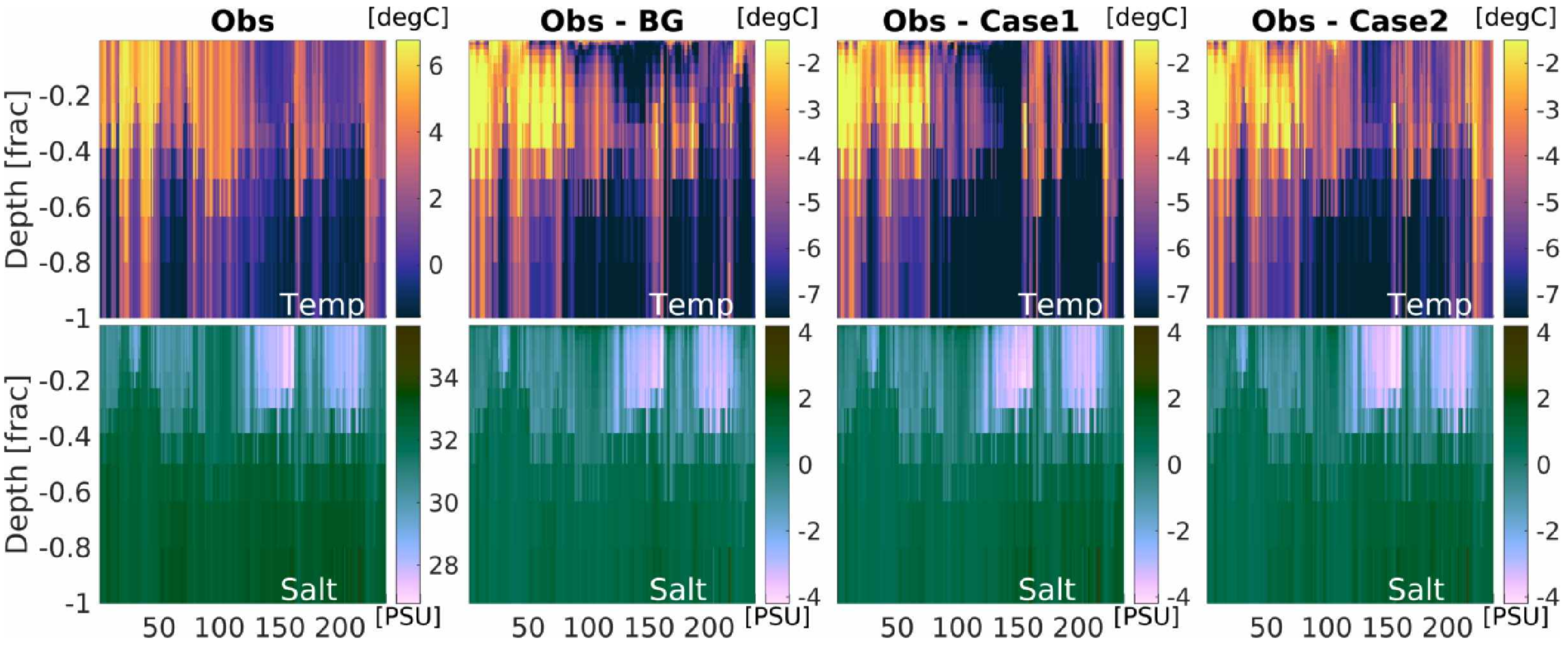

Figure 4.16. CTD Observations and associated Model Errors. The top row of panels shows temperatures and the bottom row shows salinities where the horizontal axes correspond to chronologically sorted CTD observations and the vertical axes to fraction of total depth. The four columns, left to right, show CTD observations and associated errors for the background model, Case 1, and Case 2, respectively. The horizontal axis limits correspond roughly to 2012-230–270, although the spacing is not uniform.

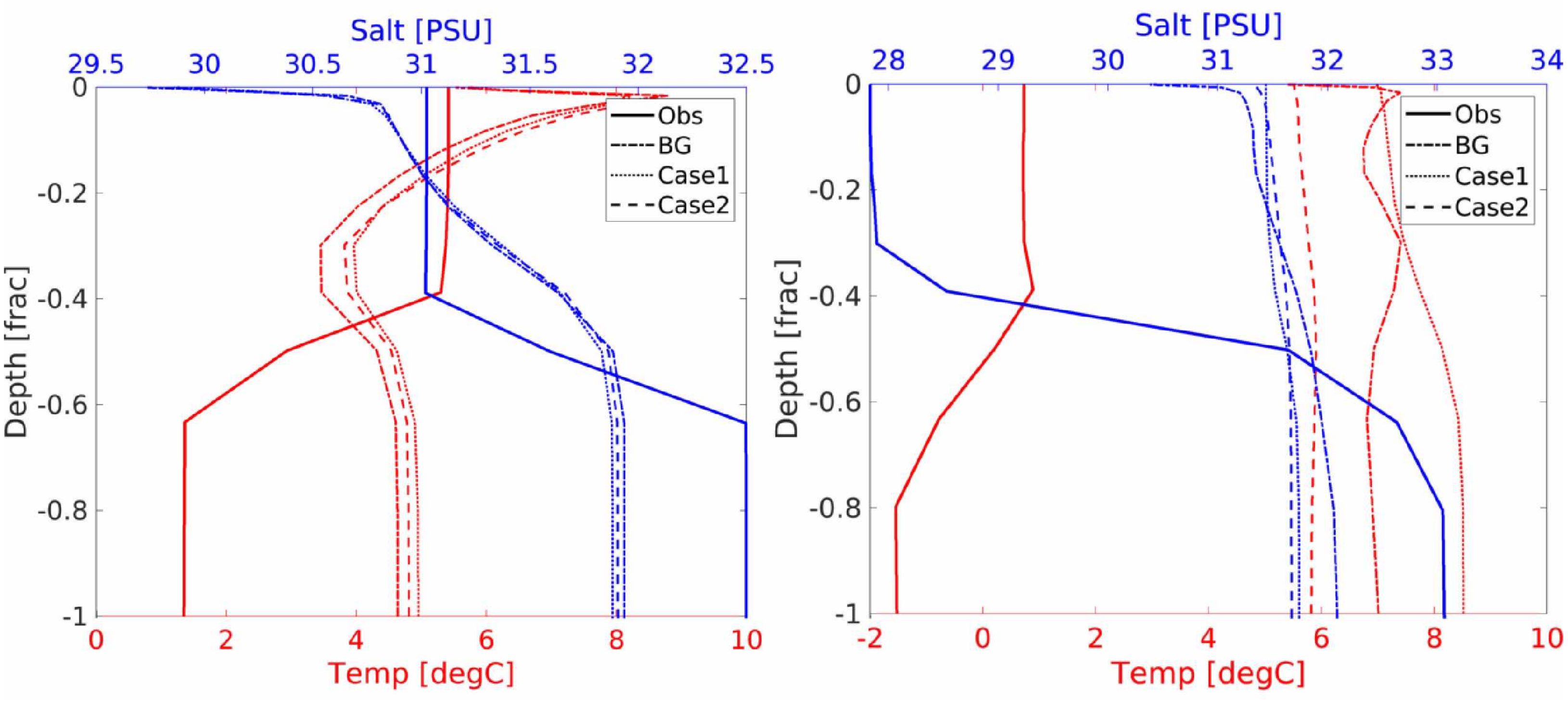

Figure 4.17. Two Example CTD and model T/S Profiles. The various temperature (red) and salinity (blue) profiles associated with CTD observations at ~jd230 (left) and ~jd270. CTD data, background forecast, Case 1 forecast, and Case 2 forecasts are shown by solid, dash-dot, dotted, and dashed lines, respectively. The difference is extreme, but illustrates the model T/S drift toward strongly biased uniform profiles.

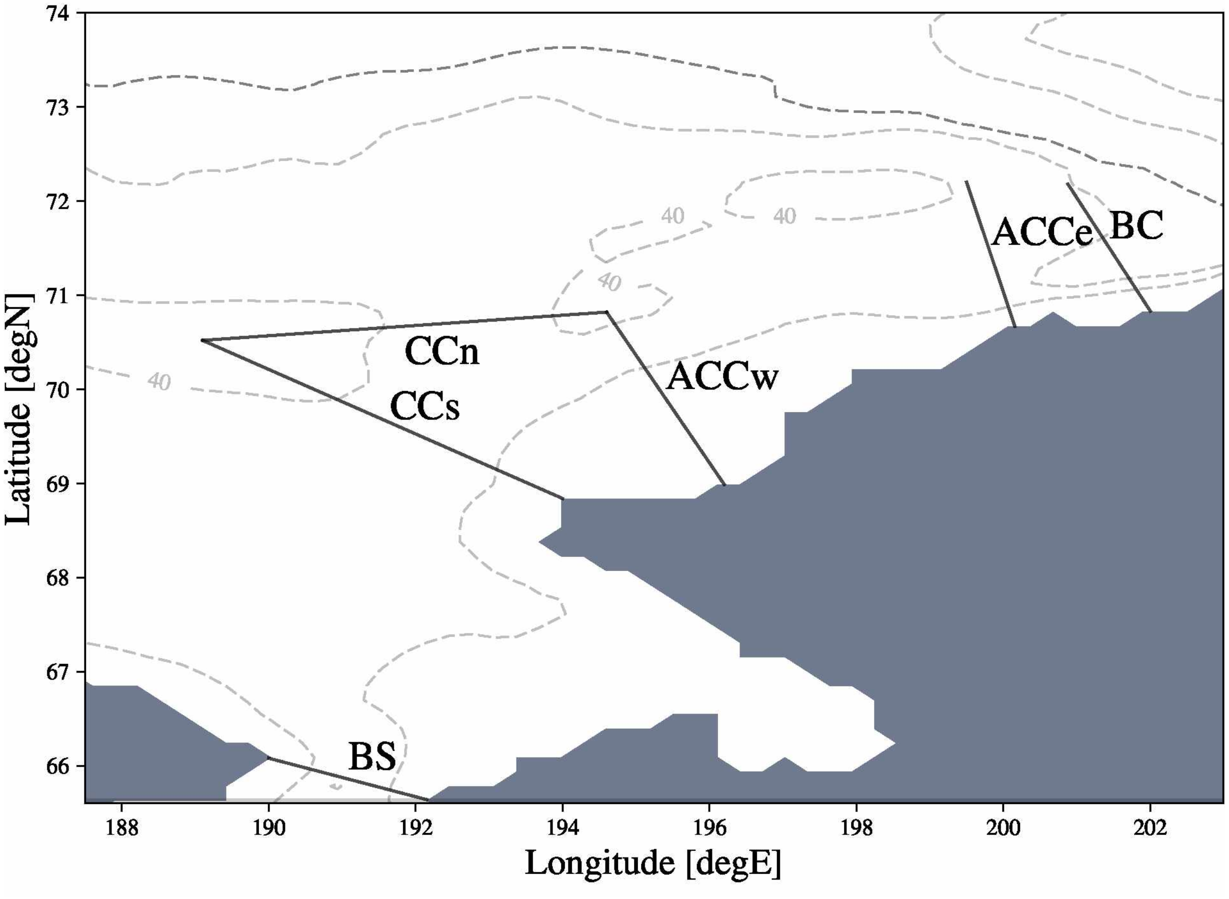

Figure 4.18. Map of Model Transects. The geographical locations of sections used for estimation of transports are shown with corresponding short identification labels for transects. Long Strait (LS) is far west of the region and is meridionally aligned at 178.8° between Wrangell and the Siberian coast. Labels are shown on the positively oriented side of each segment.

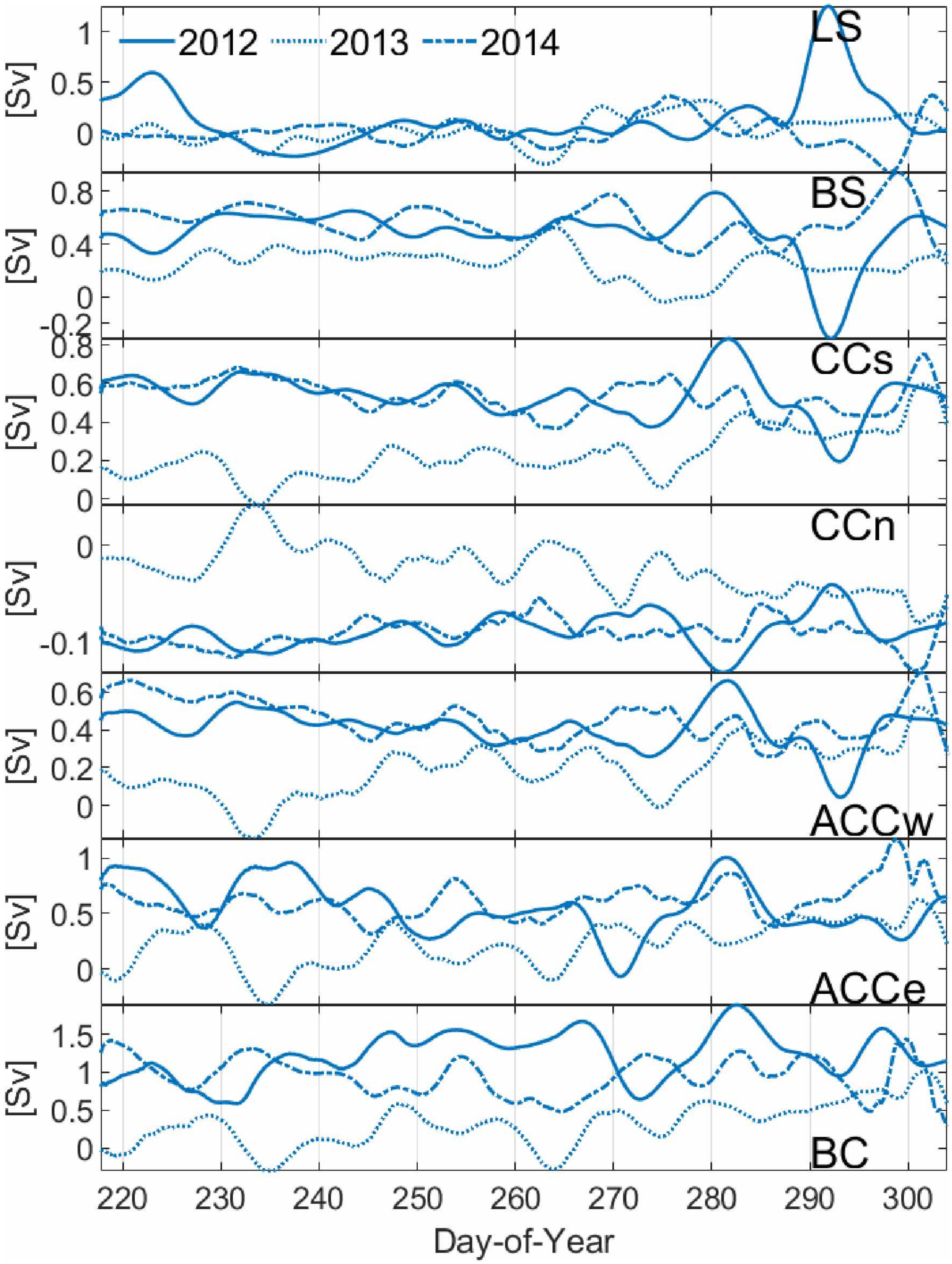

Figure 4.19. Seasonal Mass Transport Estimates 2012–2014. Mass transport estimates during 2012–2014 are shown for the various geographical transects. Plots of 2013 transport across the central channel and eastern coastal region look qualitatively different than 2012 and 2014 reconstructions. Plotted data is smoothed over 5-day intervals for presentability, while figures stated in the text use daily averages.

Bibliography

Ashkenazy, Y., and H. Gildor (2011), On the probability and spatial distribution of ocean surface currents, *Journal of Physical Oceanography*, *41*(12), 2295–2306.

Awaji, T., S. Masuda, Y. Ishikawa, N. Sugiura, T. Toyoda, and T. Nakamura (2003), State estimation of the North Pacific Ocean by a four-dimensional variational data assimilation experiment, *Journal of Oceanography*, *59*(6), 931–943.

Barth, A., J.-M. Beckers, A. Alvera-Azcárate, and R. H. Weisberg (2007), Filtering inertia-gravity waves from the initial conditions of the linear shallow water equations, *Ocean Modelling*, *19*(3), 204–218.

Bracco, A., E. P. Chassignet, Z. D. Garraffo, and A. Provenzale (2003), Lagrangian velocity distributions in a high-resolution numerical simulation of the North Atlantic, *Journal of Atmospheric and Oceanic Technology*, *20*(8), 1212–1220.

Brasseur, P. P., and J. A. Haus (1991), Application of a 3-D variational inverse model to the analysis of ecohydrodynamic data in the Northern Bering and Southern Chukchi Seas, *Journal of Marine Systems*, *1*(4), 383–401.

Brugler, E. T., R. S. Pickart, G. Moore, S. Roberts, T. J. Weingartner, and H. Statscewich (2014), Seasonal to interannual variability of the Pacific water boundary current in the Beaufort Sea, *Progress in Oceanography*, *127*, 1–20.

Burgers, G., P. Jan van Leeuwen, and G. Evensen (1998), Analysis Scheme in the Ensemble Kalman Filter, *Monthly Weather Review*, *126*(6), 1719–1724.

Chapman, R., L. Shay, H. Graber, J. Edson, A. Karachintsev, C. Trump, and D. Ross (1997), On the accuracy of HF radar surface current measurements: Intercomparisons with ship-based sensors, *Journal of Geophysical Research: Oceans*, *102*(C8), 18,737–18,748.

Chepurin, G. A., J. A. Carton, and D. Dee (2005), Forecast model bias correction in ocean data assimilation, *Monthly Weather Review*, *133*, 1328–1342, DOI: *10.1175/MWR2920.1*.

Coachman, L. K., L. K. Coachman, K. Aagaard, and R. Tripp (1975), *Bering Strait: the regional physical oceanography*, University of Washington Press.

Corlett, W. B., and R. S. Pickart (2017), The Chukchi slope current, *Progress in Oceanography*, *153*, 50–65, DOI: *10.1016/j.pocean.2017.04.005*.

Danielson, S. L., T. J. Weingartner, K. S. Hedstrom, K. Aagaard, R. Woodgate, E. Curchitser, and P. J. Stabeno (2014), Coupled wind-forced controls of the Bering-Chukchi shelf circulation and the Bering Strait throughflow: Ekman transport, continental shelf waves, and variations of the Pacific-Arctic sea surface height gradient, *Progress in Oceanography*, *125*, 40–61, DOI: *10.1016/j.pocean.2014.04.006*.

Danielson, S. L., E. L. Dobbins, M. Jakobsson, M. A. Johnson, T. Weingartner, W. Williams, and Y. Zarayskaya (2015), Sounding the northern seas, *Eos*, *96*.

Davis, R. E. (1985), Drifter observations of coastal surface currents during code: The statistical and dynamical views, *Journal of Geophysical Research: Oceans*, *90*(C3), 4756–4772.

Dee, D. P. (2005), Bias and data assimilation, *Quarterly Journal of the Royal Meteorological Society*, *131*(613), 3323–3343, DOI: *10.1256/qj.05.137*.

Dee, D. P., and A. M. Da Silva (1998), Data assimilation in the presence of forecast bias, *Quarterly Journal of the Royal Meteorological Society*, *124*(545), 269–295.

Evensen, G. (2003), The ensemble Kalman filter: Theoretical formulation and practical implementation, *Ocean dynamics*, *53*(4), 343–367.

ECMWF (European Center for Medium-Range Weather Forecasts. (2012), Era-interim project, single parameter 6-hourly surface analysis and surface forecast time series.

Francis, O. P., M. Yaremchuk, G. G. Panteleev, J. Zhang, and M. Kulakov (2017), Anomalous circulation in the Pacific sector of the Arctic Ocean in July–December 2008, *Ocean Modelling*, *117*, 12–27.

Gong, D., and R. S. Pickart (2015), Summertime circulation in the eastern Chukchi Sea, *Deep Sea Research Part II: Topical Studies in Oceanography*, *118*, 18–31.

Gustafsson, N. (2007), Discussion on 4D-Var or EnKF?, *Tellus A*, *59*(5), 774–777.

Houtekamer, P. L., and H. L. Mitchell (1998), Data assimilation using an ensemble Kalman filter technique, *Monthly Weather Review*, *126*(3), 796–811.

Ide, K., P. Courtier, M. Ghil, and A. C. Lorenc (1997), Unified Notation for Data Assimilation: Operational, Sequential and Variational (<Special Issue> Data Assimilation in Meteorology and Oceanography: Theory and Practice), *Journal of the Meteorological Society of Japan. Ser. II*, *75*(1B), 181–189.

Itoh, M., K. Shimada, T. Kamoshida, F. McLaughlin, E. Carmack, and S. Nishino (2012), Interannual variability of Pacific Winter Water inflow through Barrow Canyon from 2000 to 2006, *Journal of Oceanography*, *68*(4), 575–592, DOI: *10.1007/s10872-012-0120-1*.

Itoh, M., S. Nishino, Y. Kawaguchi, and T. Kikuchi (2013), Barrow Canyon volume, heat, and freshwater fluxes revealed by long-term mooring observations between 2000 and 2008, *Journal of Geophysical Research: Oceans*, *118*(9), 4363–4379.

Jazwinski, A. H. (2007), *Stochastic processes and filtering theory*, New York, NY: Courier Corporation.

Kalnay, E. (2003), *Atmospheric modeling, data assimilation and predictability*, New York, NY: Cambridge University Press.

Kim, S., R. Samelson, and C. Snyder (2009), Ensemble-based estimates of the predictability of wind-driven coastal ocean flow over topography, *Monthly Weather Review*, *137*(8), 2515–2537.

Le Dimet, F.-X., and O. Talagrand (1986), Variational algorithms for analysis and assimilation of meteorological observations: theoretical aspects, *Tellus A: Dynamic Meteorology and Oceanography*, *38*(2), 97–110.

Luchin, V., and G. Panteleev (2014), Thermal regimes in the Chukchi Sea from 1941 to 2008, *Deep Sea Research Part II: Topical Studies in Oceanography*, *109*, 14–26.

Navon, I., and D. M. Legler (1987), Conjugate-gradient methods for large-scale minimization in meteorology, *Monthly Weather Review*, *115*(8), 1479–1502.

Okkonen, S. R., C. J. Ashjian, R. G. Campbell, W. Maslowski, J. L. Clement-Kinney, and R. Potter (2009), Intrusion of warm Bering/Chukchi waters onto the shelf in the western Beaufort Sea, *Journal of Geophysical Research: Oceans*, *114*(C1).

Panteleev, G., M. Yaremchuk, and D. Nechaev (2009), Optimization of mooring observations in Northern Bering Sea, *Dynamics of Atmospheres and Oceans*, *48*(1-3), 143–154.

Panteleev, G., D. A. Nechaev, A. Proshutinsky, R. Woodgate, and J. Zhang (2010), Reconstruction and analysis of the chukchi sea circulation in 1990–1991, *Journal of Geophysical Research: Oceans*, *115*(C8).

Panteleev, G., M. Yaremchuk, P. J. Stabeno, V. Luchin, D. A. Nechaev, and T. Kikuchi (2011), Dynamic topography of the Bering Sea, *Journal of Geophysical Research: Oceans*, *116*(C5).

Panteleev, G., M. Yaremchuk, V. Luchin, D. Nechaev, and T. Kukuchi (2012), Variability of the Bering Sea circulation in the period 1992–2010, *Journal of oceanography*, *68*(4), 485–496.

Panteleev, G., M. Yaremchuk, O. Francis, and T. Kikuchi (2013), Configuring high frequency radar observations in the Southern Chukchi Sea, *Polar Science*, *7*(2), 72–81.

Panteleev, G., M. Yaremchuk, J. Stroh, P. Posey, D. Hebert, and D. A. Nechaev (2015), Optimization of the High-Frequency Radar Sites in the Bering Strait Region, *Journal of Atmospheric and Oceanic Technology*, *32*(2), 297–309.

Peralta-Ferriz, C., and R. A. Woodgate (2017), The dominant role of the East Siberian Sea in driving the oceanic flow through the Bering Strait-Conclusions from GRACE ocean mass satellite data and in situ mooring observations between 2002 and 2016, *Geophysical Research Letters*, *44*(22).

Pickart, R. S., L. J. Pratt, D. J. Torres, T. E. Whitledge, A. Y. Proshutinsky, K. Aagaard, T. A. Agnew, G. W. K. Moore, and H. J. Dail (2010), Evolution and dynamics of the flow through Herald Canyon in the western Chukchi Sea, *Deep Sea Research Part II: Topical Studies in Oceanography*, *57*(1), 5–26.

Pickart, R. S., G. W. Moore, C. Mao, F. Bahr, C. Nobre, and T. J. Weingartner (2016), Circulation of winter water on the Chukchi shelf in early Summer, *Deep-Sea Research Part II: Topical Studies in Oceanography*, *130*, DOI: *10.1016/j.dsr2.2016.05.001*.

Pires, C. A., O. Talagrand, and M. Bocquet (2010), Diagnosis and impacts of non-gaussianity of innovations in data assimilation, *Physica D: Nonlinear Phenomena*, *239*(17), 1701–1717.

Pisareva, M. N., R. S. Pickart, M. A. Spall, C. Nobre, D. J. Torres, G. W. Moore, and T. E. Whitledge (2015), Flow of pacific water in the western Chukchi Sea: Results from the 2009 RUSALCA expedition, *Deep-Sea Research Part I: Oceanographic Research Papers*, *105*, DOI: *10.1016/j.dsr.2015.08.011*.

Potter, R., T. Weingartner, D. Elizabeth, H. Statscewich, and P. Winsor (2014), Surface circulation patterns in the northeastern Chukchi Sea, in *Alaska Marine Science Symposium 2014, Anchorage, AK*, pp. 89.

Purser, R. J. (1984), A new approach to the optimal assimilation of meteorological data by iterative Bayesian analysis, in *Conference on Weather Forecasting and Analysis, 10 th, Clearwater Beach, FL*, pp. 102–105.

Purser, R. J., and D. F. Parrish (2003), A Bayesian technique for estimating continuously varying statistical parameters of a variational assimilation, *Meteorology and Atmospheric Physics*, *82*(1-4), 209–226, DOI: *10.1007/s00703-001-0583-x*.

Sakov, P., and M. Bocquet (2018), Asynchronous data assimilation with the EnKF in presence of additive model error, *Tellus A: Dynamic Meteorology and Oceanography*, *70*(1), 1414,545.

Sakov, P., G. Evensen, and L. Bertino (2010), Asynchronous data assimilation with the EnKF, *Tellus, Series A: Dynamic Meteorology and Oceanography*, *62*(1), 24–29, DOI: *10.1111/j.1600-0870.2009.00417.x*.

Shchepetkin, A. F., and J. C. McWilliams (2005), The regional oceanic modeling system (ROMS): a split-explicit, free-surface, topography-following-coordinate oceanic model, *Ocean modelling*, *9*(4), 347–404.

Sorenson, H. W. (1970), Least-squares estimation: from Gauss to Kalman, *IEEE spectrum*, *7*(7), 63–68.

Stewart, R. H., and J. W. Joy (1974), HF radio measurements of surface currents, in *Deep Sea Research and Oceanographic Abstracts*, vol. 21, pp. 1039–1049, Elsevier.

Talagrand, O. (2003), Bayesian estimation. optimal interpolation. statistical linear estimation, in R. Swinbank, V. Shutyaev, W.A. Lahoz (Eds.) *Data Assimilation for the Earth System*, pp. 21–35, Dordrecht: Springer Science & Business Media.

Teague, C. C., J. F. Vesecky, and Z. R. Hallock (2001), A comparison of multifrequency HF radar and ADCP measurements of near-surface currents during COPE-3, *IEEE Journal of Oceanic Engineering*, *26*(3), 399–405.

Thacker, W. C. (1989), The role of the Hessian matrix in fitting models to measurements, *Journal of Geophysical Research: Oceans*, *94*(C5), 6177–6196.

Weingartner, T., K. Aagaard, R. Woodgate, S. Danielson, Y. Sasaki, and D. Cavalieri (2005), Circulation on the north central Chukchi Sea shelf, *Deep Sea Research Part II: Topical Studies in Oceanography*, *52*(24), 3150–3174.

Weingartner, T., E. Dobbins, S. Danielson, P. Winsor, R. Potter, and H. Statscewich (2013), Hydrographic variability over the northeastern Chukchi Sea shelf in summer-fall 2008–2010, *Continental Shelf Research*, *67*, 5–22.

Weingartner, T., Y. C. Fang, P. Winsor, E. Dobbins, R. Potter, H. Statscewich, T. Mudge, B. Irving, L. Sousa, and K. Borg (2017a), The summer hydrographic structure of the Hanna Shoal region on the northeastern Chukchi Sea shelf: 2011–2013, *Deep-Sea Research Part II: Topical Studies in Oceanography*, *144*(August), 6–20, DOI: *10.1016/j.dsr2.2017.08.006*.

Weingartner, T. J., D. J. Cavalieri, K. Aagaard, and Y. Sasaki (1998), Circulation, dense water formation, and outflow on the northeast Chukchi Sea shelf, *Journal of Geophysical Research*, *103*(C4), 7647–7661.

Weingartner, T. J., R. A. Potter, C. A. Stoudt, E. L. Dobbins, H. Statscewich, P. R. Winsor, T. D. Mudge, and K. Borg (2017b), Transport and thermohaline variability in Barrow Canyon on the northeastern Chukchi Sea shelf, *Journal of Geophysical Research: Oceans*, *122*(5), 3565–3585.

Wikle, C. K., and L. M. Berliner (2007), A Bayesian tutorial for data assimilation, *Physica D: Nonlinear Phenomena*, *230*(1-2), 1–16, DOI: *10.1016/j.physd.2006.09.017*.

Williams, W. J., E. Shroyer, J. C. Kinney, M. Itoh, and W. Maslowski (2014), Shelf-break exchange in the Bering, Chukchi and Beaufort Seas, in J.M. Grebmeier and W. Maslowski (Eds.)*The Pacific Arctic Region*, pp. 133–165, New York, NY: Springer.

Winsor, P., and D. C. Chapman (2004), Pathways of Pacific water across the Chukchi Sea: A numerical model study, *Journal of Geophysical Research: Oceans*, *109*(C3).

Woodgate, R. A. (2018), Increases in the Pacific inflow to the Arctic from 1990 to 2015, and insights into seasonal trends and driving mechanisms from year-round Bering Strait mooring data, *Progress in Oceanography*, *160*, 124–154.

Woodgate, R. A., K. Aagaard, and T. J. Weingartner (2005), Monthly temperature, salinity, and transport variability of the Bering Strait through flow, *Geophysical Research Letters*, *32*(4).

Woodgate, R. A., K. M. Stafford, and F. G. Prahl (2015), A synthesis of year-round interdisciplinary mooring measurements in the Bering Strait (1990–2014) and the RUSALCA years (2004–2011), *Oceanography*, *28*(3), 46–67.

Wright, S., and J. Nocedal (1999), Numerical optimization, *Springer Science*, *35*(67-68), 7.

Zupanski, M. (2005), Maximum likelihood ensemble filter: Theoretical aspects, *Monthly Weather Review*, *133*(6), 1710–1726.

Zupanski, M., I. M. Navon, and D. Zupanski (2008), The Maximum Likelihood Ensemble Filter as a non-differentiable minimization algorithm, *Quarterly Journal of the Royal Meteorological Society*, *134*(633), 1039–1050.

General Conclusion

Geophysics, and more broadly many natural sciences, rely on practical knowledge from two distinct sources. First, there are numerical models which often solve systems of equations derived from time-forward discretizations of partial differential equations describing physical phenomenon. Such models are limited in resolution, make many simplifications, and often apply empirical parametrizations to unresolved processes. Second, observational data which arise from measurement processes applied to the external reality and, in addition to representing very limited knowledge of the full physical state, usually rely on a combination of empirical and analytical rules to relate them to state variables. For example, satellites do not actually measure sea-surface temperature; they measure limited bands of emitted or reflected electromagnetic spectra. These radiances are then model-transformed into representatives of temperature, which is itself a statistical representative of its net local kinetics of the water. This perspective maintains that knowledge from models and observations are inter-dependent and should not be treated independently of one another. The synthesis of the two sources together into a common stream is the aim of data assimilation (DA), whose practical application requires some knowledge of quantified uncertainty in model and observation information sources. Further, existing observational data products are not calibrated equally for all regions, and may be calibration-biased toward regions with abundant data. It is therefore important to better understand the source and distribution of uncertainties in observations and models alike for the purpose of improving future scientific work based on them and to view past works in an appropriate context.

This dissertation is a collection of works which emphasize observational data analysis and observation-informed modeling methodologies. The study region is centered on the Arctic Ocean (AO), particularly the portion strongly influenced by the Pacific Ocean. It has not focused on revealing new physical phenomenon, but rather on the use of numerical tools and methods for augmenting studies based on both data and modeling. It intends to communicate expertise in these topics sufficient to develop an independent research program focused on technical DA development or to collaborate with researchers engaged in applied research using numerical geophysical models.

Chapters 1 and 2 focused on data analysis of International Polar Year (IPY) surveys of AO, and the analysis and synthesis of IPY data is largely concluded. The decade since the multi-year IPY effort has seen the continued accumulation of data from many Arctic and sub-Arctic studies. Future work planned in this direction of research includes the production of a series of annual and seasonal snapshots of T/S in the AO for 2010–2017 by applying the distributed gridding method (*viz.* DIVA) to public collections of quality-controlled oceanographic data. Building the original analysis required the large set of IPY data, but the following analyses should require less, as supplying the IPY analysis as a first-guess state effectively conditions subsequent years' analysess on the IPY data. The potential use of these results would contribute to post-IPY climatologies and pan-AO trend analysis by comparing the series of post-IPY analyses. Secondarily, the combination of Chapters 1 and 2 present the need for improved SST background climatologies to inform satellite analyses, particularly in regions with irregular ice-cover and those previously occluded by ice.

Chapters 3 and 4 focused on data assimilation, a framework for combining models and observational data on the basis of objectively established criterion. The third chapter presented recently accepted results of ongoing work related to refining model sea ice state evolution on the basis of satellite data using flexible strength and stress parameters. The study was limited to one spatial dimension as realistic 2D sea ice applications are precluded by the need for a more complex numerical adjoint for those cases; this extension is presently pursued by funded collaborators with whom the author hopes for continued involvement.

Chapter 4 presents a statistical optimization of a regional oceanographic model to observed velocity data, which contrasts the deterministic variational inverse method of optimization in Chapter 3. The research was done under the guidance of the author's advisor without additional collaborators and constitutes the development of an original research program by the author. It is presently the only assimilation effort to use the high-frequency radar (HFR) array data in the Chukchi Sea region, and an extensive literature search also suggests it is the only oceanographic application of variational ensemble DA run in asynchronous mode. The resulting DA system is arguably suitable for use in the regional monitoring of contaminants arising from oil exploration/extraction or other maritime sources. The work intended to obtain more realistic results from the data-optimized analysis solution but was limited by significant errors in the background model. Efforts to refine the background model are ongoing with the goal of developing a practical system able to produce near-operational forecasts by ingesting data as it comes available.

This dissertation provides a basis for ongoing works by others in addition to the continuations mentioned above, particularly when it comes to the analysis of uncertainties in data and data-informed products. The closing of this work proposes a small assortment of possible, related future projects not immediately pursued by the author.

The abundant IPY dataset of T/S profiles, together with post-IPY data found in other assembled datasets, could be used to establish an updated background SST/S climatology for satellite products. This was not pursued here because estimation of surface variables from satellites is very sensor-dependent and the works herein focused on the analysis products rather than primitive raw data. In this regard, one also notes that there is little existing work done in the way of refining satellite-to-surface empirical calibration specific to the Arctic shelves. That is, technical documentation of satellite products often note that transformation of brightness temperature to SST depends on other variables including sea-surface salinity, surface roughness, and near-surface stratification. Yet in the course of preparing Chapter 1, the author found no literature discussing the co-resolution of SST and SSS. Technical construction of an error covariance model for the joint resolution of SST/S from multi-band satellite sensors appears to be missing from the literature and would be very useful to product-makers. In the event that such works do exist, their empirical bases may not be well-calibrated to the AO and it is worthwhile to improve them on in situ data. Additionally, the freshwater distribution of the AO is changing due to many processes as discussed in Chapter 2. It may be worthwhile to generate a surface freezing-temperature reference dataset for the AO which reflects its geographic and seasonal variations to better inform satellite analysis which often prescribes a spatiotemporal constant value in unobservable regions influenced by sea ice. Further, literature discussing the diurnal (*i.e.* solar driven) SST cycle in the Arctic regions is also sparse, presumably due to limited observations. An observational study of diurnal cycles over the Chukchi shelf might be beneficial for regional biologists, although the finding may not be interesting because of high winds during the ice-free season.

With regard to the data assimilation projects presented, the presented methodologies involved the use of data to improve models. However, one may also take a contrarian perspective and use assimilative models to deduce HFR observations at a higher resolution. For example, the HFR data of Chapter 4 are supplied on a 6 km grid and often contain signals with strong divergences and cross-isobath flows poorly resolved in the model; an assimilative model reconstruction could present approximations to the data at sub-observation scales for further studies related to regional Ekman pumping, effects of wind-stress curl, and the relationship of observed wind and observed ocean response to their artificial numerical model counterparts. On the more technical side of DA literature, there are very few papers regarding the temporal structure of error covariance associated with asynchronously-represented observation processes[3], and no surveyed literature clearly address bias correction in variational ensemble assimilation schemes. The method presented in

---

[3] Chapter 4 assumes that observation errors are temporally independent.

Chapter 4 would benefit strongly from such developments. Finally, the author notes that while DA is underpinned by a rigorous mathematical framework, its practical implementation is approximate and requires conceding to necessary simplifications and *ad hoc* suppositions. Many open questions remain regarding the validity of these application-specific assumptions.